Reservoir Characterisation of the Tirrawarra Sandstone in the Moorari and Fly Lake Fields, Southern Cooper Basin, South Australia

M. R. Rezaee

National Centre for Petroleum Geology & Geophysics (NCPGG), The University of Adelaide

Thesis submitted to the University of Adelaide in fulfilment of the requirement for the degree of Doctor of Philosophy

November 1996

TABLE OF CONTENTS

LIST OF FIGURES

LIST OF TABLES

LIST OF PLATES

APPENDICES

Rezaee, M.R., and Griffiths, C.M., 1996a. Pore Geometry Controls on Porosity and Permeability in the Tirrawarra Sandstone Reservoir, Cooper Basin, South Australia. *AAPG Annual Convention, San Diego, May 19-22, 1996.*

Rezaee, M.R., and Griffiths, C.M., 1996b. Porosity from Sonic Log in Kaolin-bearing Sandstones: A case study in the Tirrawarra Sandstone reservoir, Cooper Basin, Australia. *17th European Formation Evaluation Symposium,* The Netherlands, 3 - 7 June 1996, paper E-17.

Rezaee, M.R., and Griffiths, C.M., 1996c. Water saturation (S_W) of Kaolin-bearing sandstones: A case study in the Tirrawarra Sandstone reservoir, Cooper Basin, Australia. *17th European Formation Evaluation Symposium,* The Netherlands, 3 - 7 June 1996, paper E-12.

Rezaee, M.R., and Lemon, N., 1996a. Petrophysical Evaluation of Kaolinite-bearing Sandstones: I: Water saturation (S_W), an example of the Tirrawarra Sandstone reservoir, Cooper Basin, Australia. *Society of Petroleum Engineers* paper 37023, p. 539-549.

Rezaee, M.R., and Lemon, N., 1996b. Influence of depositional environment on diagenesis and reservoir quality: Tirrawarra Sandstone reservoir, southern Cooper Basin, Australia. *Journal of Petroleum Geology*, v. 19, p. 369-391.

Rezaee, M.R., and Lemon, N., 1996c. Controls on Pore Geometry in the Tirrawarra Sandstone Reservoir, Cooper Basin, Australia. *Petroleum Exploration Society of Australia Journal,* v. 24, p. 125-146.

Rezaee, M.R., and Lemon, N., 1997. Estimation of Effective Porosity, Tirrawarra Sandstone, Cooper Basin, South Australia. *Australian Society of Exploration Geophysics Bulletin,* in press.

Rezaee, M.R., and Schulz-Rojahn, J.P., 1996. Application of quantitative back-scattered electron image analysis in isotope interpretation of siderite cement: Tirrawarra Sandstone reservoir, Cooper Basin (Australia), *in* Morad, S., (ed.), Carbonate Cementation in sandstones*: International Association of Sedimentologists Special Publication*, in press.

Rezaee, M.R., and Tingate, P.R., 1996a. Precipitation temperatures and origin of quartz cement and its influence on the Tirrawarra Sandstone reservoir quality, southern Cooper Basin, South Australia. *Geological Society Of Australia, Abstract No.41*, p.362. *13th Australian Geological Convention, Canberra, February, 1996.*

Rezaee, M.R., and Tingate, P.R., 1996b. Quartz Cement Trace Element Composition: A Key to Reveal the Origin of Silica?, *International Association of Sedimentologists Workshop* (Belfast), 13-14 May, 1996.

Rezaee, M.R., and Tingate, P.R., 1997. Origin of the quartz cement, Tirrawarra Sandstone, Southern Cooper Basin, South Australia. *Journal of Sedimentary Research,* v. 67, p. 168-177.

Rezaee, M.R., Lemon, N., and Seggie, R., 1997. Tectonic fingerprints in siderite cement, Tirrawarra Sandstone, southern Cooper Basin, South Australia. *Geological Magazine*, v. 133 (7), in press.

Appendix 2 Point-count data

Appendix 3 XRD results

Appendix 4 Electron microprobe results of siderite

Appendix 5 Electron microprobe results of quartz

Appendix 6 Oxygen and carbon stable isotope results

Appendix 7 Fluid inclusions microthermometry results

Appendix 8 Mercury injection capillary pressures data

Appendix 9 CEC data

Statement of authenticity and availability

This thesis contains no material which has been accepted for the award of any other degree or diploma in any university or other tertiary institution and, to the best of my knowledge and belief, contains no material previously published or written by another person, except where due reference has been made in the text.

I give consent to this copy of my thesis, when deposited in the University Library, being available for loan and photocopying.

Mohammad Reza Rezaee

21-11-96

Reservoir Characterisation of the Tirrawarra Sandstone in the Moorari and Fly Lake Fields, Southern Cooper Basin, South Australia

Summary

This study examines the depositional and diagenetic controls on reservoir quality of the oil-bearing Permian Tirrawarra Sandstone in the Cooper Basin, South Australia. A new depositional classification of the unit is presented, together with prediction of reservoir quality. A detailed diagenetic study of the unit has been made, including models for the formation of quartz and siderite cements. The depositional and diagenetic data have been integrated with log data to produce new algorithms for calculating effective porosity and effective water saturation in kaolin-bearing sandstones.

Seven facies associations are recognised in the Tirrawarra Sandstone in the Moorari and Fly Lake Fields. These facies associations are interpreted to have been deposited in seven depositional environments including braid-delta (medial & distal), back barrier marsh, beach barrier, lacustrine, meandering fluvial and aeolian environments. Each sedimentary environment has a characteristic detrital composition controlled by its distance from the sedimentary source and the energy of the depositional environment. The relative proportions of quartz grains and rock fragments vary considerably between each sedimentary environment. The sandstone composition strongly influences the diagenetic history and subsequent reservoir quality.

The most important diagenetic processes which have modified porosity in the Tirrawarra Sandstone are mechanical compaction and quartz cementation. Mechanical compaction, evaluated by a compaction index equation, is greater in sandstones rich in rock fragments, whereas quartz cement is more developed in the quartz-rich sandstones. In this study a quantitative estimation of sandstone composition control on diagenetic events has made it possible to predict the reservoir quality of the Tirrawarra Sandstone for different depositional environments.

Based on fluid inclusion and electron microprobe analyses and CL observations, three zones of quartz cement were recognised. The first zone (Z1), formed at about 65°C, has a positive effect on reservoir quality and is derived from early dissolution of feldspar grains by acidic meteoric water flushing during late Triassic tectonic activity. The second zone of quartz cement (Z2), formed at about 100°C, originated from late dissolution of feldspar grains by organic acids generated during kerogen maturation. The third zone of quartz cement (Z3), precipitated after oil migration at about 130°C, originated mostly from stylolitization and pressure dissolution of quartz grains. The first zone of quartz cement prevented subsequent compaction and had a positive effect on the Tirrawarra Sandstone reservoir quality, whereas the later zones occluded remaining porosity.

The only carbonate cement present in the Tirrawarra Sandstone is siderite. Application of the back-scattered electron image analysis technique, together with bulk-rock isotope and fluid inclusion studies, has led to the identification of three main

generations of siderite cement. The first and second siderite cement generations were each followed by at least one dissolution event. The first generation of siderite (S1) is an homogeneous Fe-rich siderite with a $\delta^{13}C$ signature of +1.45‰, which probably formed during low-temperature methanogenesis (≤ 30°C). The second generation of siderite cement (S2) is an Mg-rich, inhomogeneous siderite characterised by complex zoning, with a $\delta^{13}C$ signature of -8.5‰. This siderite cement is thought to have formed mainly in association with the decarboxylation of organic matter at temperatures between 64 and 76°C. The third and final siderite precipitation event (S3) produced an Mg-rich, evenly banded, pore-filling siderite with average $\delta^{13}C$ of -11‰. This siderite is also interpreted to have formed during kerogen maturation, albeit at more elevated temperatures (98-110°C). The results of this study show that organic processes controlled siderite cementation over a range of different burial conditions in the study area. Integrating video-imaging and image analysis software provides an efficient means of quantifying the different siderite cement generations seen under the BSE. The results of this investigation show that caution must be exercised in the interpretation of bulk-rock isotope signatures. This study has produced a new method which enables the determination of end-member $\delta^{18}O$ and $\delta^{13}C$ compositions of individual cement generations in cases where pure, or nearly pure samples of end-member carbonate cement generations are not available for isotope analysis. Since the method can be semi-automated, the technique provides a potentially powerful tool for improved bulk-rock isotope interpretations in clastics containing multi-generation carbonate cements.

It appears that siderite cements in the Tirrawarra Sandstone record tectonic activity in the form of irregular growth and dissolution highlighted by compositional zoning with stages of strong dissolution recording particularly active times when pore waters changed composition dramatically. Some zoning could be related in part to tectonic pulses. The heterogenous, pitted and zoned S2 is thought to have formed during a time of active tectonism in the Cooper Basin whereas the evenly banded nature of S3 suggests that it precipitated during a quiet tectonic period when pore waters remained relatively constant.

The temperature recorded by each of the siderite stages allows their precipitation to be tied to a burial history curve and, by making some simple assumptions about that history, the timing of cementation can be estimated. This can be a additional tool for calibrating the thermal history of an area.

The main clay minerals present in the Tirrawarra Sandstone are kaolinite and illite. Illite largely formed from the alteration of labile components of rock fragments. Kaolinite formed during two stages. The first stage formed relatively early, at temperatures around 60°C, when acidic meteoric water invaded the reservoir and led to dissolution of feldspar grains. The second generation of kaolinite formed during late dissolution of feldspar grains by organic acids during kerogen maturation, at temperatures around 80°C. Back-scattered electron image analysis indicated an average of 20% microporosity is associated with kaolinite in the Tirrawarra Sandstone.

Tirrawarra Sandstone samples can be grouped into eight classes. The classes are separated according to the relative proportions of different kinds of porosity (microporosity, and primary and secondary macroporosity). The reservoir quality increases from class eight to class one and the classes have a predictable relationship with the sedimentary environment. Class one samples, associated with meander, aeolian or beach-barrier environments, have primary macroporosity with partial quartz cement.

Class eight, on the other hand, associated with a braid-delta environment, is dominated by microporosity.

Integration of petrographical and wireline log data led to the introduction of a new empirical equation for porosity determination from sonic log of the Tirrawarra Sandstone. The plot of sonic porosity, derived from the new equation, versus core porosity shows an r^2 value of 0.8, remembering that total porosity is being calculated using this equation. Knowing the amount of microporosity, however, it is possible to estimate the amount of macroporosity. By knowing the volume of clay and the percentage of associated microporosity, it is possible to determine the amount of macroporosity in the Tirrawarra Sandstone. This investigation also indicates that rock parameters such as composition, cementation and clay content have a clear and measurable effect on acoustic transit time. The rock parameters which affect transit time, also influence porosity, but for sandstones with a given composition, the most important parameter controlling acoustic transit time is porosity.

In this study a new equation is introduced to estimate effective water saturation in the Tirrawarra Sandstone. As the equation is based on integration of resistivity and sonic log from wells in the Moorari and Fly Lake fields where obtaining the volume of clay is difficult and unreliable, it may be useful for estimation of water saturation. This equation, which reduces calculated water saturation by about 10% for Tirrawarra Sandstone, is likely to be applicable for other kaolinite-bearing sandstones.

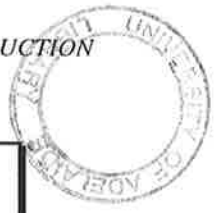

CHAPTER ONE

INTRODUCTION

1.1 Introduction

The Permo-Carboniferous to Triassic Cooper Basin in central Australia and Queensland (Fig. 1.1) is one of the major onshore petroleum provinces in Australia. In excess of 6 TCF (170 Tm^3) gas and 300 MMSTB (48 ML) gas condensate and 2000 KL of oil have been estimated in more than 110 gas and oil fields in the Cooper Basin (Heath, 1989; Laws, 1989). The basin fill has maximum thickness of 1300m and consists dominantly of lacustrine-fluvial deposits with local glacio-fluvial and rare paraglacial aeolian sediments (cf. Kapel, 1966, 1972; Gatehouse, 1972; Battersby, 1976; Thornton, 1979; Stuart, 1976; Williams et al., 1985; Fairburn, 1989).

As the basin is in a mature phase of exploration, structural prospects are decreasing in number and the focus is on stratigraphic features. A detailed knowledge of depositional environments and the controls on diagenetic processes is now essential to determine the reservoir quality of each formation in the basin. The Tirrawarra Sandstone, the object of this study, is one of the major oil and gas targets in the Cooper Basin. The scope of this study includes detailed characterisation of the Tirrawarra Sandstone, in terms of the control by depositional environment on diagenetic events, and in turn on the porosity and permeability, and the integration of petrographic data with wire-line log information in the Moorari and Fly Lake Fields.

1.2 Research Objectives

The prime objectives of this research include:

- recognition of depositional environments of the Tirrawarra Sandstone in the Moorari and Fly Lake Fields,
- timing of the diagenetic events with particular reference to the timing of hydrocarbon migration,

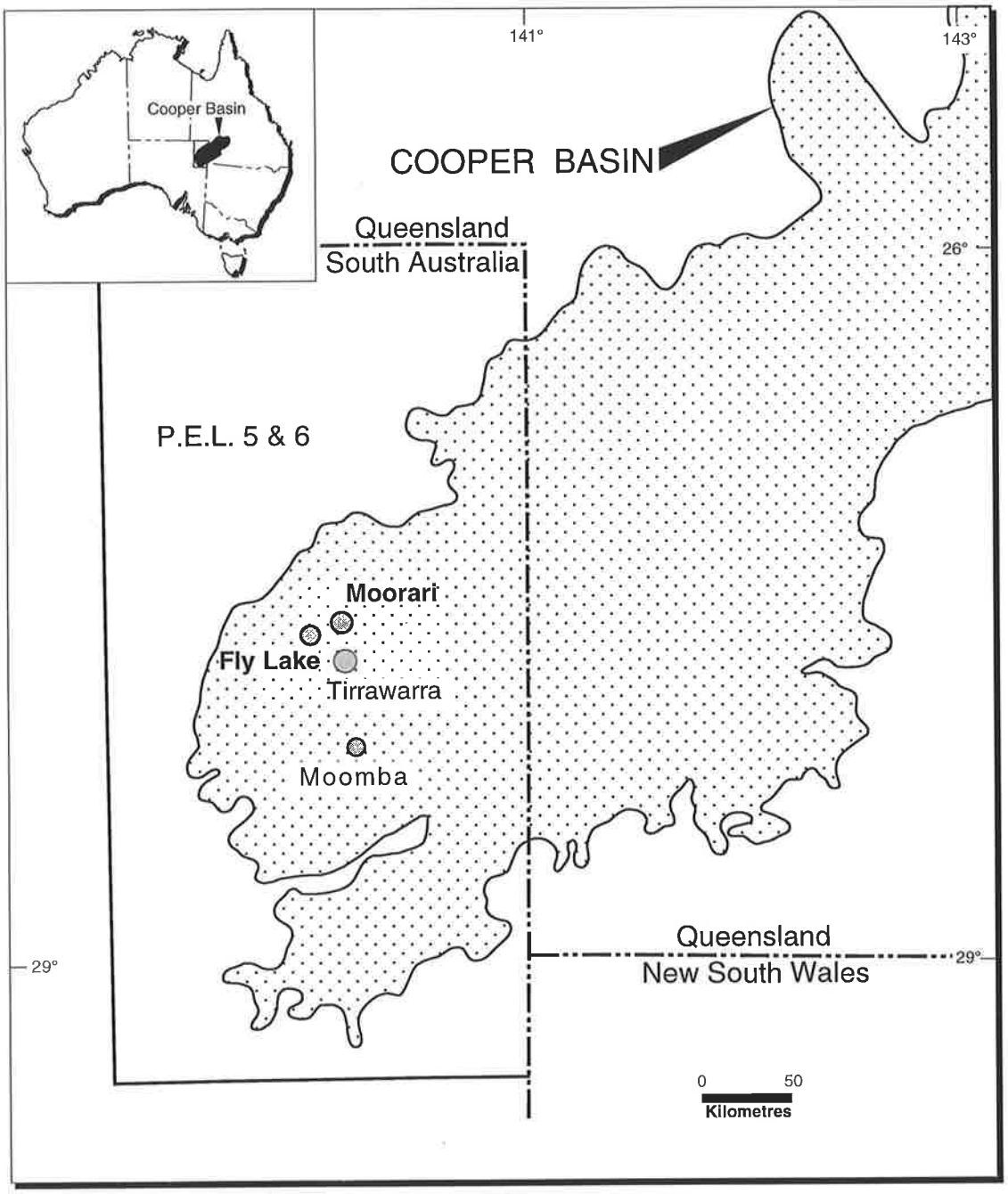

Figure 1.1 - Location map of the Moorari and Fly Lake Fields. These fields occur in Petroleum Exploration License 5 & 6 in the Cooper Basin.

- quantitative estimation of depositional environments controls on the diagenetic events,
- quantitative estimation of diagenetic controls on the reservoir quality,
- porosity and permeability trends and classification of Tirrawarra Sandstone samples based on pore geometry,
- integration of petrographic data with wire-line log information in order to enhance log analysis of the Tirrawarra Sandstone.

1.3 Previous studies

There have been few previous investigations regarding reservoir characterisation of the Tirrawarra Sandstone in terms of the influence of depositional environments on diagenetic events and reservoir quality or the integration of rock data and geophysical log information. Martin (1981, 1984) examined the Tirrawarra Sandstone in the Tirrawarra, Fly Lake and Moorari Fields. He described mineralogy, diagenetic processes and porosity and permeability trends and suggested quartz cementation and the formation of authigenic clay minerals as the most important diagenetic factors responsible for porosity reduction in the Tirrawarra Sandstone. Pianalto (1985) studied the petrography of the Tirrawarra Sandstone in the Tirrawarra Field. Bever et al. (1987) described diagenetic events in the Tirrawarra Sandstone of the Tirrawarra and Moorari Fields. They pointed to compaction as the most important factor for permeability reduction. Wild (1987) established a diagenetic sequence for the Tirrawarra Sandstone in the Tirrawarra and Merrimelia Fields. She concluded that compaction and quartz cementation were the most important diagenetic processes that reduced reservoir quality. One of the comprehensive regional studies concerning controls on the porosity and permeability of Permian sandstones is provided by Schulz-Rojahn (1991). Seggie et al. (1994) divided Tirrawarra Sandstone in the Tirrawarra Field to several flow units and described each in forms of depositional environment, petrographical and petrophysical characteristics.

The published results from the present study is shown in Appendix 1.

1.4 Study area

The Cooper Basin, located in northeastern South Australia and southwestern Queensland, is a northeast-trending structural depression covering an area of approximately 130000 km^2. The basin is underlain unconformably by Early Paleozoic marine and volcanic rocks of the Warburton Basin (Battersby, 1976; Gatehouse, 1986) and unconformably overlain by Jurassic-Cretaceous sediments of the Eromanga Basin (Exon & Senior, 1976; Senior et al., 1978; Armstrong & Barr, 1986) (Fig. 1.2).

The Tirrawarra Sandstone in the Moorari and Fly Lake Fields are the target of this study. The Moorari and Fly Lake Fields occur in the central Patchawarra Trough of the southern Cooper Basin which is separated from the rest of the basin by the Gidgealpa-Merrimelia-Innamincka trend (GMI trend), (Stuart et al., 1988).

Eight wells of the Moorari Field and six wells from the Fly Lake Field (Table 1.1) were selected for this study (Fig. 1.3). The selected wells have been extensively cored with more than 1270 feet of core available.

Table 1.1 - List of the wells, core numbers and intervals which sampled for this study.

Well	Core	Interval (Feet)
Moorari 1	3	9594 - 9461
Moorari 2	4	10090 - 10150
Moorari 3	4	9399 - 9457
Moorari 3	5	9457 - 9511
Moorari 4	3	9447 - 9494
Moorari 4	4	9494 - 9525
Moorari 4	5	9525 - 9553
Moorari 4	6	9553 - 9564
Moorari 4	7	9564 - 9581
Moorari 5	2	9458 - 9488
Moorari 5	3	9488 - 9492
Moorari 5	4	9506 - 9537
Moorari 5	5	9537 - 9567
Moorari 6	1	9675 - 9693
Moorari 6	2	9719 - 9749
Moorari 6	3	9749 - 9809
Moorari 7	2	9589 - 9619
Moorari 7	3	9619 - 9634
Moorari 7	4	9634 - 9655
Moorari 9	-	9732 - 9827
Flv Lake 1	7	9333 - 9392
Fly Lake 1	8	9393 - 9397
Fly Lake 1	8	9397 - 9434
Fly Lake 2	7	9477 - 9537
Fly Lake 2	8	9537 - 9583
Fly Lake 2	8	9583 - 9597
Fly Lake 2	9	9597 - 9605
Fly Lake 3	8	9457 - 9535
Fly Lake 3	9	9535 - 9581
Fly Lake 3	9	9581 - 9594
Fly Lake 4	5	9414 - 9432
Fly Lake 4	6	9432 - 9441
Fly Lake 4	6	9441 - 9474
Fly Lake 5	2	9417 - 9493
Fly Lake 6	1	9373 - 9403

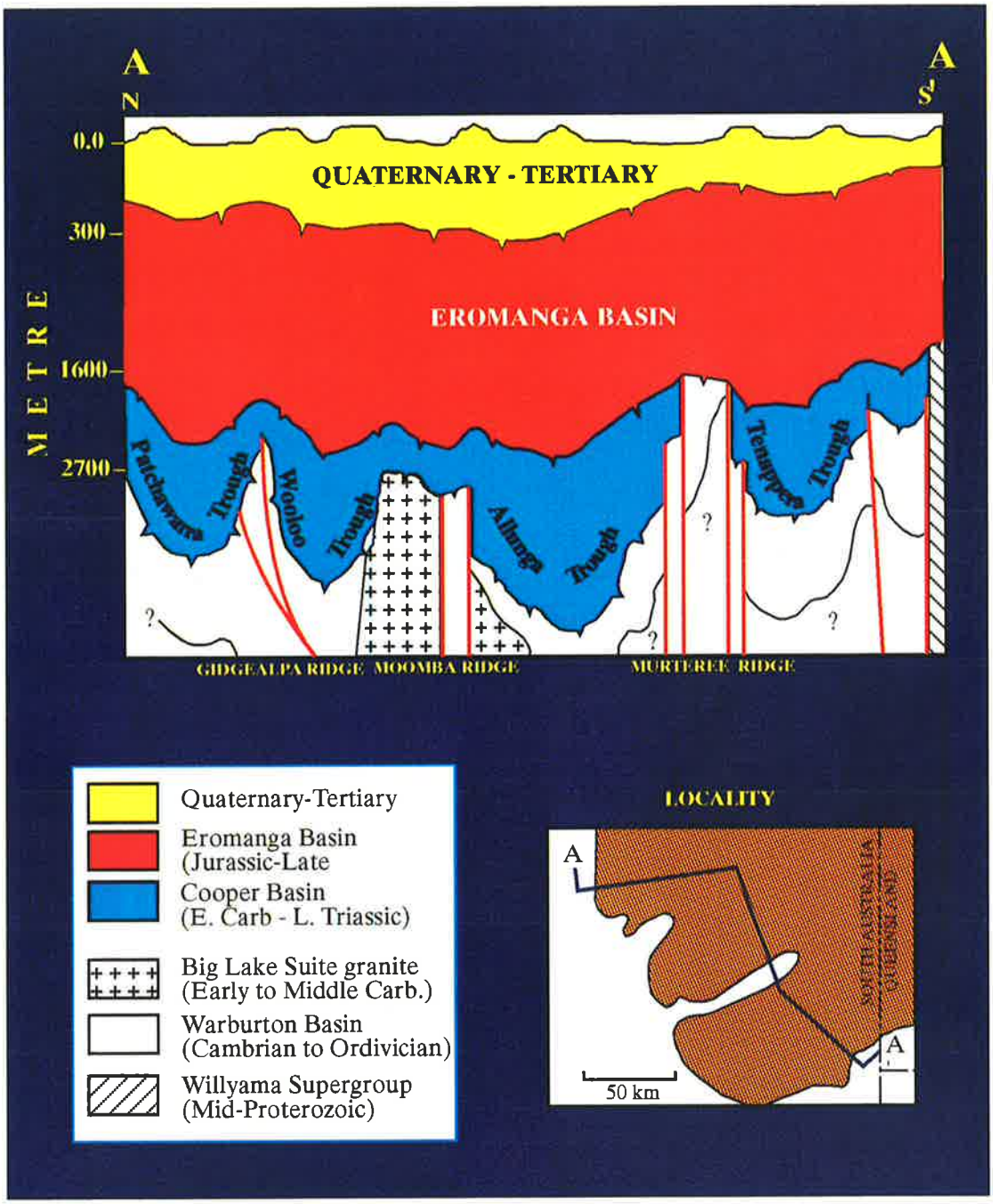

Figure 1.2 - Schematic section across the Southern Cooper Basin (modified from Hibburt, 1993).

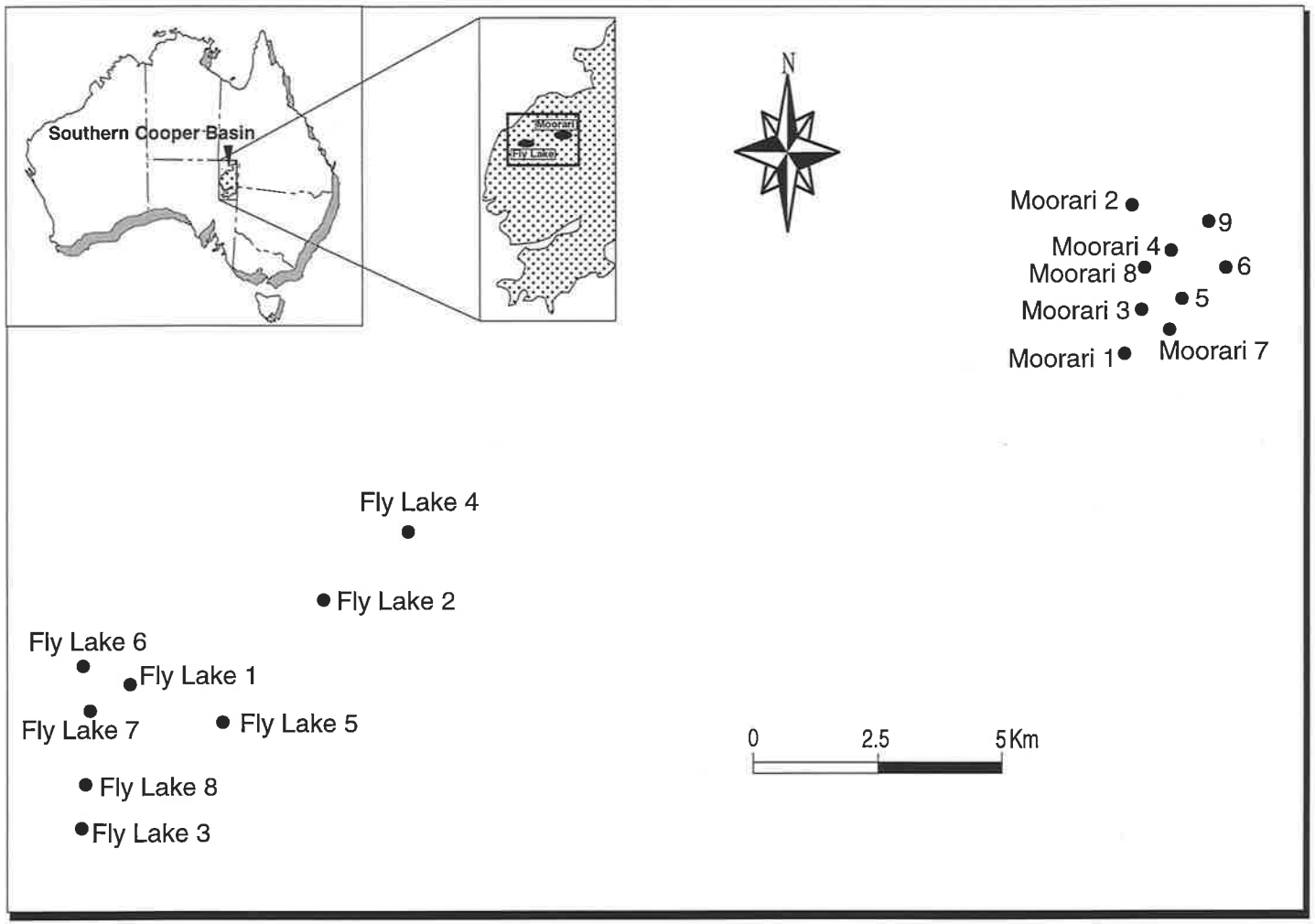

Figure 1.3 - Location of wells studied in the Moorari and Fly Lake Fields.

1.5 Methods and Materials

The sequential order of each stage of the study and the analytical techniques used for this study is illustrated in Figure 1.4.

1.5.1 Sampling

A total of 129 samples from the Tirrawarra Sandstone were collected adjacent to core plugs from cores in 14 wells in the Moorari and Fly Lake Fields (Fig. 1.5). Detailed sedimentological descriptions of the cores were carried out, and a variety of depositional environments were sampled (Fig. 1.6). Lithologies sampled were mainly sandstone, representative of different lithofacies recognised during core description. The samples were characterised using the following techniques:

1.5.2 Optical petrography

Thin sections were prepared for all samples, cut perpendicular to the bedding plane following impregnation of the samples with blue-dye epoxy resin to facilitate the recognition of porosity. Micrographs were taken of all representative features. Quantitative estimates of sandstone mineralogy (modal composition) and porosity were determined by point-counting (400-600 counts per thin section) (Appendix 2). Approximately 100 grains were measured in each slide, using the long dimension of each grain to estimate the mean grain size and sorting of the samples.

1.5.3 X-ray mineralogy

Bulk-rock XRD analyses was carried out on 45 representative core samples (Appendix 3). The samples were gently crushed in ethanol using an agate mortar and pestle, and then dried in an oven at a temperature less than 60°C to minimise clay damage. Randomly-oriented powders were prepared by pressing into a cavity-mount in an aluminium holder.

The clay fraction (< 2 μm) was separated by settling through a water column under gravity. Separated clay fractions were Mg and glycol saturated on ceramic plates held under vacuum. The prepared samples were run in a *Philips PW* 1050 X-ray diffractometer at 50 kV and 35 mA, using Co Kα radiation, at a speed scan at 2°/minute. Mineral identification was checked by comparison with Joint Committee on Powder Diffraction Standards (JCPDS) files using the CSIRO software Xplot™.

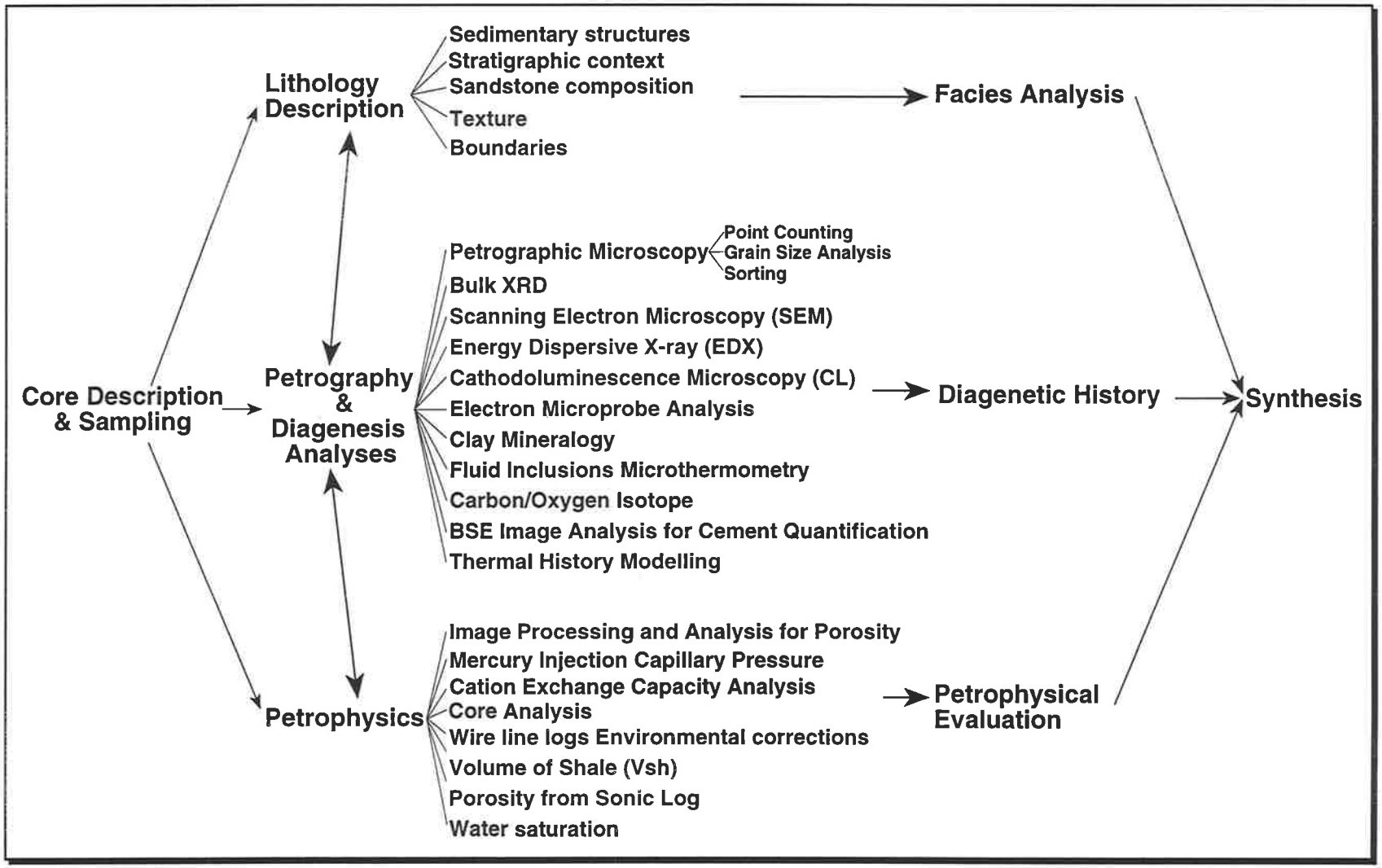

Figure 1.4 - Diagram illustrating the research procedure.

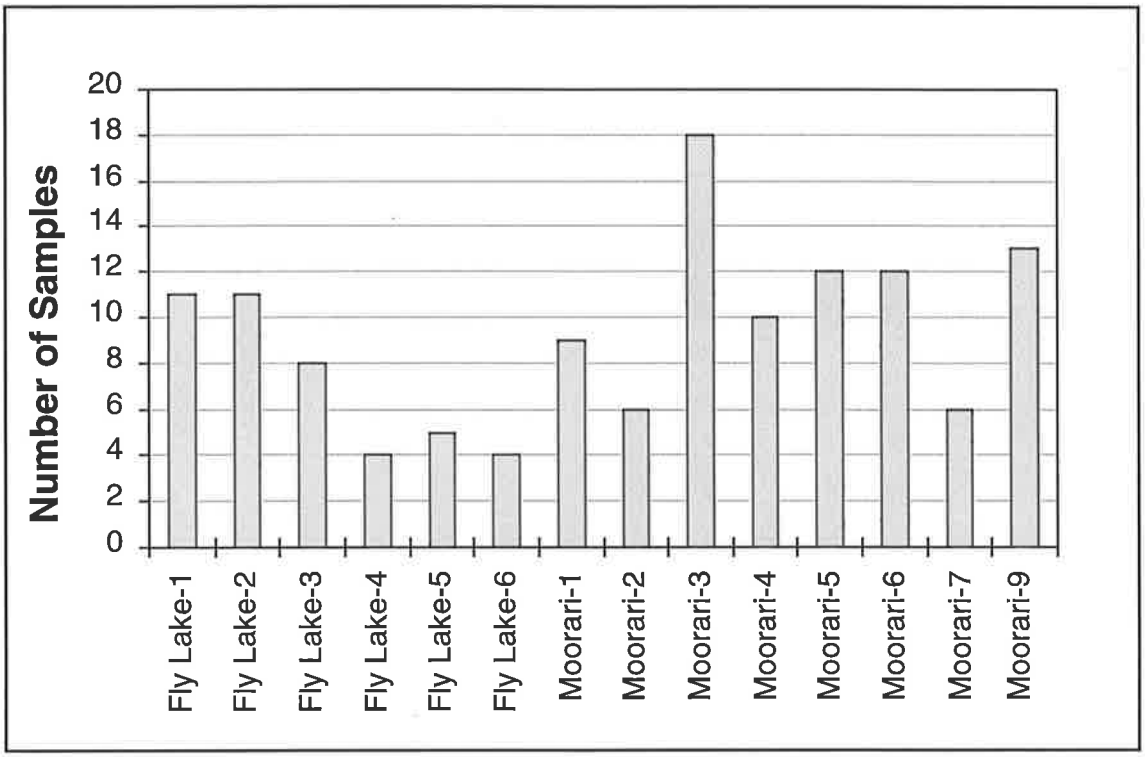

Figure 1.5 - Histogram showing the sample distribution for different wells in the Moorari and Fly Lake Fields. The abundance of the samples from different wells depends on the thickness of cored intervals and the variety of the depositional environments in each well. The total number of samples is 130.

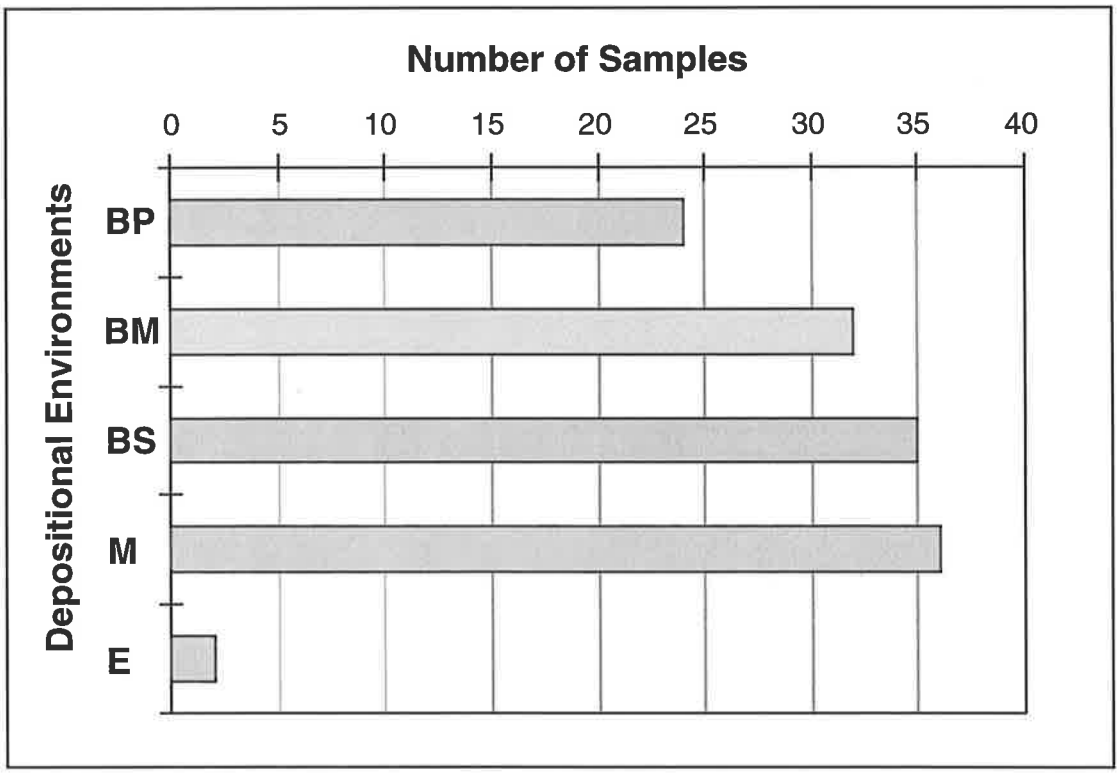

Figure 1.6 - Histogram showing the sample distribution for different depositional environments. Because the aeolian deposits are rare in the Tirrawarra Sandstone, the number of samples from this environment is very small, (BM = medial part of the braid-delta, BD = distal part of the braid-delta, BS = beach barrier, M = meandering system and E = aeolian). No samples were collected from non-reservoir intervals (back-barrier and lacustrine environments).

1.5.4 Scanning Electron Microscopy (SEM)

SEM studies were carried out on 61 representative broken rock surfaces and polished sections, coated with carbon and gold/palladium, to study the texture, pore type and authigenic minerals and to obtain additional information on paragenetic relationships of the sandstone using a *Philips XL20* electron microscope connected to a back-scattered electron (BSE) detector. Quantitative Energy dispersive X-ray (EDX) analysis was used to study the composition of representative authigenic minerals. Selected polished thin sections were examined using back-scattered electron (BSE) imaging.

1.5.5 Cathodoluminescence (CL) Microscopy

For carbonate and quartz cement stratigraphy, Cathodoluminescence (CL) petrography is a sophisticated technique. When minerals are excited by high-energy electrons, some of the minerals emit visible light, called Cathodoluminescence, in response to presence of various impurities (excitors and/or enhancers) or defects in crystal lattice.

Sixteen samples were studied by CL to identify quartz cement stratigraphy. A *Patco ELM-RX* luminoscope was used in conjunction with a *Leitz Orthomat E automatic* camera. Electron gun voltages and beam currents of 25 kV and 200 *m*A were used whilst the polished thin sections were held under vacuums between 0.07 and 0.01 Torr. CL photomicrographs were taken at 3 to 7 minute exposure times in integral metering mode with *Kodak Ektapress* 1600 ASA film.

1.5.6 Electron Microprobe Analysis

The quantitative elemental compositions of quartz and siderite cements were determined on polished thin sections covered with a thin layer of carbon, using a *CAMECA SX 51* electron microprobe at 15 kV, operating with a 20 nA beam current and 0.25-0.5 μm beam diameter. The back-scattered electron (BSE) imaging system linked to the electron microprobe was used to detect zonation in the siderite cement, and compositional analyses were carried out for each zone (Appendix 4). The ZAF correction (the effect of atomic number, absorption, and fluorescence) was used for quantitative elemental concentration. For siderite cements, results were normalised to 100 mol % Fe + Mn, Mg and Ca. The precision of analyses was 100%±2 for major elements. Standards used for siderite cements were: MgO for Mg; wollastonite for Ca; rhodonite for Mn; Fe_2O_3 for Fe. Chemical analyses of detrital and authigenic quartz on six samples were obtained using standards: garnet for Al, copper metal for Cu,

rhodonite for Mn, galena for Pb, rutile for Ti, and garnet for Fe. At 60 seconds counting time, the detection limit for Pb was 100 ppm and 80 ppm for the other elements (Appendix 5). The precision for trace-elements analysed was 10 percent ($\pm$ 2 σ).

1.5.7 Carbon and Oxygen Isotopes

Oxygen and carbon isotope analyses were carried out on 18 core samples following selection of the samples using optical and bulk XRD methods (Appendix 6). Only samples containing relatively high amounts of siderite cement were selected for stable isotope analysis. The samples were crushed to a fine dry powder, and then left to react with 100% phosphoric acid under vacuum at 100°C overnight (Rosenbaum & Sheppard, 1986). The resultant carbon dioxide was purified according to conventional techniques (McCrea, 1950) and analysed on a 6-inch, dual collector, *VG Micromass 602E* mass spectrometer. The acid correction factors of Rosenbaum and Sheppard (1986) were used to compensate for oxygen isotope fractionation. Stable isotope values are reported in the δ-notation in parts per thousands (‰). All oxygen isotope ratios are reported relative to standard mean ocean water (SMOW) (Craig, 1961), using the relation: $\delta^{18}O_{SMOW} = 1.03091*\delta^{18}O_{PDB} + 30.91$ (Coplen et al., 1983). All carbon isotope values are reported relative to the *Bellemnitella americana* from the PeeDee Formation (PDB) (Craig, 1957).

1.5.8 Fluid Inclusion Microthermometry

Fluid entrapped simultaneously during the precipitation of minerals are called primary fluid inclusions. Primary fluid inclusions carry a lot of information about the fluid entrapment temperature and nature and composition of fluid, and provide direct evidence of the diagenetic environment. The relationship with growth zonation of a mineral is a good indicator for recognition of primary fluid inclusions (Goldstein & Reynolds, 1994). Fluid inclusions are commonly small and need high magnification to be recognised. A Fluid Inc. Reynolds stage equipped with a higher power objective, combined with high power oculars, permits reproducible microthermometry of tiny inclusions by using the cycling method (Reynolds, 1978). Interpretation of stable isotope values of authigenic minerals can be better carried out by understanding of fluid temperature and composition by fluid inclusions combined study. Fluid inclusions in

diagenetic minerals and their application in geology are reviewed by several workers (Hollister & Crawford, 1981; Roeddes, 1984; Goldstein & Reynolds, 1994).

A total of 18 samples were selected for fluid inclusion microthermometry of siderite and quartz cements (Appendix 7). Fluid inclusion microthermometry was carried out using double-sided polished sections approximately 140 microns thick, prepared at temperatures below 40°C. Only primary fluid inclusions, which represent minimum precipitation temperatures (Roedder, 1979; Jourdan et al., 1987; Walderhaug, 1990) were analysed using a Fluid Inc. Reynolds stage and a Leitz optical microscope equipped with a 100× objective combined with 12.5× oculars. Reproducible microthermometry of inclusions ranging in size between 2 and 6 microns was achieved using the cycling method (Reynolds, 1978). In all of the quartz cement samples, two-phase liquid-vapour fluid inclusions were trapped close to the surface of the detrital grain and along CL boundaries within the quartz cement. In the siderite cements, the fluid inclusions were mostly equidimensional suggesting that no stretching had occurred. Because the fluid inclusions were small, it was not possible to observe the final melting of ice. The microthermometry measurement precision is ± 1°C.

1.5.9 Image Analysis Technique for Siderite Cement Quantification

A Philips image analysis system in conjunction with a *Philips XL20 SEM* with back-scattered electron (BSE) detector was employed to quantitatively estimate the relative proportions of siderite cements in representative samples of the Tirrawarra Sandstone. In the course of this part of the study, a new method was introduced for enhancement of isotope interpretation of siderite cement. A detailed description of the method is introduced in chapter 5.

1.5.10 Thermal Modelling

Thermal modelling was undertaken by Dr. P. R. Tingate of the NCPGG, Adelaide. Modelling was carried out using *BasinMod 4.20* on a *Sun* workstation using the *Lawrence Livermore* National Laboratories vitrinite calculation option. Open file vitrinite data were supplied by Santos Ltd. and Mines and Energy South Australia (MESA). Vitrinite values were calculated using a constant heatflow model calibrated on a surface temperature of 25°C and a mean corrected bottom hole temperature (BHT) of 130°C.

1.5.11 Image Processing and Analysis For Pore Space Evaluation

A petrographic Image Analysis (PIA) technique was used to evaluate relationships between porosity and permeability and pore geometry for the Tirrawarra Sandstone. Petrographical image analysis of about 66 coated polished sections was accomplished using a *Philips* image analysis system in conjunction with the SEM. The back scattered electron (BSE) images of coated polished sections were imported from the SEM in the form of grey-scale binary images using a video camera and a Windows-based software programme called Image Analysis™. BSE grey images were then converted to a binary image containing only grains (white) and porosity (black). Calculation of pore parameters such as pore area sizes, pore diameter sizes and pore perimeter sizes was accomplished by converting analog output to a digital format.

1.5.12 Mercury Injection Capillary Pressures

Mercury injection capillary pressures were used to characterise several physical properties of 31 representative selected samples (Appendix 8). A mercury injection curve is a curve which represents the increasing saturation of mercury as a function of pressure. Mercury injection curves can indicate the amount of porosity existing behind pore throats of various sizes (Purcell, 1949). As the mercury is a non-wetting phase, it must be forced to enter into the pores of the samples. Pores with the largest throats will be the first penetrated by mercury under increasing hydrostatic pressures. Pores connected with the smallest throats are the last parts of the effective porosity that may be invaded and filled by mercury at the relatively highest pressures. As the reservoir properties such as porosity and permeability are controlled by the size and arrangement of pores and throats (McCreesh et al., 1991), mercury injection method is commonly employed to characterise pore-size distribution in a porous media. Mercury injection capillary pressures were measured using a *Micromeritics Autopore 9200* at the University of South Australia.

1.5.13 Cation Exchange Capacity (CEC)

A total of 33 representative core samples from different depositional environments were analysed for their cation exchange capacity (CEC) (Appendix 9). The CEC analysis was undertaken by Dr. S. Phillips from ACS Laboratories, Australia. The samples were crushed in a Siebtechnick mill. CEC values were obtained by mixing the bulk sample with the washed sand before being saturated with 1M NH_4Cl. Samples were then

washed and the exchanged NH^{4+} back-extracted with Ca $(NO_3)_2$ / KNO_3 solution, which was analysed for NH^{4+} and residual Cl^-.

1.5.14 Core Plug Analyses

The core porosity, permeability and fluids saturation were measured by commercial core laboratories. All core porosity and permeability data, made available from the Santos Ltd. database, were obtained under ambient conditions (Appendix 10). Ambient core porosity includes porosity from either helium injection (Boyle's gas law method) or the summation of fluids techniques. All plugs were inspected for accuracy of the core analyses. Some of the plugs were deemed to be unsuitable for porosity and permeability measurements.

1.5.15 Log Analysis

Log analysis and environmental corrections of the wireline log data was accomplished using Mincom *Geolog* software on a *Sun* workstation at the National Centre for Petroleum Geology & Geophysics (NCPGG).

CHAPTER TWO

REGIONAL AND PETROLEUM GEOLOGY

2.1 Introduction

The Permo-Carboniferous to Triassic Cooper Basin sediments include sandstones, siltstones, shales and coals which are deposited in different depositional setting including fluvio-deltaic, glacial, aeolian and lacustrine environments (Kapel, 1966, 1977; Thornton, 1979; Wild, 1987; Williams et al., 1985; Williams & Wild, 1984; Seggie, 1994; Hamlin et al., 1996). The basin is unconformably over Early Paleozoic marine and volcanic rocks of the Warburton Basin (Battersby, 1976; Gatehouse, 1986) and unconformably overlain by Jurassic-Cretaceous sediments of the Eromanga Basin (Exon & Senior, 1976; Senior et al., 1978; Armstrong & Barr, 1986).

2.2 Stratigraphy of the Cooper Basin

The knowledge of stratigraphy of the Cooper Basin has been progressively developed by many works (Gatehouse, 1972; Thornton, 1973, 1978; Youngs, 1975; Battersby, 1976; Stuart, 1976; Cooper, 1981; Kantsler et al., 1983; Williams et al., 1985; Gilby & Mortimore, 1989; Fairburn, 1989; Apak, 1993, 1994) after the first introduction of the stratigraphic column by Kapel (1966). The basin which consists of dominantly lacustrine-fluvial deposits with local glacio-fluvial and rare paraglacial aeolian sediments (cf. Kapel, 1966, 1972; Gatehouse, 1972; Battersby, 1976; Thornton, 1979; Stuart, 1976; Williams et al., 1985; Fairburn, 1989) range in age from Late Carboniferous to late Middle Triassic (Fig. 2.1).

The stratigraphy adopted in this study is shown in Figure 2.1. The various formations of the Cooper Basin are briefly described in the following paragraphs.

The *Merrimelia Formation* is the basal unit in the basin and consists of interglacial, periglacial, glacio-fluvial, glacio-lacustrine and aeolian sediments (Grund,

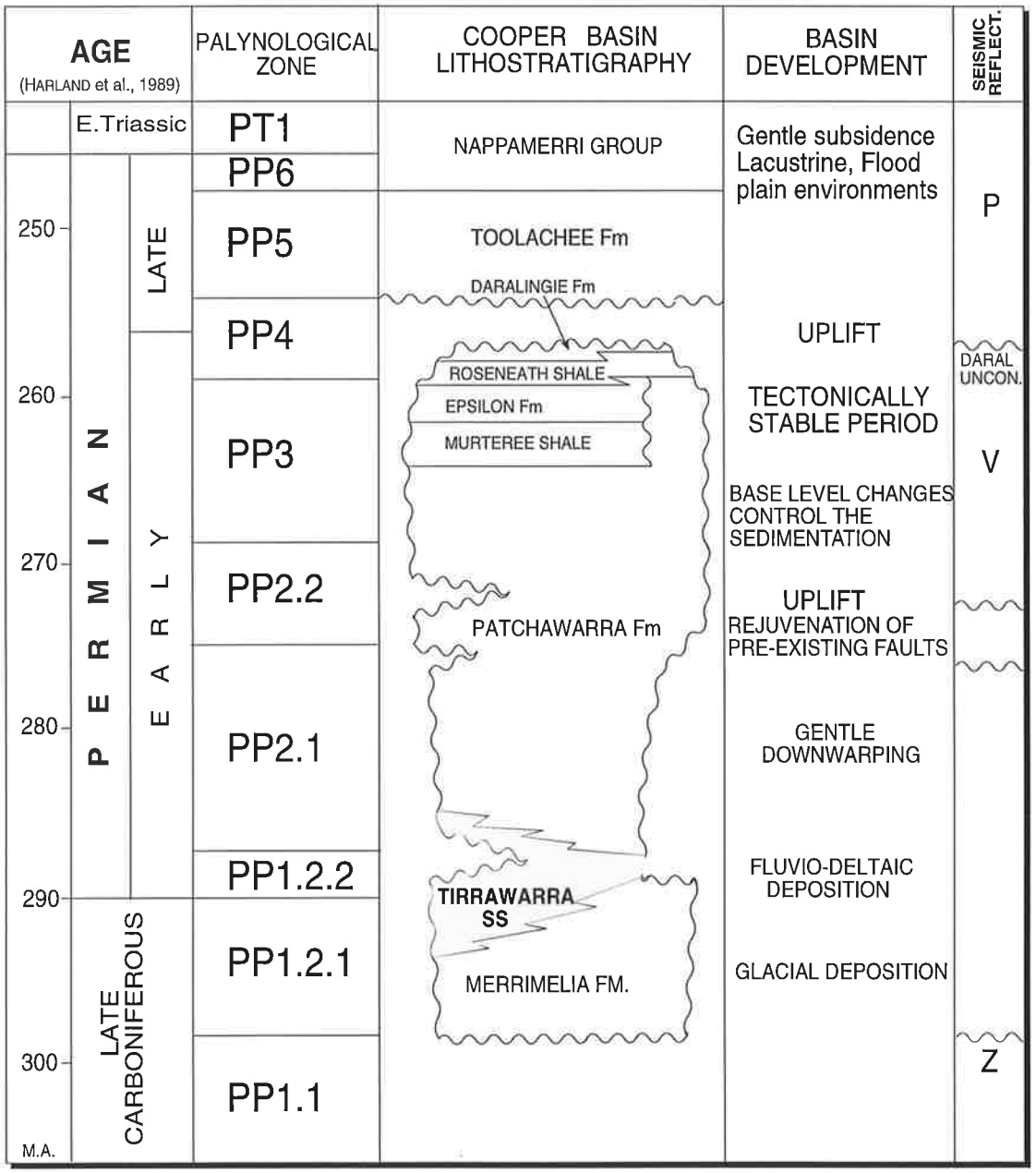

Figure 2.1 - Stratigraphic column for the southern Cooper Basin and main tectonic events. The fluvio-deltaic Tirrawarra Sandstone was deposited during the early subsidence history of the Cooper Basin (modified from Apak et al., 1993; Apak, 1994; and Seggie et al., 1994).

1966; Martin, 1967; Kapel, 1972; Battersby, 1976; Williams et al., 1985). It unconformably overlies the older rocks and consists mainly of a succession of conglomeratic sandstones and some siltstones and shales (Thornton, 1979)

The *Tirrawarra Sandstone* was first described as a part of the lower unit of the Gidgealpa Formation by Kapel (1966). The Gidgealpa Formation was later elevated to group status and a number of new formation names were introduced by Kapel (1972). The Tirrawarra Sandstone was retained as the oldest strata in the group. The Tirrawarra Sandstone is composed mainly of fine- to coarse-grained sandstones with intercalations of thin siltstones, shales and coal beds (Thornton, 1979). Sevaral depositional settings are proposed for this important oil reservoir and these are discussed in Chapter 3. The Tirrawarra Sandstone mainly occurs in the Patchawarra Trough and partly in the Nappamerri Trough. Thicker sections of the Tirrawarra Sandstone occur in the low areas and along the flanks of GMI Trend (Apak, 1994). In the Moorari and Fly Lake Fields, the thickness of the Tirrawarra Sandstone is about 200 ft. Thornton (1979) and Williams & Wild (1984) suggested that the upper part of the Tirrawarra Sandstone is diachronous with the lower part of the Patchawarra Formation but Apak (1994) recognised a local hiatus between them.

The *Patchawarra Formation*, which consists of sandstones, shales, siltstones and coals, is the thickest and most productive formation in the Cooper Basin (Kapel, 1972; Devine & Gatehouse, 1977). Three basic units were identified by Gatehouse (1972) in the Patchawarra Formation although Apak (1994) subdivided this formation into five units with the help of palynology tied to seismic reflections. This formation is considered by Thornton (1979) and Williams & Wild (1984) to have been formed in a meandering fluvial system with the key reservoirs the shoe-string, point-bar sandstones.

The Cooper Basin was drawned by an extensive lake, which transgressed from the East during deposition of the upper Patchawarra Formation, leading the deposition of the *Murteree Shale* (Stuart, 1976; Thornton, 1979). The Murteree Shale which is composed of light to dark shales with intercalations of thin siltstones and sandstones (Thornton, 1979) in most areas, conformably overlies the Patchawarra Formation.

The retreat of the Murteree Shale was followed by the deposition of the *Epsilon Formation* (Kapel, 1966; Gatehouse, 1972; Stuart, 1976). This regressive cycle is marked by the shoreline sandstones in the lower part the Epsilon Formation (Stuart,

1976). The Epsilon Formation consists mainly of shales, siltstones with thin intercalations of sandstones and coals, deposited as a lacustrine delta (Thornton, 1979).

The *Roseneath Shale* which is composed of grey to black carbonaceous shales and siltstones, was formed under the same conditions as the Murteree Shale (Battersby, 1976; Thornton, 1979).

The *Daralingie Formation* consists of a succession of thin siltstones, shales, sandstones and coals. This formation which is restricted to the Nappamerri and Tennaperra Troughs was deposited in a flood plain/deltaic environments and can be considered as a repetition of the Epsilon Formation (Battersby, 1976).

The *Toolachee Formation,* which unconformably overlies the Daralingie Formation (Wopfner, 1966; Pyecroft, 1973; Thornton, 1979; Gray & Roberts, 1984) was formed in a meandering fluvial system (Stuart, 1976; Thornton, 1979). Point-bars and channel sandstones of this formation are considered as main reservoir rocks (Stuart, 1976; Thornton, 1979; Stuart et al., 1988; Fairburn, 1989). The unconformity at the base of the Toolachee Formation is substantial as it was associated with a tectonic event. The Toolachee Formation rests on older formations over the high blocks that were active during the Daralingie event.

The *Nappamerri Group,* which consists of shales, siltstones, sandstones, and red-beds is considered to have been formed during a hot, humid and oxidising conditions typical of the Triassic (Papalia, 1969). The rocks of this formation are considered a good seal for underlying Permian reservoirs.

The Cooper Basin Permo-Carboniferous to Triassic depositional episode terminated at the end of Early-Mid Triassic with widespread compressional folding, regional uplift and erosion (Battersby, 1976).

2.3 Structure of the Cooper Basin

The Cooper Basin was considered in global basin classification scheme as a complex intracratonic basin by Klemme (1980) and Stanmore (1989). Yew and Mills (1989) described the Cooper Basin as a rift basin. Structure contour and isopach maps show three major, sinuous, narrow, fault-bounded, anticlinal zones which divide the Cooper Basin into three depositional synclinal areas (Battersby, 1976; Thornton, 1979; Apak, 1993, 1994). The anticlinal trends include Gidgealpa-Merrimelia-Innamincka (GMI), Murteree-Nappacoongee (MN) and Karmona anticlinal trends and the depositional areas

include the Patchawarra, Nappamerri and Tenappera Troughs (Kapel, 1966; Stuart, 1976; Thornton, 1979) (Fig. 2.2).

The major anticlinal zones, which are mostly steep sided, are fault-controlled basement features (Thornton, 1979) and were active during the Permian (Stuart et al., 1988). Seismic data indicate that the most common faults are normal and generally do not completely penetrate the Permian Sequence (Hollingsworth et al., 1976; Thornton, 1979). Various authors have described rejuvenation of pre-existing basement structures, compressional movement, differential vertical tectonics and compressional wrench tectonics in the Cooper Basin (Wopfner, 1960; Sprigg, 1961; Stuart, 1976; O'Driscoll, 1983; Kuang, 1985). Rejuvenation of pre-Permian faults along the flanks of many structures occurred contemporaneously with Cooper Basin deposition (Battersby, 1976; Stuart, 1976; Apak et al., 1993).

2.4 Basin History

The Cooper Basin sedimentation commenced during the Late Carboniferous to Early Permian with glacigene beds of the Merrimelia Formation (Grund, 1966; Martin, 1967; Battersby, 1976; Williams et al., 1985). These glacigene sediments are considered to have been formed during the waning stages of the major Permo-Carboniferous Gondwanan glaciation when ice sheets retreated in response to an increase in the temperature at that time (Powell & Veevers, 1987).

According to Thornton (1979), the Tirrawarra Sandstone and Patchawarra Formation formed as topographic relief diminished over geologic time in the Cooper Basin. The Cooper Basin was possibly invaded by a lake from the east during the formation of the upper part of the Patchawarra Formation leading to the deposition Murteree Shale (Stuart, 1976; Thornton, 1979). The retreat of this lake is recorded by the shoreline sandstones of the Epsilon Formation (Stuart, 1976). A second transgressive phase resulted in the deposition of the Roseneath Shale which was later followed by prograding of the delta sediments of the Daralingie Formation (Thornton, 1979). Prior to deposition of the meandering system sediments of the Toolachee Formation, a differential uplift and erosion occurred in the basin and resulted in the formation of several anticlinal closures (Battersby, 1976; Thornton, 1979; Heath, 1989). The erosion of the Permian section from the major anticlinal trends resulted in hiatus between Toolachee Formation and underlying formations (Thornton, 1979; Heath,

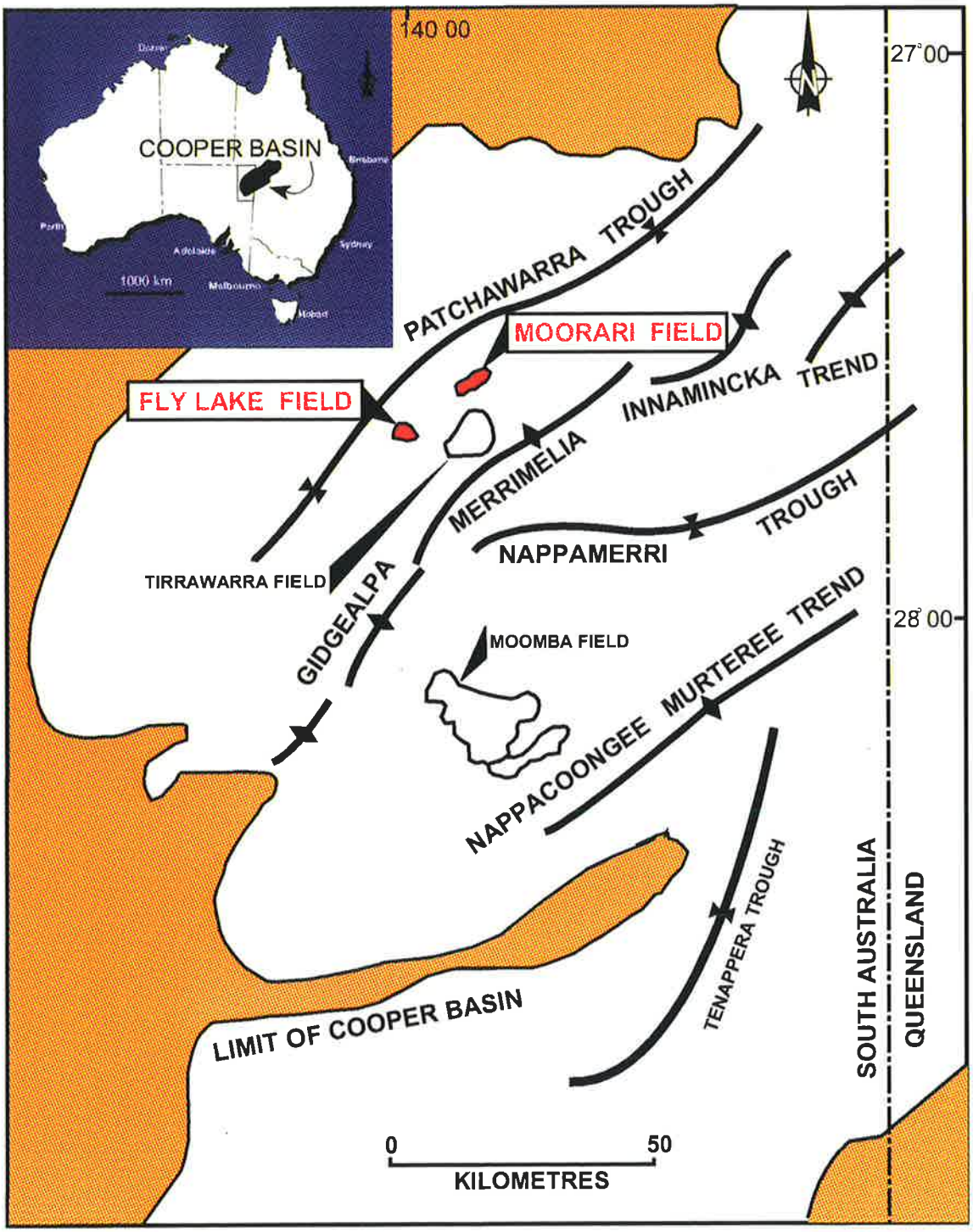

Figure 2.2 - Map of the southern Cooper Basin showing the major structural elements and the location of the Moorari and Fly Lake Fields in the Patchawarra Trough, Cooper Basin (modified from Stuart et al., 1988).

1989). Well correlations, palynological dating, and seismic records prove the unconformity between the Toolachee Formation and underlying formations (Wopfner, 1966; Kapel, 1972; Pyecroft, 1973; Hollingsworth et al., 1976; Thornton, 1979; Gray & Roberts, 1984). The tectonic activity caused major fault reactivation immediately after deposition of the Daralingie Formation (Gray & Roberts 1984), resulting angular contact between the Toolachee Formation and underlying formations (Wopfner, 1966; Kapel, 1972; Pyecroft, 1973; Thornton, 1979). A hiatus of about 12 Ma is recorded by palynological studies at the end of Early Permian (Thornton, 1979).

After deposition of the meandering system sediments of the Toolachee Formation in the Late Permian on a generally flat land surface (Thornton, 1973, 1979), fluviatile and lacustrine sediments of the Nappamerri Group were deposited in the Triassic (Thornton, 1979). The occurrence of some red beds in the Nappamerri sediments is attributed to a change in climate (Papalia, 1969; Thornton, 1979) related to the northward movement of the continent and to a global change in the Triassic (Veevers, 1984).

Deposition of Cooper Basin sediments stopped in the Late Triassic and Early Jurassic when a major phase of uplift resulted in the erosion of up to 0.5 Km of sediments in the southeastern part of the Cooper Basin (Kantsler et al., 1983; Gray & Roberts, 1984). Deposition of Eromanga Basin sediments (Jurassic - Cretaceous) commenced on the erosion surface of Cooper Basin (Kantsler et al., 1983; Heath, 1989). After rapid subsidence and the deposition of Cretaceous sediments, another phase of tectonism resulted in folding and faulting (Heath, 1989).

Three major tectonic events occurred after deposition of the Tirrawarra Sandstone (Fig. 2.3). The first major event (T1) caused uplift and erosion after deposition of the Daralingie Formation (Thornton, 1979) although two earlier subtle movements were recorded during deposition of the Patchawarra Formation (Apak, 1994). The second major tectonic event was at the end of Early-Mid Triassic when widespread compressional folding, regional uplift and erosion occurred (T2) (Battersby, 1976). The third tectonic event, T3, was after the rapid subsidence during deposition of Cretaceous sediments and this too resulted in basin deformation (Heath, 1989).

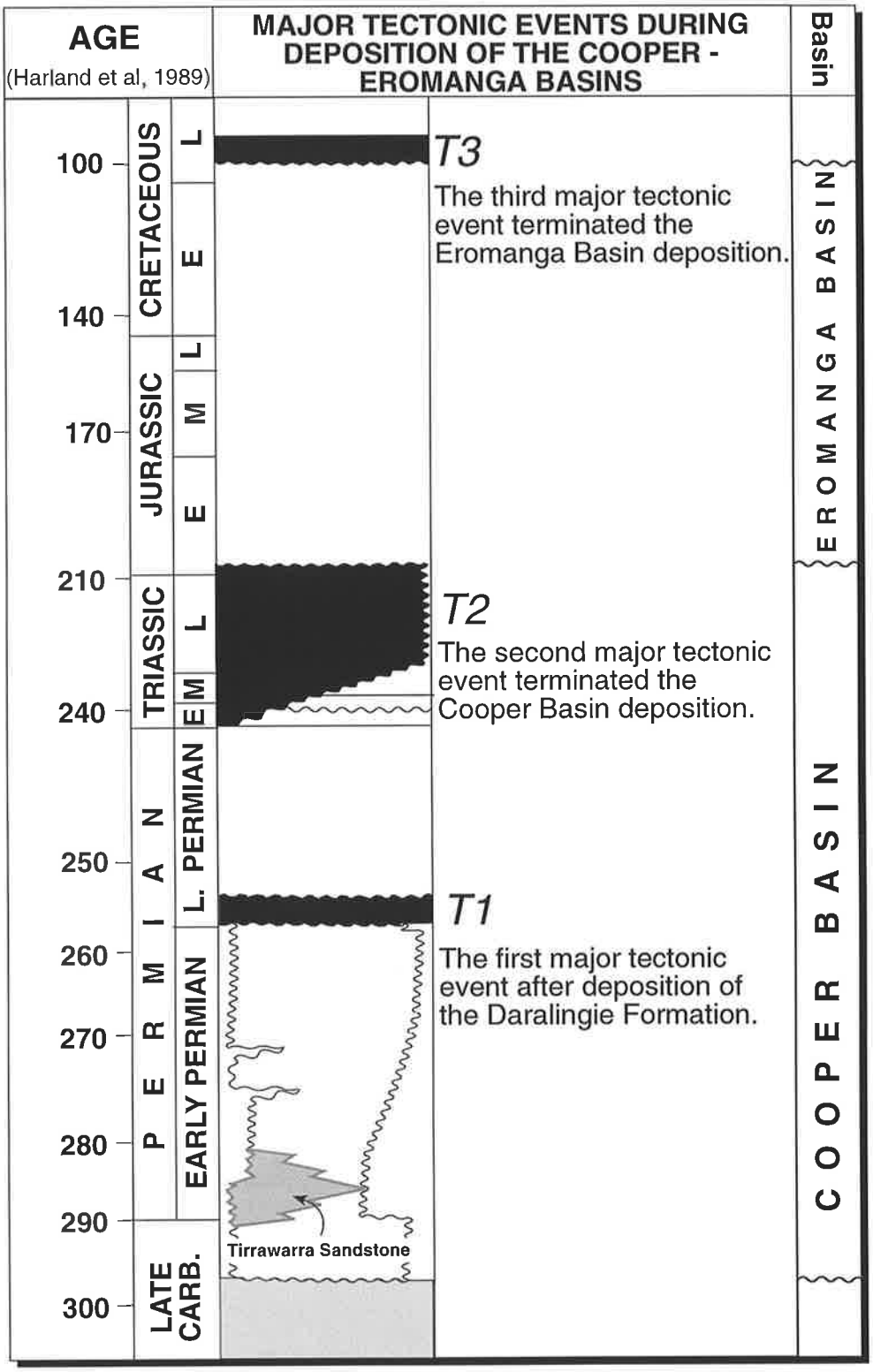

Figure 2.3 - Major tectonic events (black shaded area) during Cooper - Eromanga Basin deposition which resulted in uplift and erosion.

2.5 Exploration History of the Cooper Basin

Exploration in the Cooper Basin began in 1959 and, following several disappointments, the first commercial gas was discovered at Gidgealpa in 1963. This first discovery was followed by Moomba-1 (1966) Daralingie (1967) and Toolachee (1969). In 1970, the first oil was discovered in Tirrawarra-1 in the Patchawarra Formation and Tirrawarra Sandstone. Since that first discovery in 1963, more than 100 gas fields and 10 oil fields have been discovered in the Cooper Basin (Laws, 1989). More than 50,000 Km line of seismic have been acquired and in excess of 170 wildcat wells drilled in the Cooper/Eromanga Basins.

Fluvial sandstones at various levels within the Permian section represent the main petroleum reservoirs, including the Tirrawarra Sandstone (Smyth, 1979; Kantsler et al., 1983; Heath, 1989; Hunt et al., 1989; Yew & Mills, 1989). Most of the reservoirs in the Cooper Basin are gas producers with the Patchawarra Formation and Tirrawarra Sandstone the exceptions which produce oil. About 95% of the Cooper Basin oil is reservoired in the Tirrawarra Sandstone of the Tirrawarra Field (Heath, 1989). Additional oil reserves occur at the same stratigraphic interval in the Moorari and Fly Lake Fields (Fig. 2.2). The two fields were discovered in 1971 and are fault-bound anticlinal structures. In both fields, the Tirrawarra Sandstone reservoirs are characterised by relatively low porosities (9 to 12%), low permeabilities (0.1 to 15 mD in situ) and hence relatively low productivities (25 to 600 BOPD) (Rodda & Paspaliaris, 1989; Yew & Mills, 1989).

Source rocks in the Cooper Basin include shales and siltstones with abundant dispersed organic matter, and coal measures (Brooks et al., 1971; Battersby, 1976; McKirdy, 1989). Vitrinite and inertinite are the major macerals of the dispersed organic matter and the coal measures, having been derived from a higher plant assemblage (Heath, 1989; Hunt et al., 1989). In general, total organic carbon (TOC) in the Cooper Basin source rocks varies from 1 to 5 percent (Schwebel et al., 1980; Smyth, 1983; Jenkins, 1989).

As the source rocks are dominated by Type III kerogen, the source rocks are generally gas prone (Kantsler et al., 1983). The oil in the Tirrawarra Sandstone is believed to have been generated from a local concentration of exinite-rich source rocks

and biodegraded organic material most likely from within the Patchawarra Formation (Kantsler et al., 1989; Taylor et al., 1988; Hunt et al., 1989).

The Murteree Shale, the Roseneath Shale and some parts of the Nappamerri Group provide regional sealing units for the major reservoir intervals which intraformational shale and coal are local seals intercalated with the reservoirs (Kantsler et al., 1983; Heath, 1989; Powis, 1989; and Stanmore, 1989).

Anticlinal or fault-bound anticlinal structures, as described by many workers (Beddoes, 1973; Battersby, 1976; and Yew & Mills, 1989), form most of the hydrocarbon traps discovered in the Cooper Basin. As structural plays in the Cooper Basin decrease in number, the focus has gradually shifted to stratigraphic traps. Stratigraphic traps described in the Cooper Basin include pinchouts onto major highs (Stuart, 1976; Stanmore & Johnstone, 1988; Heath, 1989; Apak, 1994) and intraformational facies changes (Stuart, 1976; Stanmore, 1989).

The generation of hydrocarbons occurred at different times in various part of the Cooper Basin with expulsion of hydrocarbons over a wide maturity range (Kantsler et al., 1983; Tupper & Burckhardt, 1990). The Permian source rocks entered the oil window either after the Cretaceous (Kantsler et al., 1983) or in the early Late Cretaceous (Tupper & Burckhardt, 1990) in the Patchawarra Trough.

CHAPTER THREE

FACIES ANALYSIS OF THE TIRRAWARRA SANDSTONE

3.1 Introduction

Facies associations representative of the Tirrawarra Sandstone were identified and interpreted from cores and later annotated against wireline log signatures. Approximately 1270 feet of core taken from 14 wells of the Moorari and Fly Lake Fields was examined (Fig.1.3; Table 1.1).

The main objective of core examination was to divide the Tirrawarra Sandstone into separate correlative units with the same genetic characteristics. To do this, lithology, texture, and sedimentary structures were the focus of core logging. From combinations of these parameters, seven facies associations were recognised each related to different depositional environments. The lithofacies code of Miall (1977, 1978, 1985, and 1988) was used as part of the core description (Table 3.1).

3.2 Previous investigations

Various workers have commented on the depositional nature of the Tirrawarra Sandstone. Kapel (1972) recognised the Tirrawarra Sandstone as fluvial sediments. Gostin (1973) described three units of braided stream and fluvial channel origin for the Tirrawarra Sandstone in the Tirrawarra Field. A braided river system was suggested by Thornton (1979) and Wild (1987). Williams and Wild (1984) proposed a low sinuosity, bed-load dominated, fluvial-channel origin and indicated a transitional contact between the Merrimelia Formation and the Tirrawarra Sandstone and suggested that the upper part of the Tirrawarra Sandstone is diachronous with the lower part of the Patchawarra Formation. Seggie et al. (1994) and Hamlin et al., (1996) proposed a braid-delta origin for the Tirrawarra Sandstone in the Tirrawarra Field.

A series of depositional environments are suggested by the present study, for the Tirrawarra Sandstone in the Moorari and Fly Lake Fields. These environments were associated with lakes which formed during the waning stages of the Carboniferous to Permian glaciation.

3.3 Facies Association Description

Seven facies associations within the Moorari and Fly Lake fields (Table 3.2) are recognised in the Tirrawarra Sandstone. These facies associations are described in this section, followed by the interpretation of depositional environments.

3.3.1 Facies Association 1

This facies association is composed of conglomerates and coarse-to very coarse-grained pebbly, lithic sandstones. The main bedforms in the conglomerates are massive (Gm) and trough cross-bedded (Gt). Conglomerates are polymictic, poorly-sorted but clast-supported and are well-cemented. Pebbles range in diameter from 0.5 to 4 cm and are subangular to subrounded in shape with weakly-defined imbrication. Clasts are composed of metamorphic, sedimentary, and volcanic rock fragments, suggesting a complex sediment provenance. The contacts of the conglomerates with underling units are erosional and the upper contact is sharp.

The overlying sandstones in facies association 1 are coarse-to very coarse-grained (0.6-1.8 mm), pebbly and poorly to very poorly sorted (σ=1.1-2.9). Compositionally, the sandstones are mostly litharenites and have planar (Sp) and trough cross-beds (St). The sandstones shows sharp basal contacts with underlying conglomerates. Disturbed by dewatering or synsedimentary movement, several sandstone intervals are massive and do not display any internal structures. In this facies association, mudstone is very rare. The thickness of facies association 1 ranges from 10 to 45 feet.

Examples of this facies association: Moorari 3 (9423-9431 feet); Moorari 4 (9453-9464 feet); Moorari 9 (9817-9830 feet); Fly Lake 1 (9431-9434 feet).

The raw data on which the interpretation in Chapter 3 is derived from, are included in another Appendix, floppy disk inside the back cover.
The example below shows the format of this appendix.

WELL NAME: MOORARI #1

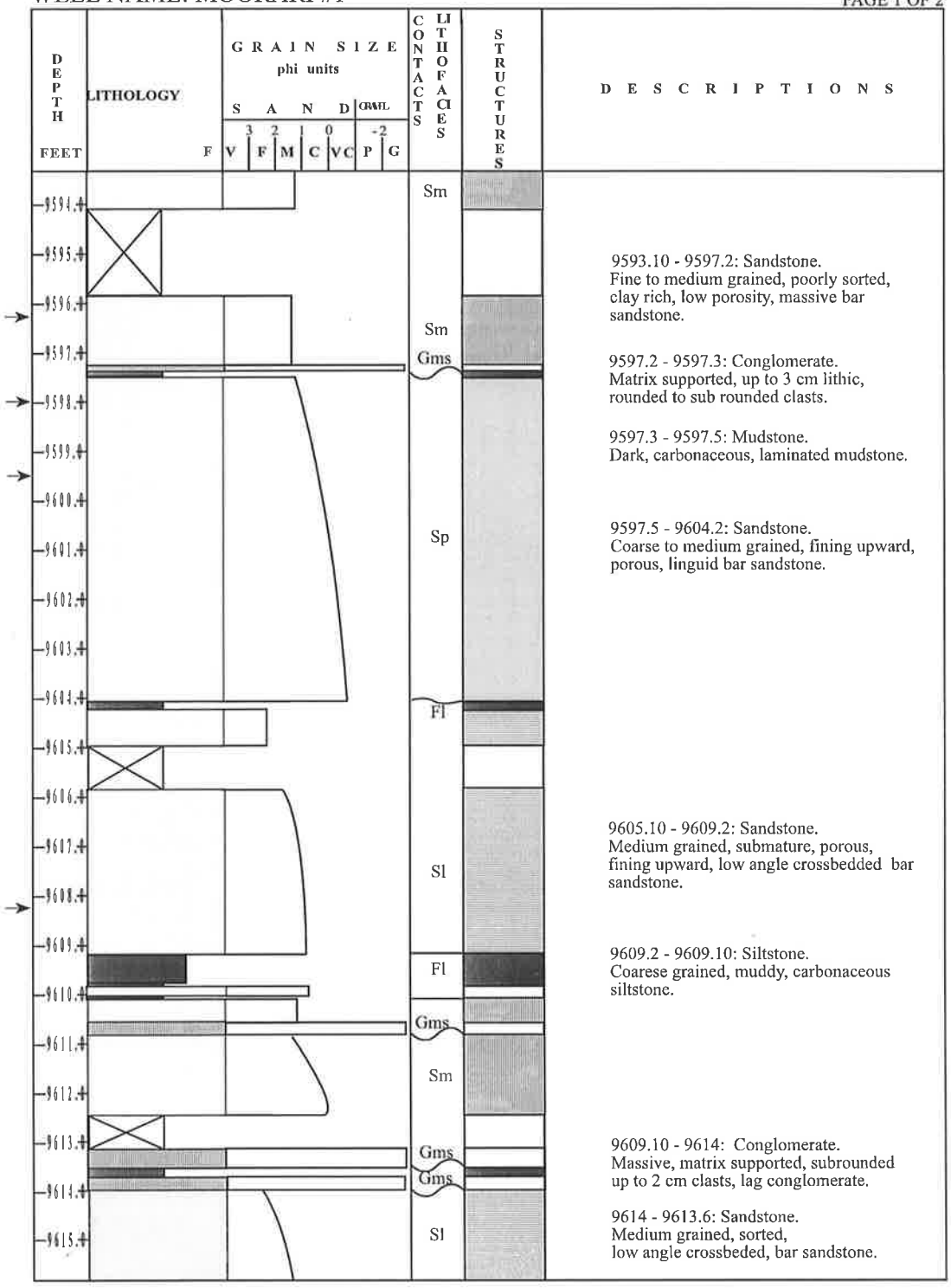

Table 3.1 - Lithofacies Codes used for Core Description. (modified from Miall, 1978, 1985, and 1988).

Facies Code	Lithofacies	Sedimentary Structures	Interpretation
Gms	Massive, matrix-supported gravel	Grading	Debris-flow deposits
Gm	Massive or crudely-bedded gravel	Horizontal bedding, imbrication	Longitudinal bars, lag deposits, sieve deposits
Gt	Gravel, stratified	Trough cross-beds	Minor channel-fills
Gp	Gravel, stratified	planar cross-beds	Longitudinal bars,
St	Sand, medium to very coarse, may be pebbly	Solitary or grouped trough cross-beds	Dune (lower flow regime)
Sp	Sand, medium to very coarse, may be pebbly	Solitary or grouped planar cross-beds	Linguoid, transverse bars, sand waves (lower flow regime)
Sr	Sand, very fine to coarse	Ripple marks	Ripples(lower flow regime)
Sh	Sand, very fine to very coarse, may be pebbly	Horizontal lamination, horizontal bedding	planar bed flow (upper flow regime)
Sl	Sand, very fine to very coarse, may be pebbly	Low angle (<10) cross-beds	Scour fills, washed out dunes, antidunes
Sm	Sand, very fine to very coarse, may be pebbly	Structureless, homogenous	Dewatered or slumped
Fl	Silt, mud	Fine lamination, very small ripples	Overbank or waning flood deposits
Fm	Mud, silt	Massive, desiccation cracks	Overbank or drape deposits
Fc	Mud, silt	contorted	Prodelta
C	Coal	Plant, mud films	Swamp deposits
P	Carbonate	Pedogenic features	Paleosol

3.3.2 Facies Association 2

This facies association consists of medium- to coarse-grained (0.4-0.8 mm), pebbly, poorly- to moderately-sorted (σ=0.7-2.0) sublitharenites, interbedded with fine-to medium-grained sandstones and dark, carbonaceous, silty mudstone. The facies association shows a weakly-defined fining-upwards trend which starts with coarse-grained pebbly sandstone and grades upward to fine- to medium-grained planar and low angle cross-bedded sandstones (Sp and Sl) and abruptly overlain by massive (Fm) or flat-laminated carbonaceous mudstones. Basal sandstones, which have a lower scour surface, are massive (Sm) or trough cross-bedded (St) and contain sparse mudstone rip-up clasts. In facies association 2, several interbeds of very fine- to fine-grained, moderately-sorted sandstones and flat-laminated mudstone exist. Dewatering and soft-sediment deformation are the possible factors controlling the formation of massive sandstones in the facies association. The lower and upper contacts of this facies are sharp.

Flat-laminated (Fl) or massive (Fm) mudstones in facies association 2 display soft-sediment deformation or dewatering. Some thin layers of siltstones are intercalated in the mudstone. The thickness of facies association 2 ranges from 10 to 40 feet.
Examples of this facies association: Moorari 4 (9520-9528 feet); Moorari 6 (9757-9770 feet); Fly Lake 1 (9397-9419 feet).

3.3.3 Facies Association 3

This facies association comprises fine-to coarse-grained (0.2-0.6 mm), moderately- to well-sorted (σ=0.2-0.6) homogenous, sublitharenites to quartzarenites with occasional interbeds of mudstones and conglomerates. The bedding of these sandstones is horizontal (Sh), massive (Sm) or with low angle crossbeds (Sl). The most remarkable aspect of the sandstones of this facies association is its uniform appearance, related to the absence of discrete bedding planes. The thickness of facies association 3 ranges from 5 to 15 feet. This facies show a gradational boundaries with facies association 4 and 5.

Examples of this facies association: Moorari 5 (9506-9511 feet); Moorari 6 (9723-9730 feet); Moorari 9 (9789-9810 feet).

Table 3.2 - Tirrawarra Sandstone Facies Characteristics. (Lithofacies assemblages are given in order of increasing volumetric significance).

Facies	Lithofacies Assemblage	Structures	Lithology & Texture	Sorting	Composition
Lacustrine **Below wave base** **Above wave base**	 Fl,Fm,Fc,Sm Sr,Sd,Sm	Parallel laminated, massive, convoluted bedding, wavy lamina, ripple cross- laminar	very fine- to fine-grained clayey sand; interbedded very fine-grained sand and silt	Moderately-sorted	Quartzarenite
Beach barrier	Sh,Sm,Sl	Homogenous, parallel stratified	Medium-grained, mature sand	well-sorted	Quartzarenite to sublitharenite
Back barrier marsh	Fm,Fl,Sm,Sr,C	Massive or bioturbated, flat-laminated, ripple laminated	dark carbonaceous mudstone, very fine-grained sand, coal	Poorly-sorted	Sublitharenite
Distal part of braid-delta	St,Sp,Sl,Sh,Sm, Fl,Fm	Trough, planar,low angle cross-bedded, horizontal and flat-laminated, massive	Coarse- to medium-grained sand; very coarse-grained pebbly sand; mudstone	Moderately- to poorly-sorted	Sublitharenite
Medial part of braid-delta	Gms,Gt,Sp,St	Massive, trough and planar cross-bedded	Clast supported, polymictic gravels, very coarse-grained pebbly sands	Poorly-sorted	Sublitharenite to litharenite
Meandering system	St,Sh,Sm,Fm,Fl, C, Gm	Trough cross-bedded, horizontal bedded, flat-laminated, massive	medium- to fine-grained sands, mudstone, coal, matrix supported oligomictic gravels	moderately- to well-sorted	Quartzarenite to sublitharenite
Aeolian	Sm	Massive	Medium-grained supermature sands	very well-sorted	Quartzarenite

3.3.4 Facies Association 4

This facies association is mostly composed of massive, carbonaceous, bioturbated mudstone (Fm), with root structures, and several intervals of very thin coal. There are also contorted and slumped fine-grained sandstones. Although this facies is very thin, it can be readily correlated from well to well in the Moorari Field. The thickness of this facies association ranges from 1 to 3 feet.

Examples of this facies association are seen in Moorari 4 (9499-9503 feet); Moorari 9 (9788-9793 feet).

3.3.5 Facies Association 5

This facies association is composed of very fine-grained, moderately-to poorly-sorted sandstones to siltstones and carbonaceous mudstone. Very fine-grained sandstones and siltstones show either dish dewatering structures or have wave-and current-ripples. The

facies show a fining- and thinning-upwards trend. Mudstones of this facies mostly exhibit very fine, flat laminations (Fl) which occasionally are contorted by soft sediment deformation. The thickness of facies association 5 ranges from 10 to 20 feet.

Examples of this facies association occur in Moorari 3 (9441-9464 feet); Moorari 4 (9464-9480 feet); Moorari 9 (9756-9767 feet).

3.3.6 Facies Association 6

In this facies association, fine- to medium-grained, well-sorted and well-cemented clean sandstones are dominant. It displays a good fining-upwards trend from basal conglomerates to coal beds. The basal conglomerates are matrix supported, oligomictic and massive. The lower contact is a scoured surface and the upper contact is gradational. Bedding of these sandstones is variable either trough cross-bedding (St), horizontal bedding (Sh) or is massive (Sm).

Carbonaceous mudstone and coal beds occur in the upper parts of facies association 6. Mudstones are massive (Fm) or flat-laminated (Fl). The thickness of this facies association ranges from 15 to 30 feet.

Examples of this facies association were observed in Moorari 3 (9404-9417 feet); Moorari 9 (9716-9725 feet); Fly Lake 1 (9367-9385 feet).

3.3.7 Facies Association 7

Facies association 7 occurs as thin intervals (less than one foot) mostly within facies association 6. It is comprised medium-grained, very well-sorted and rounded porous sandstones. The facies overlies bar deposits of facies association 6 with an abrupt contact.

Moorari 3 (9411-9412 feet) shows an example of this facies.

3.4 Interpreted Depositional Facies

Apart from an interval of lacustrine beds, the Tirrawarra Sandstone in the Moorari and Fly Lake Fields is interpreted as a deposit which accumulated in a dominantly fluvial-deltaic environment. The lack of marine fossils, the stratigraphic context, sandstone composition and texture, abundant pebble conglomerates and trough cross-bedded sandstones, with erosional lower boundaries all support this interpretation.

Except for facies associations 5, 6, and 7, which are respectively considered to have accumulated in lacustrine, meandering, and aeolian environments, the remaining facies which form the main body of the Tirrawarra Sandstone are considered as braid-delta type sediments as described by Mcpherson et al. (1987) and Soegaard (1990). The abundance of sandstones and their extensive lateral continuity, rapid changes in grainsize, low or weak cyclicity, small vertical spacing of erosional surfaces, lack of thick floodplain sediments, multiple stacked amalgamated sand and gravel deposits, all suggest deposition in a unconfined, shallow, bed-load dominated, low-sinuosity river system which, from upstream to downstream, gravelly bed-load changes to pebbly sand and finally to sand. In a braided system, the relative proportion of linguoid to longitudinal bars increase downstream, with the fractionation of its load into finer sizes downstream. Longitudinal bars are coarse, poorly-sorted sediments, whereas linguoid bars are finer grained, better sorted sediments. Longitudinal bars represent a proximal to medial braided system and linguoid bars represent distal, braided-system deposits (Williams & Rust, 1969; Smith, 1970).

3.4.1 Facies Association 1 (BM)

This facies association is the coarsest part of the Tirrawarra Sandstone and mainly comprises conglomerates and coarse-grained, pebbly sandstones. Mudstones are rare in this facies and occur as very thin intervals.

Many authors (Williams & Rust, 1969; Rust, 1972; Boothroyd & Ashley 1975; Boothroyd & Numedal,1978) have described massive, clast-supported conglomerates as proximal, braided-system longitudinal bars. These conglomerates are formed by transportation and deposition of coarse-grained bed load by powerful currents followed by subsequent infiltration of sand matrix during stages of lower water. Intercalation of coarse-grained sandstones and conglomerates in the facies indicate decreasing and increasing flow competencies, respectively.

Sandstones with trough crossbedding (St), which can be formed by migration of subaqueous, sinuous crested dunes (Harms et al., 1982) are usually generated at the margin of bars during low discharge or may be formed in shallow channels which are cut through bar surfaces as the flow stage decreases (Rust, 1972; Boothroyd & Ashley, 1975; and Boothroyd & Nummedal, 1978). Interbedded lag gravel (Gm) and channel-fill

sands (St) likely indicate an alternation of flow competency, i.e. lag gravels represent an increase in flow competency and channel-fill sands, a decrease.

One of the significant features of facies association 1 is the paucity of mudstone. The lack of mudstone is likely to be due to a significant lateral migration of channels, which tend to rework fine sediments and transport it downstream as a result of steeper depositional gradients and high discharge. This interpretation is supported by the lack of significant amounts of rip-up clasts in this facies association in comparison with the more distal facies association 2 which exhibits more clay rip-up clasts in the basal beds.

Stacked, amalgamated conglomerates and sandstones in facies association 1 indicate multiple, high-water stage events which are common in low sinuosity channels (Costello & Walker, 1972). The lack of fine-grained, vegetated overbank deposits, which can inhibit channel migration, led to an increased frequents of avulsion. This, plus vertical aggradation, led to the lateral continuity of facies association 1.

From the above-mentioned features, it can be concluded that facies association 1 is more likely formed in channels and bars of a shallow, low sinuosity, bedload-dominated, braided stream on the medial part of a braid-delta.

3.4.2 Facies Association 2 (BD)

This facies association, which consists dominantly of sandstones and pebbly sandstones, can be separated from facies association 1 by the lack of Gm and the presence of some massive (Fm) and laminated carbonaceous mudstone (Fl).

Trough cross-bedded sandstones (St) at the base of this facies represent the migration of sinuous-crested dunes on the channel floor. These sandstones, which have mudstone rip-up clasts and a basal scoured surface, suggest channel lateral migration cutting through overbank sediments.

The presence of planar cross-bedded sandstones (Sp) in the facies suggest a more constant discharge regime where channel floors are covered by straight crested bed forms like those that exist in Platte River (Smith, 1970). Planar cross-bedded sandstones in this facies association can also be emplaced by linguoid bars.

Low-angle, cross-bedded sandstones (Sl), which form in shallow flows close to upper flow regimes conditions, can be generated on linguoid bar tops.

The fine-grained sediments, such as mudstones, are suspended muds which can be deposited when flow is slow. Such a condition exists on bar tops or in abandoned

channels or on overbank or during flood stages (Rust, 1972; Boothroyd & Ashley, 1975; Campbell, 1976; Boothroyd & Nummedal, 1978). The presence of mudstone and mud clasts in this facies indicate that during low discharge the deposition of mud was extensive on the floodplain. The alternating succession of very fine-grained sandstones and mudstone in this facies association is interpreted as crevasse splays.

Facies association 2 is more likely the down stream or more distal part of the braid-delta system. It can be also mentioned that this facies association is generated from reworking of facies association 1 components.

Proximal, medial and distal reaches of braided streams are terms suggested by Boothroyd and Ashley (1975). The distance of the transition from proximal to distal reach is a function of slope angle and discharge (Miall, 1985).

3.4.3 Facies Association 3 (BS)

This facies association is dominantly homogenous, horizontally-stratified (Sh) massive (Sm), fine- to coarse-grained, well-sorted sandstones. Both very fine-grained and very coarse-grained sandstones are absent or very rare in this facies association. The facies association has close relationship with back-barrier marsh and upper shoreface sediments of a lacustrine environment, respectively at its lower and upper contacts. The lower contact of this facies is gradational with laterally-continuous fine-grained mudstone and siltstone beds which will be later documented as a back-barrier marsh environment. The upper contact of the facies is gradual with the upper shoreface of a lacustrine environment.

This facies association can be laterally correlated from well to well in the Moorari Field, and is associated with marsh deposits (below) and lacustrine deposits (above). The sandwiching of this facies association between these two deposits suggests it is a wave-dominated, shore-line barrier deposit, separated from the braided system by a shallow marsh, formed behind the barrier. In other words, the sandstones of this facies association are more likely a wave-reworked foreshore deposit within a delta-front succession. The lack of ripple cross-lamination may well be due to long ripple wave length or very low amplitude wave ripples relative to the large mean grainsize.

3.4.4 Facies Association 4 (MBB)

This facies association mostly comprises carbonaceous mudstone and thin intervals of siltstones and sandstones.

As discussed before in this chapter, the deposition of fine-grained sediments requires slow-moving or standing water for sediments to settle out of suspension. This situation occurs in many fluvial environments such as abandoned channels, bar tops, vegetated islands, overbanks, sloughs (Williams & Rust, 1969; Rust, 1972; Boothroyd & Nummedal, 1978; Miall, 1988). These types of environments, however, are local and often cannot be traced between wells on a field scale. As this facies association is well developed laterally throughout the Moorari Field, a more widespread depositional environment is envisioned. A shallow back-barrier marsh where mudstones and abundant carbonaceous matter can be deposited in a more-widespread elongate environment is a good candidate. The thin intervals of fine-grained, slumped sandstones and siltstones in this facies are interpreted as washover deposits. They are formed during wind-generated storms cut the barrier to allow sand to enter the marsh. The lower and upper contacts of facies association 4 are gradational. Facies association 4 can be differentiated from lake deposits by its thinness and presence of root structures and coal beds.

3.4.5 Facies Association 5 (L)

This facies association consists of flat-laminated or plane-bedded carbonaceous mudstone and very fine-grained wave-rippled sandstones and siltstones. Laminated mudstone (Fl) with common soft sediment deformation and microfaulting, is interpreted as having been deposited in a lacustrine environment. The lake beds are typically plane-bedded, silty, carbonaceous mudstone, with minor lenticular beds of structureless very fine-grained sandstone. These sandstones often display contorted bedding. They are formed as a result of gravity flows in a prodelta environment. A trend towards deeper-water conditions is indicated by a fining-upwards cycle in which the thickness, abundance and grainsize of sandstones, together with wave and ripple lamination, decrease up section. The lower contact with facies association 3 is gradational, and upper contact is abrupt.

3.4.6 Facies Association 6 (M)

This facies association can be recognised from other facies by:

- thick carbonaceous mudstone,
- relatively thick coal beds,
- common fining-upwards cyclicity.

The above evidence favours the likely accumulation in a meandering system. Fine-grained sediments and coal beds are more common above this facies association.

According to Collinson (1986), two major components exist in meandering systems, a coarse component, comprising channel sediments and a fine component, consisting of inter-channel sediments. These components can be readily distinguished in facies association 6 (M). Although sandstones of this facies association appear massive, they exhibit faint trough cross-stratification (St). These sandstones occasionally occur above massive channel lag conglomerates (Gm) which have an erosional lower boundary. The basal lag conglomerates frequently contain coaly fragments which probably are derived by bank caving. Trough cross-bedded sandstones (St), which can be generated from subaqueous migration of dunes (Harms et al., 1982), are reported from studies of modern meandering rivers (Boothroyd & Ashley, 1975; Levey, 1978). Several of these sandstones display a lower, scoured surface representing dune migration on channel floors. The occurrence of horizontally-bedded sandstones (Sh) above trough cross-bedded sandstones (St) and displaying a fining-upwards trend, suggest a decrease in flow energy and depth. This situation has been reported by Leeder (1973) as lateral accretion on pointbar sediments. Massive (Fm) and flat-laminated mudstones (Fl) form the uppermost part of the fining-upwards trend as vertical accretion of floodplain sediments. Coal beds of facies association 6 were probably formed within a floodplain swamp or abandoned channels.

This facies association was deposited in a meandering fluvial system rather than a distal braided system, although the difference is probably not very significant.

3.4.7 Facies Association 7 (E)

Intervals of very well-sorted and very well-rounded, supermature sandstones, with high porosity (16%) and permeability (320 mD) have been deposited in a environment different from those described for previous facies associations. These supermature sandstones are believed more likely to be wind blown sandstones or aeolinites. In the

Ganges River, on the surface of pointbars which are exposed to wind activity, wind blown sands are present (Singh & Kumar, 1974). This situation also is reported in the Colorado River by McGowen and Garner (1970) and in the Donjek River by Rust (1972). The sand arrives in the environment from outside the immediate area by aeolian activity and can display vastly improved maturity parameters. These situations provide a model for an aeolinite origin for these supermature sandstones in the upper part of the Tirrawarra Sandstone which were formed at the top of bars during times of low water discharge.

The facies association relationship in vertical succession developed during this study suggests three depositional units for the Tirrawarra Sandstone in the Moorari and Fly Lake Fields (Fig 3.1). The vertical succession records progradation and retreat of a braid-delta into a lacustrine environment. The lower part of the Tirrawarra Sandstone starts with a progradational unit which continues into a retrogradational unit and ends with another progradational unit. The remaining upper part of the sandstones displays sudden changes in sedimentary environment from a braided system to a meandering fluvial environment. This sudden change which can be detected by a thin widespread conglomerate with an erosional lower contact which suggests a gap between this part and the lower part of the Tirrawarra Sandstone.

The progradational unit, in ascending order composed of a lower then upper shore-face of a lacustrine environment, the distal part of a braid-delta and the medial part of a braid-delta. The retrograde unit in ascending order is composed of the medial part of a braid-delta, the distal part of braid-delta, a back barrier marsh, beach barrier sandstones, and the upper and then lower shoreface of a lacustrine environment. Depending on the amount of erosion during progradation, the second progradation unit starts with beach barrier sandstones or the distal part of a braid-delta or even the medial part of a braid-delta.

3.5 Wire-Line Log Facies

The set of log responses that characterises a sediment and permits the sediments to be distinguished from others were defined as an electrofacies (Serra, 1980). In this study wire-line facies are established through correlation with facies associations on the cored intervals. The different facies association of the Tirrawarra Sandstone in the Moorari

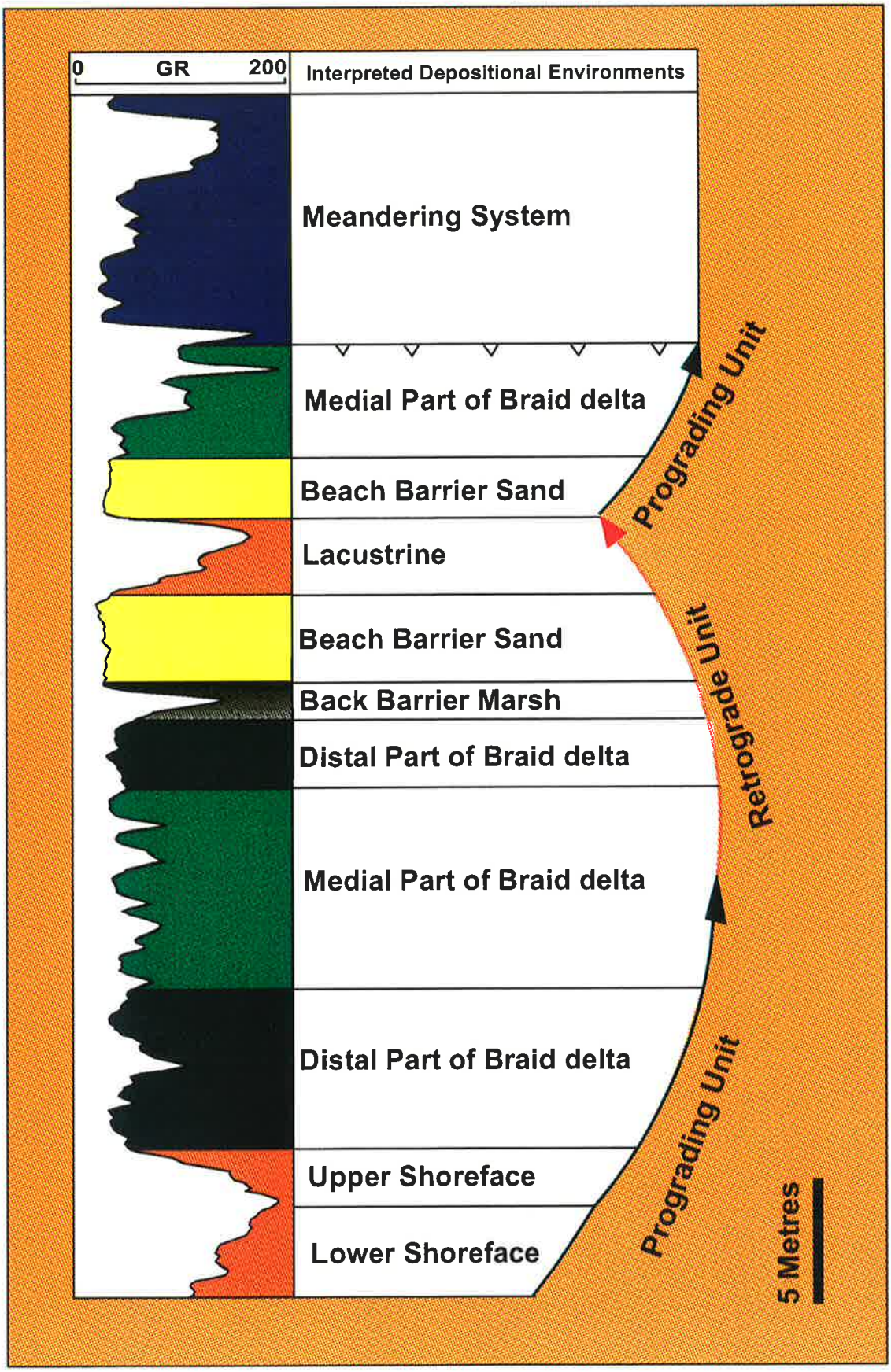

Figure 3.1 - Example of the different depositional environments, and progradational and retrogradational cycles of the Tirrawarra Sandstone in the Moorari and Fly Lake Fields. The gamma ray log trace is derived from the Moorari-9 well.

and Fly Lake Fields are recognised by gamma-ray log responses. Each facies association displays a different gamma-ray log motif related to the different lithology assemblage. Correlation of facies associations throughout the field can be achieved using log motifs.

3.5.1 Facies Association 1 (BM) Log Motif

As described previously, this facies association is predominantly gravelly, and mudstone intervals are almost absent. Although this facies association has no or little mudstone a smooth cylindrical gamma-ray log response might be expected but the gamma-ray log response is a serrated cylinder (Fig. 3.2a). The high gamma-ray deflection in this facies association is due to present of authigenic illite. As will be discussed in Chapter 4, most of unstable rock fragments are altered to illite. With abundant rock fragments, a relatively large amount of illite present. The presence of illite, which contains potassium in its lattice, can greatly effect the gamma-ray response. So in facies association 1, gravelly intervals which indicate mostly longitudinal bars can be separated from channel-fill sandstones by their higher gamma-ray deflection.

3.5.2 Facies Association 2 (BD) Log Motif

In this facies association, which is chiefly sandstone with some thin intervals of mudstone, the gamma-ray log motif is a relatively smooth cylinder with some short deflections (Fig. 3.2b). The deflections are due to thin muddy intervals and, in some instances where the thickness of the muddy intervals increase, the gamma-ray deflection increases and the log pattern become very similar to facies association 1 (BM).

3.5.3 Facies Association 3 (BS) Log Motif

This facies association is an almost homogeneous sandstone which is nearly free from rock fragments (i.e. is a sublitharenite to quartzarenite), leading to a very smooth gamma-ray response for this facies association. This facies can be easily recognised from others by the very smooth cylindrical shape (Fig. 3.2c).

3.5.4 Facies Association 4 (MBB) Log Motif

This facies association which is usually muddy, can be recognised by a high deflection of gamma-ray (Fig. 3.2d). This facies, despite its thinness, can be traced in throughout the Moorari Field.

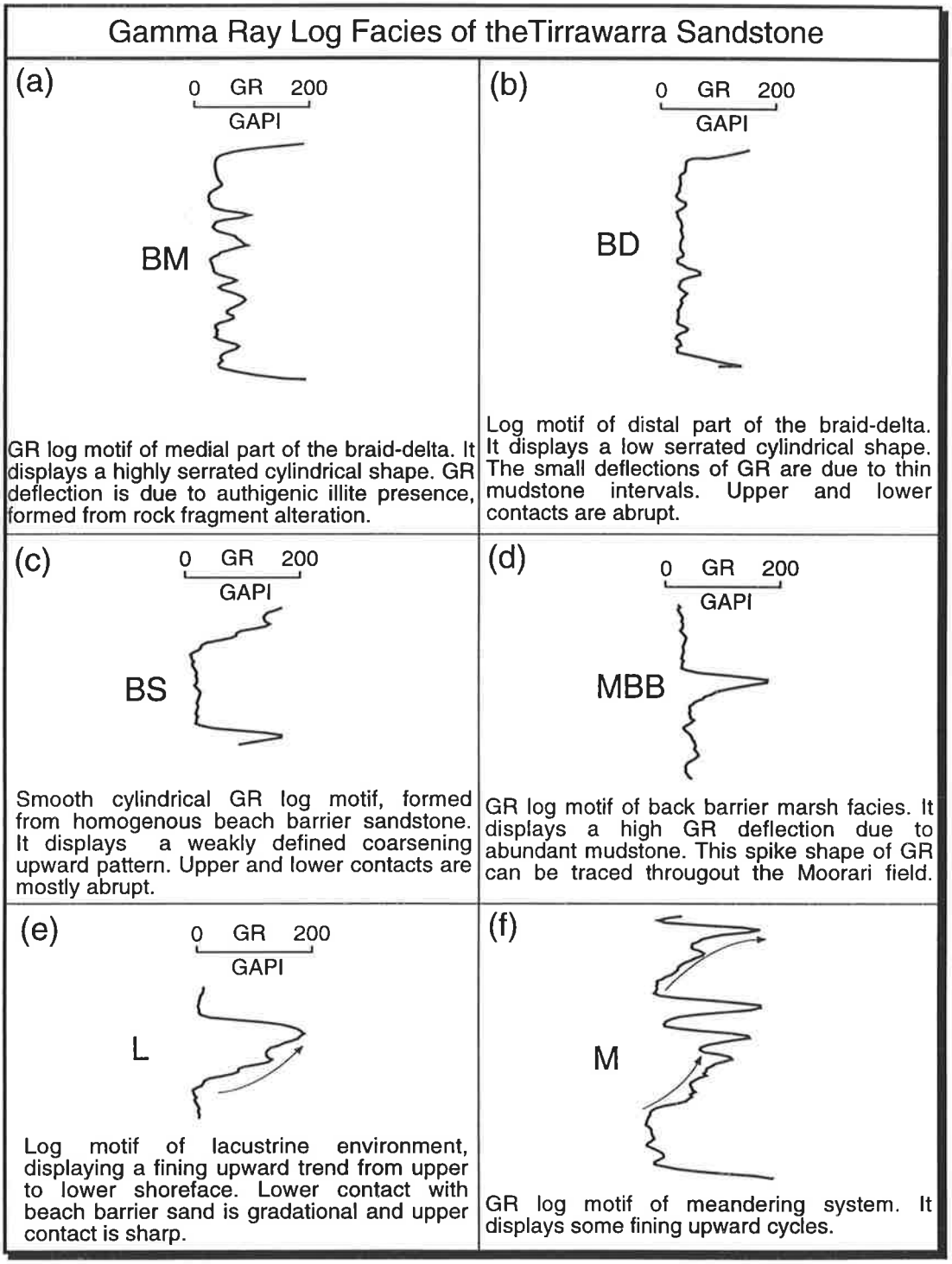

Figure 3.2 - Gamma-ray log motifs for different depositional environments in the Tirrawarra Sandstone.

3.5.5 Facies Association 5 (L) Log Motif

The log motif of this facies association, with its abundant muddy materials, shows a high deflection of gamma-ray (Fig. 3.2e). As this facies association gradually grades from upper shore-face sandy materials to lower shore-face mostly muddy materials, its lower contact is gradational and displays a fining-upwards trend. The upper contact is abrupt.

3.5.6 Facies Association 6 (M) Log Motif

This facies association shows relatively well defined fining-upwards cyclicity from coarse materials to mudstone and coal beds. Consequently the gamma-ray log response is composed of several fining-upwards trends (Fig. 3.2f).

3.5.7 Facies Association 7 (E) Log Motif

Aeolian beds which are associated with pointbar sandstones can not be readily recognised by their gamma ray log pattern. This is due to similarity of sandstone composition in pointbar and aeolian environments, which results in a similar gamma-ray log pattern.

3.6 Conclusions

Seven depositional environments are interpreted in the Tirrawarra Sandstone in the Moorari and Fly Lake Fields. These are:

- Lacustrine environments with upper and lower shorefaces;
- Parallel beach barriers;
- Back barrier marshes with outwash beds;
- Distal parts of a braid-delta with linguoid bars, inter-channel bay deposits and splays;
- Medial parts of a braid-delta with longitudinal bars;
- a Meandering fluvial system;
- an Aeolian environment.

The lacustrine environment contains both an upper shoreface and lower shore-face. The upper shoreface is dominantly very fine-to fine-grained wave-rippled sandstones (Sr) which were formed above wave-base level. The lower shore-face is planar bedded, varve-like dark mudstone with thin lenses of siltstone.

Parallel beach barrier sandstones are chiefly medium-grained, well-sorted quartzarenite. They were formed by reworking of foreshore sediments by beach parallel waves and currents.

Back barrier marsh deposits are composed of massive mudstones, fine-grained sandstones and thin coal beds. They were formed in a shallow, elongate marsh behind barrier sand bars.

The distal part of the braid-delta is dominantly composed of medium-to coarse-grained, moderately-sorted sandstones and some thin intercalations of mudstone. These beds were formed in linguoid bars, channels, overbanks, and crevasse splays.

The medial part of the braid-delta is composed of massive and crudely-trough-cross-bedded conglomerates (Gms, Gt) and pebbly trough- and planar- cross-bedded very coarse-grained, poorly-sorted sandstones (St, Sp). They are considered to have been deposited in longitudinal bars and channels.

The meandering fluvial system is composed of matrix-supported, oligomictic, lag gravel, medium-grained, well-sorted, pointbar quartzarenite, and floodplain mudstone and coal intervals.

Aeolian beds are composed of thin, medium-grained, supermature quartzarenite intervals which were probably formed on the pointbar sands during times of low water discharge.

CHAPTER FOUR

PETROGRAPHY AND DIAGENESIS

4.1 Introduction

This chapter discusses the petrography and diagenetic history of the Tirrawarra Sandstone reservoirs in the Moorari and Fly Lake Fields. The main factors that control the porosity, permeability and other reservoir properties are discussed in detail. Understanding the diagenetic events and their influence on the porosity and permeability trends can enhance the prediction of the reservoir quality.

4.2 PETROGRAPHY OF THE TIRRAWARRA SANDSTONE

4.2.1 Textural Petrography

The grain size of the samples ranges from very coarse-grained sandstones (1 mm), to fine-grained sandstones (0.2 mm), and is closely related to the depositional facies (Fig. 4.1).

The standard deviation of the measured grain sizes covers a broad spectrum. Using the normal phi standard deviation sorting scale of Folk (1974), sorting ranges from very well-sorted to very poorly-sorted, depending on depositional facies (Fig. 4.2).

Visual comparision charts (Powers, 1953) were used to evaluate grain roundness of the samples. The roundness of the samples ranges from subangular to very well-rounded. In general, most of the samples show a bimodal roundness, having both very well-rounded and sub-rounded grains. This situation is due to bimodal sources of the sediments. The rounded quartz grains are possibly from aeolinite source which were mixed with fluvial sediments during sediment accumulation.

A contact index (CI = average number of contacts per grain: Pettijohn et al., 1987) was used to evaluate compaction. At the depositional surface or in shallow-buried sediments, this index is very low, but increases as the depth of burial increases. The

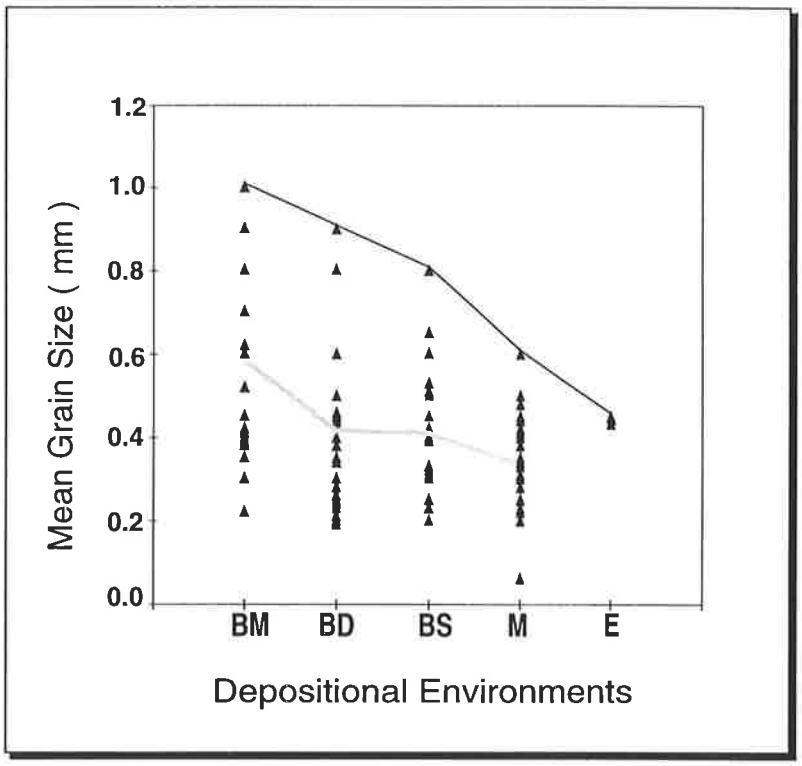

Figure 4.1 - Mean grain size plotted against depositional environment. Grain size decreases from medial braid-delta to aeolian environments . The average value of mean grain size in each depositional environment is connected with a thick grey line. BM= medial part of the braid-delta, BD= distal part of the braid-delta, BS= beach barrier, M= meandering system and E= aeolian.

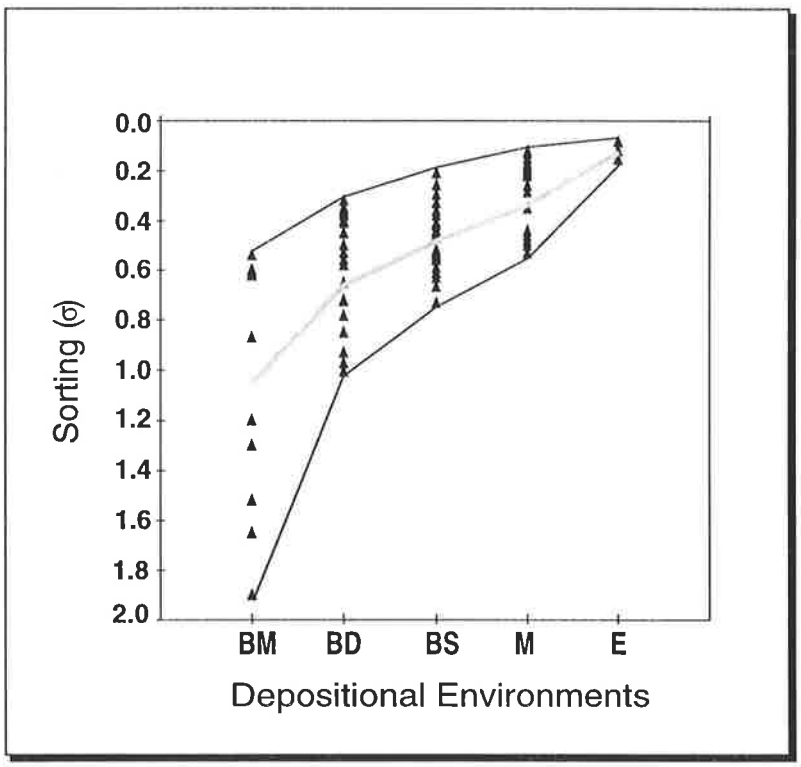

Figure 4.2 - Sorting plotted against depositional environment. Sorting improves from medial braid-delta to aeolian environments. The thick grey line represents the mean sorting value for each depositional environment.

depth of burial, the time of cementation relative to compaction, and sandstone composition can control CI. The CI values for Holocene fluvial, beach, and dune sands have been estimated as 0.9, 0.79 and 1.02 respectively (Edward, 1989); and 0.3 and 0.23, for Recent river and beach deposits (Wilson & McBride, 1988). For the Tirrawarra Sandstone samples, approximately 100 grains per sample were counted for CI evaluation which was found to range from 1.6 to 2.8, and was mainly controlled by composition and cementation. With an increase in rock fragments, the CI increases; and conversely, the index decreases as quartz cement increases.

4.2.2 Compositional petrography

4.2.2.1 Framework Grain Composition

Compositional point counts were performed on all of the samples to quantify mineral composition and thin section porosity (Appendix 1). For point counting, the standard techniques of Pettijohn et al., (1987) were applied. The rock fragments or mineralogically composite grains were identified as observed and their components were ignored (Zuffa, 1985).

The main component of the Tirrawarra Sandstone samples is quartz, mainly single grains with undulose extinction. In samples with lower mineralogical maturity, grains of stretched metamorphic quartz were also common. The proportion of quartz in the samples ranged from 30% to 72%, with an average of 57% (Table 4.1).

The next most significant component is rock fragments, including metamorphic, sedimentary and volcanic grains. Schists and shales are the most common fragments, and these were deformed in a ductile manner during compaction. The proportion of rock fragments varies widely, ranging from 1.3% to 67%, with an average of 16% (Table 4.1).

The proportions of quartz and rock fragments are controlled by depositional environments, and each environment had a near characteristic composition with only some overlap (Fig. 4.3).

A few samples had a few, heavily-altered feldspar grains, but feldspars were absent from the rest of the samples.

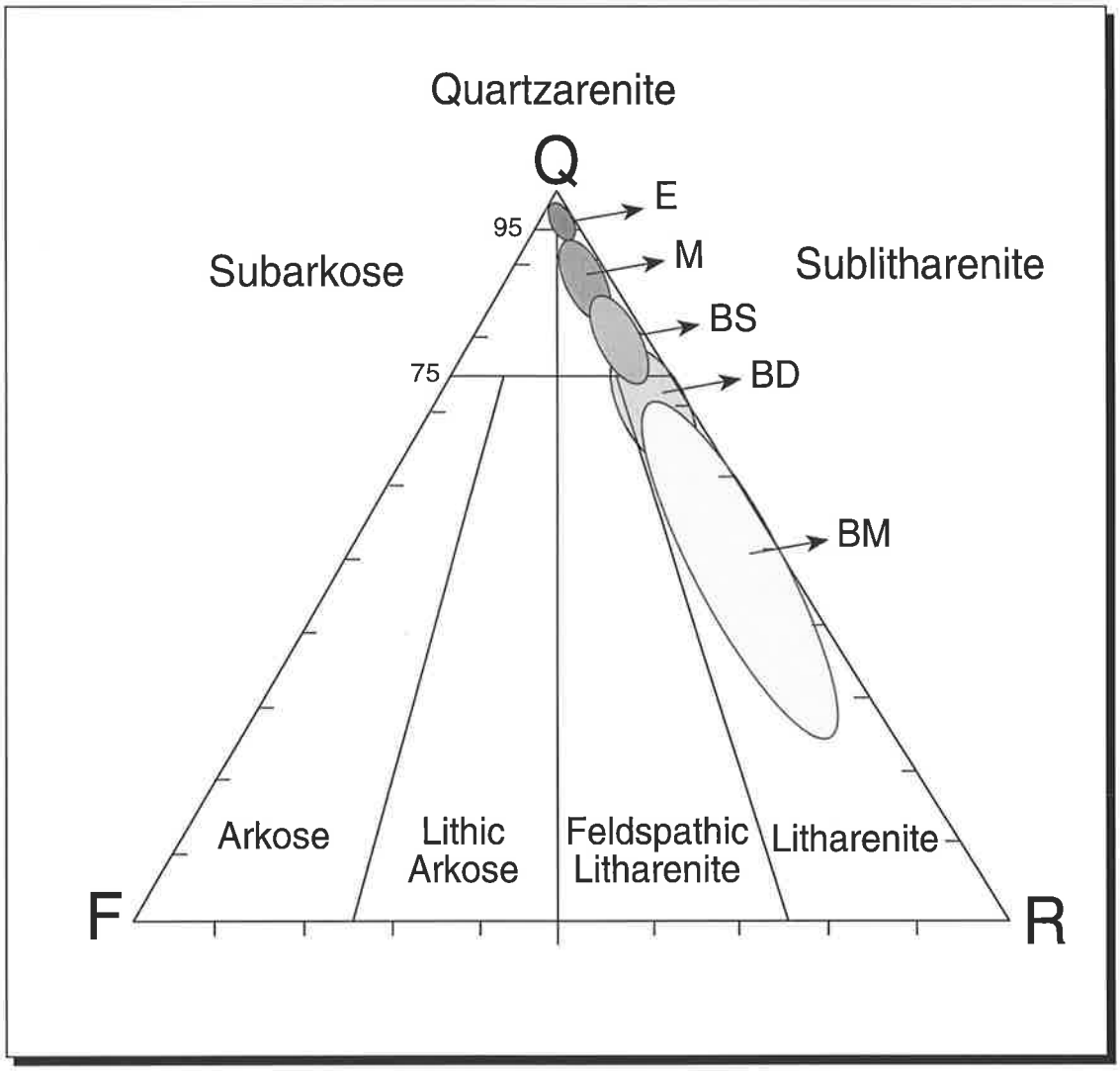

Figure 4.3 - QFR ternary diagram showing the inferred framework grain composition of the Tirrawarra Sandstone at deposition for different depositional environments (Classification after Folk, 1974). BM= medial part of braid-delta, BM= medial part of the braid-delta, BD= distal part of the braid-delta, BS= beach barrier, M= meandering system and E= aeolian.

4.2.2.2 Minor Components

Minor components of the Tirrawarra Sandstone (accounting for less than 1% of the sample) consist of heavy minerals (principally zircon and tourmaline), carbonaceous material, dead oil and micas, most of which were derived from the disintegration of metamorphic rock clasts.

4.2.2.3 XRD results and Interpretation

The bulk-sample X-ray diffraction results of the representative samples indicate that quartz, kaolinite and siderite are the major components of the Tirrawarra Sandstone (Appendix 3). Illite occurs in minor amounts in most of the samples. The relative abundance of each mineral was assessed by comparison of the main peak heights (Table 4.2). Mineral identification was checked by comparison with Joint Committee on Powder Diffraction Standards (JCPDS) files using the CSIRO software Xplot^{TM}.

Based on bulk XRD analysis for 45 representative samples, the Tirrawarra Sandstone can be classified to three groups. An example of each group is shown in Figures 4.4a-c. The first group are samples in which quartz is the dominant component and clay minerals and siderite cement occur only in trace amounts. The second group has quartz and kaolinite as the major elements with siderite as a trace component. In the third group, quartz and siderite are dominant components. The first group contains mainly aeolian, point bar and beach barrier sands, the second group is charactrised of the braid-delta environment deposits and the third group contains deposits from marsh and lacustrine environments.

The identification of kaolin polytypes by randomly oriented, powder XRD method was accomplished by checking the presence or absence of peaks at 2-θ = 27.0° (3.834Å) and 2-θ = 45.0° (2.324 Å) (Co K_α radiation). The results indicate kaolinite as the main kaolin type and only trace amounts of dickite were identified.

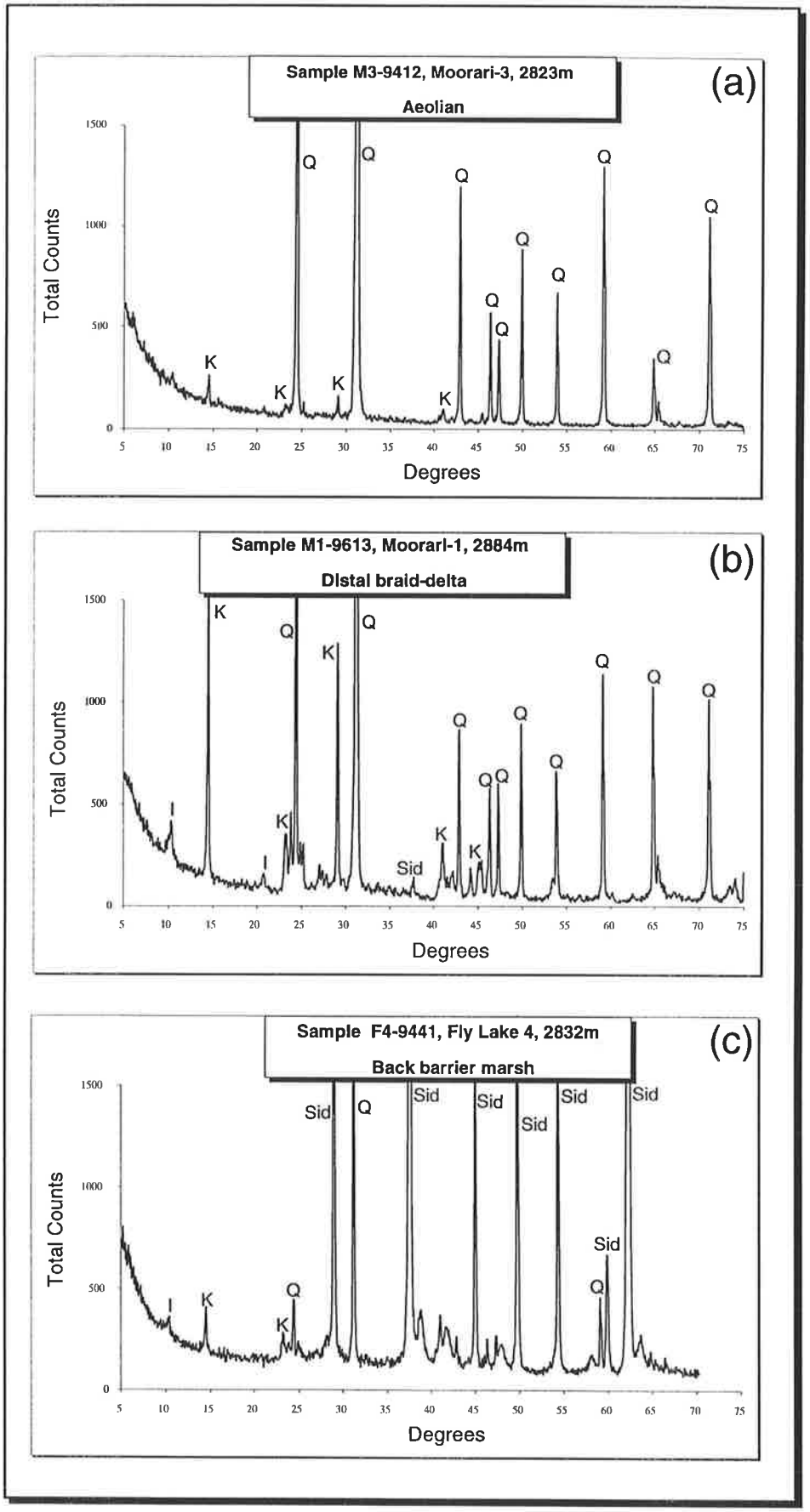

Figure 4.4a-c - Representative XRD peak patterns for, **a)** quartz-rich, **b)** kaolinite-rich and **c)** siderite-rich samples, (I = illite, K = kaolinite, Q = quartz, Sid = siderite).

Table 4.1 - Summary of petrographic point count data for 130 thin sections from the Tirrawarra Sandstone.

	Max.	Min.	Ave.	St.Dev
Quartz	72.8	30	57	6
Non-ductile rock fragments	19	0	3	4
Ductile rock fragments	52	0.5	13	10
Total rock fragments	67	1.5	16	11
Feldspar	0.5	0	0	0.1
Replacement kaolinite	5	0	2	1
Pore-filling kaolinite	8	0	4	2
Quartz cement	19	0	9	4
Siderite cement	30	0	2.5	3
Total cement	23	0	14	5
Secondary porosity	14	0	4	4
Primary porosity	14	0	2.5	2.6
Macroporosity	20	0	6	5
Microporosity	8	0	4	2
Total porosity	23	0	10	5
Intergranular volume	37	0	21.5	8
Original intergranular volume	43	25	36	4
Compaction Index	95	3	41	21
Grain size (mm)	2	0.1	0.4	0.2
Sorting (ϕ)	2	0.1	0.7	0.5

Table 4.2 - Origin and composition of Tirrawarra Sandstone core samples. Mineralogy was determined by semi-quantitative bulk-rock XRD analysis. Siderite is the only carbonate cement present but occurs in varying proportions. Qtz = quartz; Kao = kaolinite; I/M = illite, muscovite; D = dominant (peak>1200 counts); S = subdominant (800<main peak>1200); M = minor (400<main peak>800); T = trace (peak<400).

Well Name	Sample No.	Depth (mKB)	Qtz	Kao.	I/M	Sid.
Fly Lake 1	F1-9397	2864.2	D	M	T	D
Fly Lake 1	F1-9417	2825.1	D	M	T	M
Fly Lake 1	F1-9431	2875.2	D	D	T	S
Fly Lake 2	F2-9554	2912.1	D	T	T	T
Fly Lake 2	F2-9561	2914.2	D	T	T	?
Fly Lake 2	F2-9568	2916.3	D	T	T	T
Fly Lake 2	F2-9570	2916.9	D	S	T	T
Fly Lake 2	F2-9583	2920.9	D	M	T	D
Fly Lake 2	F2-9590	2923.0	D	D	T	S
Fly Lake 2	F2-9598	2924.3	D	S	T	M
Fly Lake 3	F3-9588	2921.5	D	M	T	M
Fly Lake 3	F3-9593	2923.9	D	D	T	T
Fly Lake 4	F4-9441	2877.6	D	T	T	D
Fly Lake 5	F5-9401	2865.4	D	T	T	T
Fly Lake 5	F5-9454	2881.6	D	T	T	-
Fly Lake 6	F6-9398	2864.5	D	T	T	-
Fly Lake 6	F6-9401	2865.4	D	T	T	T
Moorari 1	M1-9420	2872.4	D	T	T	M
Moorari 1	M1-9596	2924.9	D	T	T	T
Moorari 1	M1-9598	2925.5	D	T	T	M
Moorari 1	M1-9613	2930.0	D	D	T	T
Moorari 1	M1-9620	2936.1	D	M	T	S
Moorari 2	M2-10090	3075.4	D	T	T	M
Moorari 2	M2-10116	3083.4	D	T	T	M
Moorari 2	M2-10127	3086.7	D	T	T	T
Moorari 2	M2-10145	3092.2	D	T	T	T
Moorari 3	M3-9422	2868.8	D	T	T	M
Moorari 3	M3-9440	2874.6	D	M	T	T
Moorari 3	M3-9465	2884.9	D	T	T	T
Moorari 3	M3-9465	2885.2	D	M	T	-
Moorari 3	M3-9501	2895.9	D	T	T	T
Moorari 3	M3-9503	2896.5	D	M	T	T
Moorari 4	M4-9507	2897.7	D	T	T	-
Moorari 4	M4-9523	2902.6	D	T	T	-
Moorari 4	M4-9531	2905.0	D	T	T	-
Moorari 4	M4-9554	2912.1	D	M	T	M
Moorari 5	M5-9458	2882.8	D	D	T	T
Moorari 5	M5-9463	2884.3	D	T	T	-
Moorari 5	M5-9510	2898.6	D	M	T	T
Moorari 5	M5-9513	2899.6	D	M	T	T
Moorari 5	M5-9528	2904.1	D	T	T	-
Moorari 5	M5-9583	2874.8	D	T	T	T
Moorari 6	M6-9780	2980.9	D	T	T	T
Moorari 7	M7-9589	2922.7	D	S	T	T
Moorari 9	M9-9732	2966.3	D	M	T	D

4.3 DIAGENETIC EVENTS

According to McBride (1989), diagenesis is defined as the chemical and physical modification of sediments after deposition and prior to the onset metamorphism. Mechanical compaction, chemical compaction, cementation, dissolution, and replacement are the diagenetic processes that are responsible for modification of original intergranular porosity. Diagenetic events have resulted in reduction of porosity and permeability of the Tirrawarra Sandstone in the Moorari and Fly Lake Fields (Rezaee, 1994). Dissolution of labile detrital grains and cement in the course of diagenesis is the only exception to this trend. Mechanical compaction and cementation are the principle factors which influence primary porosity. The effect of these two factors is controlled by composition, a facies-dependent parameter.

4.3.1 Compaction

4.3.1.1 Mechanical compaction

Mechanical compaction, mainly induced by lithostatic pressure, causes bulk-volume reduction in sediments (Houseknecht, 1987). This usually involves reduction of the intergranular volume, but if ductile grains are present, framework-grain volume reduction may also occur. Evidence of mechanical compaction in the Tirrawarra Sandstone seen in thin-section, includes plastic deformation of rock fragments, grain slippage and rearrangement and mica bending (Plate 1).

Two methods are used to evaluate compaction. The first, the Compaction Index, was used by Houseknecht (1987) to evaluate the loss of original porosity as a result of compaction. The Compaction Index in the present study was defined by the following equation:

$$Compaction\ Index = \left[\frac{IGV_O - IGV}{IGV_O}\right] \times 100$$

where IGVo is the original intergranular volume at the time of deposition; and IGV is the present intergranular volume. IGVo was calculated for each sample following the method

Plate 1

Micrographs of Mechanical Compaction

A - Photomicrograph showing mechanical compaction of a ductile rock fragment. Ductile rock fragments are very sensitive to compaction and can be readily deformed and squeezed into the adjacent pores. Sample F3-9593, Fly Lake-3, 2878 m. Scale bar = 250 μm.

B - Quartz cement is not developed at the quartz grain - rock fragment contact (upper arrow), whereas between quartz grains, development of a relatively thick overgrowth can be seen (lower arrow). In sandstones rich in rock fragments with less quartz cementation, mechanical compaction and porosity loss is greater. Sample F3-9593, Fly Lake-3, 2878 m. Scale bar = 250 μm.

C - Plastic deformation of rock fragment by mechanical compaction; it has squeezed the ductile rock fragment into the adjacent pore spaces. Mechanical compaction is one of the prime digenetic processes which modifies porosity in the Tirrawarra Sandstone. Sample M1-9633, Moorari-1, 2889.9 m. Scale bar = 250 μm.

D - At the detrital quartz and rock fragment contact (right arrow), quartz cement often does not develop, allowing compaction to continue. At the quartz-quartz contact (left arrow), quartz cement tends to grow and this prevents subsequent compaction and preserves porosity. Scanning electron micrograph of sample M6-9733.2, Moorari-6, 2920 m. Scale bar = 200 μm.

E - Photomicrograph showing mica bent by mechanical compaction. Sample M3-9435, Moorari-3, 2830.5 m. Scale bar = 250 μm.

F - Plastic response of a low-grade metamorphic rock fragment to overburden pressure. Note to the sutured contact between quartz grains due to pressure solution on the right hand side of the micrograph. Sample M3-9403.6, Moorari-3, 2821 m. Scale bar = 250 μm.

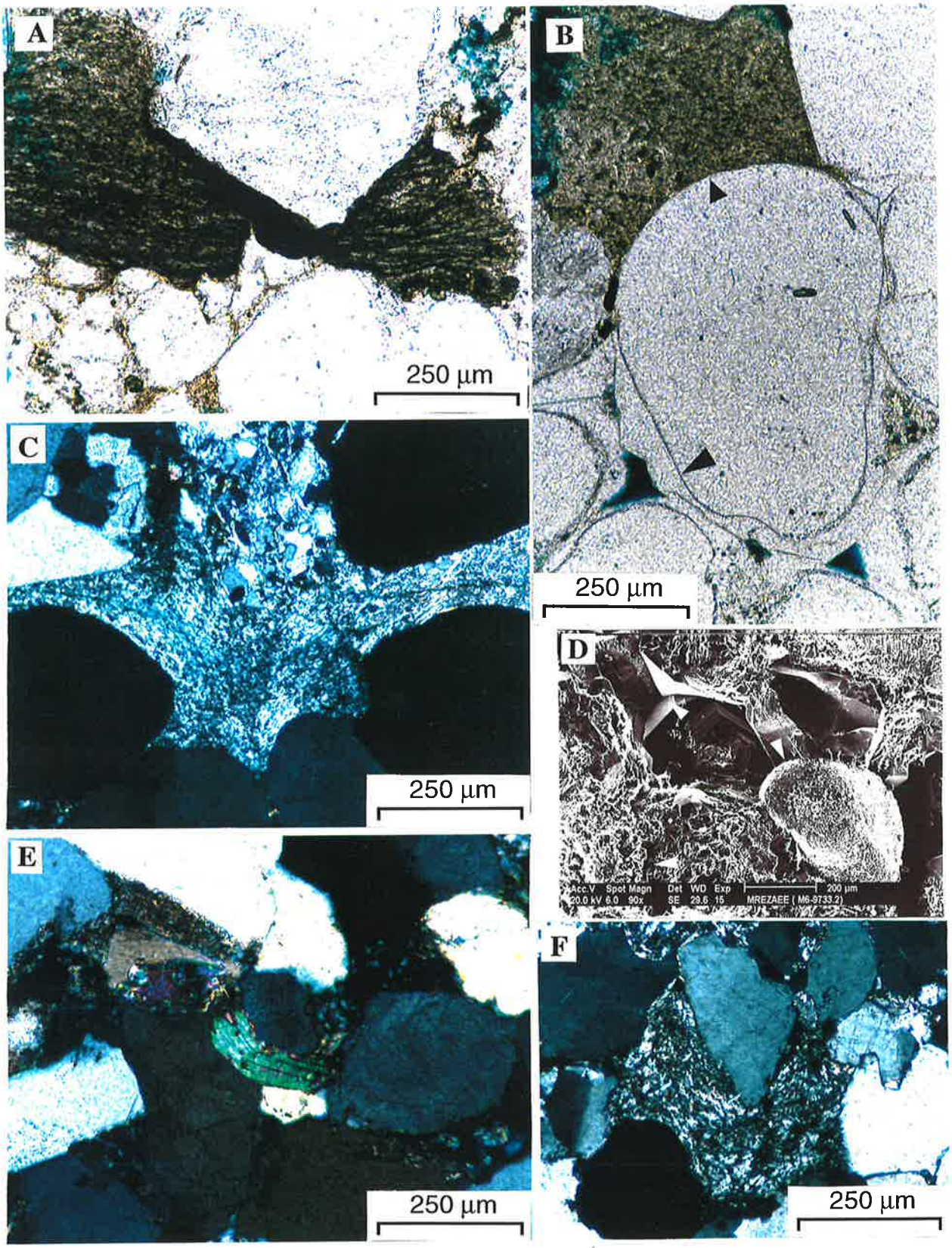
A
250 µm
B
250 µm
C
250 µm
D
Acc.V Spot Magn Det WD Exp 200 µm
20.0 kV 6.0 90x SE 29.6 15 MREZAEE (M6-9733.2)
E
250 µm
F
250 µm

of Beard and Weyl (1973), using knowledge of sample grain size and sorting. IGV is the sum of intergranular porosity and total cement.

Compaction in the Tirrawarra Sandstone varies from 3% to 95%. Since the maximum depth of burial of the samples studied does not vary significantly, the major parameters which control compaction are mineralogical composition and the occurrence of quartz cement, factors which are in turn controlled by depositional processes.

The second method used to estimate compaction was the contact index (CI). Figure 4.5 indicates that there is a negative relationship between this index and intergranular volume. As expected, the number of contacts between grains decreases as the proportion of rock fragments decreases and the amount of quartz cement increases. The CI varies in the samples studied from 1.6 to 2.8.

4.3.1.2 Chemical Compaction

Chemical compaction was defined by Houseknecht (1987) as "bulk volume reduction caused by the dissolution of framework grains at the contact points due to overburden pressure". Durney (1972) and Engelder et al., (1981) suggested that overburden pressure and tectonic forces are causes for dissolution of rock-forming components. This diagenetic process was named pressure dissolution by Bathurst (1987).

In the Tirrawarra Sandstone, chemical compaction can be distinguished both in thin sections and hand specimens by the presence of stylolites, concavo-convex and sutured grain contacts and pressure dissolution seams (Plate 2). It is common in finer-grained samples containing clay, pseudomatrix, and carbonaceous material. In these types of sandstones, the effect of carbonaceous materials and clays to promote chemical dissolution is obvious (cf. Heald, 1959; Thomson, 1959; Weyl, 1959; Füchtbauer, 1967; Houseknecht & Hathon, 1987; Ehrenberg, 1990; Bjørkum, 1996). Pressure solution in the Tirrawarra Sandstone is facies-dependent, and is most prominent in intervals that were originally low in permeability and porosity.

Railsback (1993) indicated that pressure dissolution surfaces in Paleozoic carbonate rocks from mideastern United States varies with rock fabric. In the Tirrawarra Sandstone, the form of dissolution through pressure solution is apparently is controlled by the nature of the grains that come in contact with each other. Three different situations in respect to grain contact can be recognised in the Tirrawarra Sandstone.

of Beard and Weyl (1973), using knowledge of sample grain size and sorting. IGV is the sum of intergranular porosity and total cement.

Compaction in the Tirrawarra Sandstone varies from 3% to 95%. Since the maximum depth of burial of the samples studied does not vary significantly, the major parameters which control compaction are mineralogical composition and the occurrence of quartz cement, factors which are in turn controlled by depositional processes.

The second method used to estimate compaction was the contact index (CI). Figure 4.5 indicates that there is a negative relationship between this index and intergranular volume. As expected, the number of contacts between grains decreases as the proportion of rock fragments decreases and the amount of quartz cement increases. The CI varies in the samples studied from 1.6 to 2.8.

4.3.1.2 Chemical Compaction

Chemical compaction was defined by Houseknecht (1987) as "bulk volume reduction caused by the dissolution of framework grains at the contact points due to overburden pressure". Durney (1972) and Engelder et al., (1981) suggested that overburden pressure and tectonic forces are causes for dissolution of rock-forming components. This diagenetic process was named pressure dissolution by Bathurst (1987).

In the Tirrawarra Sandstone, chemical compaction can be distinguished both in thin sections and hand specimens by the presence of stylolites, concavo-convex and sutured grain contacts and pressure dissolution seams (Plate 2). It is common in finer-grained samples containing clay, pseudomatrix, and carbonaceous material. In these types of sandstones, the effect of carbonaceous materials and clays to promote chemical dissolution is obvious (cf. Heald, 1959; Thomson, 1959; Weyl, 1959; Füchtbauer, 1967; Houseknecht & Hathon, 1987; Ehrenberg, 1990; Bjørkum, 1996). Pressure solution in the Tirrawarra Sandstone is facies-dependent, and is most prominent in intervals that were originally low in permeability and porosity.

Railsback (1993) indicated that pressure dissolution surfaces in Paleozoic carbonate rocks from mideastern United States varies with rock fabric. In the Tirrawarra Sandstone, the form of dissolution through pressure solution is apparently is controlled by the nature of the grains that come in contact with each other. Three different situations in respect to grain contact can be recognised in the Tirrawarra Sandstone.

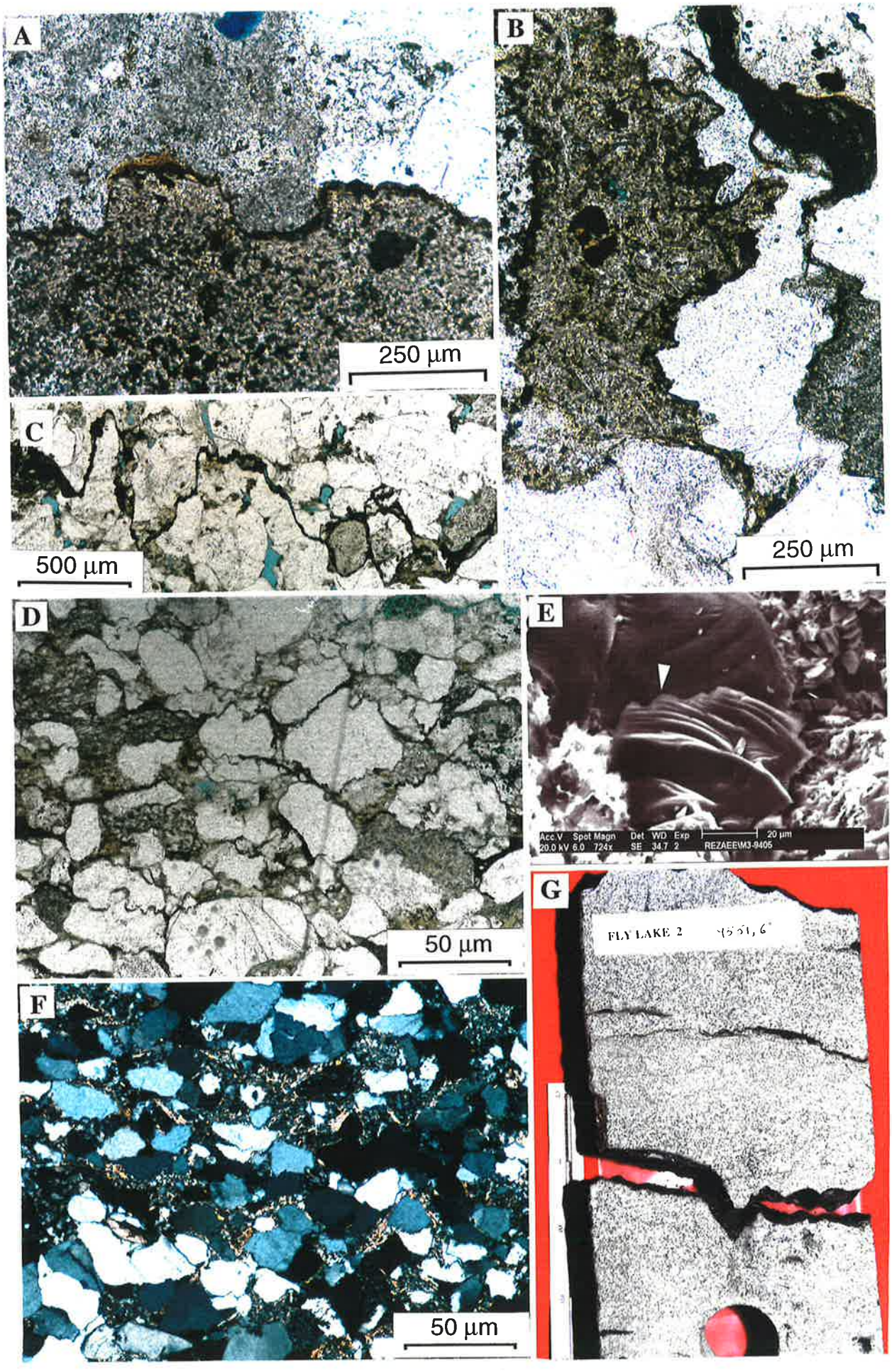
A
250 µm
B
250 µm
C
500 µm
D
50 µm
E
Acc.V Spot Magn Det WD Exp
20.0 kV 6.0 724x SE 34.7 2
20 µm
REZAEE\M3-9405
F
50 µm
G
FLY LAKE 2

These are rock fragment-rock fragment (Rf-Rf), quartz-quartz (Qtz-Qtz), and quartz-rock fragment (Qtz-Rf) contacts. At Qtz-Qtz contacts (Plate 2 C) the dissolution is deep and narrow, whereas at Rf-Rf contacts the dissolution is shallow and board (Plate 2A). Qtz-Rf contacts show an intermediate form (Plate 2B).

4.3.2 Cementation

Cements in the Tirrawarra Sandstone include quartz, clay species and siderite. Quartz cementation, though pervasive in the Tirrawarra Sandstone, is less important than mechanical compaction in porosity reduction, especially in sandstones rich in rock fragments.

4.3.2.1 Quartz Cements

Quartz, in the form of syntaxial rims, is the dominant cement in the Tirrawarra Sandstone (Plates 3 & 4 & 5), and ranges from zero to 19% (Table 4.1). The proportion of quartz cement is controlled by the composition of the sandstones. As the percentage of rock fragments increases, the amount of quartz cement decreases (Fig. 4.6). Quartz cementation appears to be developed very early in some samples with a low concentration of ductile rock fragments (Plate 4A). This is indicated by the preservation of the original intergranular volume (IGVo) (Plate 4A). Quartz overgrowths grew into the primary pores, largely filling them (Plates 3E & 4B), although the initial intergranular porosity is not completely occluded in this way.

The development of quartz cement is inhibited by the presence of any grains other than quartz (Plates 1B 1D & 4H). Quartz overgrowths either completely envelope detrital quartz grains as continuous layers with euhedral margins (Plate 3), or it partially covers the grains (Plate 5 F). The development of quartz cement in some instances is in the form of druse, numerous crystals grown on the surface of a quartz grain (Plate 5A-C). Quartz-cement development occurs preferentially along the c-axis direction and in CL and SEM it can be seen that it often partially covers the detrital grains (Plates 5E-G & 6). Inhibition of growth may be due to the presence of impurities on the quartz surface or interference from neighbouring crystals or grains (Plates 4H & 5F). Quartz cement on composite metamorphic quartz grains is in the form of individual small druse growing on the surface of the grain (Plate 5 A-C)

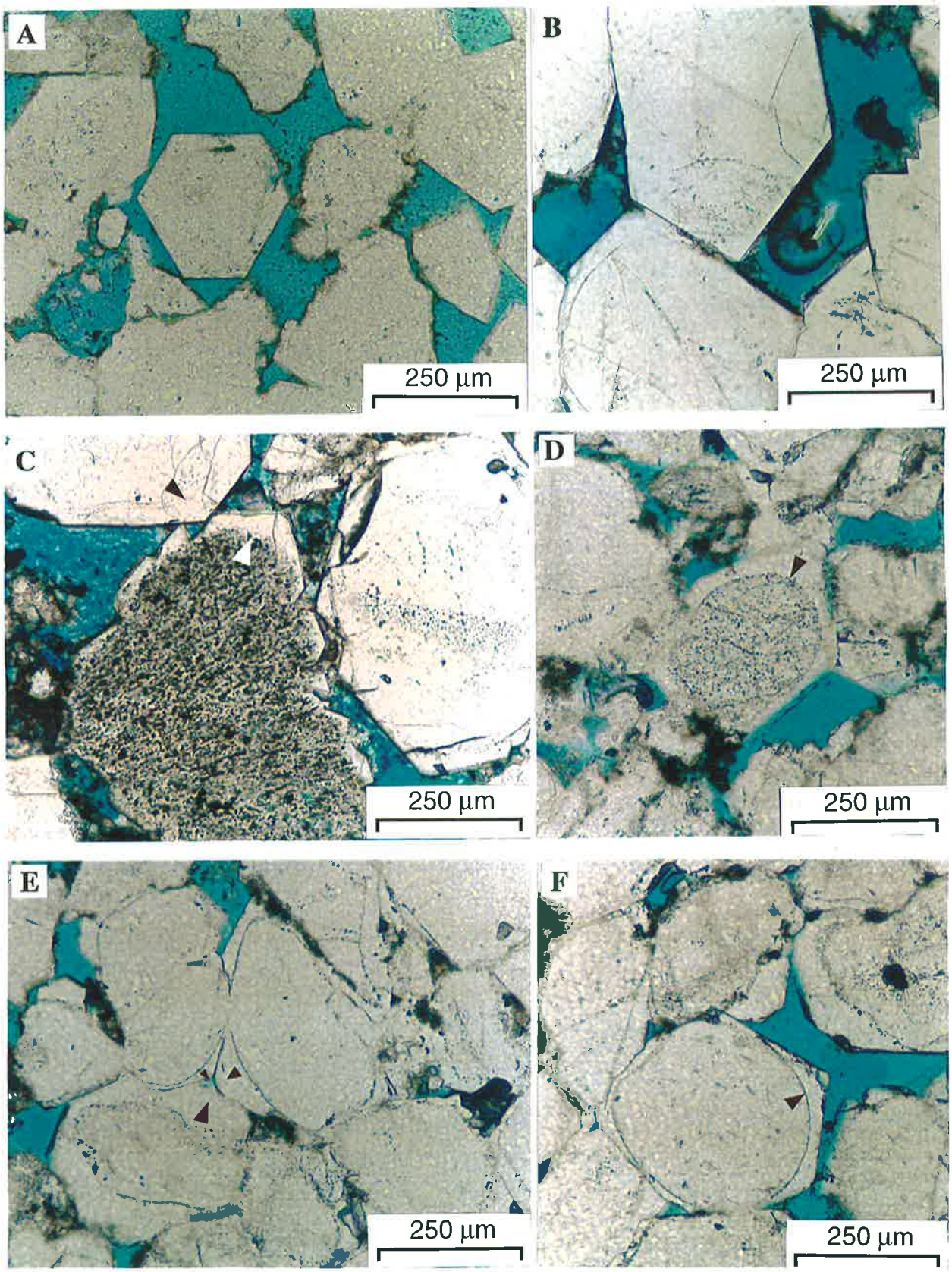
A
250 µm
B
250 µm
C
250 µm
D
250 µm
E
250 µm
F
250 µm

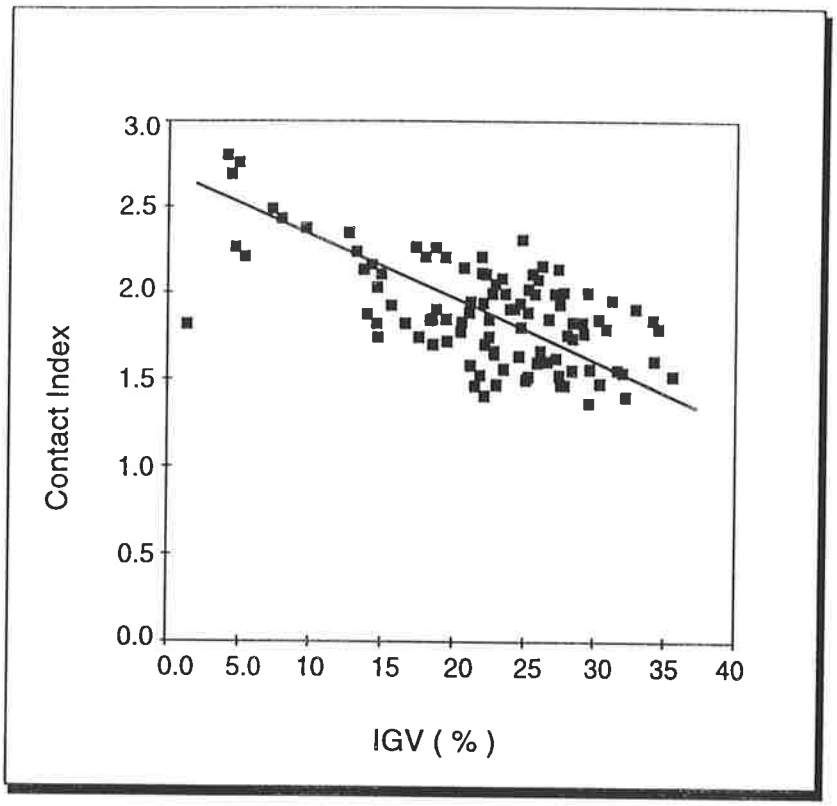

Figure 4.5 - Intergranular volume (IGV) (%) plotted against contact index.

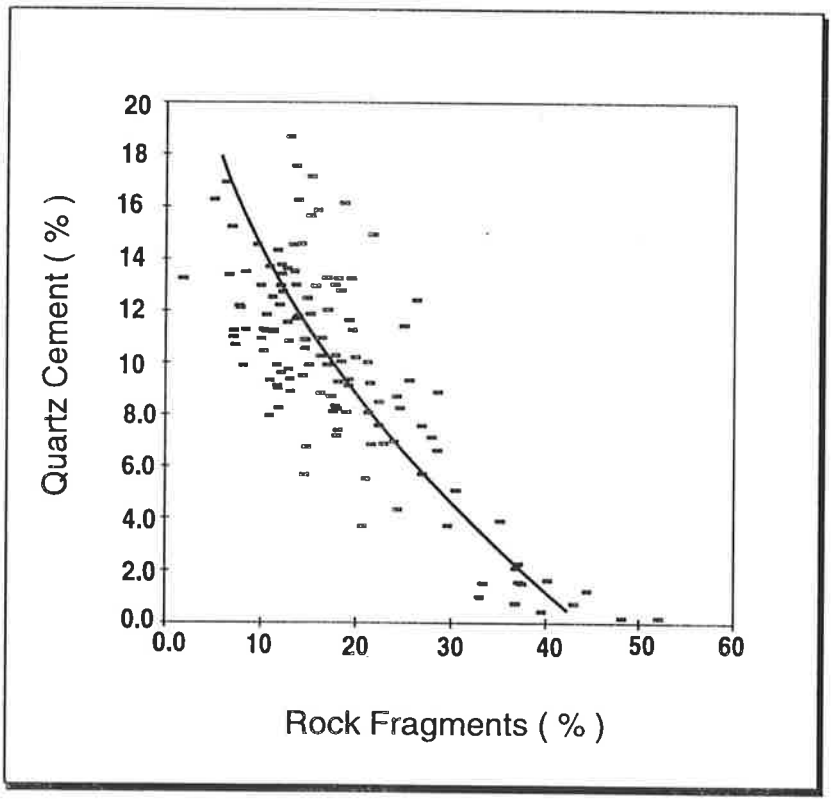

Figure 4.6 - Rock-fragment percentage (%) plotted against quartz cement (%). As the amount of rock fragments increases, the percentage of quartz cement, which inhibits later compaction, decreases.

Plate 4

Micrographs of Quartz Cement (II)

A - SEM micrograph showing well-developed quartz overgrowth. Note the preservation of intergranular porosity between euhedral faces of quartz cement. Sample M3-9405, Moorari-3, 2821.5 m. Scale bar = 100 μm.

B - In this SEM view, an interlocking structure of quartz overgrowths can be seen in a quartz-rich, medium-grained sandstone. The remnant intergranular porosity is between euhedral faces of quartz cement. Sample M3-9412, Moorari-3, 2823.6 m. Scale bar = 200 μm.

C - In some cases, the development of quartz overgrowth is not complete (compare with **A**). In this case, quartz cement appears to be developed as discrete prisms of different size. Sample M3-9405, Moorari-3, 2821.5 m. Scale bar = 100 μm.

D - SEM view showing growth of euhedral quartz prisms into the pore space. Note the presence of complete as well as discrete prisms of quartz overgrowth on different grains. Sample M3-9405, Moorari-3, 2821.5 m. Scale bar = 200 μm.

E - The growth of euhedral quartz prisms into the secondary porosity suggesting that the formation of this quartz cement occurred after dissolution of some labile grains. Sample F6-9388, Fly Lake-6, 2816 m. Scale bar = 20 μm.

F - A close up view of discrete euhedral quartz prisms. Sample F6-9398, Fly Lake-6, 2819.5 m. Scale bar = 250 μm.

G - SEM view showing a clay rim between detrital quartz grain and quartz overgrowth (lower arrow) and another dust rim associated with dissolution? between earlier stage of quartz cement and later ones (upper arrow). Sample M3-9405, Moorari-3, 2821.5 m. Scale bar = 50 μm.

H - At a quartz-quartz contact, quartz cement can develop which makes a rigid framework that helps prevent subsequent compaction and preserve porosity (right arrow). At a quartz grain - rock fragment contact, quartz cement does not develop and grain framework can squeeze into pore spaces by overburden pressure (left arrow). Sample M3-9405, Moorari-3, 2821.5 m. Scale bar = 100 μm.

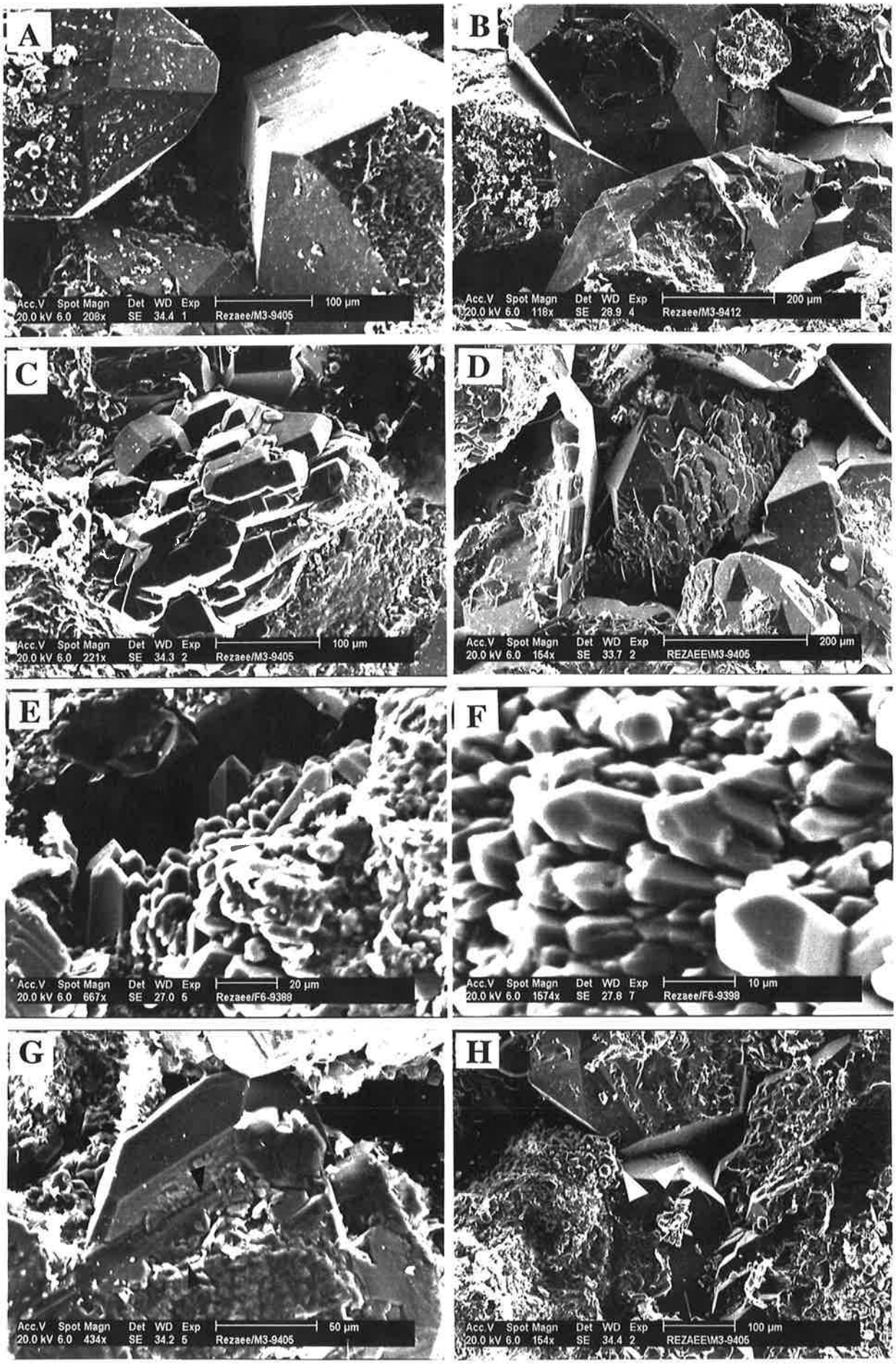
A
Acc.V Spot Magn Det WD Exp 100 µm
20.0 kV 6.0 208x SE 34.4 1 Rezaee/M3-9405
B
Acc.V Spot Magn Det WD Exp 200 µm
20.0 kV 6.0 118x SE 28.9 4 Rezaee/M3-9412
C
Acc.V Spot Magn Det WD Exp 100 µm
20.0 kV 6.0 221x SE 34.3 2 Rezaee/M3-9405
D
Acc.V Spot Magn Det WD Exp 200 µm
20.0 kV 6.0 154x SE 33.7 2 REZAEE\M3-9405
E
Acc.V Spot Magn Det WD Exp 20 µm
20.0 kV 6.0 667x SE 27.0 5 Rezaee/F6-9388
F
Acc.V Spot Magn Det WD Exp 10 µm
20.0 kV 6.0 1574x SE 27.8 7 Rezaee/F6-9398
G
Acc.V Spot Magn Det WD Exp 50 µm
20.0 kV 6.0 434x SE 34.2 5 Rezaee/M3-9405
H
Acc.V Spot Magn Det WD Exp 100 µm
20.0 kV 6.0 154x SE 34.4 2 REZAEE\M3-9405

In some samples, recognition of quartz overgrowth is impossible without cathodoluminescence microscopy (CL), but there were usually some indicators that made it possible to distinguish quartz cement from original quartz grains (Plate 3). The presence of euhedral crystal faces and straight contacts between adjacent grains and dust or clay rims between quartz grains and cement, are useful indicators (Plate 3). In addition, detrital quartz grains are often rich in inclusions, whereas most of the quartz cement is clear (Plate 3C & 3D). In some rare instances in the Tirrawarra Sandstone, volcanic or hydrothermal quartz grains show inherited zonation (Plate 5H) which is similar to quartz overgrowth. The presence of inherited, rounded quartz overgrowth (Plate 5I) indicate that some of the quartz grains originated from a sedimentary source rock.

4.3.2.1.1 Cathodoluminescence Microscopy of Quartz Overgrowth

Although detrital quartz grains display a wide variety of cathodoluminescence colours, quartz overgrowths mostly show very dull CL colours (Zinkernagel, 1978; Matter & Ramseyer, 1985; Henry et al., 1986). Several factors have been identified which influence quartz CL colours, including Ti/Fe ratio, Al content, the presence of positively charged ions with small ionic radii and the degree of lattice order (Sprunt, 1981; Matter & Ramseyer, 1985). CL observation of 16 Tirrawarra samples revealed that three zones of quartz cement (Plates 6 & 7) can be recognised within the Moorari and Fly Lake Fields (Rezaee & Tingate, 1996a; 1997). The earliest zone (dark, yellowish-brown luminescence) is here termed Z1 and occurs as overgrowths developed on detrital quartz grains (Plates 6A, 6C and 7). The second zone (Z2) has a bright blue luminescence that can be easily distinguished from that of the other zones (Plate 6A & 6C). The third and latest zone (Z3) has similar CL colours to the Z1 cement (Plates 6A, 6C and 7). Where the second zone is absent, it is not possible to differentiate the first and the third zones. All cement zones tend to be thicker in the c-axis direction. Where quartz cement is developed unevenly around quartz grains, all cement zones normally show the same irregular distribution (Plate 6A). Two to three smaller cement stages can be occasionally recognised within Z1 and Z3 as faint banding under CL (Plate 6A). Since these smaller cement stages are not found in each sample they are not discussed further.

Plate 5

Micrographs of Quartz Cement (III)

A & C - Crossed nichols and plane light of a detrital composite quartz grain which also has minor quartz cement. Quartz cement in this case is in the form of discrete small quartz druse growing on the surface of detrital grain. In this photomicrograph it can be seen that the nature of detrital grain can control the habit of quartz cement. Sample M3-9435, Moorari-3, 2830.5 m. Scale bar = 250 μm.

B - SEM view of discrete drusy quartz crystals growing on the surface of detrital grain. Sample F6-9398, Fly Lake-6, 2819.5 m. Scale bar = 50 μm.

D & E - Photomicrograph and SEM view of quartz overgrowth developed along c-axis of quartz grain. It can be seen that development of quartz overgrowth on both ends of the quartz grain is well developed. In the middle it is in the form of small discrete prisms along the c-axis of detrital grain. Sample M3-9405, Moorari-3, 2821.5 m. Scale bar = 50 μm.

F - The presence of clays or any impurity on the quartz grain surface may inhibit quartz cementation. In this photomicrograph it can be seen where impurities are present quartz cement has not developed. Sample F2-9548, Fly Lake-2, 2864.4 m. Scale bar = 20 μm.

G - SEM view of euhedral quartz prisms developing into the pore spaces. Note the presence of large euhedral faces of quartz overgrowth in the same sample. Sample M3-9412, Moorari-3, 2823.6 m. Scale bar = 100 μm.

H - Photomicrograph of a volcanic or hydrothermal quartz grain which displays inherited zonation that can be mistaken as quartz overgrowth. In this example only the last inclusion-free zone is authigenic quartz cement. Sample M3-9403.6, Moorari-3, 2821 m. Scale bar = 1000 μm.

I - Another example of inherited quartz cement. In this example the first generation of quartz cement (arrow) which is rounded is inherited from sedimentary source. A thick quartz overgrowth covering this inherited quartz cement and developing into the pore space with euhedral faces. Sample M1-9637, Moorari-1, 2891 m. Scale bar = 250 μm.

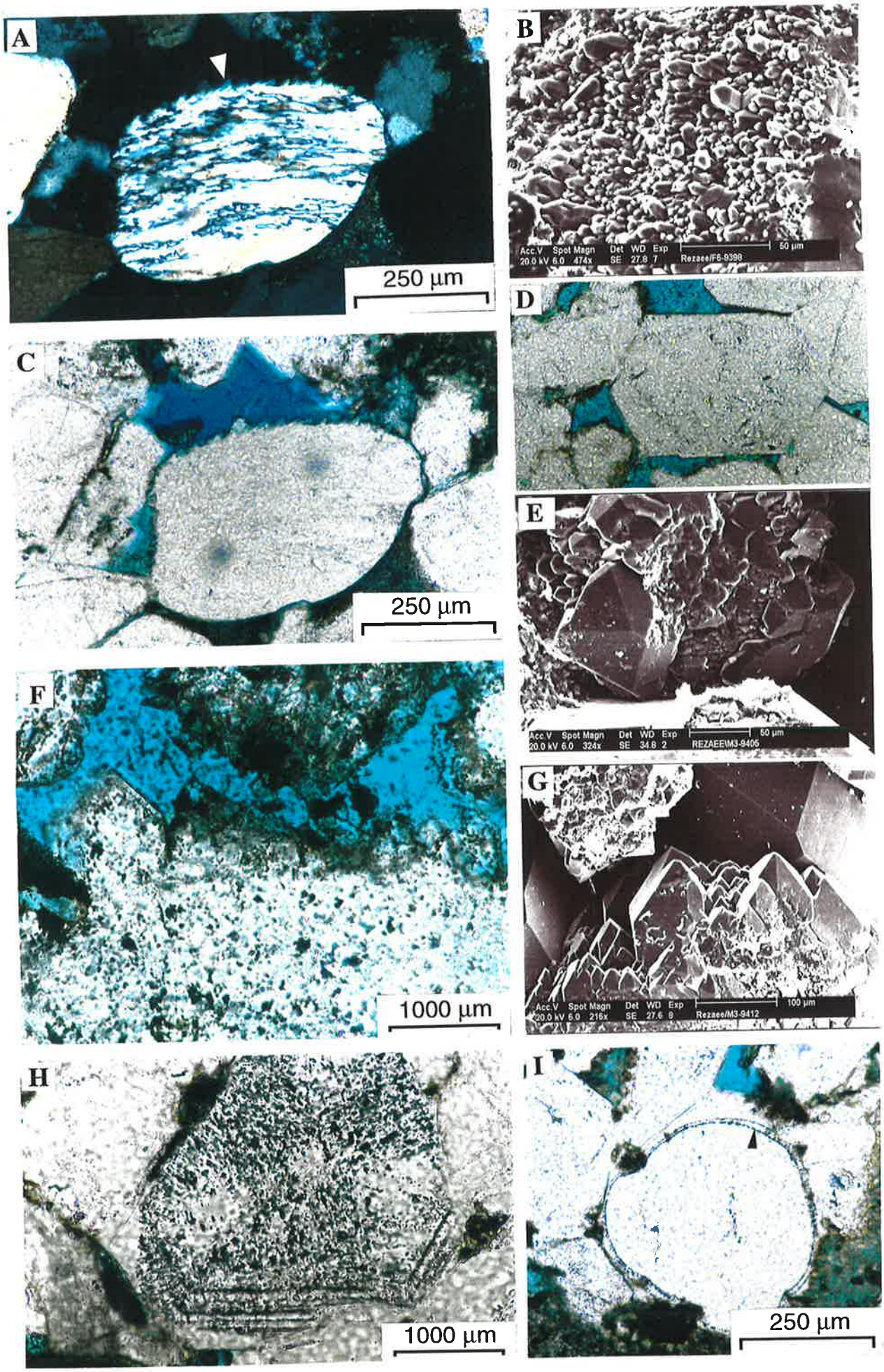
A
250 µm
B
Acc.V Spot Magn Det WD Exp
20.0 kV 6.0 474x SE 27.8 7
50 µm
Rezaee/F6-9398
C
250 µm
D
E
Acc.V Spot Magn Det WD Exp
20.0 kV 6.0 324x SE 34.8 2
50 µm
REZAEE\M3-9405
F
1000 µm
G
Acc.V Spot Magn Det WD Exp
20.0 kV 6.0 216x SE 27.6 8
100 µm
Rezaee/M3-9412
H
1000 µm
I
250 µm

4.3.2.1.2 *Electron Microprobe Analyses of Quartz Overgrowth*

Electron microprobe analyses were carried out on different zones of quartz cement for six elements (Fe, Ti, Mn, Al, Cu and Pb), which are associated with enhanced quartz cathodoluminescence (Sprunt, 1981; Matter & Ramseyer, 1985) (Appendix 5). Except for aluminium, the rest of the elements do not show meaningful variation between cement zones (Table 4.3). The average aluminium concentration is 237, 538 and 58 ppm for Z1, Z2 and Z3 quartz cements (Table 4.4). The bright blue colour of the Z2 quartz cement appears to be related to its high aluminium content, which is possibly associated with accompanying charge balancing cations (Ramseyer & Mullis, 1990; Perny et al., 1992). Electron microprobe analysis was also carried out on several detrital grains in the Tirrawarra Sandstone which have an average aluminium concentration of 35 (ppm) (Table 4.4). EDX analysis also indicated that quartz cement has higher aluminium content than detrital quartz grains (Fig 4.7).

4.3.2.1.3 *Quartz Overgrowth Fluid-inclusion Homogenisation Temperatures*

Fluid-inclusion homogenisation temperatures of quartz overgrowths were measured in nine samples (Fig. 4.8) (Appendix 7). Point count data and depositional facies for these samples are shown in Table 4.5. Fluid-inclusion microthermometry was accomplished using primary fluid-inclusions trapped within each cement zone. Based on petrography and CL observations, each fluid-inclusion was assigned to a zone of quartz cement. The measured size of the fluid-inclusions ranged from two to five microns (Plate 8C-E). Homogenisation temperatures of fluid-inclusions within the quartz cement indicate that quartz cement precipitated at temperatures between 65 and 130°C, unless the fluid-inclusions re-equilibrated during burial (cf. Osborne & Haszeldine, 1993; Haszeldine & Osborne, 1993). However, the consistent differences in homogenisation temperatures between different zones of quartz cement indicate that the fluid-inclusions have not reequilibrated (Fig. 4.9). Low-temperature fluid-inclusions (65 - 80°C) occur in

Plate 6

CL Micrographs of Quartz Cement (I)

A - Cathodoluminescence micrograph of quartz cement; arrows point to where there are three zones of quartz cements. Quartz cements include an inner-most zone of brown-luminescing cement (Z1), a middle zone of relatively thick bright blue-luminescing cement (Z2) and an outer zone of brown-luminescing cement (Z3). Note the fractured quartz grain which is probably healed by Z3 quartz cement (arrow). Detrital quartz grains have pale-blue to beige luminescence. Sample M3-9412, Moorari-3, 2823.6 m. Scale bar = 500 μm.

B - Plane light view of **A**. The brown patches are resin (pores) burnt by the electron beam.

C - CL view showing three zones of quartz cement (arrow). Note the bright blue colour of the kaolinite patches at left hand side of the micrograph. In some instances deformed and fractured quartz grains show orange luminescence (lower right corner). Sample M3-9403.6, Moorari-3, 2821 m. Scale bar = 500 μm.

D - Plane light view of **C**.

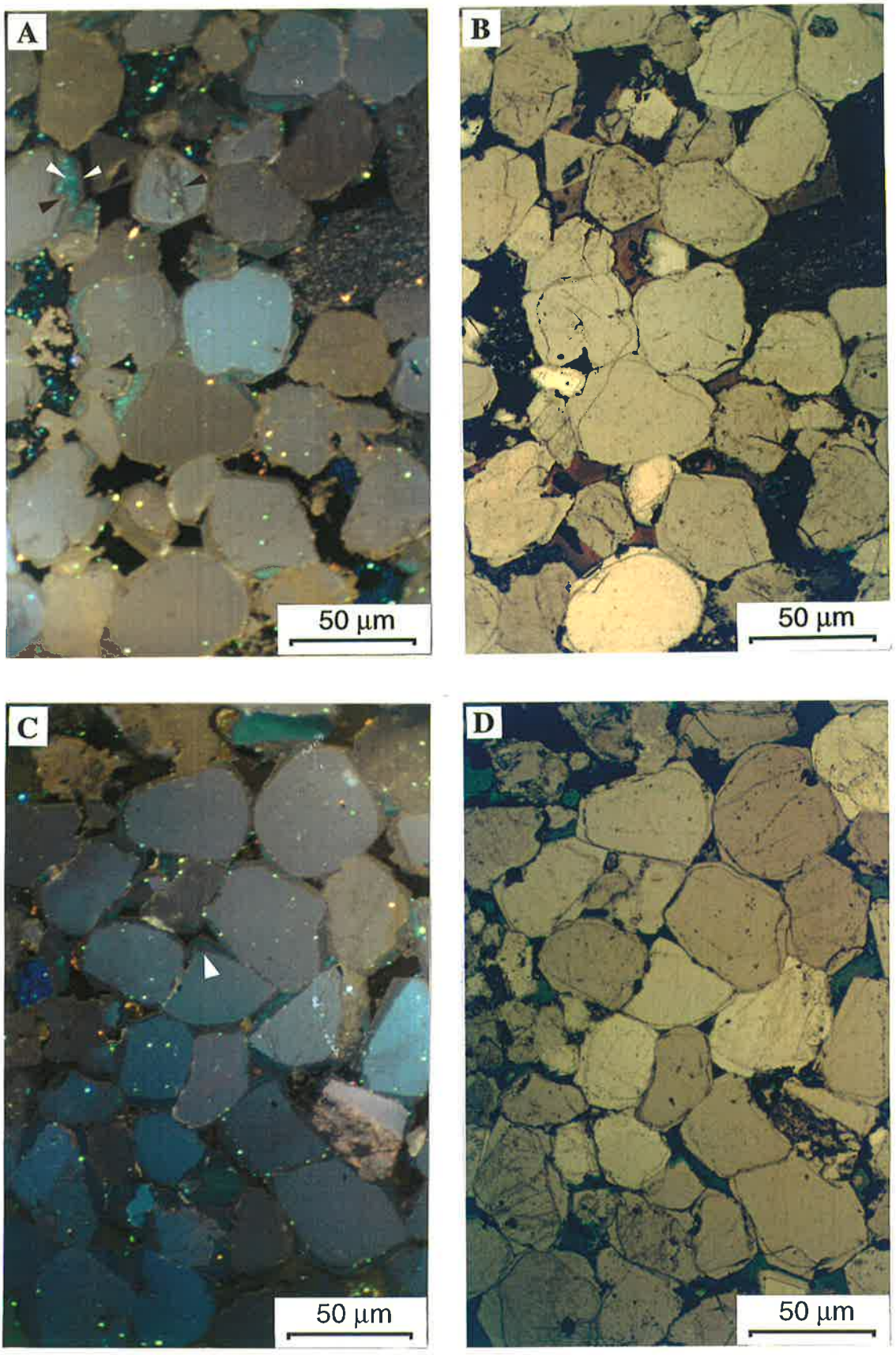
A
50 µm
B
50 µm
C
50 µm
D
50 µm

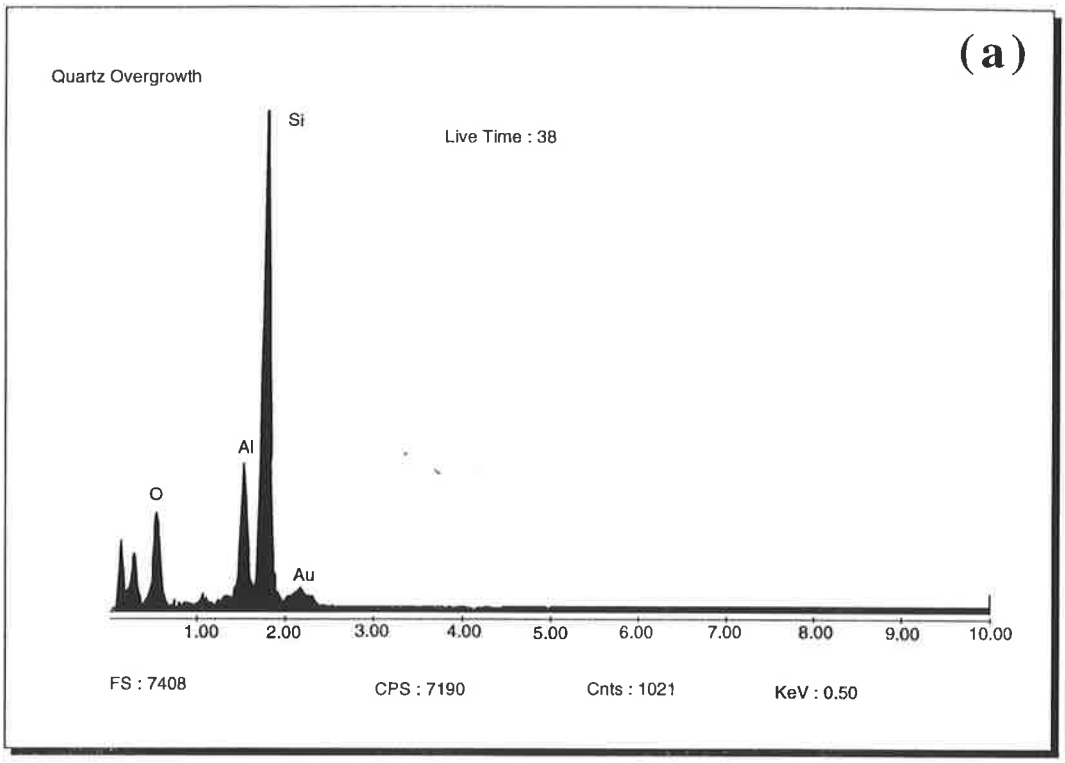

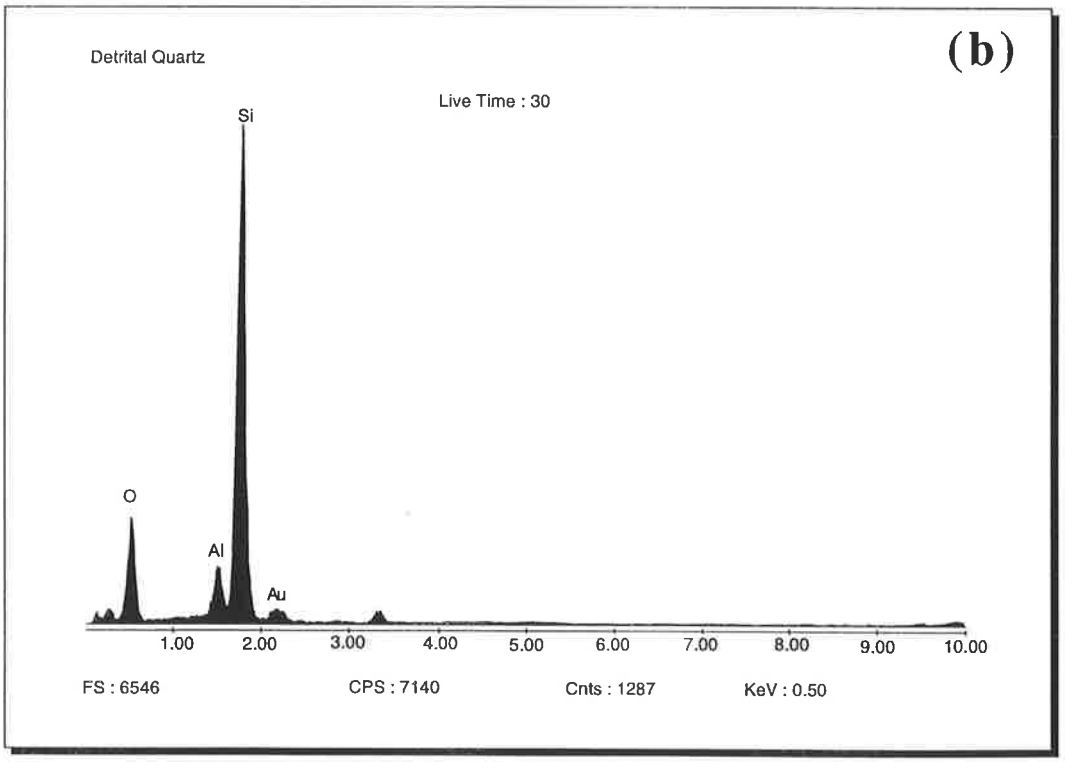

Figure 4.7 - The results of EDX analysis for quartz overgrowth (**a**) and quartz grain (**b**) shows that relatively more aluminium is incorporated in quartz overgrowth lattice.

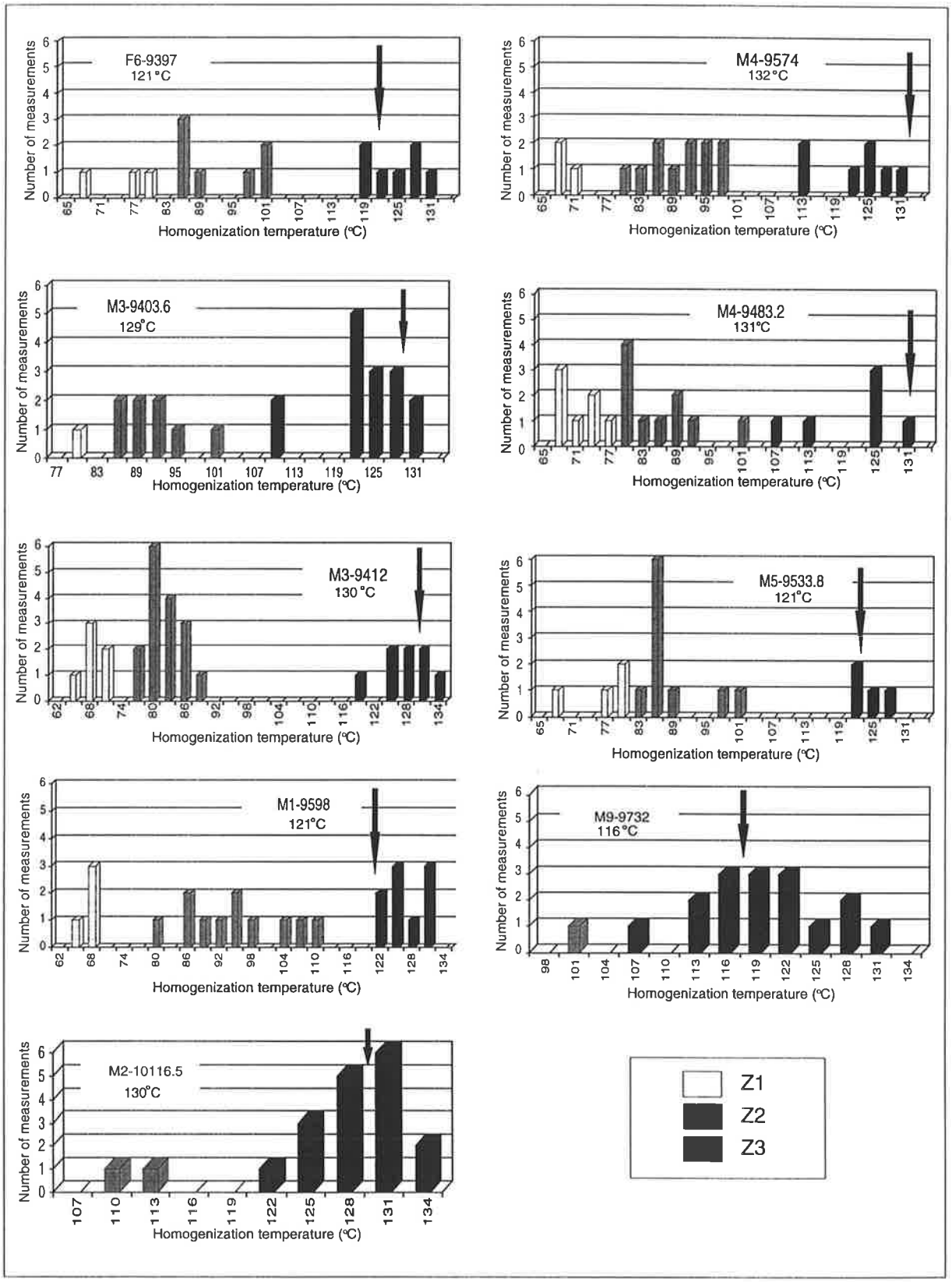

Figure 4.8 - Homogenization temperatures of quartz overgrowths for individual samples. Fluid inclusion homogenization temperatures for each zone of quartz cement are displayed with different patterns. The present temperature of each sample is shown on the diagrams (arrows).

Table 4.3 - Electron microprobe analyses of quartz cement and detrital quartz of the Tirrawarra Sandstone (values in ppm). (bdl = values below detection limit).

Zones	Al	Fe	Ti	Mn	Cu	Pb
Z2	677	166	bdl	bdl	178	bdl
Z2	633	bdl	bdl	265	319	bdl
Z2	621	518	bdl	87	507	390
Z2	617	bdl	134	bdl	bdl	bdl
Z2	584	bdl	bdl	285	424	bdl
Z2	584	101	bdl	bdl	252	bdl
Z2	550	507	bdl	87	497	435
Z2	544	91	bdl	182	bdl	bdl
Z2	526	bdl	134	bdl	bdl	bdl
Z2	461	bdl	bdl	176	181	bdl
Z2	451	bdl	bdl	212	bdl	bdl
Z2	443	bdl	bdl	159	180	bdl
Z2	427	103	bdl	bdl	106	bdl
Z2	421	bdl	bdl	bdl	bdl	bdl
Z1	379	bdl	bdl	101	89	140
Z1	373	82	bdl	bdl	503	141
Z1	289	118	bdl	321	bdl	338
Z1	214	bdl	130	bdl	284	bdl
Z1	212	160	bdl	167	bdl	bdl
Z1	162	bdl	bdl	142	bdl	956
Z1	150	181	bdl	142	bdl	386
Z1	118	bdl	248	bdl	bdl	bdl
Z3	87	368	335	bdl	bdl	329
Z3	80	172	bdl	195	bdl	bdl
Z3	bdl	343	bdl	397	bdl	bdl
Z3	bdl	bdl	bdl	bdl	bdl	bdl
Z3	bdl	265	374	257	bdl	bdl
Z3	bdl	bdl	111	88	bdl	1212
Z3	bdl	338	bdl	bdl	226	479
Z3	bdl	94	bdl	233	385	bdl
Grain	bdl	bdl	88	283	bdl	bdl
Grain	bdl	bdl	128	165	bdl	bdl
Grain	bdl	bdl	80	bdl	95	103
Grain	bdl	bdl	215	bdl	bdl	bdl
Grain	bdl	bdl	bdl	bdl	bdl	bdl
Grain	bdl	bdl	bdl	bdl	bdl	241
Grain	bdl	bdl	128	256	bdl	bdl
Grain	bdl	bdl	bdl	bdl	518	241
Grain	bdl	bdl	175	bdl	bdl	bdl
Grain	bdl	bdl	bdl	bdl	bdl	483
Grain	81	bdl	bdl	bdl	bdl	127
Grain	bdl	186	bdl	356	bdl	103
Grain	81	bdl	bdl	bdl	bdl	bdl
Grain	bdl	bdl	151	bdl	95	bdl
Grain	bdl	bdl	bdl	bdl	bdl	bdl
Grain	bdl	bdl	159	91	bdl	bdl
Grain	bdl	bdl	88	bdl	bdl	bdl
Grain	81	400	135	bdl	bdl	bdl
Grain	bdl	bdl	151	bdl	bdl	bdl
Grain	bdl	bdl	bdl	bdl	bdl	379
Grain	bdl	223	bdl	bdl	285	276

Z1 quartz cement which is well developed in samples with a quartzarenite composition and high intergranular volume (IGV). Primary fluid-inclusions within Z2 cement have a homogenisation temperature range of 80 to 100°C. Homogenisation temperatures of most fluid-inclusions within Z3 cement were approximately 130°C, indicating the minimum precipitation temperature of the late stages of quartz cement.

Table 4.4 - Mean values of trace elements for different zones of quartz cement and detrital quartz grains.

	Z1 (ppm)	Z2 (ppm)	Z3 (ppm)	Grain (ppm)
Al_2O_3	237	538	58	35
FeO	74	119	206	39
TiO_2	75	24	112	84
MnO	113	104	146	60
CuO	125	191	76	52
PbO	251	70	276	149

Plate 7

CL Micrographs of Quartz Cement (II)

A - CL view of a fine-grained sandstone showing development of a relatively thin quartz cement. Quartz cement displays a pale-brown luminescence, whereas quartz grains are pale-blue to beige in luminescence. The bright blue luminescent patches are kaolinite (k). Sample F6-9388, Fly Lake-6, 2816 m. Scale bar = 500 μm.

B - CL view of a medium to coarse-grained sandstone with a relatively thick development of quartz cement (arrows). In samples where Z2 quartz cement is not present, Z1 and Z2, which have the same luminescence, cannot be differentiated. Sample M3-9405, Moorari-3, 2821.5 m. Scale bar = 500 μm.

C - Variation of quartz grain luminescence in the same sample is most likely due to different provenance. The luminescence of quartz grains ranges from blue to brown. Quartz cement consists a pale-brown luminescing overgrowth. Sample M3-9405, Moorari-3, 2821.5 m. Scale bar = 500 μm.

D - Cathodoluminescence view showing relatively-thick brown-luminescing quartz cement. F2-9548, Fly Lake-2, 2864.4 m. Scale bar = 500 μm.

E - CL view of medium to fine-grained sandstone. Comparing to **B** and **D** the development of quartz cement is less and consists mainly of relatively thin pale-brown luminescing cement. In samples which are subjected to early compaction, only Z3 quartz cement has developed, proven by fluid inclusion homogenisation temperatures study. Sample M3-9403.6, Moorari-3, 2821 m. Scale bar = 500 μm.

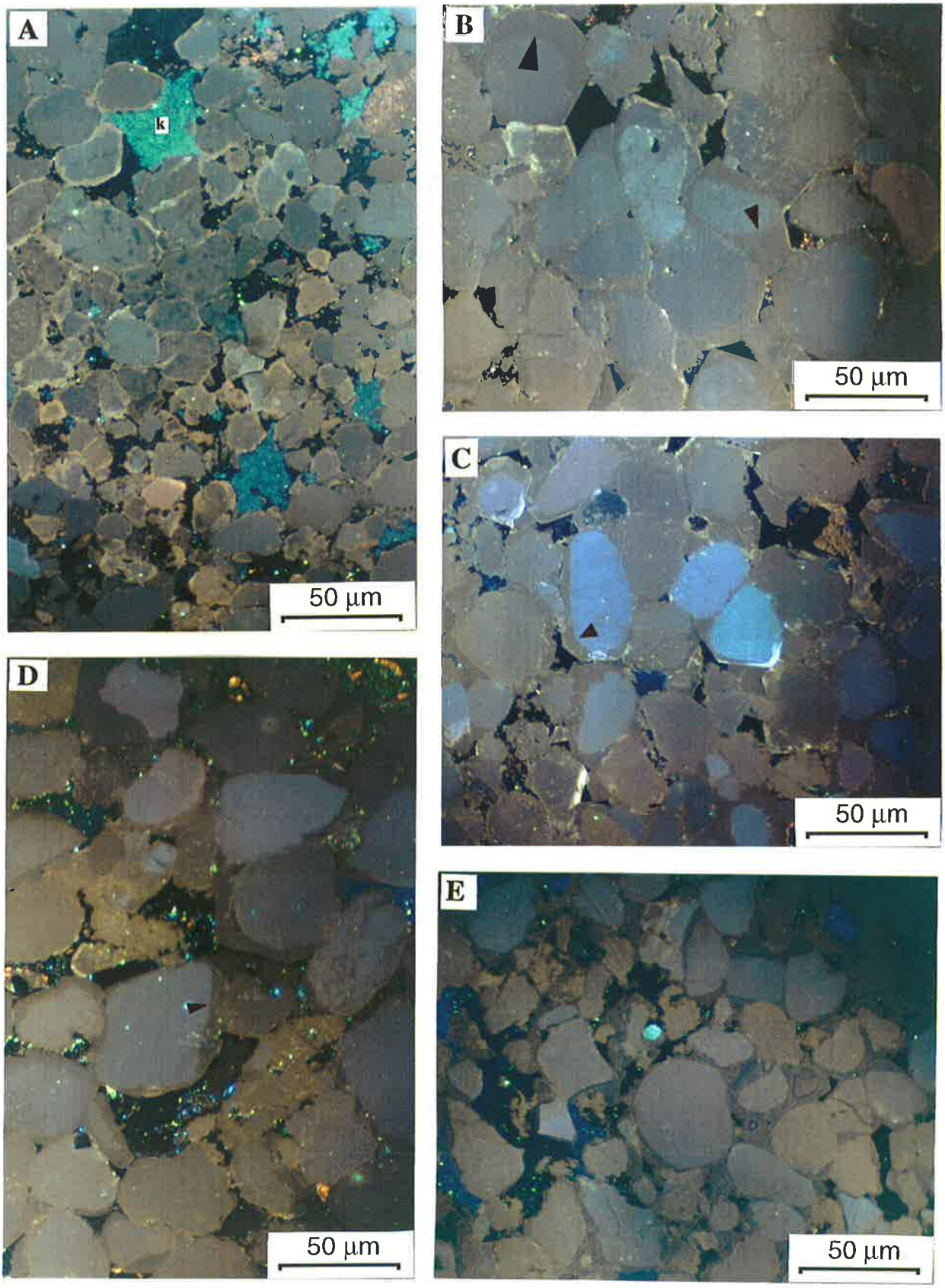
A
k
50 µm
B
50 µm
C
50 µm
D
50 µm
E
50 µm

Table 4.5 - Petrographic point count and depositional facies data for samples used in fluid-inclusion study.

Sample	F6-9397	M1-9598	M2-10116.2	M3-9403	M3-9412	M4-9483.2	M4-9574.6	M5-9553.8	M9-9732
Well	Fly Lake6	Moorari1	Moorari2	Moorari3	Moorari3	Moorari4	Moorari4	Moorari5	Moorari9
Depth(m)	2864.2	2925.5	3083.4	2866.3	2868.8	2890.6	2918.4	2912.0	2966.3
Temp(°C)	121	121	130	129	130	131	132	121	116
QTZ	73	59	45.5	64.4	61	52	60	56	42.6
RFnd	0.5	2.0	3.5	3.4	1.0	1.0	1.4	1.2	4.5
RFd	5	9.5	32	1	5.0	8.7	1	10.8	31.8
FELD	0.0	0.0	0.0	0.0	0.0	0.0	0.0	0.0	0.0
Krep	1.4	1.6	2.9	0.3	1	2.7	1.3	2.3	4.6
Ckaol	2.7	1.1	5.6	1.0	2.2	5.0	0.3	4.4	2.0
Cqtz	8.0	19	1.5	4.0	11	14.5	9.9	15.6	2.3
Csid	0.0	2.8	2	0.4	0.2	0.0	1.4	0.4	7.4
Ctotal	11	23	9.0	5.6	13	19.6	11.6	20.4	11.6
Ps	2.0	2.4	0.6	11	1.6	4.6	7.0	3.0	1.0
Pp	4.6	0.8	0.2	3.4	14	6.4	6.0	2.5	0.0
IGV	23.5	24	14	9.7	30.4	34.5	18	29	13
IGVo	38	40	34	41	40	38.8	38	34	33
Gsize	0.4	0.20	0.4	0.2	0.45	0.4	0.3	0.4	0.6
Sorting	0.4	0.4	0.5	0.3	0.1	0.4	0.4	0.6	0.6
K (mD)	1.2	3.2	<0.5	1.3	328	12	1.3	1.1	0.2
D.Facies	M	BD	BS	M	E	BS	BS	BD	BM

(Qtz= quartz grains, RFnd = non-ductile rock fragments, RFd = ductile rock fragments, RFtotal = total rock fragments, Feld = feldspar, Krep= replacement kaolinite, Ckaol = pore-filling kaolinite, Cqtz = quartz cement, Csid = siderite cement, Ctotal= total cement, Ps = secondary porosity, Pp = primary porosity, IGV = intergranular volume, IGVo = original intergranular volume, Gsize = Grain size, K = Permeability (mD), D. Facies = depositional facies, BD= Distal part of braid-delta, BS = Parallel beach barrier, M = meandering system, E = Aeolian environment, and BM= Medial part of braid-delta). Temp(°C) is present-day temperature of sample.

Plate 8

Micrographs of Fluid Inclusions

A - Two-phase liquid-vapour fluid inclusions are common in middle and late stages of siderite cement. In this micrograph an equidimensional primary fluid inclusion within siderite cement (arrow) can be seen. The diameter of this fluid inclusion which occurs in a late stage of siderite (S3) is about 3 microns. Its homogenisation temperature is approximately 102°C. F2-9583, Fly Lake-2, 2875 m. Scale bar = 50 μm.

B - Two-phase liquid-vapour primary fluid inclusions (arrows) within middle stage of siderite cement. The homogenisation temperatures of these fluid inclusions are around 70°C. Sample F1-9431.4, Fly Lake-1, 2829.4 m. Scale bar = 50 μm.

C - Two-phase liquid-vapour primary fluid inclusions (arrow) are present both along the boundary of a grain and quartz overgrowth and within the body of the overgrowth. In this example many fluid inclusions can be seen along the boundary of the grain and cement. Sample M3-9412, Moorari-3, 2823.6 m. Scale bar = 50 μm.

D & E - In these two photomicrographs it can be seen that, in addition to fluid inclusions along grain and cement boundary, many fluid inclusions exist in the body of the overgrowth (arrows). This allows measurement of homogenisation temperatures of different zones for quartz cements. Sample M5-9553.8, Moorari-5, 2866m. Scale bar = 50 μm.

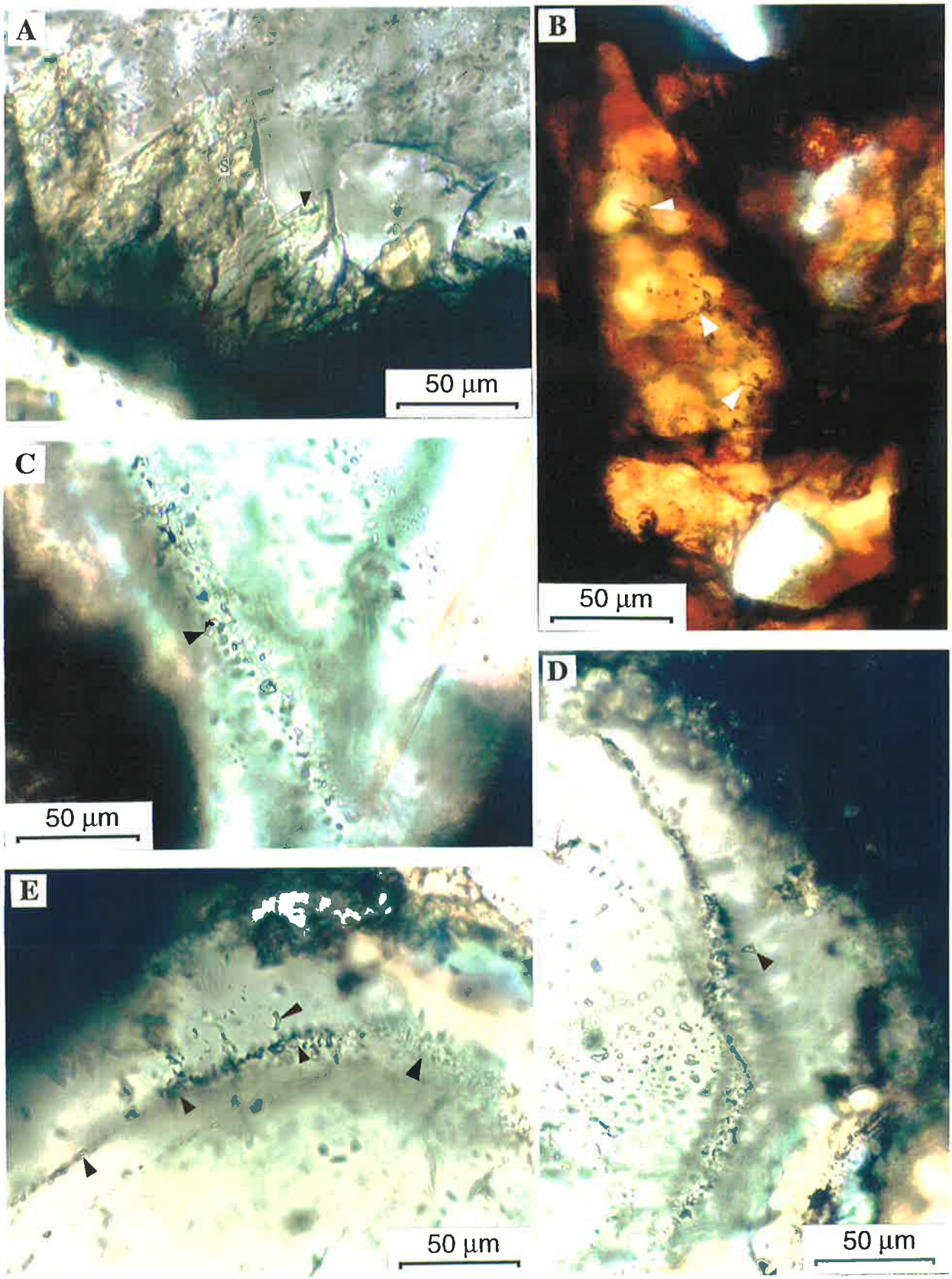
A
B
C
D
E
50 µm
50 µm
50 µm
50 µm

4.3.2.2 Siderite cements

Based on the XRD, SEM, EDX, and electron microprobe studies, siderite is the only carbonate cement within the Tirrawarra Sandstone in the studied area (Table 4.2). Siderite cement occurs in varying proportions in the Tirrawarra Sandstone, and constitutes up to about 30% of rock volume in some samples as determined by point-counting. Under the petrographic microscope and SEM, the siderite habit is generally micritic, isolated, or a pore-filling cement, although a variety of different crystal habits are apparent, including rhombohedral, blocky and radial forms (Plates 9, 10, 11). The relative proportion of micritic siderite cement is higher in the siltstones and fine-grained sandstones. Both petrographic and XRD results suggest a single-phase cement, and only rarely the presence of different generations of siderite cement are evident under the petrographic microscope (Plate 10A & 10D). However, when viewed under the SEM and electron microprobe and using BSE imaging techniques, three main generations of siderite cement are identified, including an early (S1), middle (S2), and late generation cement (S3) (Plates 10B & 11A-B) which are discussed in detail in the following chapter. Fluid-inclusion data indicate that the different siderite cement generations precipitated under different temperature conditions. The S1 siderite cement is more common in a back barrier marsh environment, whereas S2 and S3 can be seen in most of the environments defined in this study.

Evidence for siderite dissolution (Plate 10C, 10E & 10F), exists in the Tirrawarra Sandstone. In a few samples siderite is associated with open porosity (Plate 10F) indicating that dissolution phases of siderite cement may have had a significant role in porosity increase.

4.3.2.2.1 Early Generation Siderite Cement (S1)

Under the optical microscope, S1 has a blotchy appearance, displays a moderately light to dark brown colour (Plates 10B, 11A & 11E) and appears devoid of Fluid-inclusions. In some samples, S1 is the only siderite cement, especially in fine-grained, poorly-sorted marsh sediments rich in organic matter (Plate 11E & 11F). In samples where S1 completely cements the rock, quartz grains are characterised by a very loose grain packing, with individual grains seemingly 'floating' in the siderite matrix (Plate 11E). Where other siderite cement generations are present, S1 generally represents the

Plate 9

Micrographs of Siderite Cement (I)

A - Siderite cement is present in the Tirrawarra Sandstone in different crystal habits. In this example siderite cement is in the form of radially aggregated rhombic crystals filling secondary porosity. Sample F2-9590, Fly Lake-2, 2877 m. Scale bar = 250 μm.

B - In fine-grained back-barrier-marsh sandstones, siderite cement can be seen as radial micritic aggregates. Sample F4-9441.6, Fly Lake-4, 2832.5 m. Scale bar = 250 μm.

C - Sparry siderite cement (S) infilling porosity. Note thick quartz cement separated by a dust rim from a quartz grain. Sample F5-9445, Fly Lake-5, 2833.5 m. Scale bar = 250 μm.

D - A general view of brown, early-stage siderite cement (S1), completely cementing a fine-grained back barrier marsh sandstone. The floating texture suggests it is a relatively early digenetic cement as there is little apparent etching of the framework grains. Sample F2-9583, Fly Lake-2, 2874.9 m. Scale bar = 1000 μm.

E - Siderite crystals postdating quartz overgrowth (arrow). Sample M9-9732, Moorari-9, 2919.6 m. Scale bar = 100 μm.

F - In this photomicrograph, a siderite rhomb is enclosed by quartz overgrowth (arrow). This indicates that later stages of quartz cement postdate siderite cementation. Sample M9-9732, Moorari-9, 2919.6 m. Scale bar = 250 μm.

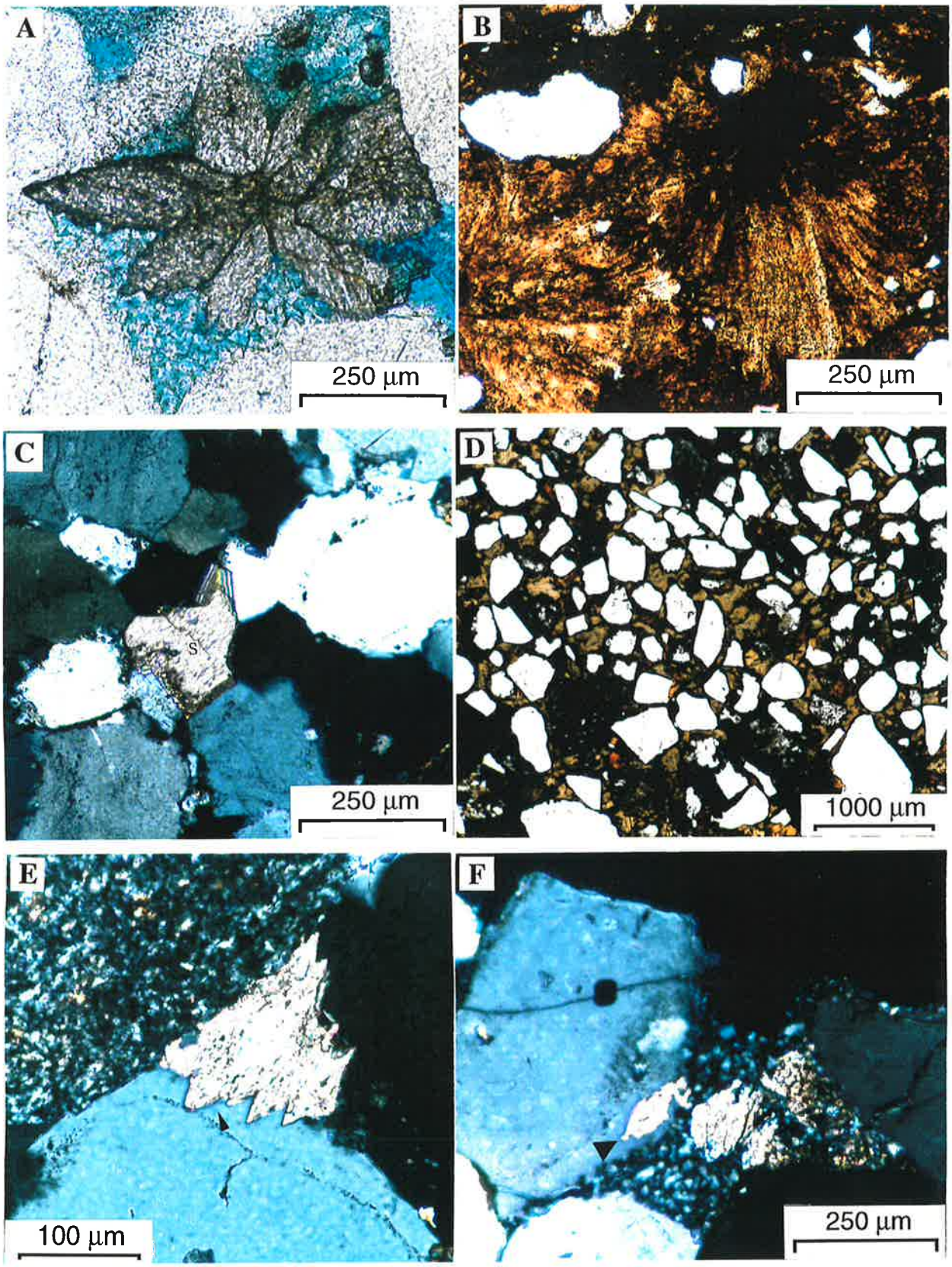
A
250 µm
B
250 µm
C
S
250 µm
D
1000 µm
E
100 µm
F
250 µm

substrate or nucleus for the middle generation of siderite cement (S2) (Plates 10A-B, 10D & 11A). The boundary between S1 and S2 is not always distinct but is typically characterised by irregular and serrated edges, indicating partial dissolution of S1 prior to S2 cementation (Plates 10A-B & 11A). In BSE images, S1 is white and appears homogenous (Plates 10A-B, 10D &11 A).

4.3.2.2.2 Middle Generation Siderite Cement (S2)

Petrographically, S2 is mostly in the form of colourless rhombs which enclose S1 (Plates 10 A-B, 10D & 11A). In BSE images, S2 has the appearance of rhombs which generally enclose S1 nuclei (Plates 10B & 11A) and which are, in turn, engulfed by S3. Differentiation between S2 and S3 is difficult under the optical microscope except where small dissolution pits occur along the boundaries between S2 and S3 (Plate 10A). S2 is characterised by many small (3-5μm) primary fluid-inclusions whilst S3 has fewer inclusions (Plate 8). Locally, S2 is engulfed by quartz cement, indicating that some quartz cementation postdates S2 precipitation (Plates 9F & 11H). In BSE images, S2 displays distinct irregular compositional zoning and minor dissolution indicating pore fluid chemistry fluctuations occurred during cementation.

Based on grey-scale characteristics, three main zones of S2 precipitation are evident, namely dark, moderate, and light zones.

4.3.2.2.3 Late Generation Siderite Cement (S3)

Under the optical microscope, S3 is a blocky, colourless, very clear cement (Plate 10 A), postdating S1 and S2. The boundary between S2 and S3 is characterised by an irregular, serrated outline, implying partial dissolution of S2 prior to precipitation of S3. In some samples, dead oil concentrates in fluid-inclusions in the boundary zone between S2 and S3, indicating that hydrocarbon migration occurred synchronous with, or after the dissolution event but prior to S3 precipitation. BSE images show that S3 is a relatively evenly banded cement phase, characterised by an initial high Mg content (pistomsite) grading into a relatively thick, homogenous sideroplesite cement (Plates 10B & 11A).

Plate 10

Micrographs of Siderite Cement (II)

A - Plain polarised view of the main siderite cement generations that can rarely be distinguished under the optical microscope. S1 has a brownish colour whilst S2 and S3 are clear and colourless. S1 is typically engulfed by S2. Note the concentration of fluid inclusions in S2, and the irregular serrated boundary between S2 and S3 (arrow) implying partial dissolution of S2 prior to precipitation of S3. Sample M1-9598, Moorari-1, 2925.5 m. Scale bar = 50 μm.

B - BSE image showing the same view as shown in **A**. S1 displays a white colour whilst the surrounding S2 (medium grey) is characterised by a variable internal composition and complex zoning. S3 is a relatively homogeneous, late-generation pore-filling cement. Note the irregular dissolution boundary between S1 and S2, and between S2 and S3 (arrows). The cement relationships are typical of the Tirrawarra Sandstone. Sample M1-9598, Moorari-1, 2925.5 m. Scale bar = 50 μm.

C - SEM micrograph showing euhedral, blocky siderite thought to represent the S3 cement generation that developed on an earlier, partly dissolved siderite cement surface (S2) (arrow). Sample M3-9405, Moorari-3, 2847.8 m. Scale bar = 50 μm.

D - Colourless middle generation of siderite cement (S2) engulfing brown earlier-generation of siderite cement (S1). Sample M9-9732, Moorari-9, 2919.6 m. Scale bar = 250 μm.

E - More typical, homogeneous-looking siderite spar with irregular, serrated edges adjacent to kaolinite booklets (arrow) indicating partial siderite dissolution prior to kaolinite precipitation. Sample M3-9503, Moorari-3, 2896.5 m. Plain polarised view. Scale bar = 250 μm.

F - Dissolution of siderite cement in the Tirrawarra Sandstone may have a significant influence on generation of secondary porosity. In this photomicrograph, secondary porosity is associated with siderite cement dissolution. Sample M9-9732, Moorari-9, 2919.6 m. Scale bar = 250 μm.

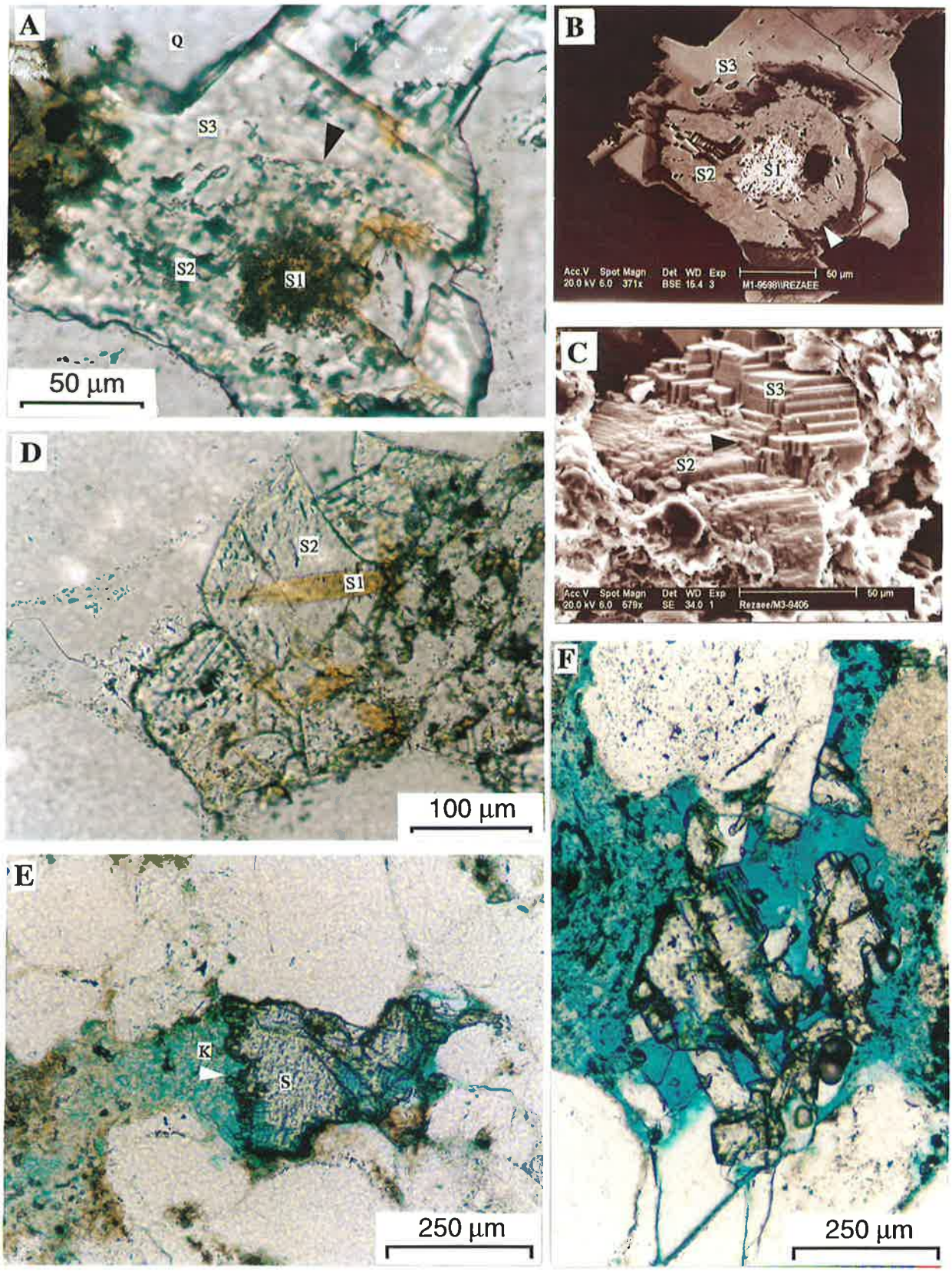
A
Q
S3
S2
S1
50 µm
B
S3
S2
S1
Acc.V Spot Magn Det WD Exp
20.0 kV 6.0 371x BSE 15.4 3
50 µm
M1-9698\REZAEE
C
S3
S2
Acc.V Spot Magn Det WD Exp
20.0 kV 6.0 579x SE 34.0 1
50 µm
Rezaee/M3-9406
D
S2
S1
100 µm
E
K
S
250 µm
F
250 µm

4.3.2.2.4 Siderite Cement Fluid-inclusion Analysis

Twelve samples were selected for fluid-inclusion analysis (Appendix 7). S1 siderite cement is devoid of fluid-inclusions while S2 and S3 siderite cements have equidimensional fluid-inclusions (Plate 8). Homogenisation temperatures of S2 fluid-inclusions range from 66 to 76°C, with a median around 68°C (Fig. 4.10). Fluid-inclusion results for S3 indicate an homogenisation temperature of between 98 and 114°C, with a median about 102°C (Fig. 4.10).

Compositional zoning is evident in the S2 siderite cement indicating that the cements precipitated from solution and did not undergo recrystallisation during burial diagenesis. No unstable precursor for siderite is known, and there exists no documented case of siderite recrystallisation (Mozley & Carothers, 1992). For these reasons, fluid-inclusions are thought to provide a genuine record of the temperatures at which the siderites in the Tirrawarra Sandstone crystallised, unless resetting of the inclusions (Prezbindowski & Larese, 1987; McLimans, 1987; Prezbindowski & Tapp, 1991) occurred. However, consistent differences in homogenisation temperatures between S2 and S3 (Fig. 4.10) suggest the fluid-inclusions did not undergo reequilibration in view of the fact that appreciable differences in the size of the fluid-inclusions were not detected between S2 and S3.

The present temperatures at reservoir level exceed the maximum homogenisation temperatures of S3 by at least 20 to 30°C, indicating that the fluid-inclusions did not reset during recent geological times. Geohistory modelling shows that the Cooper Basin sediments did not undergo major subsidence in the last few million years in the Patchawarra Trough (Tupper & Burckhardt, 1990). S2, therefore, precipitated at a mean water temperature of about 68°C whilst S3 formed at about 102°C on average (Fig. 4.10).

No fluid-inclusion data are available for S1, but the cement stratigraphy would suggest that S1 crystallised at temperatures lower than those for S2, ie. less than about 68°C.

4.3.2.3 Clay Cements

Two major clay mineral groups were recognised by thin-section, scanning electron microscopy (SEM), energy dispersive X-ray (EDX) and X-ray Diffraction (XRD) analyses (Table 4.2). In the Tirrawarra Sandstone, XRD analyses of the clay fraction (<

Plate 11

Micrographs of Siderite Cement (III)

A - In this BSE image, S1 occurs as isolated patchy remnants (white) within S2 cement (medium grey) that is characterised by an inhomogeneous appearance and complex zoning. S2 is enclosed by an evenly banded, euhedral S3 cement displaying some broad compositional zoning. Note the presence of dissolution pits in S2 and the characteristic dissolution boundary between S2 and S3. Sample M1-9598, Moorari-1, 2925.5 m. Scale bar = 50 μm.

B - BSE image of the middle generation of siderite cement (S2). Note extensive complex zoning due to variation in Mg content. Sample M9-9732, Moorari-9, 2919.6 m. Scale bar = 20 μm.

C - SEM view of euhedral siderite cement (S) against quartz cement (Q). Sample M3-9405, Moorari-3, 2821.5 m. Scale bar = 20 μm.

D - SEM view of euhedral siderite (S) cement growing in secondary porosity after the precipitation of a euhedral quartz overgrowth (Q). Sample M3-9405, Moorari-3, 2821.5 m. Scale bar = 50 μm.

E - BSE image of a fine-grained, moderate to poorly sorted, back- barrier marsh sample completely cemented by S1 (white). Note the angular quartz grains (Q) and very high IGV (>50%) which suggest the replacement of part of the margins of quartz grains by siderite cement. Sample F4-9441, Fly Lake-4, 2877.6 m. Scale bar = 500 μm.

F - SEM view of back- barrier marsh sample which is cemented by S1. Note that S1 is anhedral and completely infills pore spaces among well-rounded quartz grains (Q). There is no evidence of quartz overgrowth on the quartz grains. F2-9583, Fly Lake-2, 2874.9 m. Scale bar = 100 μm.

G - BSE image showing siderite cement (S) etching quartz overgrowth (Q). Sample F1-9433, Fly Lake-1, 2875.2 m. Scale bar = 20 μm.

H - BSE image showing the intergrowth between S2 cement (S, white) displaying characteristic rhombs and quartz overgrowths (medium grey). Locally, the siderite is completely engulfed by the quartz cement (Q), indicating that some siderite cementation preceded quartz cementation. Sample F1-9433, Fly Lake-1, 2875.2 m. Scale bar = 50 μm.

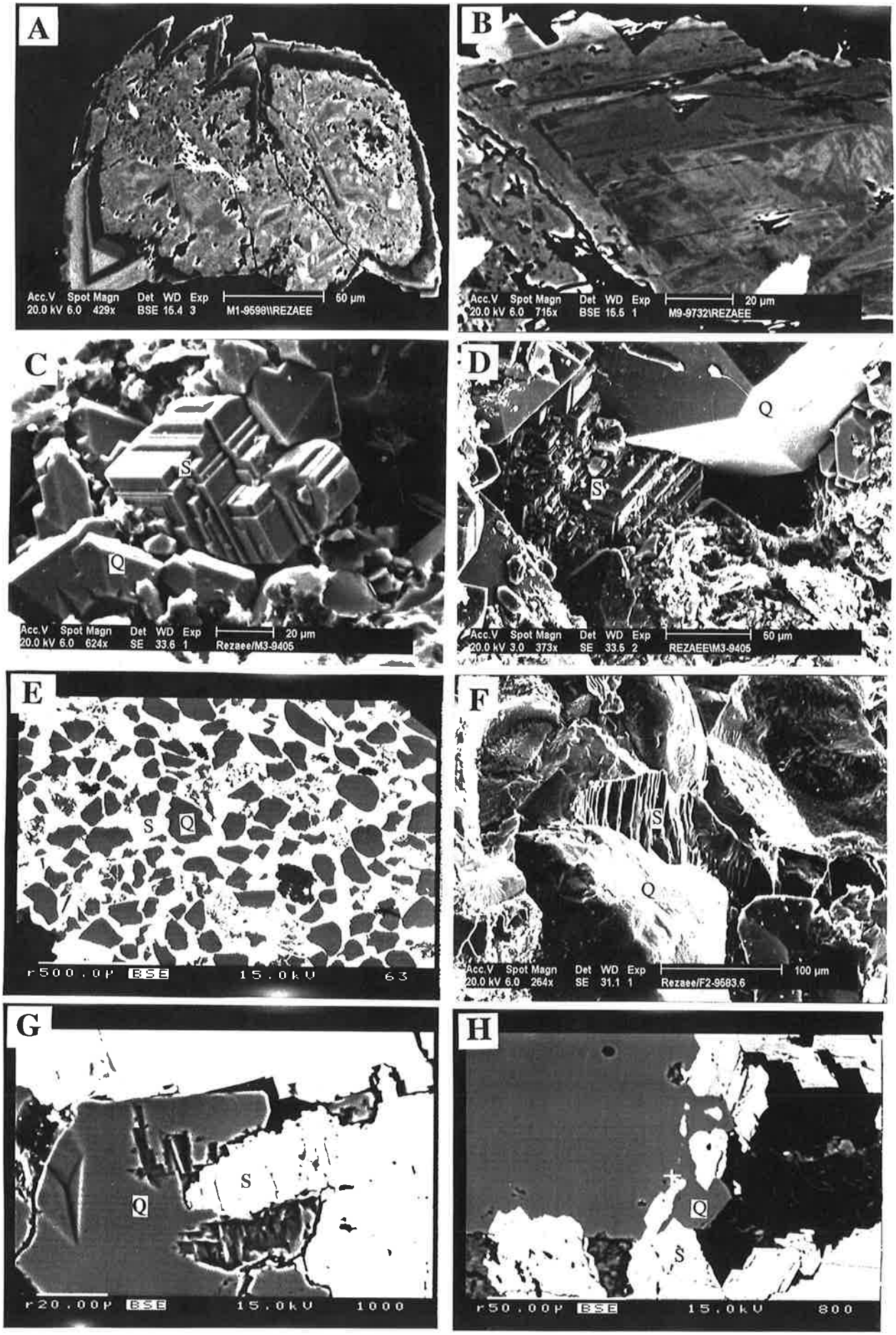
A
Acc.V Spot Magn Det WD Exp
20.0 kV 6.0 429x BSE 15.4 3 M1-9598\\REZAEE
50 µm
B
Acc.V Spot Magn Det WD Exp
20.0 kV 6.0 715x BSE 15.5 1 M9-9732\REZAEE
20 µm
C
S
Q
Acc.V Spot Magn Det WD Exp
20.0 kV 6.0 624x SE 33.6 1 Rezaee/M3-9405
20 µm
D
Q
S
Acc.V Spot Magn Det WD Exp
20.0 kV 3.0 373x SE 33.5 2 REZAEE\M3-9405
50 µm
E
S
Q
r500.0µ BSE 15.0kV 63
F
S
Q
Acc.V Spot Magn Det WD Exp
20.0 kV 6.0 264x SE 31.1 1 Rezaee/F2-9583.6
100 µm
G
Q
S
r20.00µ BSE 15.0kV 1000
H
Q
S
r50.00µ BSE 15.0kV 800

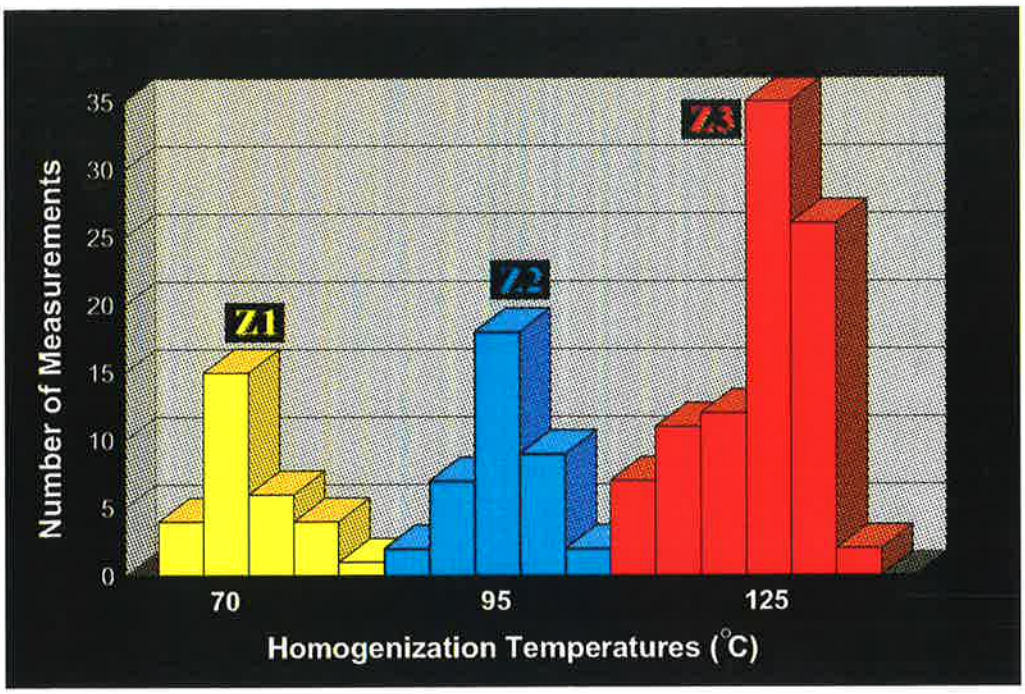

Figure 4.9 - A generalised histogram illustrating fluid inclusion homogenization temperatures for different zones of quartz cement. (Z1 = innermost zone, Z2 = middle zone and Z3 = outermost zone of quartz cement).

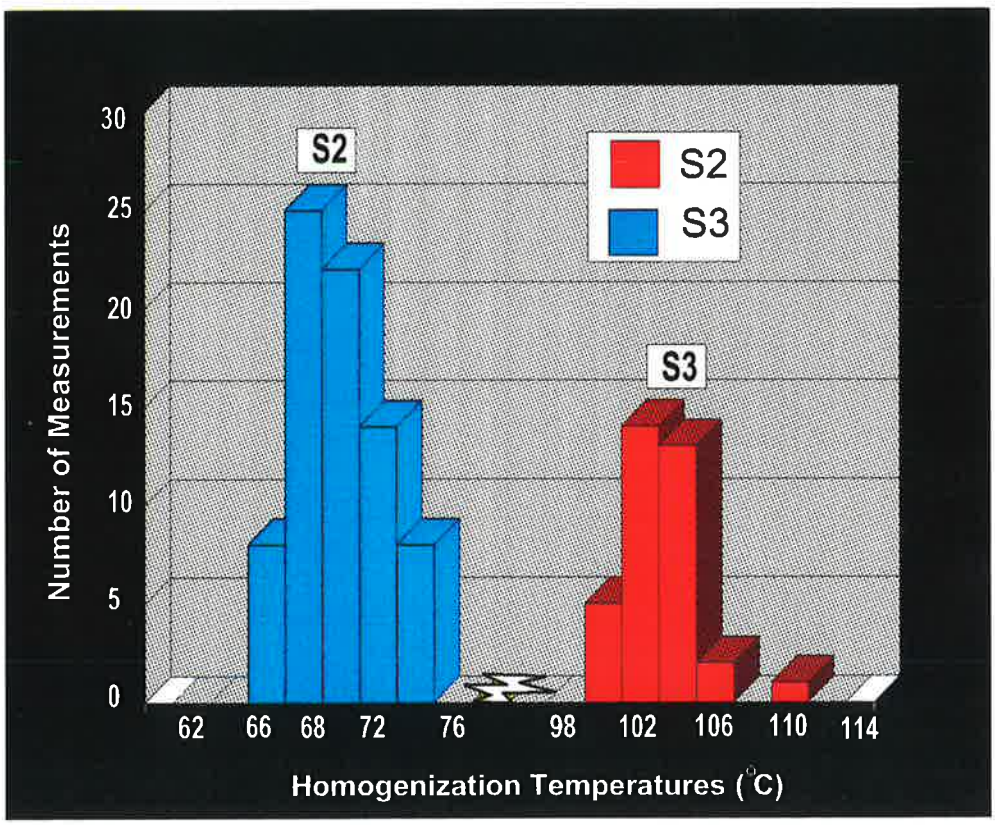

Figure 4.10 - Fluid inclusion homogenization temperatures for the middle (S2) and late generations (S3) of the Tirrawarra Sandstone siderites. The fluid inclusions are considered to be of primary origin, and did not experience stretching. S2 formed at much lower temperatures than S3.

2 μm size) for 18 samples indicate that the clays are dominated by kaolinite and illite (Fig. 4.11) (Appendix 3).

Under the optical microscope and SEM, kaolinite occurs as euhedral booklets which infill pore spaces and are intergrown with quartz overgrowths (Plates 12, 13 & 14). The contact between quartz overgrowths and kaolinite may be either jagged, due to intergrowth of quartz cement and kaolinite (Plates 12C, 12E, 13C, 13E & 13F), or is smooth, without any intergrowth (Plate 12A, 12B & 12D). Kaolinite in the form of pseudo-hexagonal stacked plates is pervasive in nearly all of the Tirrawarra Sandstone samples. There are two modes for clay occurrence in these sandstones. The first mode is that of detrital or allogenic clays which are deposited or mixed with other sediment component during deposition, except for mechanically infiltrated clay minerals which mix with sediments after deposition (Moraes & De Ros, 1990). The second mode is that of in-situ or authigenic clay minerals. They may be formed either from direct precipitation from a pore fluid in suitable conditions (neoformation), or from reaction between original grains and pore fluid (regeneration) (Wilson and Pittman, 1977). Authigenic clay minerals can be seen in different forms:

a- Pore linings or clay films, which deposit on the surface of grains and may inhibit syntaxial rim cement formation (Houseknecht & Ross, 1992; Pittman et al., 1992; Wilson, 1992);

b- Pore-filling clays, which fill any accessible primary or secondary pores;

c- Replacement clays, which completely or partially replace original grains (Morad & Aldahan, 1987a). There are many criteria to recognise an authigenic clay from an allogenic one including composition, morphology, texture, and distribution. The purity of a clay, its delicate euhedral form, and the relationship with other grains can help to identify authigenic clay minerals (Wilson & Pittman, 1977).

Genetically, there are two types of authigenic kaolinite in the Tirrawarra Sandstone. The first type is formed by the complete replacement of an original or precursor grain. This kind of kaolinite shows the exact margin of the original grains (Plates 12A-B & 13D). The second type is precipitated directly from pore fluids. This pore-filling cement alters the intergranular macroporosity to microporosity, which exists among the kaolinite booklets. This type of kaolinite, which is coarser-grained than the first type (about 40 microns), is often vermicular (Plate 13A), shows less packing, and is also intergrown with the quartz cement (Plates 12E, 13E-H & 14C-E).

Plate 12

Micrographs of Kaolinite (I)

A - Photomicrograph of the complete replacement of an original grain (presumably feldspar). Note the smooth contact between the grain which is completely kaolinitised and neighbouring quartz grains (arrows). Sample M4-9531.8, Moorari-4, 2859.5 m. Scale bar = 250 μm.

B - Complete replacement of a precursor grain by kaolinite. Note the original margin of precursor grain (A). Pore-filling kaolin is loosely packed and has more microporosity (B). The contact between the kaolinitised grain and the quartz grain is smooth (upper arrow), whereas contact between the pore-filling kaolinite and quartz is jagged (lower arrow). Sample F1-9431.4, Fly Lake-1, 2829.5 m. Scale bar = 250 μm.

C - Pore-filling kaolinite with a significant amount of microporosity which is filled with blue epoxy. Pore-filling kaolinite usually has a jagged contact with quartz cement (arrow) which may suggest intergrowth of quartz cement and kaolinite. Note the abundant fluid inclusions between thick quartz overgrowths and quartz grains. Sample M7-9618.4, Moorari-7, 2885.5 m. Scale bar = 100 μm.

D - A view of a precursor grain which is completely replaced by kaolinite. The original shape of the grain is deformed by post-alteration compaction and squeezed into adjacent pore spaces but the margins of the grain can be distinguished (arrow). Note the presence of both intergranular and secondary porosity in this sample. Sample M3-9412, Moorari-3, 2823.6 m. Scale bar = 500 μm.

E - Close-up view of the jagged nature of pore-filling kaolinite and quartz cement (arrow). Note the presence of microporosity (filled with blue epoxy) among kaolinite booklets. Black patches are air bubbles where epoxy has been unable to permeate the microporosity. Sample M3-9478.5, Moorari-3, 2843.5 m. Scale bar = 100 μm.

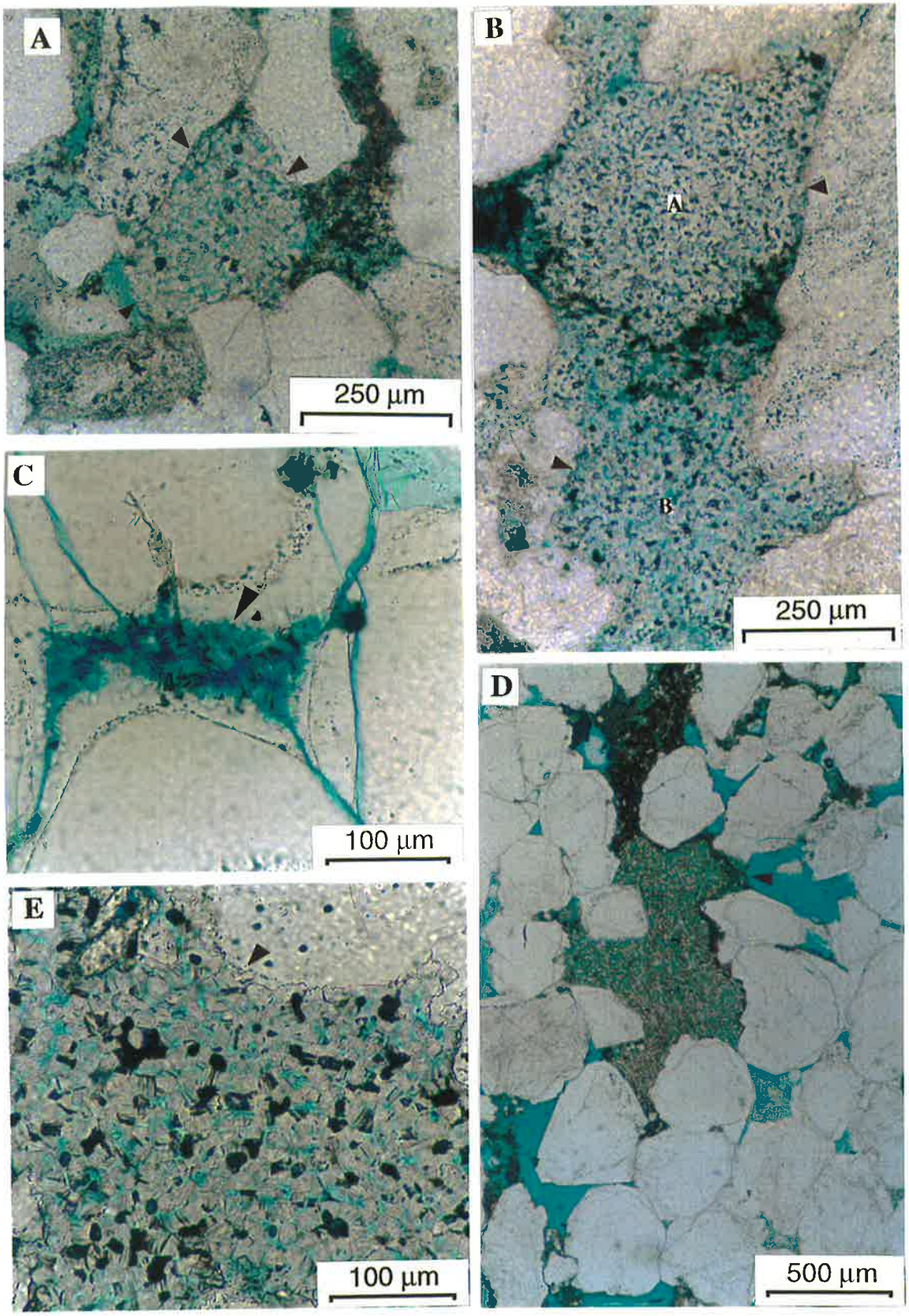
A
250 µm
B
A
B
250 µm
C
100 µm
D
500 µm
E
100 µm

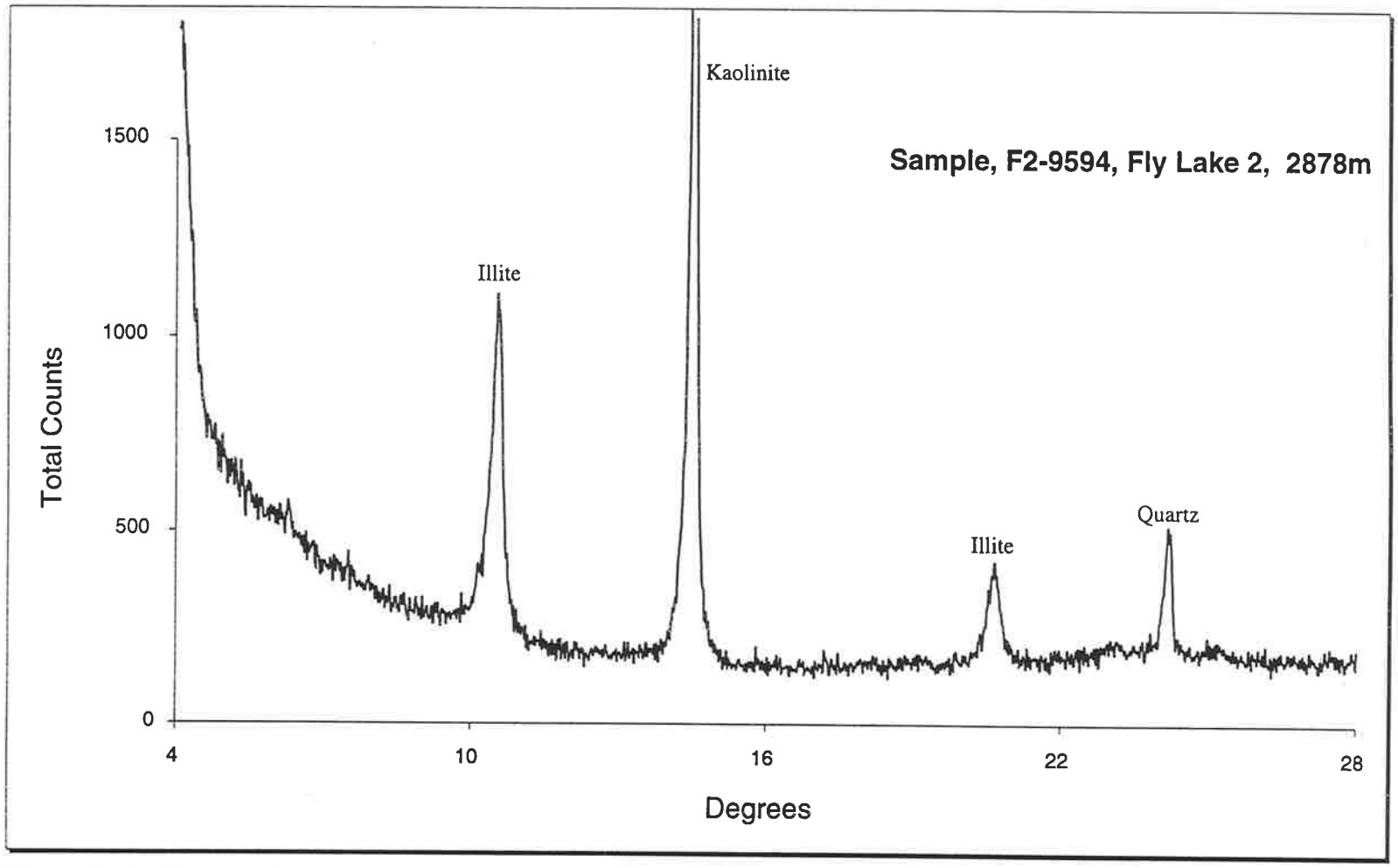

Figure 4.11 - The clay-fraction XRD peaks of a representative sample indicating that clays are dominated by kaolinite and illite. In all 20 analysed samples for clay fraction, the XRD peak patterns are very similar.

Plate 13

Micrographs of Kaolinite (II)

A - SEM view of pore-filling, euhedral kaolinite booklets. Note the abundant microporosity associated with kaolinite booklets. Sample M3-9405, Moorari-3, 2821.5 m. Scale bar = 50 μm.

B - Kaolinite booklets filling a secondary pore. Note the jagged nature of the contact between the kaolinite and surrounding quartz cement (left hand side). Sample M3-9405, Moorari-3, 2821.5 m. Scale bar = 100 μm.

C - SEM view showing pore-filling kaolinite and kaolinite booklets intergrown with a quartz overgrowth. Sample M6-9733.2, Moorari-6, 2920 m. Scale bar = 100 microns

D - SEM view showing complete replacement of original grain by kaolinite. Sample F6-9388, Fly Lake-6, 2816 m. Scale bar = 200 μm.

E & F - In the Tirrawarra Sandstone, intergrowth of kaolinite and quartz overgrowth is common and can be recognised by the jagged contact between these two authigenic minerals. The intergrown nature of kaolinite and quartz overgrowth suggest their contemporaneous precipitation. Samples M3-9412, Moorari-3, 2823.6 m. and M3-9405, Moorari-3, 2821.5 m. Scale bars = 20 μm.

G - Close-up view showing intergrowth of quartz cement and kaolinite booklets. In some cases it seems that the quartz cement postdates the kaolinite and engulfs it. Sample F6-9398, Fly Lake-6, 2819 m. Scale bar = 20 μm.

H - Back-scattered electron image from the same sample as (**G**), showing kaolinite engulfed by quartz cement. Notice pore-filling siderite cement (white) which predates kaolinite and quartz cement. Scale bar = 50μm.

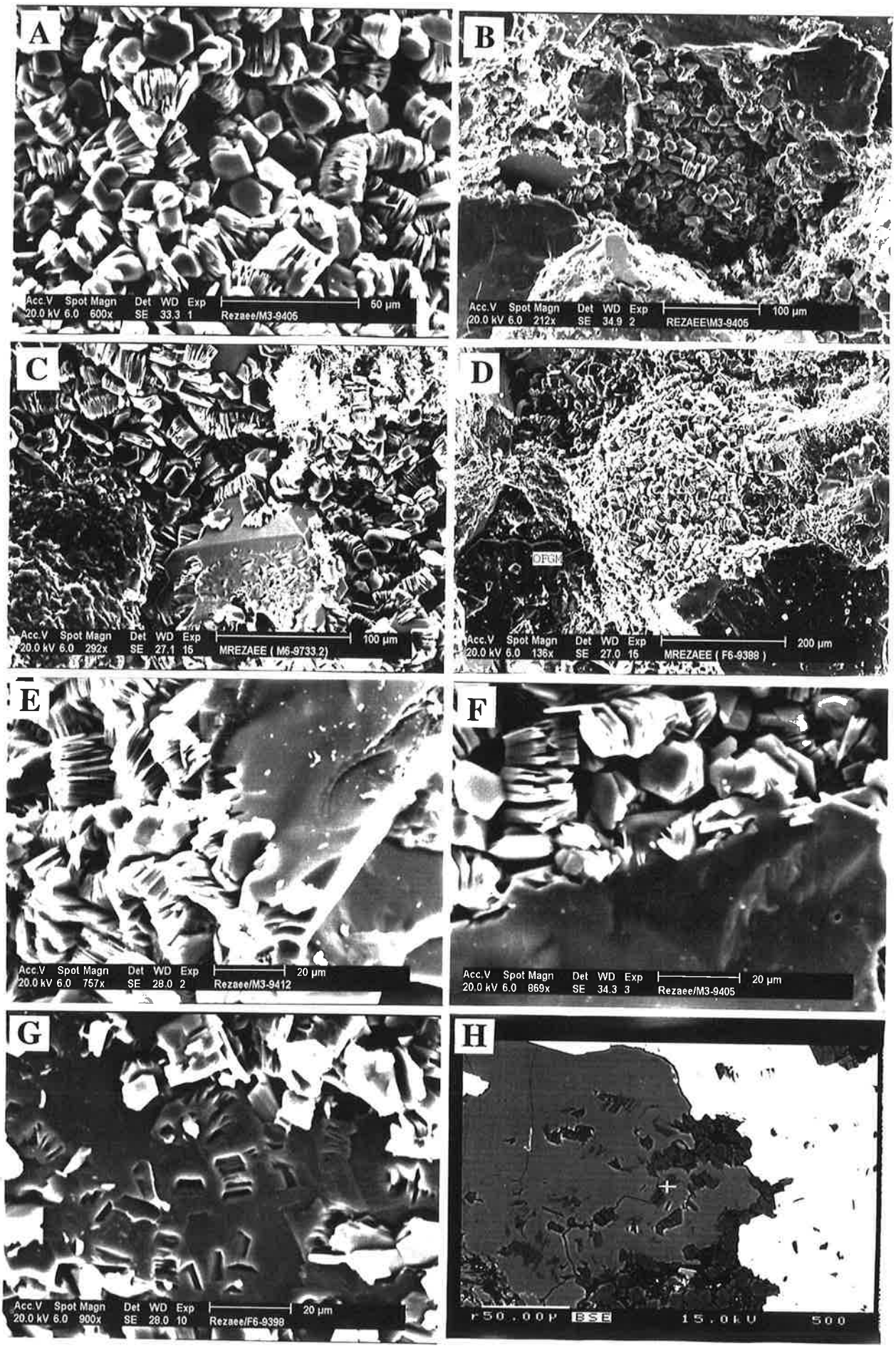
A
Acc.V Spot Magn Det WD Exp
20.0 kV 6.0 600x SE 33.3 1 Rezaee/M3-9405
50 µm
B
Acc.V Spot Magn Det WD Exp
20.0 kV 6.0 212x SE 34.9 2 REZAEE\M3-9405
100 µm
C
Acc.V Spot Magn Det WD Exp
20.0 kV 6.0 292x SE 27.1 15 MREZAEE (M6-9733.2)
100 µm
D
OFGM
Acc.V Spot Magn Det WD Exp
20.0 kV 6.0 136x SE 27.0 15 MREZAEE (F6-9388)
200 µm
E
Acc.V Spot Magn Det WD Exp
20.0 kV 6.0 757x SE 28.0 2 Rezaee/M3-9412
20 µm
F
Acc.V Spot Magn Det WD Exp
20.0 kV 6.0 869x SE 34.3 3 Rezaee/M3-9405
20 µm
G
Acc.V Spot Magn Det WD Exp
20.0 kV 6.0 900x SE 28.0 10 Rezaee/F6-9398
20 µm
H
r50.00µ BSE 15.0kV 500

On the whole, in the Tirrawarra Sandstone of the Moorari and Fly Lake Fields, the occurrence of kaolinite is mostly in the form of pore-filling and complete replacement. Four criteria were used to differentiate pore-filling from replacement kaolinite:

- **original grain margin:** In some samples, the original grain margin can be easily recognised, thereby helping to distinguish replacement kaolinite from pore-filling types (Plates 12A-B, 12D & 13D).
- **pore shape:** In some samples, the shape of pores which are occupied with kaolinite can help to differentiate replacement kaolinite from pore-filling kaolinite. Occupied pores which are bigger or smaller than the maximum and minimum grain size in the sample may help to identify pore-filling kaolinite from replacement kaolinite (Plate 12C & 12E).
- **size:** Pore-filling kaolinite often has a larger grain size (Plate 14C). The average size of replacement kaolinite is nearly 20 whereas pore-filling kaolinite is about 40 microns.
- **packing:** Replacement kaolinite shows closer packing, whereas pore-filling kaolinite is less compacted and shows greater microporosity (Plates 12B & 13A).

The amount of kaolinite in the samples is very variable and is facies-dependent. Replacement kaolinite ranges from zero to 5%, with an average of 2%; and pore-filling kaolinite ranges from zero to 8%, with an average of 4% (Table 4.1).

Illite is the next most important clay mineral in most of the samples. Its authigenic nature is evident from its fibrous, lath- or lettuce-like habit (Plate 15). The mineral is thought to have largely formed as a replacement product of chemically unstable rock fragments. In some rare instances illite occurs as pore bridging cement (Plate 15C & 15F).

Plate 14

Micrographs of Kaolinite (III)

A - Photomicrograph showing the formation of large kaolinite platelets (70 μm) between mica flakes. Sample M1-9633, Moorari-1, 2890 m. Scale bar = 100 μm.

B - Crossed-nichols view of the large kaolinite crystals grown between mica flakes. Note the smaller kaolinite in the background. Sample F3-9593, Fly Lake-3, 2878 m. Scale bar = 100 μm.

C - A photomicrograph showing the difference in size between replacement (B) and pore-filling kaolinite (A). Replacement kaolinite commonly has a smaller (~ 15 μm) diameter than pore-filling kaolinite (35 μm). Sample M5-9510, Moorari-5, 2853 m. Scale bar = 250 μm.

D - Crossed-nichols view showing late quartz cement completely engulfing kaolinite booklets. Sample M4-9496.10, Moorari-4, 2849 m. Scale bar = 100 μm.

E - Enclosure of kaolinite crystals (arrow) by late quartz cement (plane light view). Sample M4-9440, Moorari-4, 2832 m. Scale bar = 100 μm.

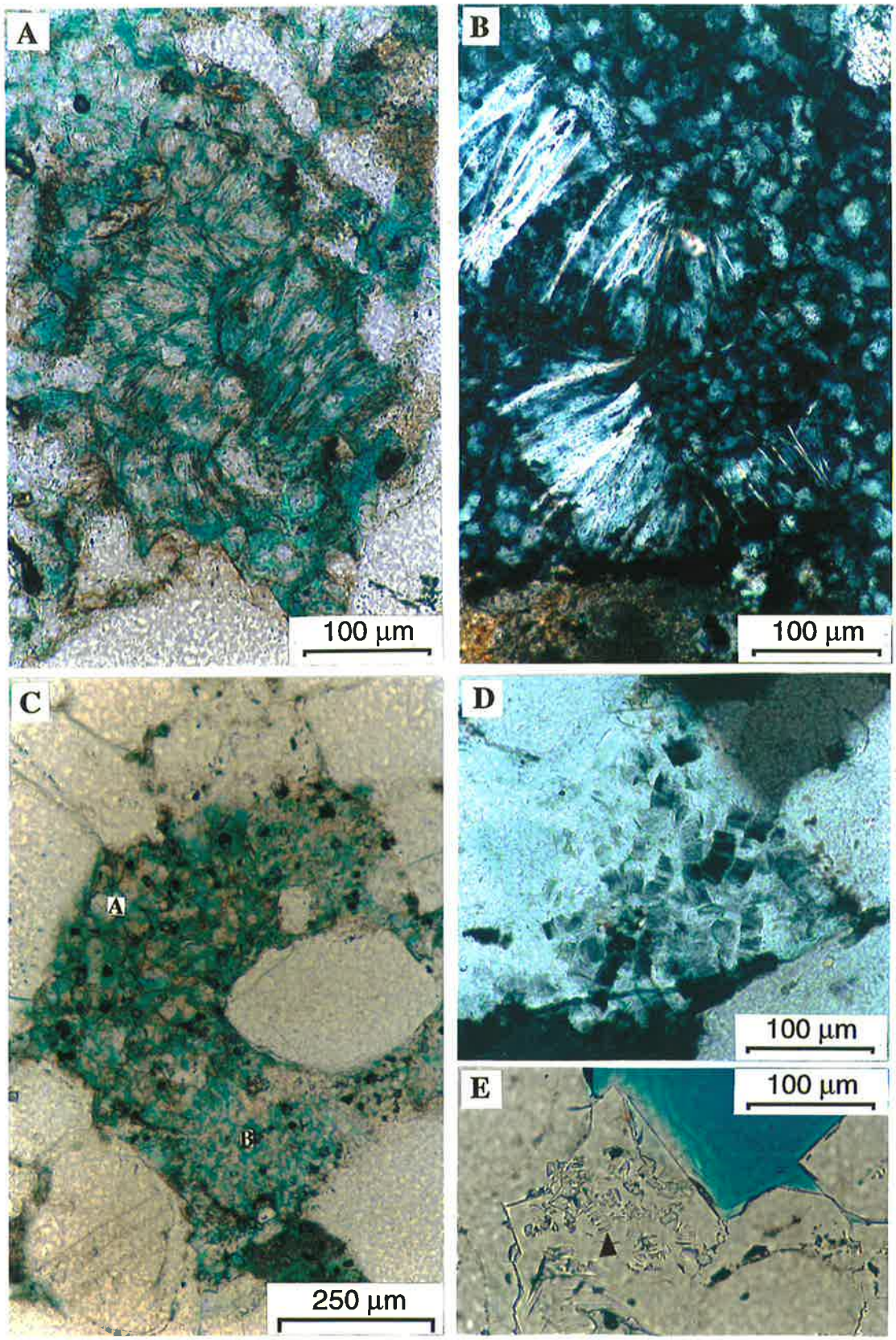
A
100 µm
B
100 µm
C
A
B
250 µm
D
100 µm
E
100 µm

4.4 DISCUSSION

4.4.1 QUARTZ CEMENT

4.4.1.1 Introduction

Quartz cement in siliciclastic sequences is commonly a major diagenetic phase that affects hydrocarbon reservoir quality. In most sedimentary basins, it forms at temperatures between 60 and 145°C (Walderhaug, 1994) and many sources of silica have been proposed. McBride (1989) reviewed over 20 silica sources for quartz cement proposed by various workers in numerous basins. Amongst the most important silica sources for quartz cement are; alteration or dissolution of felspar grains (Fothergill 1955; Siever, 1957; Hawkins, 1978; Morad & Aldahan, 1987b), dissolution of more-soluble phases of silica (Swineford & Franks, 1959; Keene, 1975; Füchtbauer, 1974), transformation of clay minerals (Siever, 1962; Towe, 1962; Hower et al., 1976; Boles & Franks, 1979), pressure solution (Waldschmidt, 1941; Heald, 1955; Füchtbauer, 1974; Sibley & Blatt, 1976; Bjørlyyke et al., 1986; Houseknecht, 1988; Dutton & Diggs, 1990; Morad et al., 1991; Bjørlyyke & Egeberg, 1993; Dutton ,1993; Walderhaug, 1994; Oelkers et al., 1996), and quartz replacement by carbonate cement (Walker, 1960; Burley & Kantorowicz, 1986).

In most studies concerning the source of silica, the trace-element composition of quartz cement has been ignored. Al, H, Li, and Na are recognised as the most important trace-elements in quartz (Lehmann & Bambauer, 1973; Cohen, 1985; Perny et al., 1992) and their incorporation is affected by several factors, including pore-fluid chemistry (Merino et al., 1989). In the present study, trace-element content and precipitation temperatures of quartz cement are linked to petrographic studies in order to indicate possible sources of quartz cement in the Tirrawarra Sandstone.

Previous studies concerning quartz cement in the Tirrawarra Sandstone are limited. Martin (1981, 1984) examined the Tirrawarra Sandstone in the Tirrawarra, Fly Lake and Moorari Fields and suggested that quartz cementation and authigenic clay minerals were the most important diagenetic factors affecting porosity reduction. Wild (1987) concluded that compaction and quartz cementation were the most important diagenetic processes that reduced reservoir quality. Schulz-Rojahn & Phillips (1989) and Stuart et al. (1990) mentioned that the formation of quartz overgrowths in Permian

Plate 15

Micrographs of Illite

A - SEM view showing replacement of kaolinite to lettuce-like illite. This digenetic process is not common in the Tirrawarra Sandstone. Sample M3-9405, Moorari-3, 2821.5 m. Scale bar = 20 μm.

B - In some cases in the Tirrawarra Sandstone, illite bridges pore spaces as shown here. Sample M3-9405, Moorari-3, 2821.5 m. Scale bar = 50 μm.

C - SEM view of illite and kaolinite which completely filling pore throats. This process, which can drastically reduce hydraulic conductivity of a reservoir, is rare in the Tirrawarra Sandstone. Sample M3-9405, Moorari-3, 2821.5 m. Scale bar = 50 μm.

D - Close-up view of a mass of illite formed from complete alteration of a labile detrital grain. Sample M3-9405, Moorari-3, 2821.5 m. Scale bar = 50 μm.

E - In the Tirrawarra Sandstone, most of the illite is in the form of complete or partial alteration of labile detrital grains. In this example, a mass of illite (I) can be seen among euhedral faces of quartz overgrowth. Sample M3-9405, Moorari-3, 2821.5 m. Scale bar = 100 μm.

F - Close-up view of illite bridging a pore space. Note the sharp euhedral faces of the quartz overgrowths. Sample M6-9733.2, Moorari-6, 2920 m. Scale bar = 20 μm.

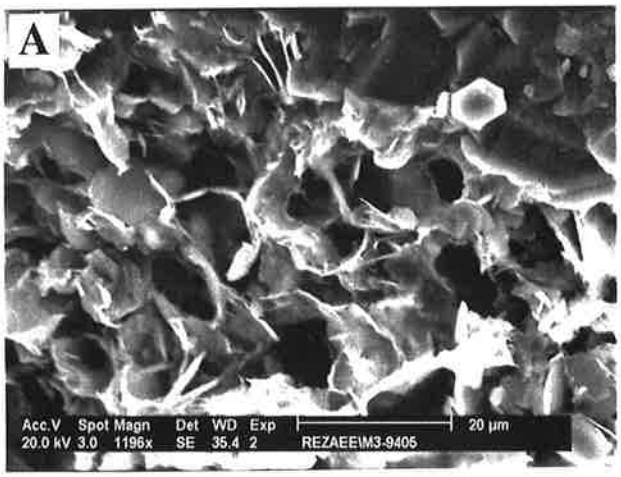
A
Acc.V Spot Magn Det WD Exp
20.0 kV 3.0 1196x SE 35.4 2
20 µm
REZAEE\M3-9405

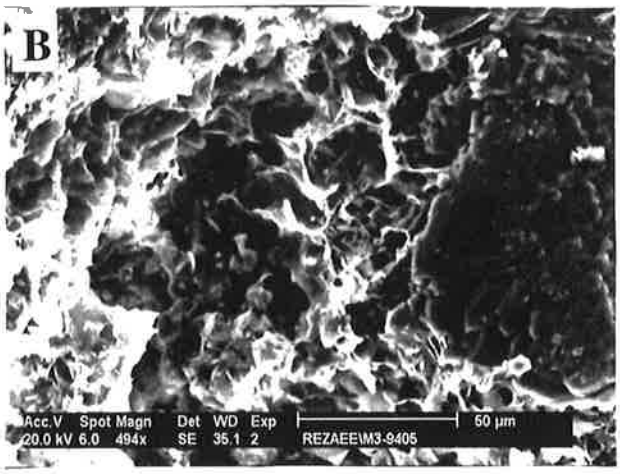
B
Acc.V Spot Magn Det WD Exp
20.0 kV 6.0 494x SE 35.1 2
50 µm
REZAEE\M3-9405

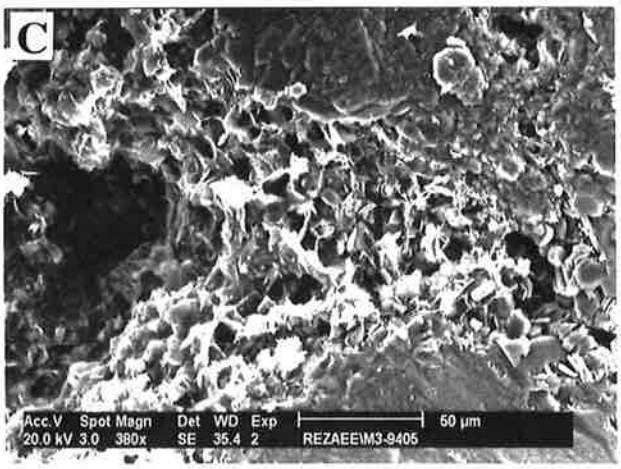
C
Acc.V Spot Magn Det WD Exp
20.0 kV 3.0 380x SE 35.4 2
50 µm
REZAEE\M3-9405

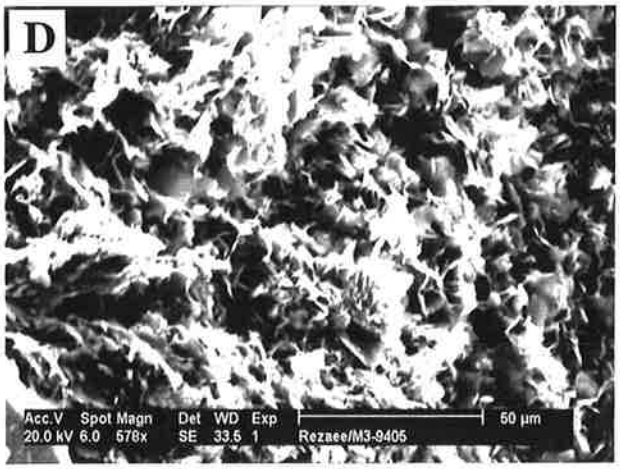
D
Acc.V Spot Magn Det WD Exp
20.0 kV 6.0 578x SE 33.5 1
50 µm
Rezaee/M3-9405

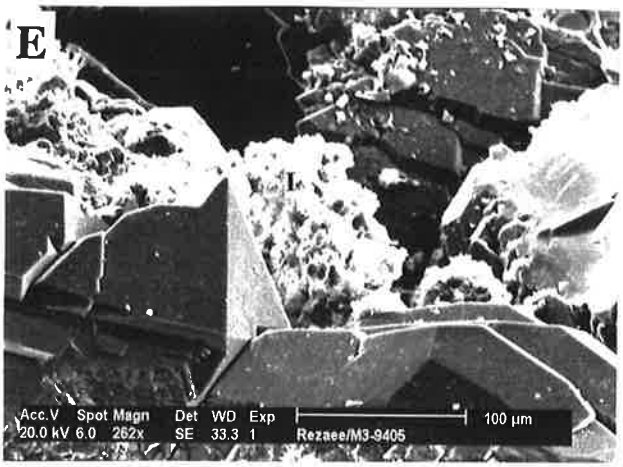
E
Acc.V Spot Magn Det WD Exp
20.0 kV 6.0 262x SE 33.3 1
100 µm
Rezaee/M3-9405

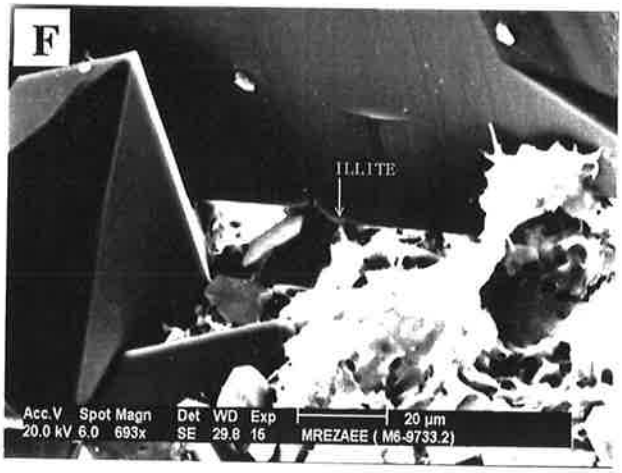
F
ILLITE
Acc.V Spot Magn Det WD Exp
20.0 kV 6.0 693x SE 29.8 16
20 µm
MREZAEE (M6-9733.2)

sandstones in the Cooper Basin occurred during several stages of diagenesis and proposed several sources of silica. Tingate & Luo (1992) also studied Permian reservoirs in the Cooper Basin but outside the study area and found that quartz and kaolinite cements influenced pore geometry and reservoir quality.

A wide range of techniques have been applied to the Tirrawarra Sandstone in order to constrain the depositional and diagenetic controls on quartz cement. They include core logging, sandstone petrology, cathodoluminescence (CL), fluid-inclusion studies, quartz cement chemistry, and thermal history modelling. From these data, distinct phases of quartz cement can be recognised and constraints placed upon their timing and conditions of precipitation. Using these constraints, sources of silica are discussed for each phase.

4.4.1.2 Silica sources in the Tirrawarra Sandstone

During diagenesis, sediments are subjected to different conditions, and several sources of silica for quartz cement are possible. The most likely sources of silica for quartz cement in the Tirrawarra Sandstone are discussed below.

- **Alteration or Dissolution of Feldspar Grains**

Dissolution of feldspar is reported as a silica source for quartz cement (Fothergill, 1955; Siever, 1957; Hawkins, 1978; Morad & Aldahan, 1987b). During feldspar dissolution, kaolin forms and silica is released according to the reaction:

$$2H_2CO_3 + H_2O + 2KAlSi_3O_8 \rightarrow Al_2Si_2O_5(OH)_4 + 4SiO_{2(aq.)} + 2K^+ + 2HCO_3^-$$

In this reaction, $1cm^3$ of K-feldspar yields 0.43 cm^3 of quartz and 0.46 cm^3 of kaolinite. In the Tirrawarra Sandstone, apart from a few heavily-altered feldspar grains, the great majority of samples contain no feldspar. Prismatic kaolinite pseudomorphs and oversize pores suggest that feldspar was an important detrital component at deposition. Williams et al. (1985) has also suggested that feldspathic acid igneous rocks were a major sediment source for the Tirrawarra Sandstone. The absence of feldspar and the abundance of authigenic kaolinite suggests that the kaolinite was derived from feldspar alteration. Assuming all kaolinite in the Tirrawarra Sandstone samples was derived

from feldspar alteration, mass balance calculations indicate that the silica generated would have been sufficient to produce 61 percent of the total observed quartz cement.

- **Pressure Solution**

Pressure solution of quartz grains at grain contacts can be an important source of silica (Waldschmidt, 1941; Heald, 1955; Füchtbauer, 1974; Sibley & Blatt, 1976; Bjørlyyke et al., 1986; Houseknecht, 1988; Dutton & Diggs, 1990; Bjørlyyke & Egeberg, 1993; Dutton, 1993; Walderhaug, 1994; Oelkers et al., 1996). Pressure solution is more extensive in finer-grained sandstones than in coarse-grained sandstones (Stephan, 1970; Pittman, 1979; Houseknecht, 1984; Bjørlykke et al., 1986; Porter & James, 1986; Houseknecht & Hathon, 1987; and Bjørlykke & Egeberg, 1993). Chemical compaction in the form of intergranular pressure solution and stylolites is very common in the Tirrawarra Sandstone. This feature is significant in finer-grained sandstones and sandstones rich in rock fragments and is considered to be an important source of silica for quartz cement in the Tirrawarra Sandstone.

- **Replacement of quartz by carbonate cement**

Replacement of quartz grains by carbonate minerals has been reported by many authors (e.g., Walker, 1960; Burley & Kantorowicz, 1986). In the Tirrawarra Sandstone, quartz overgrowths and quartz grains are embayed by siderite cement. This replacement, however, is not very common and this process cannot be considered an important source for silica.

- **Dissolution of More Soluble Phases of Silica**

Silica released during hydrolysis of volcanic glasses can be a source for quartz cementation (Swineford & Franks, 1959; Keene, 1975; Füchtbauer, 1974). Quartz cement derived from dissolution of amorphous silica commonly has a microcrystalline, chert-like texture due to supersaturation during precipitation (Bjørlyyke & Egeberg, 1993). Although devitrified volcanic glasses are relatively common in the Tirrawarra Sandstone, the lack of microcrystalline texture in quartz cement and the lack of significant dissolution of volcanic rock fragments suggest that this source of silica is volumetrically unimportant in the Tirrawarra Sandstone.

- **Transformation of Clay Minerals**

Many authors (Siever, 1962; Towe, 1962; Hower et al., 1976; Boles & Franks, 1979) argue that, during transformation of clay minerals, silica is released and therefore, clays can be a potential silica source for quartz cementation. Clay fraction XRD of selected representative samples of the Tirrawarra Sandstone indicates kaolinite and illite are the major clay minerals in the Tirrawarra Sandstone. SEM observation shows that most illite is an alteration product of labile detrital grains. There is also very little shale section within the Tirrawarra Sandstone making clay transformation an unlikely source for significant amounts of quartz cement.

4.4.1.2.1 Controls on Aluminium Content in Quartz

Al, H, Li, and Na are recognised as the most important trace elements in quartz crystals (Lehman & Bambauer, 1973; Cohen, 1985; Perny et al., 1992). Al^{+3} substitutes for Si^{+4} in the tetrahedral coordination and H^{+}, Li^{+}, and Na^{+} are coupled to balance the charge (Jain & Nowick, 1982; Smith & Steele, 1984).

The different zones of quartz cement in the Tirrawarra Sandstone represent precipitation under different chemical and physical conditions. Fluid-inclusion data indicate that multiple episodes of quartz cementation have occurred. The electron microprobe data revealed differing aluminium concentrations within each zone, suggesting that the pore-fluid chemistry was different during precipitation of each zone (Rezaee & Tingate, 1996b).

Incorporation of aluminium in quartz crystals is controlled by several factors including growth direction (Brown & Thomas, 1960), temperature and pressure (Dennen & Blackburn, 1970; Pavlishin et al., 1978), solution chemistry (Brown & Thomas, 1960; Pavlishin et al.,1978), and pH (Merino et al., 1989). Perny et al. (1992) suggested that variations in aluminium content over one order of magnitude in the same growth direction probably reflect changes in the fluid chemistry, either in trace-element concentrations or pH. Aluminium analyses of different zones of quartz cement show that large differences in aluminium content occur in the same growth direction, indicating that crystallographic orientation is not the major control on variation in aluminium incorporation between cement zones. Aluminium uptake by quartz also tends to increase with increasing temperature and pressure (Dennen & Blackburn, 1970; and

Pavlishin et al., 1978) but the pattern of varying aluminium content in Z1 to Z3 cements is not consistent with this mechanism. In addition, the range in temperature and pressure represented by the Tirrawarra Sandstone cements is unlikely to be of sufficient magnitude to cause the observed compositional variation.

It is likely that changes in pore-water aluminium concentration (Brown & Thomas, 1960; Staats & Kopp, 1974) and pH (Merino et al., 1989) are the main controls on aluminium uptake by quartz in the Tirrawarra Sandstone. Merino et al. (1989) suggested that incorporation of aluminium species in quartz is not only affected by the aqueous aluminium concentration but the type of aluminium in solution. Tetrahedrally-coordinated aluminium complexes (Al_{tet}) are preferentially substituted into silicate lattices over octahedrally-coordinated aluminium (Al_{oct}). Merino et al. (1989) predicted that aqueous aluminium changes from predominantly Al_{oct} to Al_{tet} over a narrow pH range of 4 to 5 at a temperature of 100°C. This transformation occurs at slightly higher pH values at lower temperatures.

The pore-water aluminium content during precipitation of different zones of quartz cement in the Tirrawarra Sandstone is unknown. Assuming that the aluminium concentration in Tirrawarra Sandstone pore fluids was constant and pH controls the variation of aluminium uptake in quartz cement, Z3 quartz cement should have formed at pH < 4 (using the relationship in Merino et al., (1989)). Analysis of formation water collected in drill stem tests from the Fly Lake Field show a pH of 6.7. Assuming this value is representative of the water that precipitated late Z3 cements and is not considerably contaminated during later burial, the predicted aluminium content in Z3 cements is greater than that measured. It is more likely that total aluminium concentrations have fluctuated over the diagenetic history of the Tirrawarra Sandstone. The formation has experienced discrete episodes of feldspar dissolution and kaolinite precipitation which were probably associated with pore fluids of higher aluminium content. Contemporaneous Z1 and Z2 quartz cements have a high aluminium content, reflecting an elevated aluminium content in the pore fluid. Z3 cement, in contrast, formed later, without this contemporaneous aluminium source. Although the aluminium variation in all quartz cements cannot be explained by variation in formation water pH alone, the relatively high levels of aluminium in Z1 and Z2 cements suggest that they formed with pH > 5, using the model of Merino et al. (1989). Combining this pH constraint with others derived from contemporaneous kaolinite formation and

siderite dissolution suggests a pH range of 5 to 7 for quartz cementation in the Tirrawarra Sandstone.

4.4.1.2.2 Silica Source for Z1 Cement

Fluid inclusions with low homogenisation temperatures (65°C - 80°C) from Z1 quartz cement, occur in sandstones with very high intergranular volume (IGV). These sandstones are not strongly compacted and their low-temperature fluid-inclusions (approximately 65°C) support relatively early quartz cementation. The most likely origin of silica for this stage of quartz cement is the early dissolution of feldspar grains, possibly related to an influx of acidic meteoric water. Figure 4.12 shows that uplift and erosion at ~200 Ma would have been a suitable time for the influx of meteoritic water. Although alteration of silicates other than quartz and feldspars in meteoric water is mentioned as a source for silica by several authors (Kantorowicz, 1985; Dutta & Suttner, 1986), the lack of these types of grains in the Tirrawarra Sandstone suggests they could not have been an important source for silica. Evidence for feldspar dissolution in the Tirrawarra Sandstone is pervasive and is consistent with the moderate aluminium content found in the Z1 quartz cement.

4.4.1.2.3 Silica Source for Z2 Cement

Isolated primary fluid-inclusions within the Z2 quartz cement indicate a formation temperature range from 80° to 100°C. This stage of cement only occurs in samples which have high IGV values and relatively high permeability. The fluids that precipitated Z2 quartz cement are likely to have been richer in aluminium than the fluid that precipitated Z3 quartz cement. The precipitation-temperature range of Z2 quartz cement is consistent with early hydrocarbon migration in the Tirrawarra Sandstone (Rezaee & Schulz-Rojahn, 1996). Fluids released during kerogen maturation are effective in contributing to feldspar dissolution (Huang & Keller, 1970; Surdam et al. 1984). Increase in pH of these aluminium-rich fluids due to solution of carbonates causes supersaturation leading to kaolinite precipitation (Curtis, 1983). Dissolution of the middle generation of siderite cement (S2) predates late kaolinite precipitation (Plate 10E). The precipitation temperature of S2 siderite cement is about 68°C and its dissolution is attributed to acidic fluids generated during source rock maturation

Plate 16

Micrographs of quartz Cement and Sandstone Composition

A - In some quartz-rich sandstones, quartz overgrowth development is significant leading to occluded pore spaces. In this example, the sandstone displays a high intergranular volume (IGV) preserved by quartz cementation. Quartz overgrowth in this example can be readily recognised by its distinct dust rims. Sample F3-9588, Fly Lake-3, 2876.4 m. Scale bar = 250 μm.

B - In most quartz-rich samples in which development of quartz cement is significant, remnant intergranular porosity can be seen. Notice the presence of dead oil in the pore spaces suggesting that the main charge of oil occurred after quartz cementation. Sample M3-9405, Moorari-3, 2821.5 m. Scale bar = 250 μm.

C - A photomicrograph of a fine-grained sandstone in which the development of quartz cement is significant, leading to occlusion of intergranular pore spaces. Most of the quartz cement can be recognised by the presence of dust rims. Sample M4-9409.7, Moorari-4, 2823 m. Scale bar = 500 μm.

D - Crossed-nichols view of the same sample as **C**.

E - In a sandstone rich in rock fragments where mechanical compaction is significant, the development of quartz cement is minor. M3-9428, Moorari-3, 2828.4 m. Scale bar = 1000 μm.

F - Crossed nichols view of **E**.

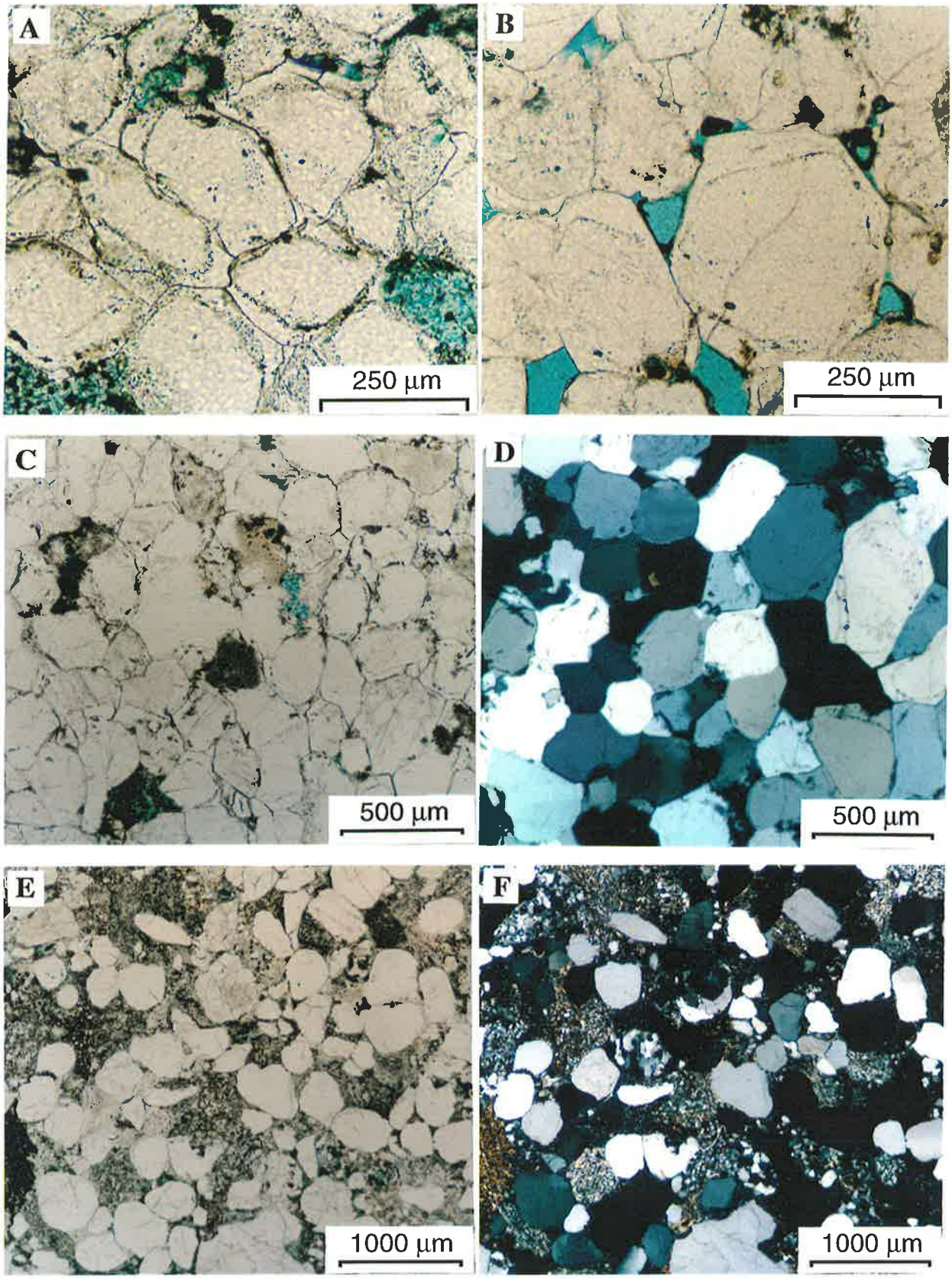
A
250 µm
B
250 µm
C
500 µm
D
500 µm
E
1000 µm
F
1000 µm

(Rezaee & Schulz-Rojahn, 1996). Considering the precipitation temperature and high aluminium content of Z2 quartz cement, it is reasonable to suggest that the source of silica was late feldspar dissolution by acidic fluids from associated hydrocarbon generation. A pH between 5 and 7 would provide optimum conditions for the formation of quartz cement and incorporation of tetrahedrally coordinated aluminium from solution.

Mass balance calculations show that feldspar alteration in the Tirrawarra Sandstone could have approximately generated the combined volume of Z1 + Z2 cements.

4.4.1.2.4 Silica Source for Z3 Cement

Fluid-inclusions in Z3 quartz cement have the highest homogenisation temperatures (about 130°C). Z3 quartz cement is also best developed in lithologies with well-developed pressure solution. It is likely that the source of silica was detrital quartz dissolution associated with the comprehensive stylolitisation which is common in fine-grained and rock-fragment-rich samples of the Tirrawarra Sandstone. Such a source of silica is consistent with the low aluminium content in Z3 cements which is similar to that of the detrital quartz grains from which it is derived (Table 4.4).

Rapid burial by the Cretaceous section of the overlying Eromanga Basin is the likely driving mechanism for the pressure solution of quartz grains.

4.4.1.3 Effect of Quartz Cementation on the Reservoir Quality

Quartz cement has both positive and negative effects on reservoir quality in the Tirrawarra Sandstone. The early stage of the quartz cement (Z1) has a positive effect on reservoir quality as it leads to a strengthening of the grain framework and a reduction of compaction in quartz-rich sandstones. In samples with significant early quartz cement, the Compaction Index is very low and consequently intergranular volume (IGV) is high (Plate 16A-D). In samples that have little or no early quartz cement, the Compaction Index is very high and IGV is very low (Plate 16E & 16F). In general, as the amount of quartz cement increases, intergranular volume (IGV) significantly increases (Fig. 4.13), indicating that quartz cement has helped prevent porosity loss by compaction. In some samples with high proportions of quartz cement, the present IGV is close to its

estimated original value (Fig. 4.13). The late stages (Z2, Z3) of quartz cement have had a negative effect on reservoir quality as they have reduced the remaining porosity.

The amount of quartz cement in the samples has a close relationship with the amount of detrital quartz. As the amount of detrital quartz in the samples increases, the percentage of quartz cement increases. In turn, the amount of detrital quartz grains and rock fragments in the sandstones are controlled by the depositional facies (Fig. 4.14). The ratio of rock fragments to detrital quartz decreases from the medial part of the braid-delta to the meandering fluvial and aeolian environments. The depositional facies control sandstone composition and consequently influence the amount of quartz cement and therefore porosity and permeability.

The best reservoir lithologies are composed of sandstones containing mainly Z1 and Z2 quartz cements (Rezaee & Tingate, 1996a). They are typically well-sorted, quartz-rich sandstones that formed in aeolian and point bar environments and have relatively higher porosities (14-17%). Reservoir lithologies which display all these zones of quartz cement, have a high proportion of IGV but low porosity. Although these sorts of sandstones are clean, they are sandwiched between facies that are prone to stylolitisation and provide silica for the Z3 cements. Parts of the reservoir which contain no quartz cement or only a small amounts of Z3, have a very low IGV and no visual porosity. These are the finer-grained sandstones that display comprehensive stylolitisation. They have had high levels of compaction before developing any type of quartz cement.

4.4.1.4 Thermal History Modelling and the Timing of Quartz Cements

Various thermal scenarios were modelled using vitrinite data in order to constrain the timing of the quartz cements in the Tirrawarra Sandstone using *Basinmod*. Measured vitrinite reflectance values and values calculated from the methylphananthrene index (MPI) using oil in the Tirrawarra Sandstone within the Fly Lake and Moorari Fields are both close to 1.0 (Tupper and Burckhardt, 1990), suggesting that migration was local or both reservoir and oil have been affected by post-emplacement burial. In a simple thermal model with a constant (present) heatflow without erosion at unconformities, the dominant feature in the thermal history is Cretaceous burial. This causes rapid heating of the Tirrawarra Sandstone and forces it inter the oil window (Fig. 4.12). Model

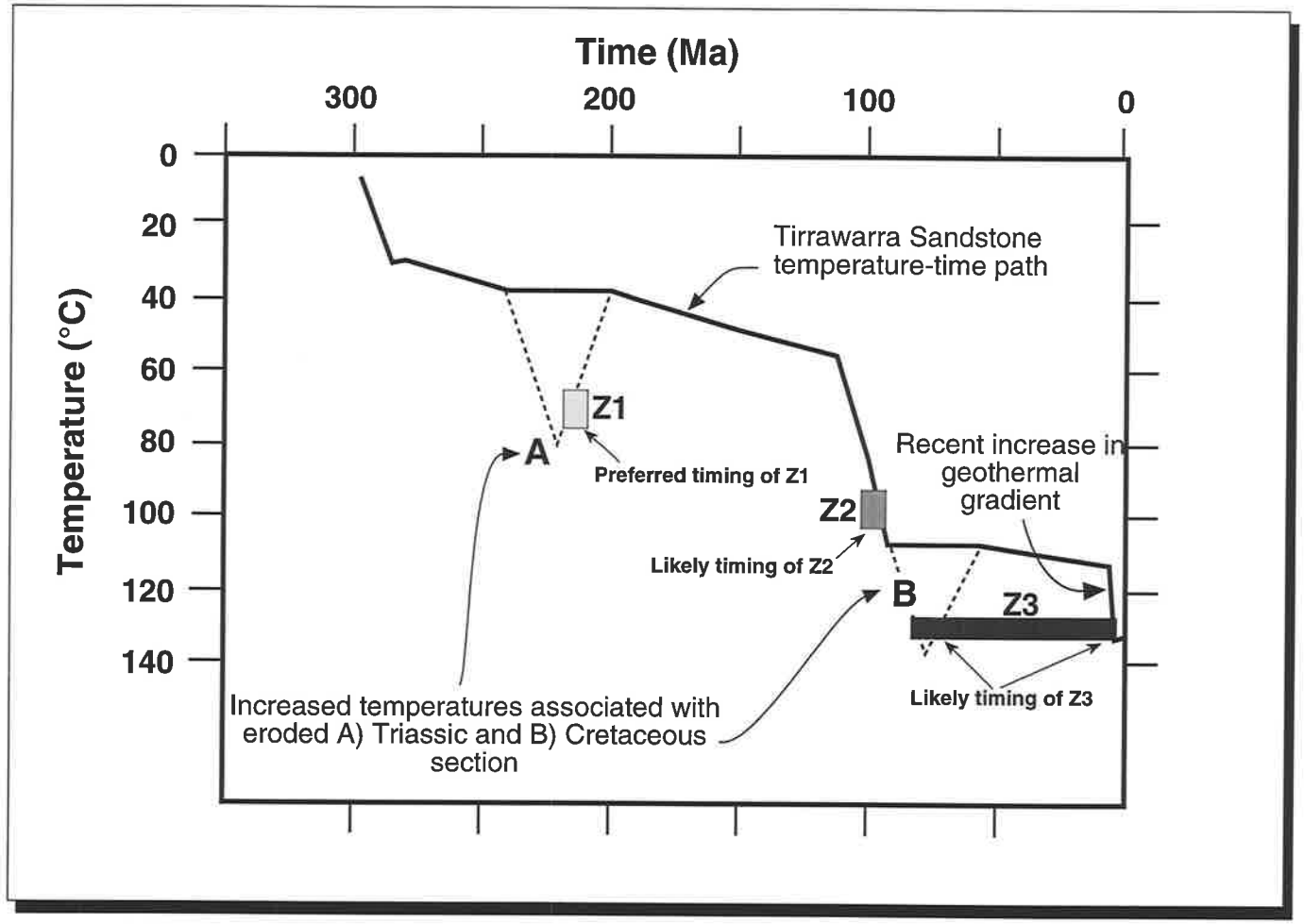

Figure 4.12 - Schematic thermal history of the Tirrawarra Sandstone, Fly Lake Field. Temperatures of precipitation for different zones of quartz cement are displayed on the diagram.

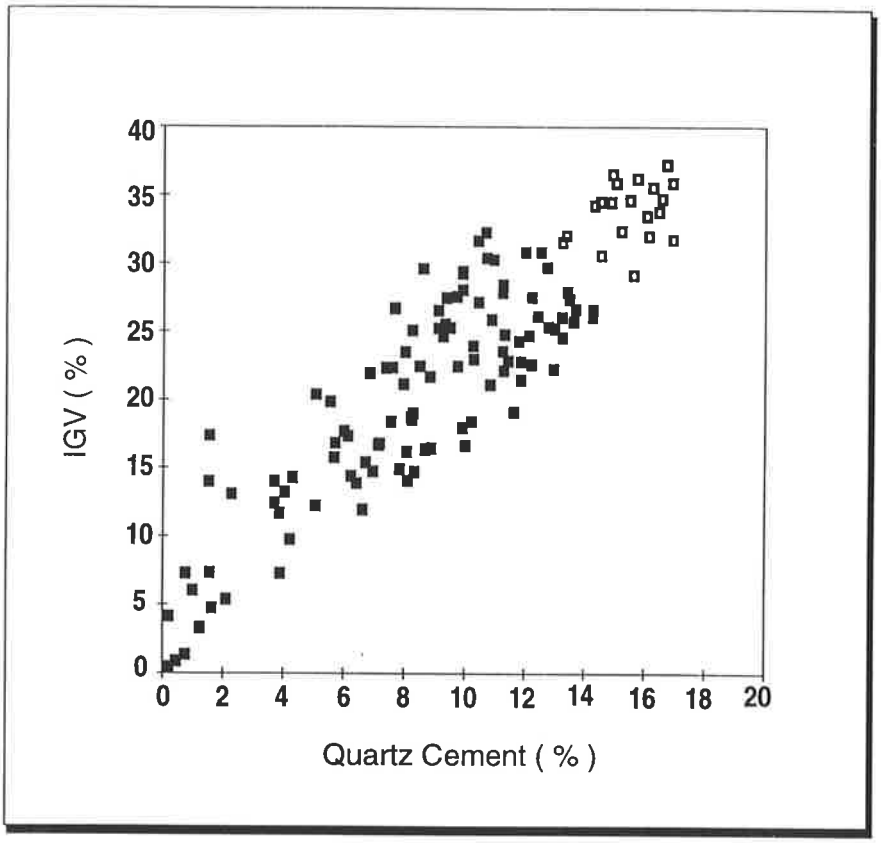

Figure 4.13 - Quartz cement (%) plotted against intergranular volume (IGV) (%). IGV is only slightly reduced in samples with high proportion of quartz cement (more than 14%, open square values).

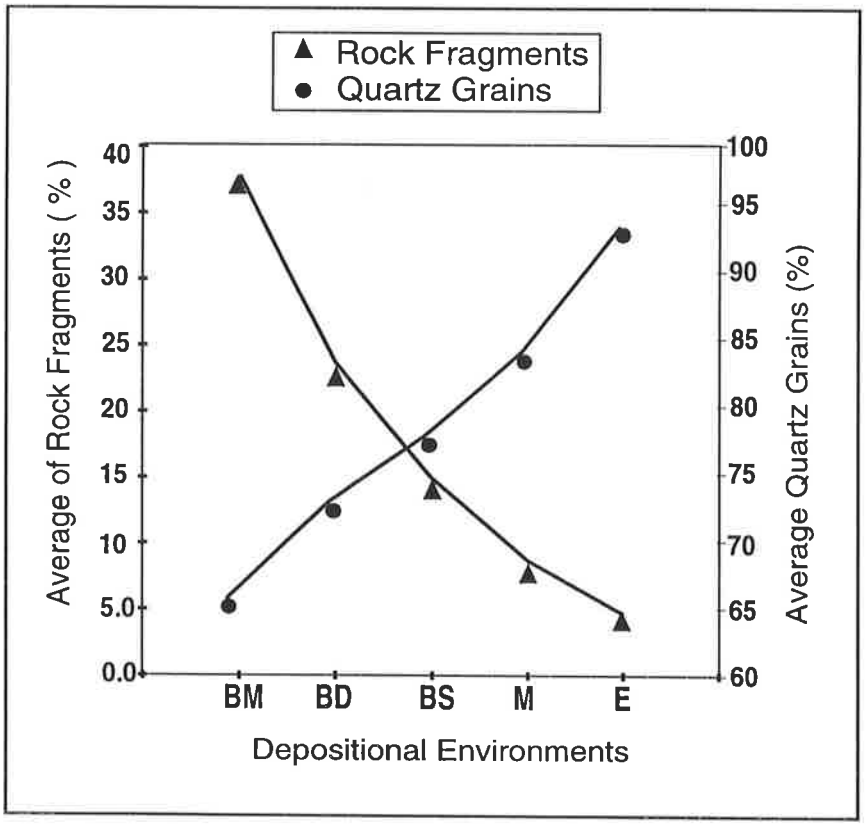

Fig. 4.14 - Depositional environment plotted against average content of rock fragments and detrital quartz. The proportion of ductile rock fragments increases from the aeolian to the braided system, whereas the proportion of detrital quartz decreases. BM= medial part of the braid-delta; BD= distal part of the braid-delta; BS= beach barrier; M= meandering system; E= aeolian.

vitrinite values are close to those measured at the level of the Tirrawarra Sandstone. However, measured vitrinite values from higher up the studied wells are significantly less than the calculated values. This is likely to be related to a recent increase in geothermal gradients and localised aquifer-related heating, noted in other parts of the Cooper/Eromanga Basins (Gleadow et al., 1988). If a recent increase in geothermal gradients has occurred, then the similarity between calculated and measured vitrinite values in the Tirrawarra Sandstone is fortuitous and the measured vitrinite values reflect earlier rather than present thermal conditions.

Figure 4.12 shows a schematic time-temperature path for the Tirrawarra Sandstone based upon thermal modelling. In this history, the likely time ranges for the formation of the three groups of quartz cements are illustrated. Based on the precipitation temperature of middle generation of siderite cement (S2), which is about 68°C, an erosion of about 550 meters considered to have occurred during the late Triassic in the studied area (discussed in detail in the following chapter). If 550 m erosion is considered as the maximum erosion in the studied area, Z1 has been formed at approximately 200 Ma and Z2 quartz cement could have been formed at approximately 100 Ma, while Z3 quartz cement is considered to accompany or postdate oil migration into the Tirrawarra Sandstone and is believed to have formed between 100 Ma and present.

4.4.2 Siderite cement

Siderite has a very limited stability and can occur only at high P_{CO2}, low dissolved sulfur, and where reducing conditions prevail (Nordstorm & Munoz, 1986). A Fe/Ca ratio greater than 0.05 is also required for the formation of siderite instead of calcite (Keltz and Hsü, 1978). In spite of the limited conditions for precipitation of siderite cement, it can form in a wide variety of depositional environments, including marine, brackish and freshwater environments (Gould & Smith, 1979; Matsumoto & Iijima, 1981; Gautier, 1982; Curtis & Coleman, 1986; Carpenter et al., 1988; Bahrig, 1989; Mozley, 1989; Mozley & Carothers, 1992; Spiro et al., 1993; Baker et al., 1996; Middleton & Nelson, 1996; Morad et al., 1996). Early diagenetic siderite from fresh-water depositional environments is characterised by a relatively pure composition (e.g. greater than 90 mol% $FeCO_3$) (Mozley, 1989). Based on electron microprobe analysis of

siderite cement (discussed in detail in the following chapter), the early generation of siderite cement in the Tirrawarra Sandstone is also a pure, Fe-rich siderite with an average composition of $(Fe_{96\%}Mg_{1\%}Ca_{1.7\%}Mn_{1.3\%})CO_3$.

The elemental composition of siderite is influenced by the concentrations of Fe^{+2}, Mg^{+2}, and Ca^{+2} in the waters from which it precipitates (Matsumoto & Ijima, 1981; Curtis & Coleman, 1986; Mozley, 1989; Mozley & Carothers, 1992; Macaulay and Haszeldine, 1993). The increase in Mg in late generations of siderite cements can be induced by several possible sources. The origin of Mg may be from the alteration of Mg-rich minerals such as micas, which are abundant in nearly all of the Tirrawarra Sandstone samples, including metamorphic rock fragments. The presence of partly leached biotite supports this idea. The same source of Mg was suggested by Macaulay and Haszeldine (1993) for siderite cements in the Magnus Sandstone, North Sea. The marine limestones of the Warburton Basin underlying the Cooper Basin could also have provided a source of Mg. Such a source is also suggested by Morad et al. (1994) for siderite cement of Triassic reservoir sandstones from southern Tunisia. Alternatively, Mg was released from kerogen after burial (Desborough, 1978). According to Desborough (1978), the higher content of magnesium with respect to calcium in kerogen-rich rocks is probably due the preferential concentration of magnesium by blue-green algae whose remains released magnesium during kerogen maturation.

The sequence of precipitation of low Mg siderite then high Mg siderite cement in the Tirrawarra Sandstone in the Cooper Basin, agrees with the sequence of formation of low and high magnesian siderites in Japanese oil fields with fresh water sediments (cf. Matsumoto and Iijima, 1981) and in the Westphalian of Yorkshire (cf. Pearson, 1974a & 1974b).

4.4.3 Clay Minerals

The authigenic origin of the kaolinite in the Tirrawarra Sandstone is supported by the euhedral habit. Koalinite is stable at pH between 5 to 8 and forms at low to moderate temperatures (May et al., 1979; Hurst, 1980). Early authigenic kaolinite forms in meteoric pore waters with low pH and low ionic concentrations at the expense of feldspars and micas (Sommer, 1978; Bjørlykke & Brendsdal, 1986; Bjørlykke, 1988; Glasmann et al., 1989). In a large number of samples, the occurrence of kaolinite is associated with the original grains, identified by the original margin (Plates 12A & 12B, 13D). The more likely precursors are believed to be feldspar grains, now completely

absent in most of the Tirrawarra Sandstone samples. CL observation by Schulz-Rojahn (1991) also indicated partial and complete replacement of feldspar grains by kaolinite in the Cooper Basin. The replacement of micas by kaolinite also can be seen in a few samples (Plate 14A & 14B) although this type of kaolinitisation is not pervasive. According to Curtis (1983), late kaolinite can be formed from Al-bearing acidic pore waters, derived mainly from maturing kerogen, in which the pH has been increased by dissolution of carbonate materials. Increasing pH causes supersaturation of the fluid which finally leads to kaolinite precipitation. In the Tirrawarra Sandstone, some of the kaolinite is formed after dissolution of the middle or late generation of siderite cement (Plate 10E) suggesting that it formed late.

The crystal habit of illite in the Tirrawarra Sandstone is related to its authigenic origin. The formation of illite in the Tirrawarra Sandstone is related mainly to alteration of the labile component of rock fragments, possibly during relatively late diagenesis. In some rare instances under SEM, fine illite fibers are formed close to kaolinite booklets (Plate 15A). This may suggest that illitization of kaolinite has occurred in the Tirrawarra Sandstone. Illitization of kaolinite is mentioned by Bjørlykke (1984, 1992) and by Bjørlykke et al., (1986) to takes place at temperatures of 130 - 150°C in a closed system in presence of K-feldspar to act as the source of potassium. Hurst and Irwin (1982) reported that illitization of kaolinite may take place in an open system at temperatures less than 120°C depending on the influx of potassium. Bjørkum and Gjelsvik (1988) indicated that illitization of kaolinite may take place at temperatures as low as 50°C, depending to the silica activity in the formation water and the presence of K-feldspar. In the Tirrawarra Sandstone, illitization of both early and late kaolinite suggests that this process has took place at high temperature (Fig 4.15) after late feldspar dissolution by organic acids generated from decarboxylation.

Authigenic illite which forms from direct precipitation of pore fluid, often occurs as pore lining, and/or pore-throat-bridging materials. Although this kind of illite does not greatly effect porosity, it can dramatically decrease permeability (Howard, 1992). In the Tirrawarra Sandstone samples, replacement illite is confined to around the original labile grains and does not bridge the pore throats, so has no great effect on permeability. The results of the X-ray diffraction (XRD) analyses, which may be influenced during sample preparation by disintegration of the illite-bearing labile grains,

must be treated with caution and be supplemented by SEM study to identify the real role of illite on the petrophysical characteristics of the samples.

4.4.4 Diagenetic Sequence

A combination of petrographic, stable isotope, fluid-inclusion, SEM, CL, Electron microprobe, XRD and image analysis studies were employed to construct diagenetic sequences for the studied samples.

The diagenetic sequence established during the present study (Fig. 4.15), in approximate chronological order, is as follows:

1. Mechanical compaction, which started soon after the deposition of the sediments;
2. Precipitation of an early generation of siderite cement (S1) at about 30°C;
3. A first phase of siderite dissolution (D1), at a temperature between 30° and 65°C, influenced by flushing with acidic meteoric waters;
4. Early dissolution of feldspar grains associated with flushing by acidic meteoric water;
5. Generation of early kaolinite, also during meteoric flushing;
6. Formation of early quartz cement (Z1) at a temperatures around 65°C;
7. Precipitation of a second generation of siderite (S2) at a temperatures of around 68° C;
8. Formation of late kaolinite during late dissolution of feldspar grains by organic acids generated during kerogen maturation;
9. A second dissolution phase of siderite (D2) at temperatures of between 68° and 102°C, by organic acids generated during kerogen maturation;
10. Formation of a second stage of quartz cement (Z2) at temperatures of between 80° and 100°C;
11. Precipitation of a late generation of siderite cement (S3) at temperatures about 102°C;
12. Illitization of labile components of rock fragments;
13. Hydrocarbon migration at temperatures of between 80° and 102°C;
14. Chemical compaction by stylolitisation and intergranular pressure solution;
15. Formation of late quartz cement derived from pressure solution at temperatures of between 100 and 130°C.

The paragenesis has a degree of overlap between diagenetic events.

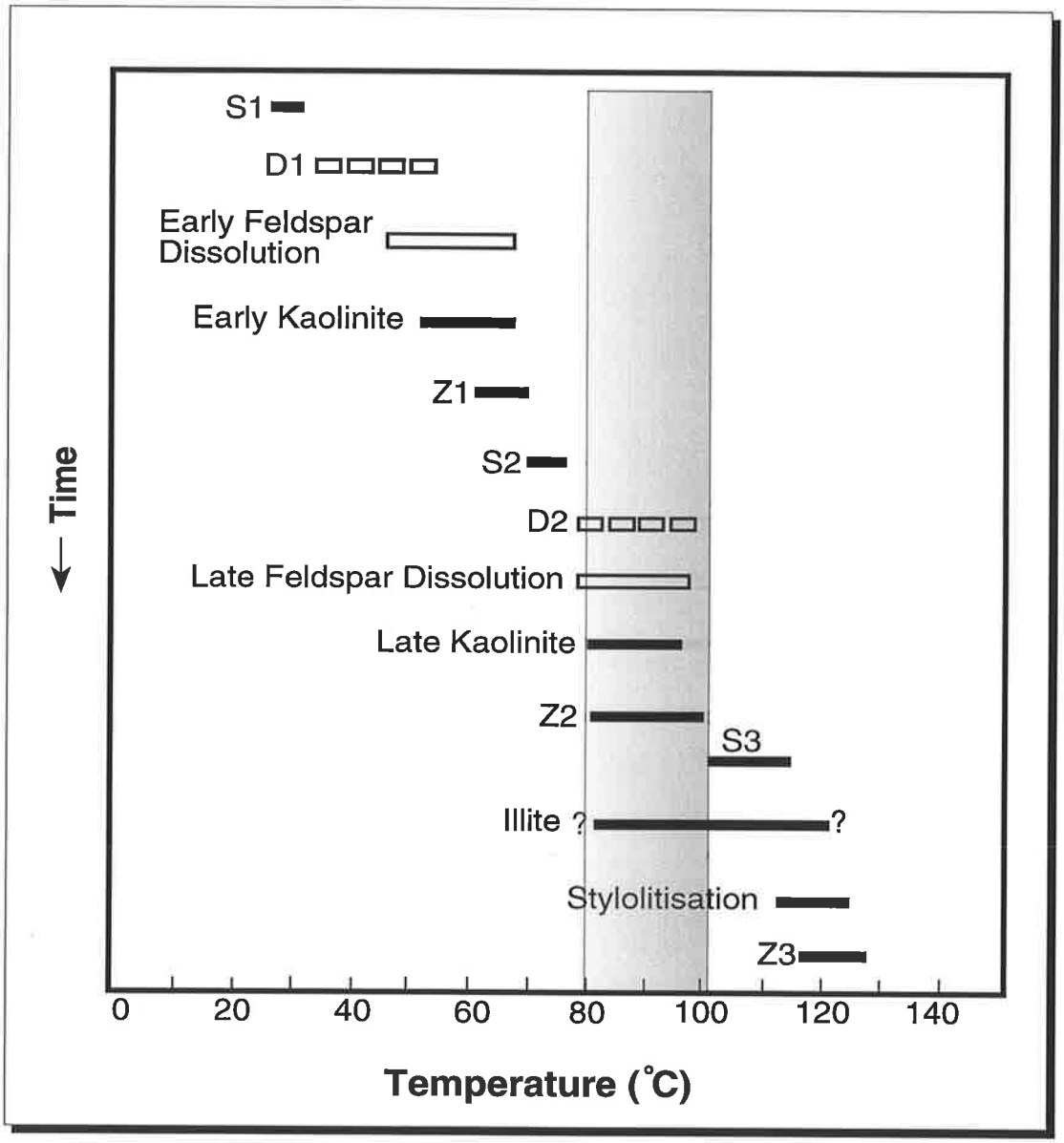

Figure 4.15 - Generalised paragenetic sequence for the Tirrawarra Sandstone in the Moorari and Fly Lake Fields. The interpretation is based on the integration of petrographic, isotope, and fluid inclusions results. The estimated temperature of early hydrocarbon generation and migration is indicated (shaded zone), (S1 = early stage of siderite cement; S2 = middle stage of siderite cement; S3 = late stage of siderite cement; Z1 = early quartz cement; Z2 = middle quartz cement; Z3 = late quartz cement; D1 and D2 = first and second phase of siderite dissolution respectively).

4.4.5 The Influence of Sedimentary Environment on Diagenesis and Reservoir Quality.

During the present study, a series of depositional environments was suggested for the Tirrawarra Sandstone in the Moorari and Fly Lake Fields (Chapter 3). These environments were associated with lakes formed during the waning stages of the Carboniferous to Permian glaciation. Each sedimentary environment has a characteristic detrital composition controlled by the distance from the sedimentary source and the energy of the depositional environment. The relative proportions of quartz grains and rock fragments vary considerably between each sedimentary environment. This situation provides an opportunity to quantitatively evaluate the control exerted by depositional facies on the composition of detrital grains and how detrital composition influences diagenesis and reservoir quality in the Tirrawarra Sandstone (Rezaee & Lemon, 1996a). An understanding of the diagenetic events which influenced reservoir quality should help to maximise the recovery of oil and gas from this important reservoir unit. Each sedimentary environment presented in this study can be recognised by its characteristic texture, composition and diagenetic events. Reservoir quality, i.e. porosity and permeability, is highest in the aeolian sandstones and decreases through the meandering and beach barrier sandstones to the beds associated with the braided system (Figures 4.16; 4.17). Aeolian beds have porosities and permeabilities of about 16% and 320mD, respectively, whereas sandstones deposited in the braid-delta environments have average porosities and permeabilities of about 5% and 0.5mD.

The most likely controls on reservoir quality are the texture and composition of the sediments.

The texture of sand grains greatly affects porosity and permeability at the depositional surface; porosity and permeability increase as sorting improves and grain size increases (Beard and Weyl, 1973; Pryor, 1973). However, textural parameters have no significant control on reservoir quality in the Tirrawarra Sandstone. Although the grain size increases from aeolian to braid-delta deposits (Fig. 4.1), the porosity and permeability decrease (Figs. 4.16; 4.17). The sorting of most of the samples is around 0.5 phi, and the highest values of sorting are similar for the samples from most environments. However, porosity and permeability are very different and appear to be independent of sorting.

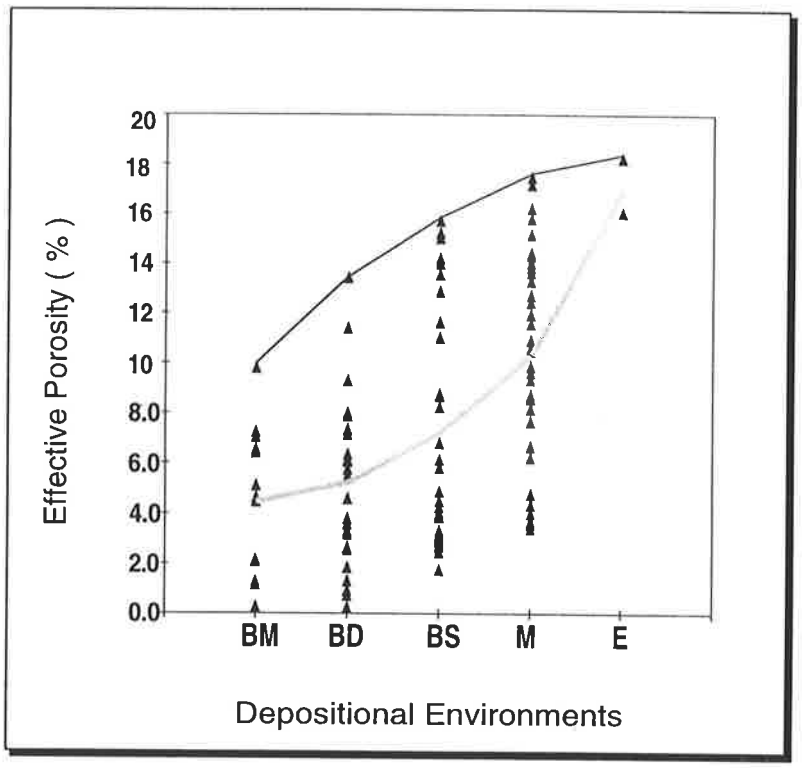

Figure 4.16 - Depositional environment plotted against point count porosity (%). Average porosity values in each depositional environment are connected with a thick grey line. BM= medial part of the braid-delta, BD= distal part of the braid-delta, BS= beach barrier, M= meandering system and E= aeolian.

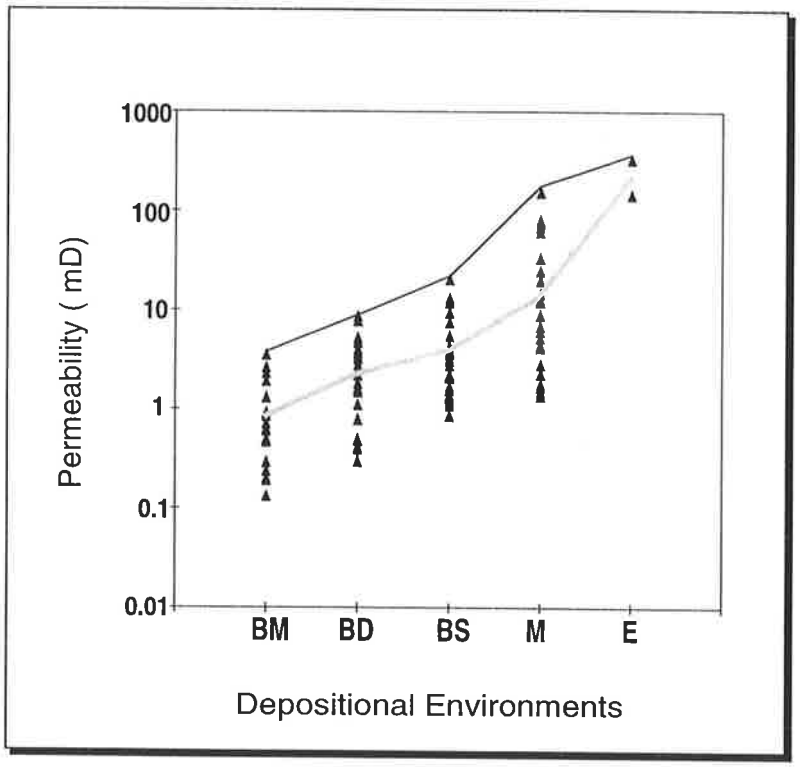

Figure 4.17 - Semi-log crossplot of permeability (mD) versus depositional environment. Average values of permeability in each depositional environment are connected with a thick grey line.

The detrital composition of sandstones, i.e. the quartz and rock fragment content of sandstones, is controlled by depositional processes. Deposits from each sedimentary environment display a distinct compositional range (Fig. 4.3). Figure 4.14 shows that the amount of ductile rock fragments increases from the aeolian to the braided system. The influence of compaction is high in the rock-fragment-rich sandstones (Fig. 4.18). Figure 4.19 shows that, as the proportion of rock fragments increases, porosity decreases, indicating that deposits with less rock fragments will have a higher reservoir quality.

4.4.5.1 The Influence of Sedimentary Environment on Diagenetic Events

Original intergranular volume (IGVo) varies in each sedimentary environment as a function of grain size and sorting, and decreases from the aeolian and meandering environments towards those of the medial braid-delta (Fig. 4.20). This decrease is not very pronounced in comparison with the decrease in the present intergranular volume (IGV) (Fig. 4.21).

The depth of burial, and consequent lithostatic pressure (Wilson and McBride, 1988; Dutton and Diggs, 1992), the relative timing of cementation, and the composition (Rittenhouse, 1971) are all likely to control the amount of compaction. The variation in the depth of burial of the Tirrawarra Sandstone in the Moorari and Fly Lake Fields is not great, so the influence of differing lithostatic pressures on compaction of the study samples is very small. There is no significant correlation between porosity and depth in the intervals studied (Fig. 4.22).

The relative timing of cementation appears to have had the greatest effect on the preservation of intergranular volume. Cementation in the Tirrawarra Sandstone is completely controlled by mineralogical composition. In quartz-rich sandstones, early quartz cementation has an important role in the preservation of intergranular volume. As the proportion of rock fragments increases, the proportion of quartz cement (which inhibits later compaction) decreases (Fig. 4.6). Figure 23 shows that the proportion of quartz cement increases from deposits in environments with higher proportions of rock fragments (braid-delta environment) toward deposits from environments with higher proportions of quartz grains (aeolian environment).

Rittenhouse (1971) showed experimentally that one of the factors which controls the reduction of pore space and bed thickness is the presence of ductile rock fragments. This

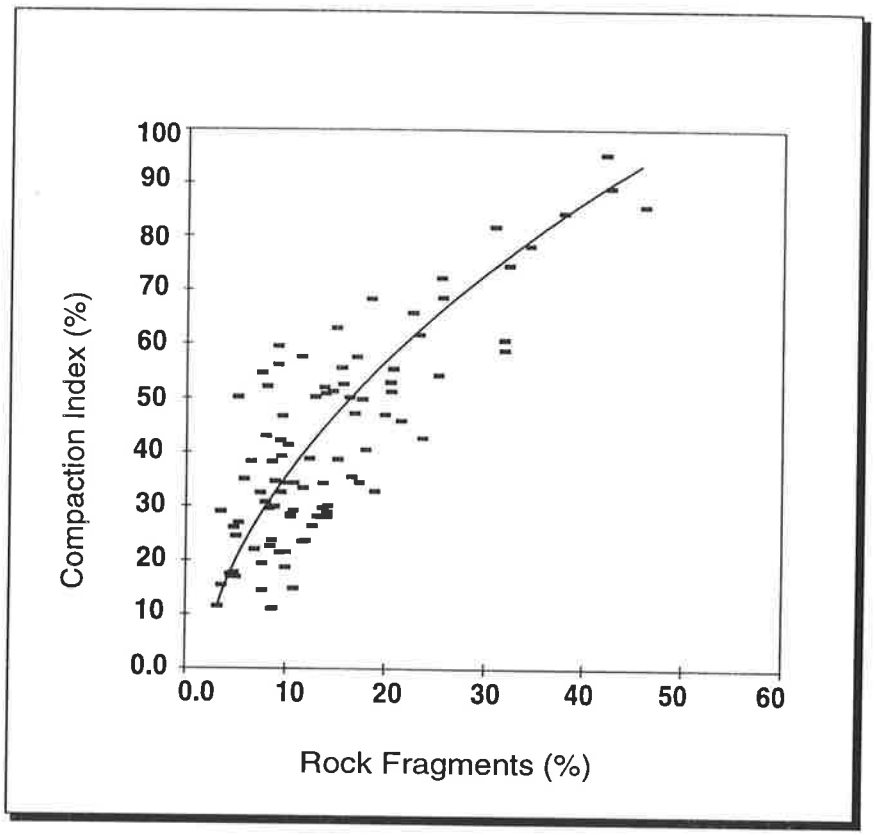

Figure 4.18 - Rock fragment percentage (%) plotted against Compaction Index (%). Compaction increases with the percentage of ductile rock fragments.

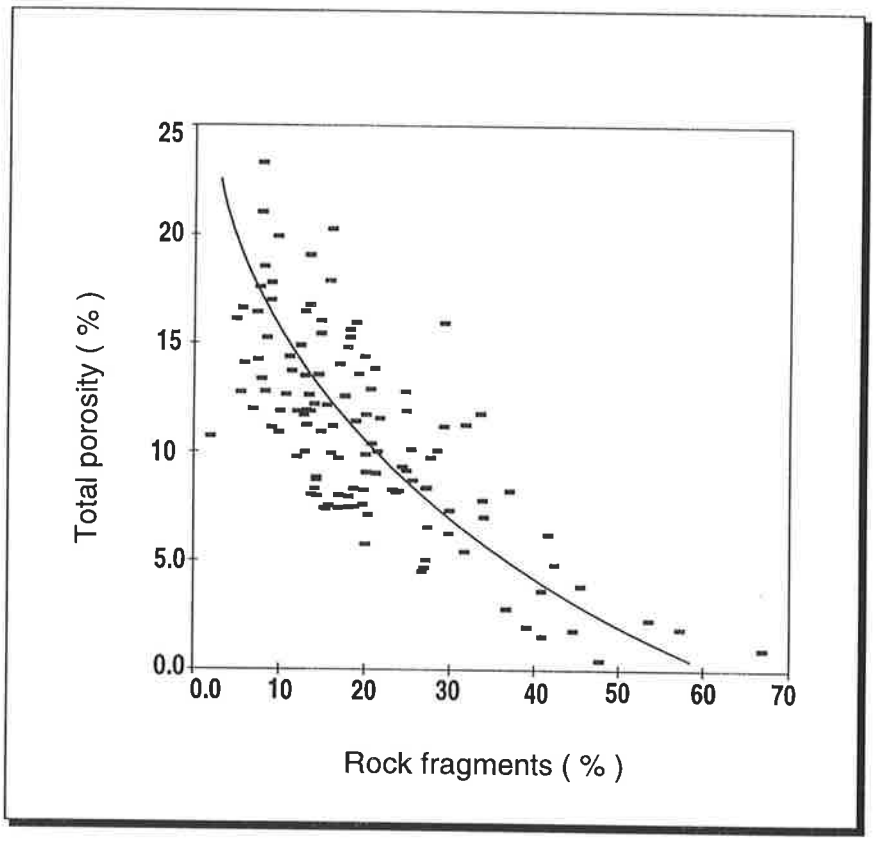

Figure 4.19 - Rock fragment percentage plotted againt total porosity (%). With increasing rock fragment content, the porosity decreases, indicating that environments with less rock fragments have higher reservoir quality.

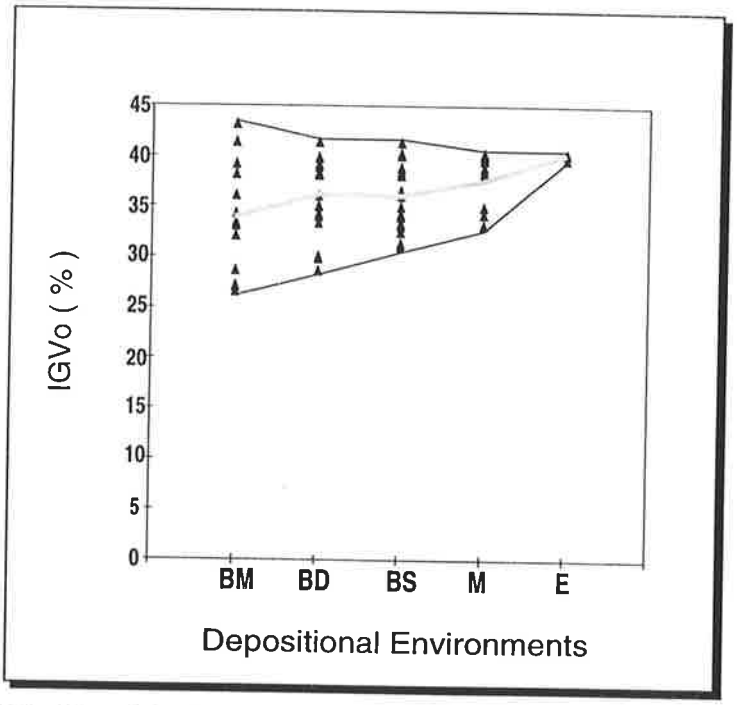

Figure 4.20 - Depositional environment plotted against original intergranular volume (IGVo). IGVo decreases slightly from the aeolian and meandering environments to the medial braid-delta. Average value of IGVo in each depositional environment are connected with a thick grey line. BM= medial part of the braid-delta, BD= distal part of the braid-delta, BS= beach barrier, M= meandering system and E= aeolian.

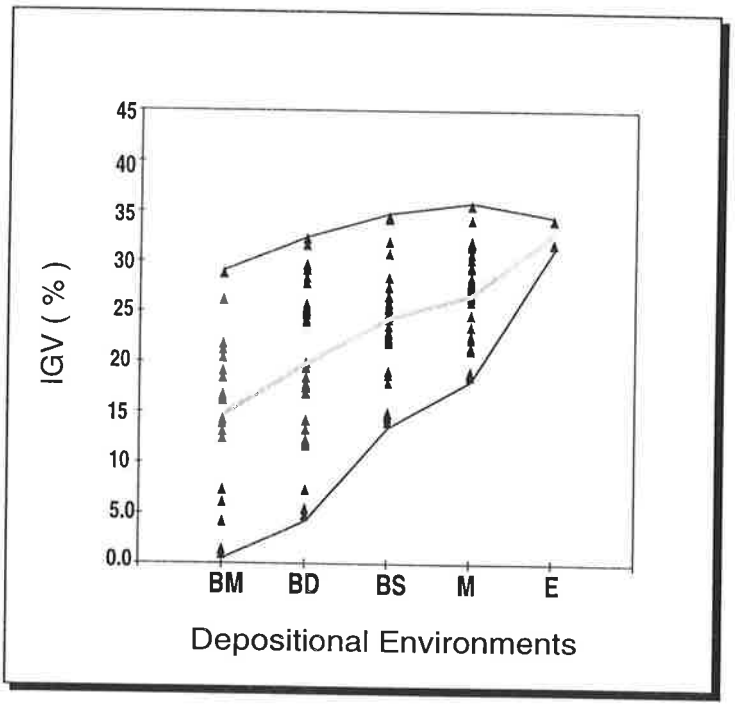

Figure 4.21 - Depositional environment plotted against intergranular volume (IGV). The reduction of IGVo from the aeolian to the braid-delta environment is not very pronounced (Fig. 4.20) in comparison to the reduction in the present intergranular volume (IGV). This is due to the fact that from the aeolian to the braid-delta environment the proportion of rock fragment increases leading to less development of quartz cement and subsequently more reduction of intergranular porosity by mechanical compaction. Average value of IGV in each depositional environment are connected with a thick grey line.

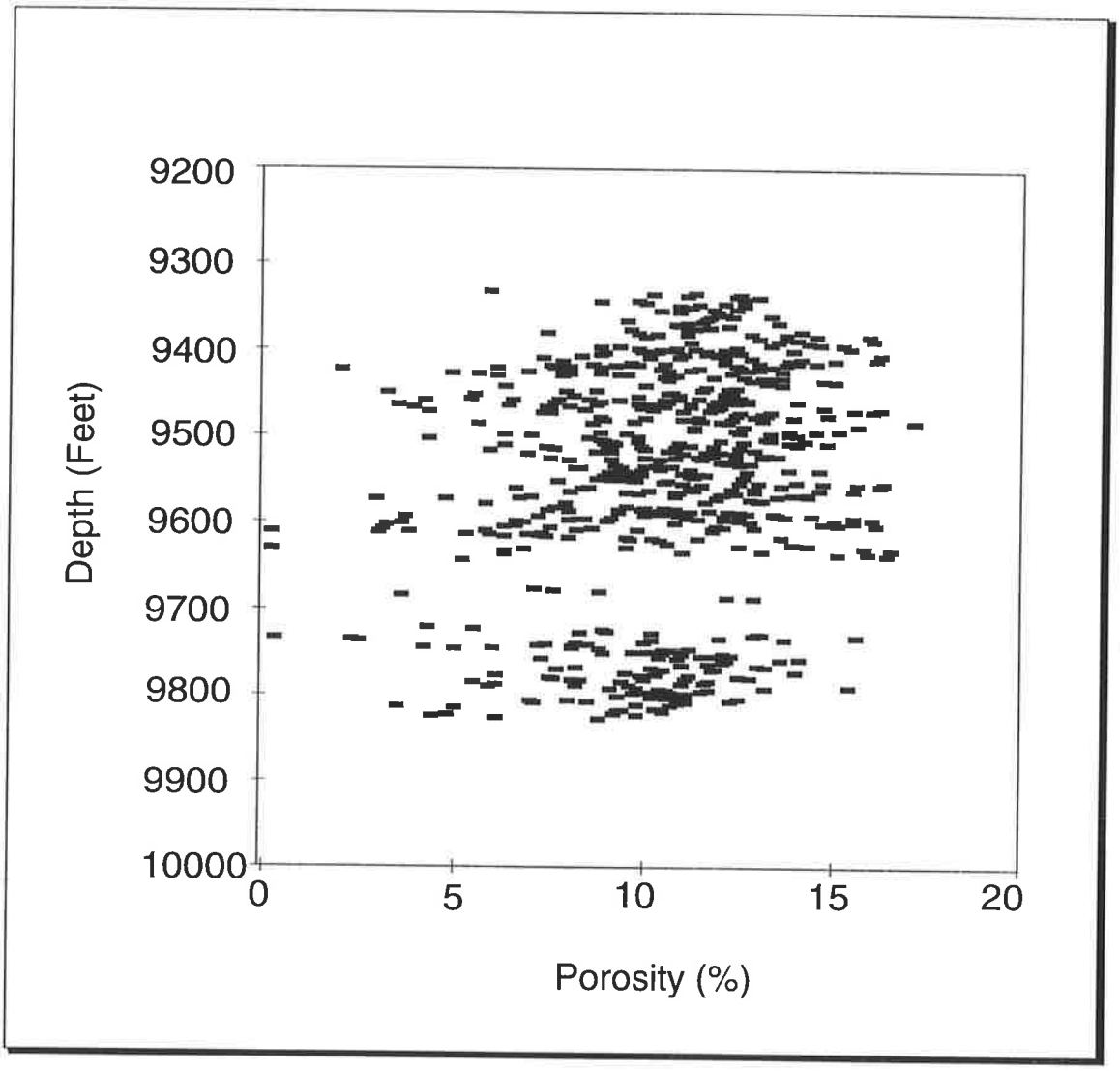

Figure 4.22 - Porosity (%) plotted against depth (ft). Because the variation of depth of burial for Tirrawarra Sandstone in the Moorari and Fly Lake fields is not great, there is no significant correlation between porosity and depth.

study of the Tirrawarra Sandstone shows that the principle parameters which control compaction are mineralogical composition and the occurrence of quartz cement, factors which are in turn controlled by depositional processes in the Tirrawarra Sandstone. Figure 4.21 shows that the decrease of IGV is very sharp, and can be exactly correlated with the content of rock fragments. This is supported by the Compaction Index of sediments from each environment (Fig. 4.24). Mechanical compaction has a strong relationship with the composition of the sandstones. As the proportion of rock fragments increases, the magnitude of compaction also increases (Fig. 4.18) because the grains are mostly ductile metamorphic and sedimentary fragments.

Three factors arise from the presence of ductile fragments which induce greater compaction in the samples:

(a) Quartz cement does not develop at a contact between a quartz grain and a rock fragment, whereas development of a thick overgrowth can be seen at quartz-quartz contacts, even in the same sample (Plate 1B, 1D, & 4H). As the proportion of rock fragments increases, the development of quartz cement decreases (Fig. 4.6). Thus, quartz cementation increases with an increase of quartz grains. The development of early quartz cement spreads the overburden pressure over a wider area of each grain, thereby inhibiting subsequent compaction. In some samples, free of ductile rock fragments, the extensive quartz cement has protected IGVo from destruction by compaction (Plate 16a & 16B).

(b) Ductile rock fragments can readily be deformed, and squeezed into adjacent pores (Plate 1A) thus occluding porosity and reducing the bulk volume of sediments.

(c) Ductile rock fragments (especially mica schists and phyllites) can readily be crushed to pseudomatrix (Nagtegaal,1978). This may occlude porosity, and may also promote pressure solution which in turn reduces the bulk volume of the sediments.

4.4.5.2 Geological Implications

A quantitative approach to the control of diagenetic events by depositional environments, makes it possible to predict the reservoir quality. In the present study, the compositional range of each sedimentary environment has been established. Compaction and quartz cementation are the principle factors controlling reservoir quality in the Tirrawarra Sandstone and, as they are completely under compositional control, they can be predicted for each depositional facies. In Figure 4.25, which is constructed from a combination of five cross-plots, it can be seen that the significance

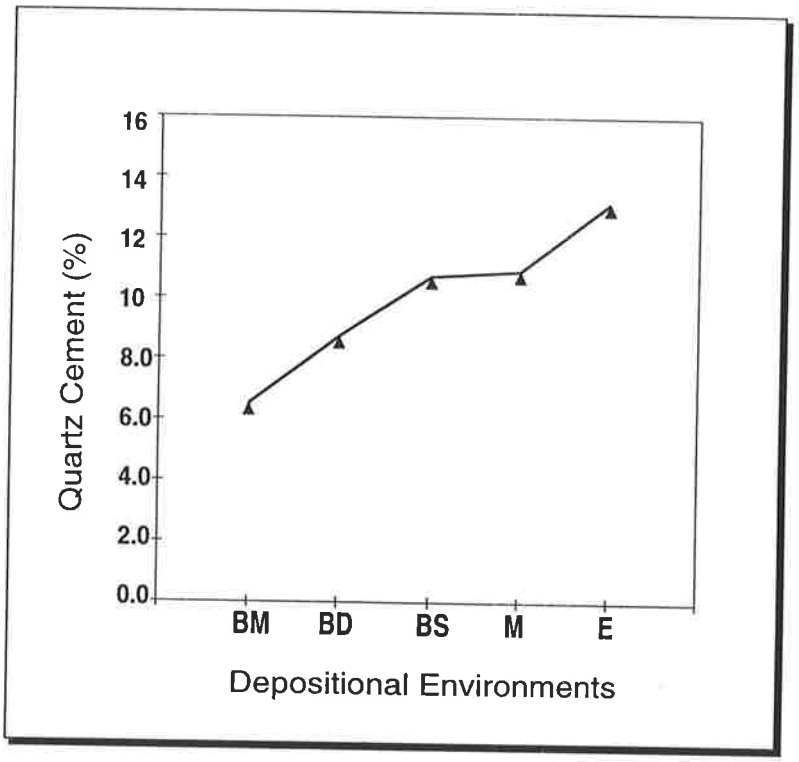

Figure 4.23 - Depositional environment plotted against quartz cement. From braid delta to aeolian environments which the proportion of rock fragment decrease, the amount of quartz cement increases.

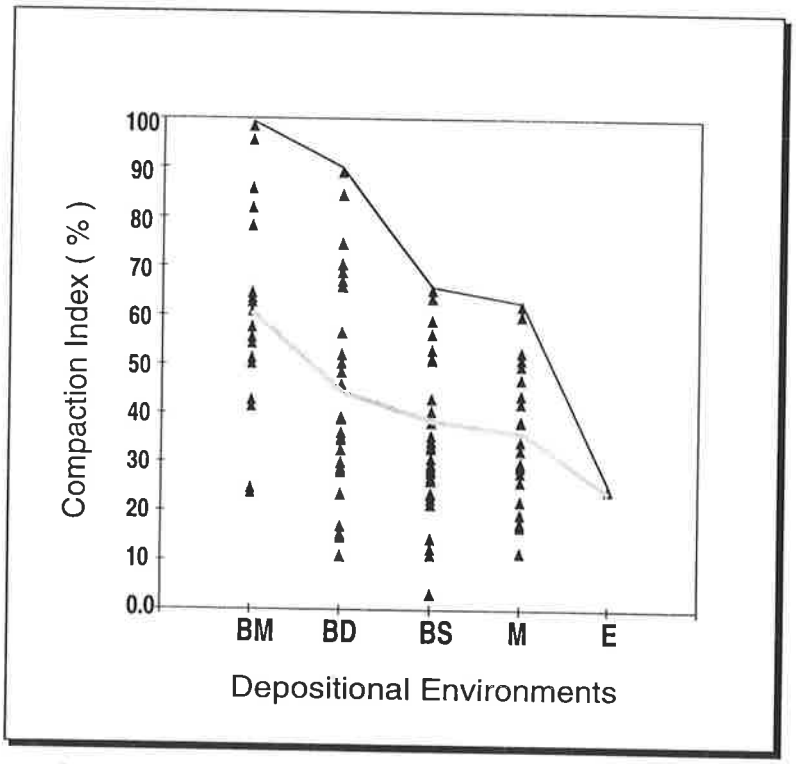

Figure 4.24 - Depositional environment plotted against compaction index (%). Environments with higher proportion of rock fragments show higher compaction. Average value of compaction index in each depositional environment are connected with a thick grey line. BM= medial part of the braid-delta, BD= distal part of the braid-delta, BS= beach barrier, M= meandering system and E= aeolian.

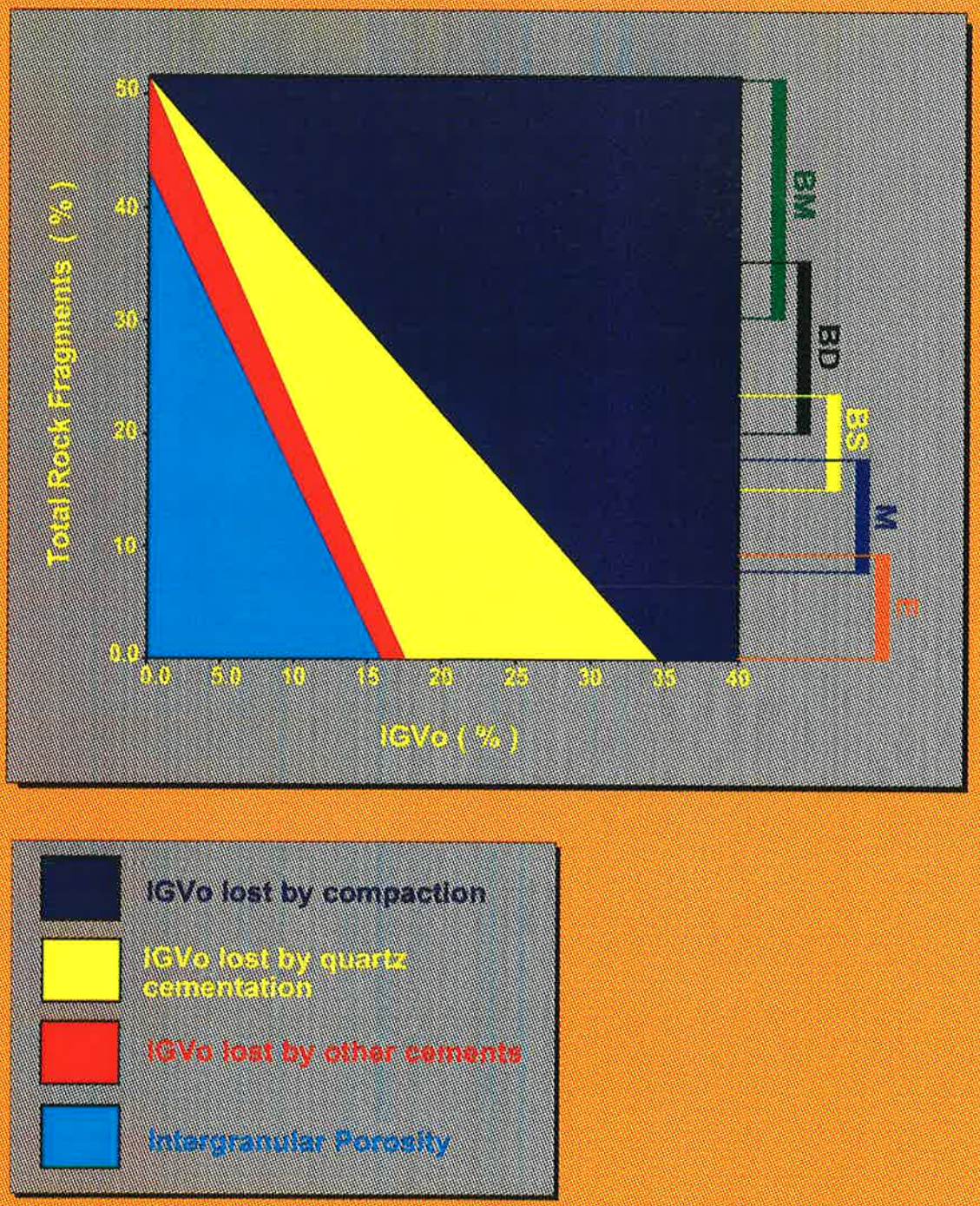

Figure 4.25 - Diagram showing the effect of rock fragment content on compaction and quartz cementation. As the amount of rock fragment increases, IGV loss by compaction increases, whereas the amount of quartz cement decreases. For each depositional environment it is possible to predict the amount of porosity loss by compaction and quartz cementation by specifying the range of rock fragment content. IGVo = original intergranular volume, BM= medial part of the braid-delta, BD= distal part of the braid-delta, BS= beach barrier, M= meandering system and E= aeolian.

of different diagenetic events varies for samples from each depositional environment. For example, in sandstones from the medial part of the braid-delta, where the proportion of rock fragments changes from 30% to 50%, the main diagenetic event reducing porosity is compaction, and porosity retained is less than 5%. On the other hand, in samples from the aeolian environment which are poor in rock fragments, the effects of compaction are small but quartz cementation is significant; the possible porosity range is around 15%. Thus, it will be possible to estimate the intensity of these two important diagenetic processes in the Tirrawarra Sandstone, and to predict reservoir quality during basin development.

4.5 OIL MIGRATION

There is a close relationship between the two phases of siderite dissolution and quartz cement precipitation. The early generation of siderite cement (S1) dissolved at temperatures above 30°C and below 68°C, probably due to low-pH meteoric water interaction during which early dissolution of feldspar grains occurred. The second siderite dissolution phase, which acted on the middle generation of siderite cement (S2), occurred at temperatures between 68°C and 102°C, probably related to acidic fluids generated from kerogen maturation (Plate 10E). Z1 and Z2 quartz cement precipitation coincided with the dissolution phases of siderite cement. Z1 formed during meteoric water flushing that led to silica release from early feldspar dissolution and also led to S1 dissolution. Z2 quartz cement precipitated during kerogen maturation, when fluid generated led to dissolution of feldspar grains and S2 siderite. Both S2 and S3 siderite and Z1 and Z2 quartz cements have bitumen trapped between them. In some samples, dead oil concentrates in the boundary zone between S2 and S3, indicating that hydrocarbon migration occurred synchronous with, or after the dissolution event but prior to S3 precipitation. This phenomenon has also occurred for the quartz cement and it can be seen that bitumen is trapped between quartz cement zones (Plate 17) especially between the earlier and latest (Z3) zones (Plate 17C & 17E). Entrapment of hydrocarbon in only quartz cement, indicates early migration of hydrocarbon between 80°C and 130°C. But the occurrence of hydrocarbon between S2 and S3 indicates narrower temperature range between 80°C and 102°C for hydrocarbon migration (Fig. 4.15).

This relationship suggests that the late stage of quartz cement (Z3) formed after an early oil migration event and was followed by the main oil charge which can be seen

Plate 17

Micrographs of Dead Oil Entrapped in Quartz Cement

In these photomicrographs it can be seen that quartz cementation continued after early migration of hydrocarbons into the Tirrawarra Sandstone reservoir.

A - Dead oil is trapped between quartz overgrowths (arrows). Sample M3-9403.6, Moorari-3, 2821 m. Scale bar = 100 μm.

B - Patches of dead oil (black) are trapped between detrital quartz and quartz cements (arrow). Note the presence of intergranular porosity between euhedral faces of quartz overgrowths. Sample M4-9483.2, Moorari-4, 2845 m. Scale bar = 100 μm.

C - Early generated hydrocarbons have been trapped prior to the latest zones of quartz cement. In this example it can be seen that a relatively thin zone of quartz overgrowth (arrow) is separated by dead oil from earlier quartz cements. Sample M3-9415, Moorari-3, 2824.5 m. Scale bar = 100 μm.

D - A coarse-grained sandstone in which dead oil is trapped between quartz cements. Note most of the intergranular porosity is occluded by extensive development of quartz cement. Sample M9-9820, Moorari-9, 2946 m. Scale bar = 250 μm.

E - Close-up view showing entrapment of dead oil between quartz cements (arrow). Sample M3-9415, Moorari-3, 2824.5 m. Scale bar = 50 μm.

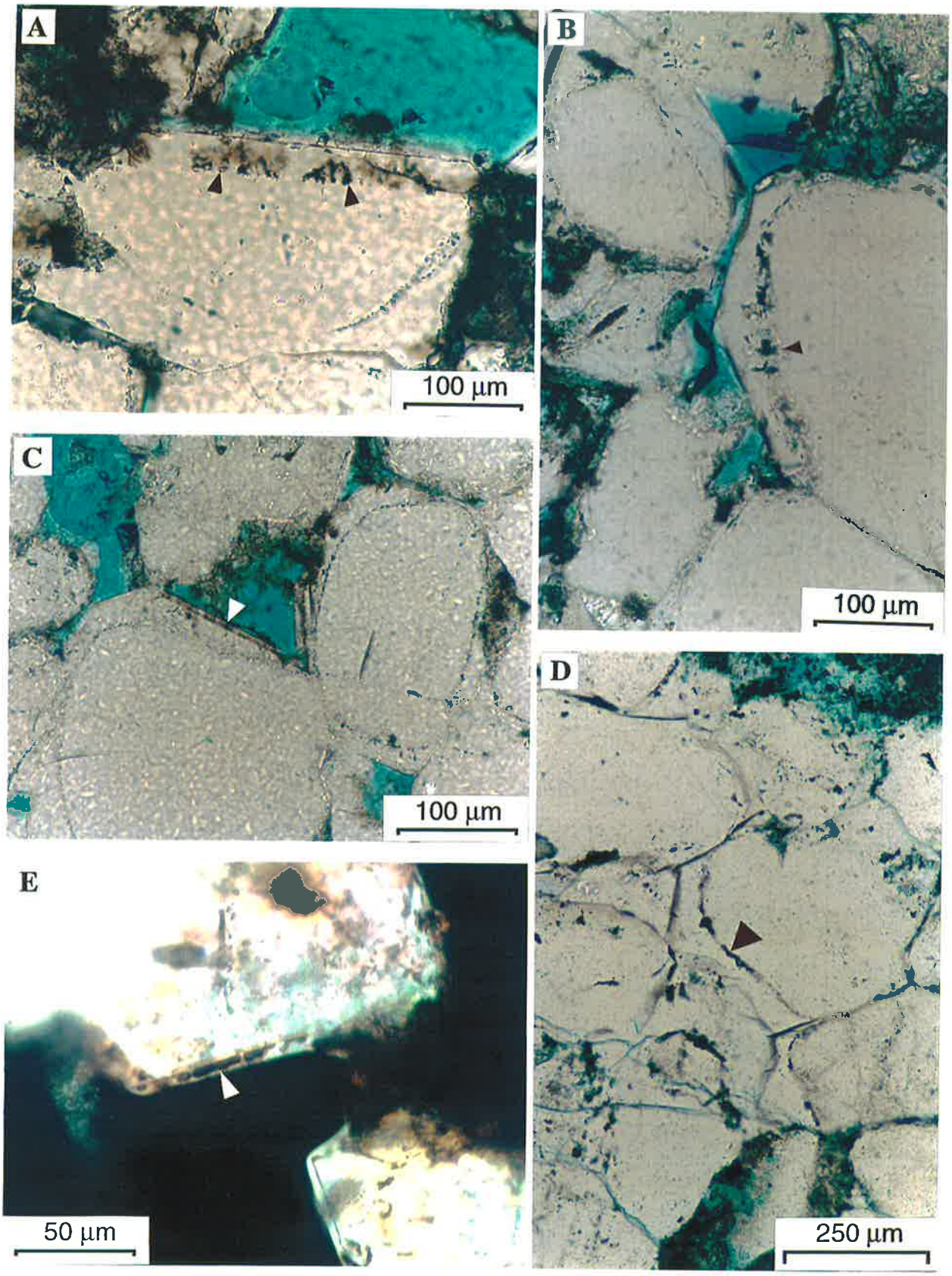
A
100 µm
B
100 µm
C
100 µm
D
250 µm
E
50 µm

as oil droplets snapped off in pore spaces (Plate 18). Quartz cementation after hydrocarbon emplacement is also reported by several workers in other basins (Walderhaug, 1990; Bjørlyyke and Egeberg, 1993; Walderhaug, 1994).

The occurrence of Permian-sourced oils in the Eromanga Basin (Alexander et al., 1988) suggests that maximum temperatures within the Permian section occurred sometime during or after Cretaceous deposition about 100 Ma.

4.6 CONCLUSIONS

The Tirrawarra Sandstone is a fine to coarse-grained, mostly lithic-sandstone in which the detrital composition is controlled by depositional environments. Mechanical compaction and quartz cementation are the prime diagenetic events responsible for porosity modification. The intensity of these diagenetic events is controlled by the composition of the sandstone. Mechanical compaction is more pronounced in lithic sandstones, whereas quartz cementation is widespread in quartz-rich sandstones. A quantitative approach to the estimation of sandstone composition controls on compaction and quartz cementation, makes it possible to predict reservoir quality during basin development.

Based on the integration of data derived from different techniques, a detailed sequence of diagenetic events was established for the Tirrawarra Sandstone in the studied area.

The combination of petrography, fluid-inclusion studies, electron microprobe and cathodoluminescence examinations in the Tirrawarra Sandstone gave an indication of the most likely silica sources for quartz cement. Three zones of quartz cement were recognised which were precipitated at different temperatures. The distribution of Al content is different in each zone:

- Z1 quartz cement formed at approximately 65°C and has a moderate aluminium content (237 ppm). The silica source for Z1 is considered to be early dissolution of feldspar grains.

Plate 18

Micrographs showing occurrence of Oil in Tirrawarra Sandstone

A - Close-up view of an oil droplet isolated in pore space. Note the euhedral face of the quartz overgrowths surrounding the oil droplet. Sample F2-9601.2, Fly Lake-2, 2880.4 m. Scale bar = 100 μm.

B - Two big oil droplets within intergranular porosity. In this example it can be seen that outer margins of the quartz overgrowths are lined with oil. This means that Tirrawarra Sandstone reservoir gradually become oil-wet. Note excellent connections (pore throats) between pore spaces. Sample F6-9398, Fly Lake-6, 2819 m. Scale bar = 250 μm.

C - In this example the bigger pore spaces are filled with oil. Although there is no distinct dust rim between the quartz grains and quartz overgrowths, recognition of quartz cement is easy due to the difference in inclusion content of quartz grains and quartz overgrowth. Sample F6-9398, Fly Lake-6, 2819 m. Scale bar = 250 μm.

D - In this micrograph it can be seen that the Tirrawarra Sandstone reservoir gradually has become oil wet. In this example most of the quartz grains are rimmed by oil (arrows). Note the presence of thick quartz cement growing along the c-axis of the detrital quartz grain in the centre of micrograph. Sample M9-9716, Moorari-9, 2915 m. Scale bar = 250 μm.

E - In most of the studied samples kaolinite appears clear and water wet suggesting the entrapment of capillary water in pore space of kaolinite. In this example the kaolinite (K) is stained with oil. Staining of kaolinite probably has happened during thin section preparation. F6-9398, Fly Lake-6, 2819 m. Scale bar = 250 μm.

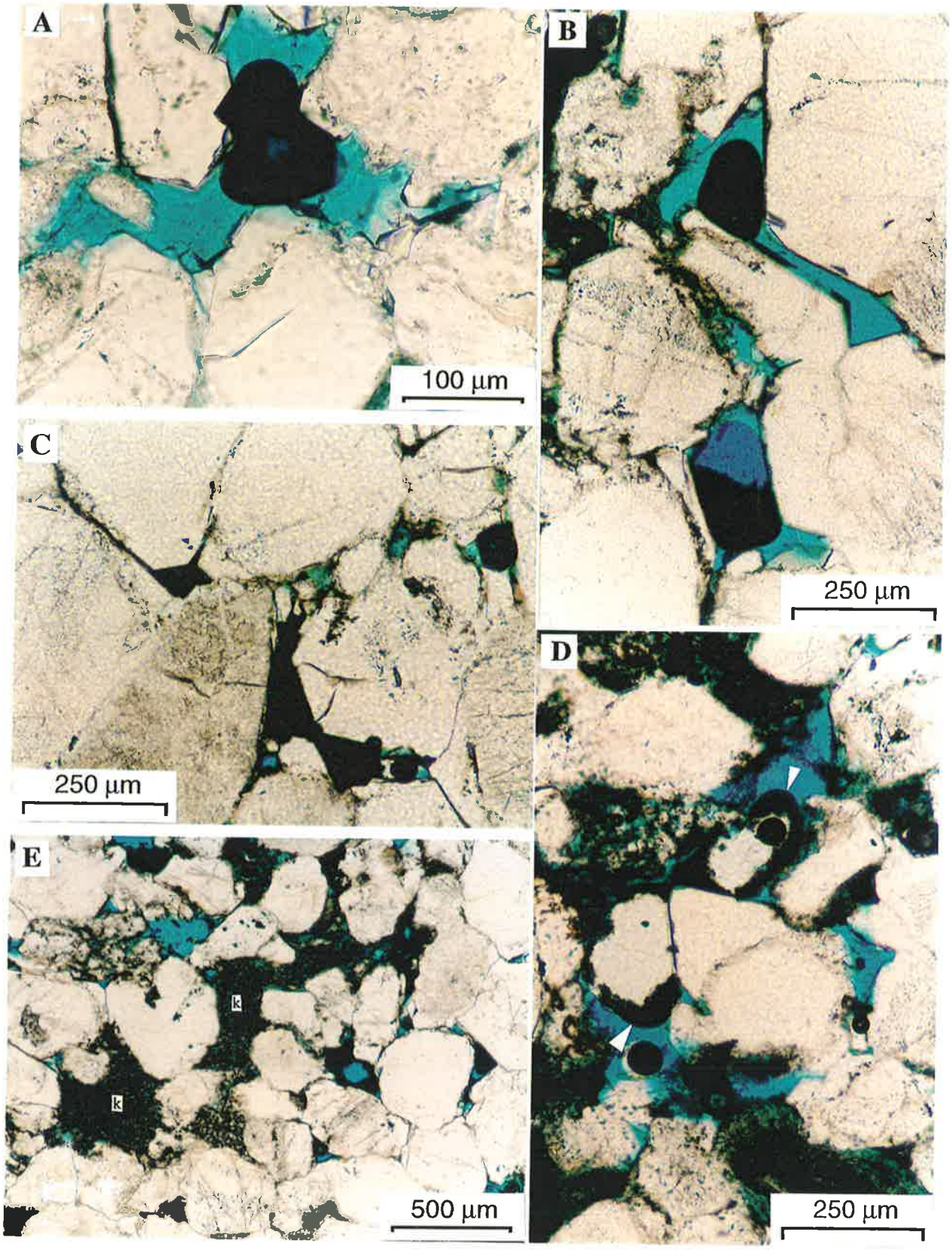
A
100 µm
B
250 µm
C
250 µm
D
250 µm
E
k
k
500 µm

- The silica source for Z2 quartz cement, which precipitated around 80°-100°C and has the highest concentration of aluminium (538 ppm), is considered to be feldspar dissolution by organic acids released during source rock maturation.

- Z3 quartz cement formed at about 130°C and has the lowest concentration of aluminium (58 ppm). The main source of silica for this cement is considered to be pressure solution.

The best reservoir lithologies are composed of sandstones containing mainly Z1 and Z2 quartz cements. They are typically well-sorted, quartz-rich sandstones that formed in aeolian and point bar environments and have relatively high porosity (14-17%). Reservoir lithologies which contain all zones of quartz cement have a high proportion of intergranular volume (IGV) but low porosity. Although these sandstones are clean, they are sandwiched between facies that are prone to stylolitisation and are able to provide silica for their Z3 cements. Parts of the reservoir which contain no quartz cement or only a small amount of Z3, have a very low IGV and no visual porosity, and it is these finer-grained sandstones that display extensive stylolitisation.

Three generations of siderite cement were recognised in the Tirrawarra Sandstone; an early (S1), a middle (S2) and a late generation (S3) which have dissolution boundaries between them, indicating dissolution phases after precipitation of the early and middle generations. S1 precipitated early, whereas S2 and S3 formed at approximately 68°C and 100°C respectively. The association of siderite with open porosity indicates that dissolution of siderite cement may have had a significant role in porosity increase.

Two types of clay minerals, kaolinite and illite, were recognised. The formation of kaolinite is more likely either from total replacement of feldspar grains or direct precipitation from pore-fluid during suitable conditions. Most of the kaolin patches appear water wet and they had a great influence on porosity modification. The pore-filling kaolinite converted macroporosity to microporosity associated with the kaolinite booklets. Illite is formed from the alteration of labile detrital grains and therefore most acts as structural clay mineral in Tirrawarra Sandstone and has no great influence on permeability reduction.

Entrapment of hydrocarbon in siderite and quartz cements indicates that migration of hydrocarbon occurred in the temperature range between 80°C and 102°C.

CHAPTER FIVE

Chemistry and Stable Isotopes of Siderite Cements,

"Application of Quantitative Back-Scattered Electron Image Analysis in Isotope Interpretation of Siderite Cement"

5.1 INTRODUCTION

Siderite can form in a wide variety of depositional and diagenetic environments, including in marine, brackish and freshwater settings (eg. Gould & Smith, 1979; Matsumoto & Iijima, 1981; Gautier, 1982; Curtis & Coleman, 1986; Carpenter et al., 1988; Bahrig, 1989; Mozley, 1989; Mozley & Carothers, 1992; Spiro et al., 1993; Morad et al., 1994; Baker et al., 1996; Middleton & Nelson, 1996; Morad et al., 1996). The mineral is most suitable for the study of pore-water evolution during sediment subsidence because siderite, unlike other carbonate minerals, probably does not undergo recrystallisation and isotope re-equilibration during burial diagenesis as the mineral has no unstable precursors or polymorphs (Curtis et al., 1975; Gautier, 1982; Pearson, 1985; Curtis & Coleman, 1986). Therefore, stable isotope data of siderite cements can provide a powerful tool for the interpretation of diagenetic events in geologic provinces. Rarely, however, is siderite the only carbonate mineral in sedimentary rocks. Mechanical and/or chemical methods must be employed to separate the siderite from other carbonate minerals in order to obtain an isotopically homogenous sample (cf. Al-Aasm et al., 1990). However, even rocks containing only one carbonate cement type can be characterised by widely-varying bulk isotope compositions in the same geologic province. The bulk-rock isotope compositional variations for rocks with only one carbonate type can be due to the presence of multiple carbonate cement generations which can not be chemically separated from each other for separate isotope analyses. In recent years, advancements in laser ablation and ion microprobe technology have led to improvements in spatially-resolved isotope analysis (eg. Dickson et al., 1990; Smalley et al., 1991; Riciputi & Paterson, 1994). These technologies, however, are not yet widely available in the scientific community, highlighting the need for alternative methods to determine the isotope signatures of single-phase, multi-generation carbonate cements.

The present investigation quantitatively examines the importance of varying amounts of different siderite cement generations on carbon and oxygen isotope signatures in the Tirrawarra Sandstone of the Moorari and Fly Lake Fields. The data are based on the integration of petrographic, electron microprobe and fluid inclusion techniques to derive a new procedure for isotope interpretation using back-scattered electron (BSE) image analysis. The data show that variations in isotope character of siderite cement that generally appears homogeneous under the optical microscope is a function of the relative proportion and composition of each generation of siderite cement that are best characterised using BSE imaging techniques in the study area (Rezaee & Schulz-Rojahn, 1996).

5.2 PREVIOUS INVESTIGATIONS

Various authigenic minerals have been identified in Cooper Basin sediments, including quartz, carbonates, kaolinite, dickite and illite, and locally clinochlore and pyrophyllite in the central Nappamerri Trough (Stanley & Halliday, 1984; Schulz-Rojahn & Phillips, 1989). Carbonate cement types include siderite, ankerite, dolomite, ferroan dolomite, and rarely calcite (Stuart et al., 1990; Schulz-Rojahn, 1991). Based on a regional database, Schulz-Rojahn (1991) noted that siderite is volumetrically about 17 times more abundant than all other carbonate varieties together in the Cooper Basin sediments and a major cause of porosity reduction, including in the Tirrawarra Sandstone. Martin (1981) studied the Tirrawarra Sandstone in six wells of the Tirrawarra Field and interpreted the siderite cement to be an early diagenetic event. Martin (1984) investigated 40 Tirrawarra Sandstone samples in the Tirrawarra, Moorari and Fly Lake Fields and concluded that the siderite predates quartz cementation in the reservoir. Bever et al. (1987, 1988) investigated the Tirrawarra Sandstone in the Tirrawarra and Moorari Fields and also concluded that the siderite is an early cement that possibly provided early structural support against grain compaction.

5.3 Image Analysis Technique for Siderite Cement Quantification

Different generations of siderite cement were identified and characterised using a *Philips* image analysis system in conjunction with the SEM. The back-scattered electron (BSE) images of carbon-coated polished thin sections were imported from the SEM in the form of grey-scale binary images (0-256 scale) using a video camera and a Windows-based software programme called Image Analysis™.

Generally, each main generation of siderite cement was characterised by a distinct range of grey-scale values in any one sample, reflecting varying elemental compositions of the carbonate cement. Quantitative estimation of these different siderite cement generations was accomplished by assigning a unique colour code to the range of grey-scale values representative of each cement generation in each sample. For all samples, the same analytical procedure was followed:

(1) acquisition of the BSE image of siderite cement. Mg-poor (early formed) siderite cement was found to be relatively light-coloured, whilst more Mg-rich siderite is darker in colour.

(2) adjustment of contrast and brightness of the grey-scale image to enhance visual differentiation of the various cement generations for each field of view.

(3) production of an on-screen histogram showing frequency distribution of the range of grey-scale values represented in each BSE image, and selection of grey-scale threshold values representative of each major cement generation for the purpose of colour-coding (eg. red (S1) = 0-80; green (S2) = 81-160; yellow (S3) = 161-256).

(4) computerised colour conversion of the grey-scale BSE image using the manually-defined pixel threshold values (Plate 19). In the Tirrawarra Sandstone, each major generation of siderite cement was generally characterised by a unique colour, reflecting different chemical compositions.

(5) automatic determination of the relative abundance of each user-defined colour zone, representing a different cement generation in this study. Machine readings were verified by random visual inspection of some micrographs using a grid overlay, and in all cases the machine results were found to be almost identical to the ones obtained by the human operator. In order to have a statistically-meaningful set of results, between 20 and 30 fields of view were analysed for each sample (magnification x100). On average, about 2 minutes were needed to analyse each field of view.

Potential shortcomings of the image analysis technique relate to the fact that BSE images only provide a two-dimensional representation of the rock volume which may lead to errors in the statistical analysis of cement (colour) abundances. In rare cases, due to compositional similarities between different generations of siderite cement and the resultant low grey-scale contrast, estimation of the relative abundance of the cement generations could not be carried out (Plate 19G & 19H). Only samples for which the relative abundance of each generation of siderite cement could be ascertained were integrated with the oxygen and carbon isotope data in this investigation. The image analysis technique cannot be applied in regions where different siderite cement generations have the same chemical composition, or overlapping compositions.

5.4 Results

5.4.1 Back Scattered (BSE) Image Characteristics

In BSE images, S1 is light-coloured and appears homogenous (Plate 19A & 19G), whereas S2 displays a distinct irregular compositional zoning (Plate 19A & 19E), indicating pore fluid chemistry fluctuations occurred during cementation. Based on grey-scale characteristics, S2 was divided into three main zones, namely dark, moderate, and light zones. BSE images show that S3 commences with even compositional banding and grades into a thick, homogenous phase in the terms of composition. S3 is characterised by an initial high Mg content (pistomsite) grading into a relatively thick, homogenous sideroplesite cement (Plate 19G) (classification of Deer et al., 1992). The proportion of each siderite cement phase quantified by BSE imagery enhancement technique (Plate 19), varies from sample to sample (Table 5.3).

5.4.2 Electron Microprobe Analysis Results

Electron microprobe analyses of S1 show a high Fe/Mg ratio (Fig. 5.1) (Appendix 4). The S1 elemental composition ranges from $(Fe_{97.7\%}Mg_{0.8\%}Ca_{0.7\%}Mn_{0.8\%})CO_3$ to $(Fe_{93.4\%}Mg_{2\%}Ca_{3.3\%}Mn_{1.3\%})CO_3$ with the average composition being $(Fe_{96\%}Mg_{1\%}Ca_{1.7\%}Mn_{1.3\%})CO_3$. The elemental composition of S1 is similar to that described by Mozley (1989) and Mozley & Carothers (1992) as early siderite cement.

Plate 19

Micrographs of BSE Image Analysis of Siderite Cement

A - BSE image illustrating the cement stratigraphy. White homogeneous S1, characterised by an irregular outer edge, is engulfed by S2 displaying uneven compositional zoning which in turn is surrounded by S3. Note that S1 and S3 cannot easily be differentiated on the basis of their grey-scale characteristics. Sample M9-9732, Moorari-9, 2966.3 m. Scale bar = 20 μm.

B - BSE image of the same view shown in (**A**), colour-enhanced. The method helps to differentiate the main generations of siderite cement. Although the settings need to be adjusted from sample to sample, each main generation of siderite cement tends to be characterised by a unique range of colours which facilitates volumetric estimation of the relative proportions of S1, S2 and S3 in each sample. In this sample, S1 is magenta in colour and thus can easily be differentiated from S3 (yellow) and S2 (dark-blue to green). Some compositional variation is evident in S1, the dissolution boundary between S1 and S2 is more enhanced, and the boundary between S2 and S3 can clearly be seen to be very sharp and of irregular nature. Note the homogeneous texture of S3.

C - BSE image showing S2 which has a variably dark-grey colour and fringes the edges of a pore that was subsequently filled by a very homogeneous, light-grey S3 cement. S2 is of a pseudo-rhombic nature and locally contains white specks that may represent remnants of S1 cement. Sample M2-10116, Moorari-2, 3083.4 m. Scale bar = 50 μm.

D - The same view as shown in (**C**), colour-enhanced. The micrograph illustrates problems with the image analysis technique in some samples. Whilst S2 (green) and S3 (dark-blue) can clearly be differentiated in most areas of the view shown, S2 locally displays a mixture of both colours, rendering volumetric estimates of the different cement generations difficult in this sample. The problem is the exception rather than the rule in the Tirrawarra Sandstones.

E - BSE image of middle generation of siderite cement (S2) showing compositional zoning and several minor dissolution events. Sample M9-9732, Moorari-9, 2966.3 m. Scale bar = 50 μm.

F - The same view as shown in (**E**), colour-enhanced. With this method it is also possible to quantify the relative proportion of the different zones of each generation of siderite cement.

G - In this BSE image, an initially banded then homogeneous S3 cement is the main pore-filling event, however examination of other micrographs shows that the relative proportion of the different siderite cement generations can vary within the same sample. Again notice the dissolution boundary between S2 and S3 (arrow), the dissolution pits associated with S2, and the isolated remnants of S1 (white) within the S2 matrix. Further observe the incipient euhedral rhombic terminations of the S3 cement that grew on the S2 dissolution surface. Sample M1-9598, Moorari-1, 2925.5 m. Scale bar = 50 μm.

H - The same view as shown in (**G**), colour-enhanced. In the cases where grey value of different generations of siderite cement is the same, image colour will be the same. In this example some part of S3 show a same blue colour of S2.

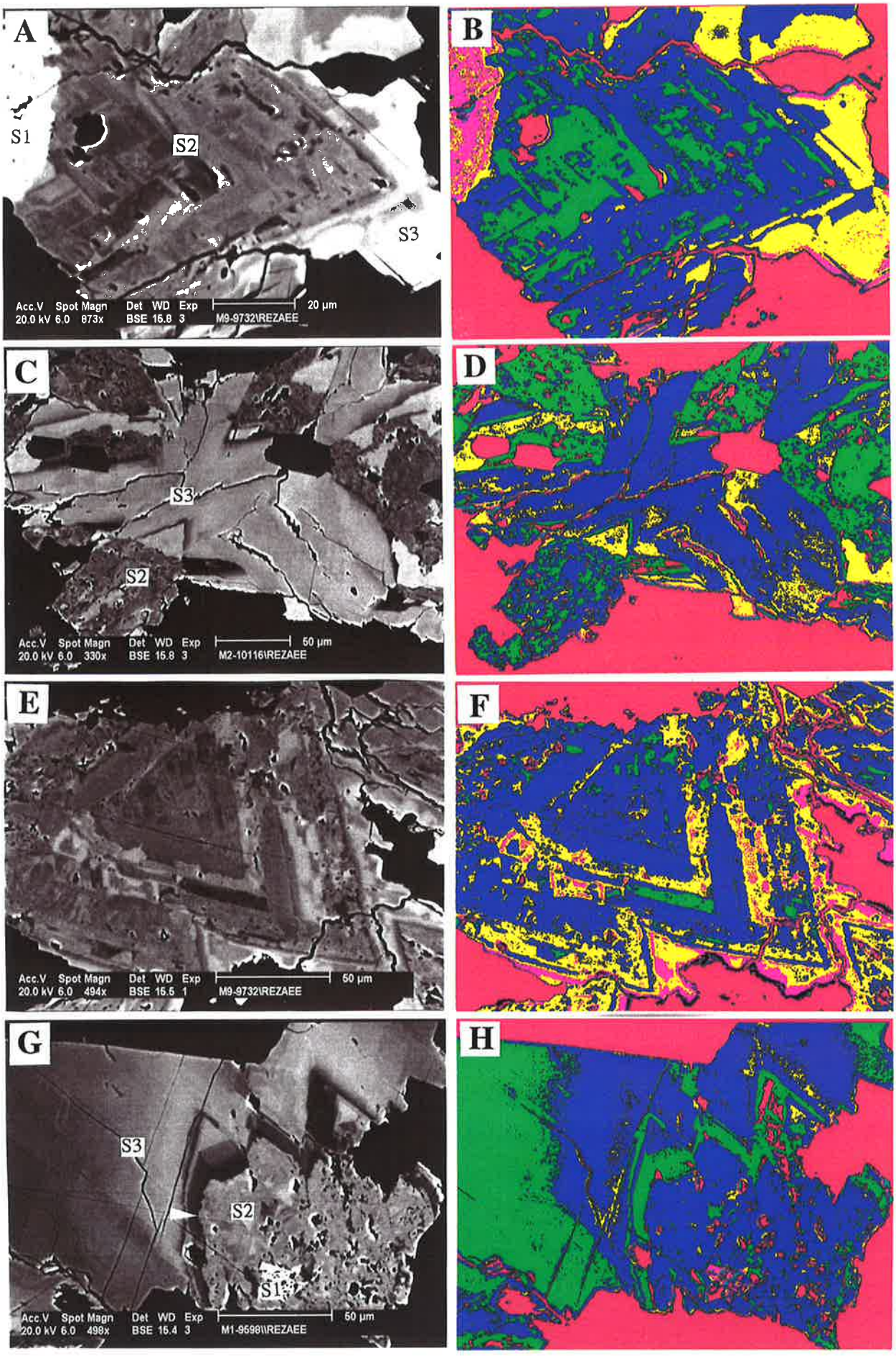
A
S1
S2
S3
Acc.V Spot Magn Det WD Exp
20.0 kV 6.0 873x BSE 15.8 3
20 µm
M9-9732\REZAEE
B
C
S3
S2
Acc.V Spot Magn Det WD Exp
20.0 kV 6.0 330x BSE 15.8 3
50 µm
M2-10116\REZAEE
D
E
Acc.V Spot Magn Det WD Exp
20.0 kV 6.0 494x BSE 15.5 1
50 µm
M9-9732\REZAEE
F
G
S3
S2
S1
Acc.V Spot Magn Det WD Exp
20.0 kV 6.0 498x BSE 15.4 3
50 µm
M1-9698\\REZAEE
H

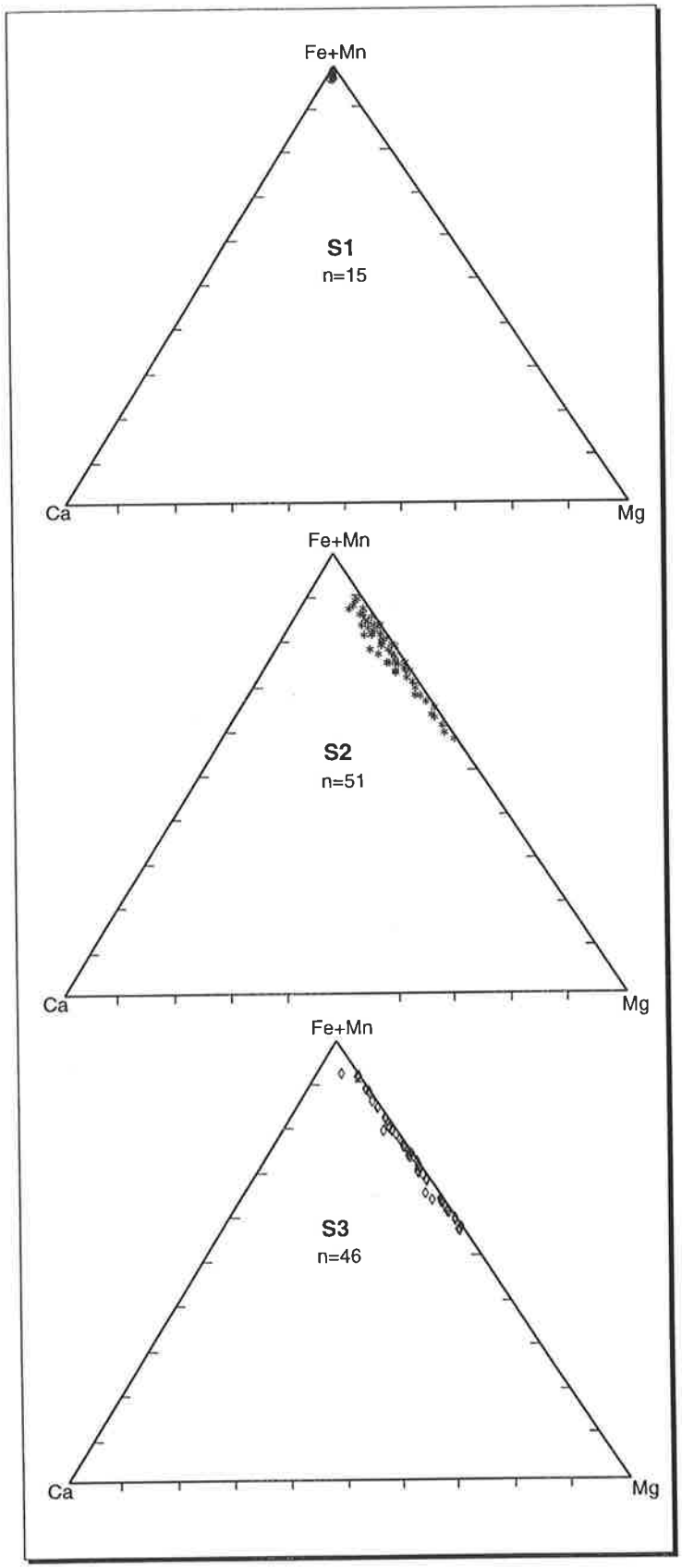

Figure 5.1 - Ternary diagrams showing electron microprobe analysis results for different generations of siderite cement in the Tirrawarra Sandstone. The early generation of the siderite cement (S1) is very rich in Fe, whereas the middle (S2) and late generations (S3) have much higher substitution of Mg and fall within the realm of sideroplesite and pistomsite. S2 and S3 have almost identical compositions except that S2 has a slightly higher Ca content.

Electron microprobe analyses reveal different elemental compositions and variable substitution of Mg for each of the S2 sub-stages (Table 5.1 & 5.2) (Appendix 4). S2 compositions range from $(Fe_{87.2\%}Mg_{9.5\%}Ca_{0.7\%}Mn_{2.6\%})CO_3$ to $(Fe_{56.7\%}Mg_{42.2\%}Ca_{0.15\%}Mn_{0.95\%})CO_3$, with the average composition being $(Fe_{74\%}Mg_{24\%}Ca_{0.8\%}Mn_{1.2\%})CO_3$ (Table 5.2) indicative of sideroplesite for the light zone and pistomsite for the moderate to dark zone (classification of Deer et al., 1992). Electron microprobe analyses indicate extensive substitution of Mg, with an average composition of $(Fe_{75.5\%}Mg_{23\%}Ca_{0.5\%}Mn_{1\%})CO_3$ for S3 (Table 5.2) (Appendix 4).

5.4.3 Oxygen and Carbon Stable Isotopes Results

Oxygen and carbon isotope analyses were carried out on 18 core samples following selection of the samples using optical and bulk XRD methods (Appendix 6). Only samples containing major amounts of siderite that lacked other carbonate cement types were selected for stable isotope analysis. In samples which contain the highest proportion of S1 (92-98%), oxygen isotope compositions range from +14.1‰ to +15.1‰, with $\delta^{13}C$ compositions varying between -3.8 and +1.45‰. The one sample in which S1 constitutes 100% of the siderite cement volume (sample F4-9441), has a $\delta^{18}O$ value of +13.97‰ and a $\delta^{13}C$ of +1.46‰ (Table 5.3). In samples in which S2 is the dominant carbonate cement phase (93-98%), oxygen isotope values range from +12.3‰ to +12.8‰ and carbon isotope values between -9.2‰ and -7.9‰. The mean $\delta^{13}C$ composition is about -8.6‰, and the average $\delta^{18}O$ composition is +12‰ for S2 (Table 5.3). In samples which contain the highest proportion of S3 (95-97%), oxygen isotope compositions range from +6.1‰ to +6.6‰, with $\delta^{13}C$ compositions varying between -11.1‰ and -10.4‰. For these samples, mean oxygen and carbon isotope values are about +6‰ and -11‰ respectively (Table 5.4).

Table 5.1 - Microprobe results (mole%) for the different siderite cement generations which can further be subdivided on the basis of colour variations under the back-scattered electron microscope. (l = light-coloured; m = moderately light-coloured; d = dark-coloured in BSE image.

Well Name	Sample No.	FeO (%)	MgO(%)	CaO(%)	MnO(%)	Colour Code
Flv Lake 1	F1-9431	60.59	37.09	1.51	0.80	S2d
	F1-9431	67.73	30.85	0.36	1.06	S2m
	F1-9431	80.24	19.03	0.07	0.66	S3l
	F1-9431	71.89	27.41	0.04	0.66	S3m
	F1-9431	68.39	29.65	1.22	0.74	S3d
	F1-9431	77.79	21.32	0.15	0.74	S3m
Flv Lake 2	F2-9570	77.17	21.55	0.51	0.77	S3l
	F2-9583	96.90	0.24	1.16	1.69	S1l
	F2-9583	75.88	22.92	0.20	1.00	S2m
Moorari 1	M1-9613	63.72	34.45	1.03	0.80	S2d
	M1-9613	85.27	11.09	2.00	1.64	S2l
	M1-9613	78.27	19.98	1.05	0.70	S2m
	M1-9620	94.81	1.09	2.50	1.61	S1l
	M1-9620	79.65	19.14	0.34	0.87	S2m
Moorari 2	M2-10116	70.66	27.92	0.46	0.96	S2d
	M2-10116	65.88	32.78	0.26	1.08	S2m
	M2-10116	63.48	34.82	0.48	1.22	S3d
	M2-10116	81.82	16.83	0.35	1.00	S3l
	M2-10116	68.49	29.78	0.56	1.17	S3m
	M2-10145	70.56	28.71	0.12	0.61	S2d
	M2-10145	77.15	20.18	0.96	1.71	S2l
	M2-10145	69.92	28.96	0.31	0.80	S2m
	M2-10145	84.97	9.07	1.57	4.39	S3l
	M2-10145	82.78	15.48	0.73	1.01	S3m
Moorari 3	M3-9422	93.89	2.02	2.83	1.26	S1l
	M3-9422	81.23	14.44	3.58	0.74	S2m
	M3-9440	81.44	17.38	0.25	0.93	S2m
	M3-9440	78.45	20.40	0.23	0.92	S3d
	M3-9440	77.13	21.51	0.41	0.95	S3m
	M3-9503	61.62	37.43	0.27	0.68	S2d
	M3-9503	83.29	13.08	1.32	2.32	S2l
	M3-9503	76.10	22.37	0.40	1.13	S2m
Moorari 4	M4-9574	63.60	35.21	0.08	1.11	S2d
	M4-9574	87.21	10.78	0.14	1.87	S2l
	M4-9574	74.39	23.78	0.49	1.34	S2m
	M4-9574	80.82	17.41	0.42	1.35	S3l
	M4-9574	77.12	20.96	0.31	1.62	S3m
Moorari 5	M5-9553	63.83	34.54	0.26	1.38	S2d
	M5-9553	82.49	14.93	0.37	2.21	S2l
	M5-9553	65.52	32.77	0.21	1.50	S2m
	M5-9553	58.97	39.72	0.14	1.18	3D
	M5-9553	72.84	25.87	0.25	1.04	S3m
	M5-9553	69.46	29.34	0.22	0.98	S3d
Moorari 6	M6-9737	89.03	9.39	0.16	1.42	S3l
	M6-9737	75.07	23.55	0.29	1.08	S3d
	M6-9737	86.32	12.32	0.12	1.23	S3m
Moorari 7	M7-9606	58.36	39.97	0.29	1.38	S2d
	M7-9606	79.67	18.27	1.16	0.89	S2m
Moorari 9	M9-9732	97.05	0.85	0.93	1.18	S1l
	M9-9732	68.05	30.30	1.06	0.59	S2d
	M9-9732	82.82	15.99	0.21	0.98	S2l
	M9-9732	75.20	23.08	0.89	0.83	S2m
	M9-9732	91.11	7.85	0.04	1.00	S3l

Table 5.2 - Average elemental composition (mole%) of different zones within the main siderite cement generations (S1, S2, S3). Subdivisions of the main siderite cement generations are based on colour differences under the BSE microscope. (l = light-coloured; m = moderately light-coloured; d = dark-coloured in BSE image.

	S1l	S2l	S2m	S2d	S3l	S3m	S3d
FeO (%)	95.7	83.0	74.7	64.6	83.6	76.8	69.0
MgO (%)	1.0	14.3	23.6	34.0	14.4	21.8	29.6
CaO (%)	1.9	0.8	0.7	0.6	0.4	0.3	0.4
MnO (%)	1.4	1.8	1.0	0.9	1.5	1.1	1.0

Table 5.3 - Carbon and oxygen isotope data of the Tirrawarra Sandstone siderite cements. A good match is observed between measured ($\delta^{18}O_{meas}$) and calculated oxygen isotope values ($\delta^{18}O_{calc}$) determined from image analysis results. The isotope data reflect the varying proportions of the different generations of siderite cement. (S1 = early siderite cement; S2 = middle generation siderite cement; S3 = late generation siderite cement; BD = distal braid-delta; BM = medial braid-delta; BS = beach barrier sandstone; MBB = back-barrier marsh).

Well Name	Sample	$\delta^{13}C$ (PDB‰)	$\delta^{18}O_{meas}$ (PDB‰)	$\delta^{18}O_{meas}$ (SMOW‰)	S1(%)	S2(%)	S3(%)	$\delta^{18}O_{calc}$ (SMOW‰)	Facies
Moorari 5	M5-9583	-10.37	-23.38	6.6	0	3	97	6.28	BD
Moorari 2	M2-10145	-11.13	-23.83	6.15	0	5	95	6.41	BD
Moorari 4	M4-9574	-10.68	-21.39	8.59	0	40	60	8.58	BS
Moorari 7	M7-9606	-10.49	-22.70	7.28	15	30	55	9.33	BM
Moorari 2	M2-10116	-8.13	-19.12	10.86	10	43	47	9.68	BS
Fly Lake 1	F1-9417	-3.83	-15.80	14.18	19	38	43	10.19	BD
Moorari 6	M6-9737	-9.70	-18.79	11.19	8	51	41	9.99	BS
Fly Lake 1	F1-9431	-4.22	-18.50	11.48	0	60	40	9.82	BD
Moorari 1	M1-9598	-7.07	-17.56	12.42	36	38	26	11.73	BD
Moorari 3	M3-9440	-5.98	-15.37	14.61	80	13	7	14.19	BS
Fly Lake 2	F2-9583	1.45	-15.84	14.14	92	3	5	14.66	MBB
Moorari 3	M3-9503	-7.97	-17.67	12.31	0	98	2	12.18	BD
Moorari 1	M1-9613	-9.22	-18.23	11.75	3	95	2	12.26	BD
Moorari 4	M4-9554	-8.95	-17.17	12.81	5	93	2	12.32	BS
Moorari 9	M9-9732	-4.99	-15.71	14.27	60	39	1	13.98	BM
Moorari 3	M3-9422	-3.87	-14.85	15.13	98	1	1	15.08	BM
Moorari 1	M1-9620	-6.23	-16.70	13.28	15	85	0	12.74	BD
Fly Lake 4	F4-9441	1.46	-16.01	13.97	100	0	0	15.20	MBB

5.4.4 Bulk $\delta^{18}O$ and $\delta^{13}C$ Trends

A broad correlation exists between $\delta^{18}O$ and $\delta^{13}C$ values for the different samples containing multiple siderite cement generations (Fig. 5.2). With increasing enrichment in $\delta^{18}O$, $\delta^{13}C$ values become less negative. Isotope results of the samples dominated by a single siderite cement generation plot within narrow zones whilst the ones derived from samples with varying proportions of the different cement generations plot between these zones in a broad scatter (Fig. 5.2). Samples deposited under marsh environments are characterised by relatively high $\delta^{13}C$ and $\delta^{18}O$ values, reflecting the dominance of S1 in these sediments. In contrast, siderites that formed in rocks deposited under different sedimentary conditions have generally more ^{13}C- and ^{18}O-depleted isotope signatures due to the greater proportion of S2 and S3 in these samples (Table 5.3).

Table 5.4 - Summary table showing the average isotope, chemical composition and fluid inclusion characteristics of the main siderite cement generations (S1, S2, S3). Th = fluid inclusion homogenisation temperature.

	S1	S2	S3
$\delta^{18}O$ (‰ SMOW)	15	12	6
$\delta^{13}C$ (‰ PDB)	1.45	-8.5	-11
$\delta^{18}O_{H2O}$ (‰ SMOW)	-15.5	-10	-13
T (°C)	30	43	80
Th (°C)	-	68	102
FeO(%)	96	74	75.5
MgO(%)	1.0	24	23
CaO(%)	1.7	0.8	0.5
MnO(%)	1.3	1.2	1.0

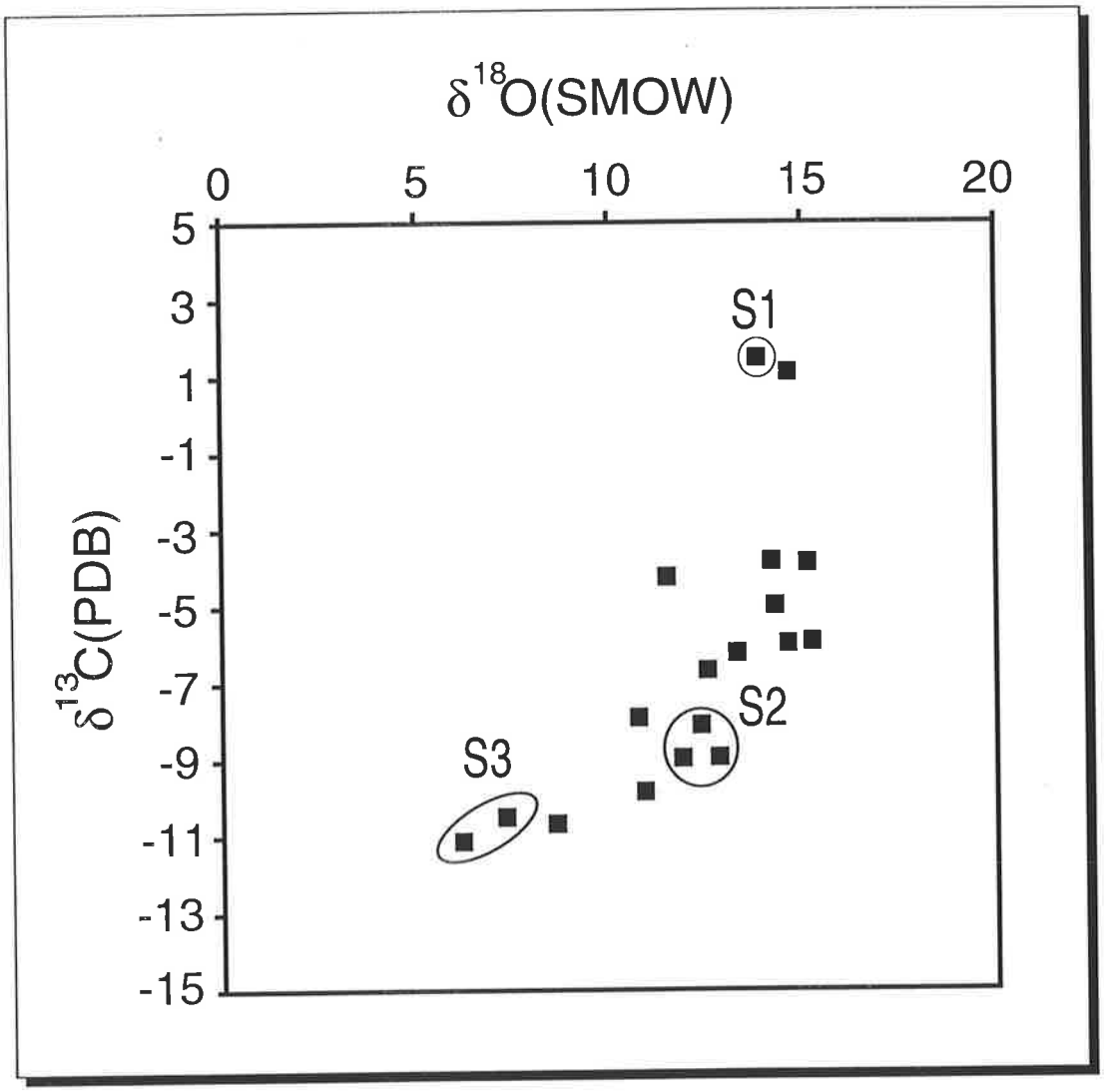

Figure 5.2 - Crossplot of carbon and oxygen isotope values for the Tirrawarra Sandstone siderites. The bulk-rock isotope signatures are the cumulative product of the varying proportions of the different siderite cement generations (S1, S2, S3). The pure end-member compositions of the different siderite cement generations can be estimated from samples which are dominated by a single cement generation (circled areas). Only the end-member isotope compositions of the different cement generations should be taken into consideration when evaluating multi-generation siderite cements.

5.5 DISCUSSION

Integration of bulk-rock isotope data with electron microprobe and image analysis results has led to the identification of a multi-generation, pore-filling siderite cement in the Tirrawarra Sandstone of the Moorari and Fly Lake Fields. Although previous workers had identified several siderite cement morphologies, they had assumed the pore-filling sparry siderite to be a single-generation precipitate in Cooper Basin sediments (Martin & Hamilton, 1981; Schulz-Rojahn & Phillips, 1989).

Results from the present investigation show that the pore-filling siderite precipitated in three main generations in the Moorari-Fly Lake area. An early, homogeneous Fe-rich siderite (S1) was followed by a generally more extensive cement generation characterised by complex compositional zoning (S2), which was in turn engulfed by a late-generation, evenly-banded then relatively homogeneous siderite cement (S3). The relative proportion of each cement generation varies between samples, and in some rocks one or two of these siderite cement generations are absent (Table 5.3). The identification of multiple siderite cement generations is of importance for the interpretation of bulk-rock oxygen and carbon isotope results in the Cooper Basin and probably in other geologic provinces.

In the Tirrawarra Sandstone, each generation of siderite cement has a distinct isotope signature as revealed by samples which are dominated by a single cement generation (≥95%). Only a small proportion of the samples fall into this category (Table 5.3). The majority of the isotope results are the cumulative product of the varying proportions of the different siderite cement generations. Failure to recognise this fact may lead to erroneous interpretations of the isotope data.

For example, the broad trend of overall more negative $\delta^{13}C$ values with increasing depletion in ^{18}O (Fig. 5.2) could be interpreted as a continuous (gradual) evolution in carbonate isotope composition during burial diagenesis. The trend is commonly observed in carbonate cements in a variety of clastic provinces (Fritz et al., 1971; Irwin et al., 1977; Irwin, 1980; Schulz-Rojahn, 1991; Mozley & Carothers, 1992; Spötl et al., 1993). However, results from the present investigation show that the pattern can also be produced by sample heterogeneity. The data demonstrate that major changes in pore-fluid isotope composition occurred between the precipitation of each major cement generation in the Tirrawarra Sandstone (Fig. 5.2). The conclusion is supported

by the presence of a dissolution boundary between each major cement generation (Plates 10A, 10B, 19A, 19C & 19G).

Further, non-recognition of the isotopically-heterogeneous nature of most Tirrawarra Sandstone samples could lead to erroneous perceptions of the major source(s) of carbon for siderite precipitation. In the study area, a high proportion of $\delta^{13}C$ values for the siderites fall within the range of about -3 and -8‰ (Fig. 5.2). Without a knowledge of the influence of differential cement development on bulk-rock isotope signatures, the values could be mainly attributed to mixing of carbon derived from marine limestones (+2 to -2‰; Hudson, 1977) and volcanic or geothermal sources (on average between -5 and -7‰; Deines, 1986). However, since the isotope values within the range of -3 and -8‰ are derived from samples which contain multiple siderite cement generations in varying proportions (Table 5.3), these hybrid data provide no useful clues to the conditions under which the different siderite cement generations formed.

The approach differs from other investigations of diagenesis in which no discrimination of the bulk-rock isotope data is applied and where all bulk-rock isotope values are used to derive a model of carbonate cementation. Difficulties in estimating the volume of individual cement generations generally prohibits a greater qualitative control on isotope interpretations. However, the present study shows that BSE image analysis can provide an efficient means of quantifying the influence of multi-generation cement development on bulk-rock isotope signatures, if it is assumed that BSE-derived cement generations are isotopically homogeneous.

5.5.1 Method for Enhanced Isotope Interpretation

In the study area, the influence of variable cement proportions on $\delta^{18}O$ can be determined by plotting the relative abundances of S1, S2 and S3 for each sample on a ternary diagram (Fig. 5.3a). The samples with the highest proportion of a single cement generation give the closest approximation to end-member $\delta^{18}O$ values, and provide the basis for the labelling of each corner of the diagram. IsoSMOW lines can then be drawn which enable the prediction of $\delta^{18}O$ values for the remainder of the samples (Fig. 5.3b). In cases where there is no end-member representative, the IsoSMOW lines established from existing values can be extrapolated to the end member locations at the corners of

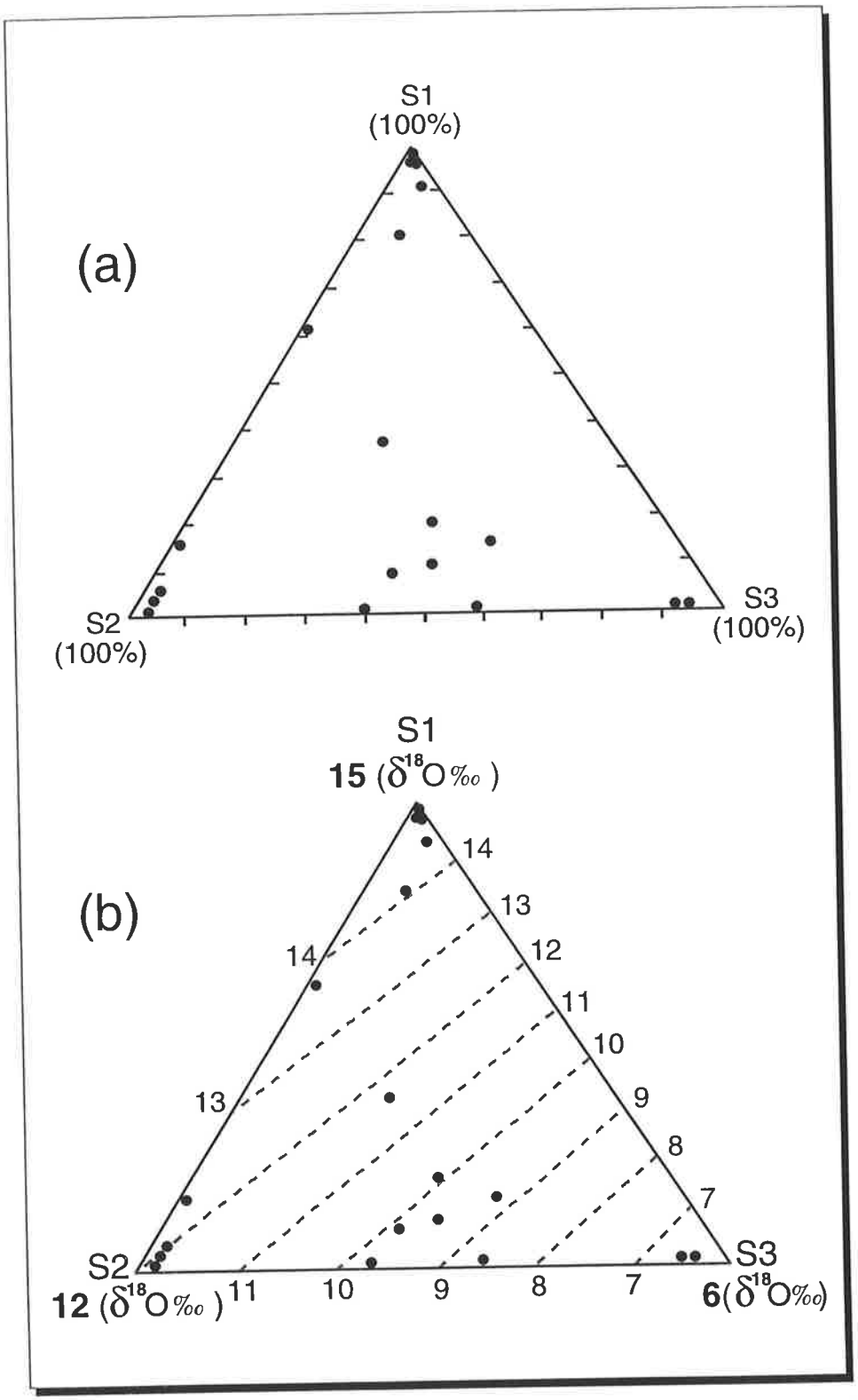

Figure 5.3a & b - (a) Ternary diagram showing the relative abundance (%) of the different siderite cement generations in the Tirrawarra Sandstone, as determined from statistical evaluation of electron microprobe and image analysis results. (b) The samples with the highest proportion of a single cement generation give the closest approximation to end-member δ18O values (+15‰, +12‰ and +6‰ were assumed for 100% pure S1, S2 and S3 respectively, based on the data shown in Table 5.3). IsoSMOW lines can then be constructed for the remainder of the samples. The application of the method is the calculation of isotope compositions for individual siderite cement generations in samples which contain more than one siderite cement generation.

the ternary diagram in order to estimate end-member $\delta^{18}O$ values. The relationship can be expressed by the equation:

$$\delta^{18}O_{(bulk)} = (V_{S1}*\delta^{18}O_{S1})+(V_{S2}*\delta^{18}O_{S2})+(V_{S3}*\delta^{18}O_{S3})$$

where $\delta^{18}O_{(bulk)}$ = oxygen isotope result of the bulk-rock analysis; V_{S1}= proportion of S1; V_{S2}= proportion of S2; V_{S3}= proportion of S3; $\delta^{18}O_{S1}$= oxygen isotope value of S1; $\delta^{18}O_{S2}$= oxygen isotope value of S2; and $\delta^{18}O_{S3}$= oxygen isotope value of S3.

Table 5.3 shows that the measured and calculated bulk-rock $\delta^{18}0$ values generally exhibit a good correlation (r^2=0.82). Minor discrepancies between the two data sets are probably due to small errors in the estimation of the volume of individual cement generations in some samples. The bulk-rock $\delta^{13}C$ composition of each sample is also controlled by the relative proportion of each generation of siderite cement, and the same mathematical formula as shown above (substituting $\delta^{13}C$ for $\delta^{18}O$) can be applied. However, the correlation coefficient for calculated $\delta^{13}C$ values (r^2= 0.64) is lower than the one for calculated $\delta^{18}O$ compositions. I am uncertain about the reason(s) for this phenomenon but believe it may be due to the fact that $\delta^{18}O$ in a cement, at any given pore-water-isotope composition, is a strongly temperature-dependent variable whereas $\delta^{13}C$ is independent of temperature.

Both $\delta^{18}O$ and $\delta^{13}C$ values for each end-member cement plot within narrow zones (Fig. 5.2), enabling a precise definition of the conditions under which the individual cement generations formed, albeit based on a small data set. The data show that the quantitative approach to isotope analysis provides added precision to routine bulk-rock isotope interpretation methods in the study area. The technique used in this study may be applicable to other geologic provinces, provided different cement generations do not have the same chemical composition. The image analysis technique is particularly valuable for rocks in which pure or nearly pure samples of carbonate cement end members do not exist.

5.5.2 Precipitation temperatures of siderite cement

The fluid inclusion data indicate that S2 precipitated at a mean water temperature of about 68°C whilst S3 formed at about 102°C (Fig. 4.12) (Appendix 7). The crystallisation temperatures of S1 cannot be determined since no fluid inclusion data are available.

During the Early Permian, the palaeolatitude of central Australia was about 70-75° South (McElhinny, 1969; Embleton & McElhinny, 1982; Veevers, 1984). The $\delta^{18}O$ of recent meteoric water is between -15 and -16‰ at this latitude (Dansgaard, 1964). Accordingly, if we assume a $\delta^{18}O$ value of -15.5‰ for Early Permian pore water, then S1 must have precipitated at a temperature of about 30°C using the isotope fractionation equation of Carothers et al. (1988). This temperature of precipitation for S1 does indeed correspond to relatively early diagenesis.

5.5.3 Interpretation of Carbon Isotope Results

In the Tirrawarra Sandstone, carbon isotope values show that major changes in conditions occurred between the precipitation of S1 and the later siderite cement generations, S2 and S3. Whilst S1 has a $\delta^{13}C$ composition of about +1.45‰, S2 and S3 are much more depleted in ^{12}C (Fig. 5.2).

The $\delta^{13}C$ character of S1 is consistent with a major source of carbon involving methanogenesis (Curtis & Coleman, 1986). During this process, strongly ^{13}C-depleted methane and ^{13}C-enriched carbon dioxide is produced by microbial activity (Rosenfeld & Silverman, 1959; Hudson, 1977). Acetate fermentation is the most likely cause of methanogenesis in fresh water environments (Whiticar et al., 1986). In modern marsh sequences, highly ^{13}C-enriched values are produced by methanogenic processes during early diagenesis (Moore et al., 1992). The carbonate cements produced from bacterial fermentation reactions start to precipitate at some depth below the sediment/water interface (≤ 10m) from pore waters supersaturated with ^{13}C-rich bicarbonate (≤ +15‰), with the $\delta^{13}C$ composition of the pore water becoming progressively poorer in ^{13}C with increasing burial depth (≥ 1000 m) (Irwin et al., 1977). In the present study, the concentration of S1 in marsh sediments, coupled with the petrographic evidence and the

fact that the elemental composition of S1 is similar to that described by Mozley (1989) for early, fresh-water siderite cement in different geologic provinces, suggests that this cement generation formed in the relatively shallow diagenetic realm. However, S1 probably precipitated below the initial zone of pore water supersaturated with ^{13}C-rich bicarbonate as described by Irwin et al. (1977) because S1 has a $\delta^{13}C$ composition of +1.45‰ rather than +15‰. Preferential removal of ^{12}C by organic materials (Schidlowski et al., 1975, 1976; Faure, 1986) can also contribute toward the ^{13}C-enrichment of siderite in organic-rich marsh sediments. In the Tirrawarra Sandstone, both this process and methanogenesis probably produced the positive $\delta^{13}C$ character of the S1 cement.

The later siderite cement generations (S2 and S3) are relatively closely related in terms of their carbon isotope signatures, having $\delta^{13}C$ values of -8.5 and -11‰ respectively (Fig. 5.2). They also have extensive substitution by Mg.

Both the $\delta^{13}C$ compositions of S2 and S3 are consistent with a major source of carbon involving the thermal decarboxylation of organic matter that produces a strongly ^{12}C-enriched carbon (cf. Irwin et al., 1977; Hudson, 1977; Carothers & Kharaka, 1980; Kharaka et al., 1983). Mixing with secondary carbon sources cannot be excluded, including atmospheric carbon ($\delta^{13}C$ = -11 to -6‰; Keeling, 1958) and carbon of igneous or geothermal origin (on average between -5 and -7‰; Deines, 1986).

Atmospheric carbon could have been transported in solution into the diagenetic environment by the meteoric invasion that probably triggered feldspar dissolution and kaolin precipitation in the Tirrawarra Sandstone. No igneous or hydrothermal activity is known in the study area. Radiometric data suggest that local granite emplacement occurred during the Late Ordovician-Carboniferous (Webb, 1974; Fanning, 1987), and possibly as early as in the Precambrian in the Cooper Basin region (Gatehouse, 1986). Geological evidence strongly suggests that igneous activity was followed by a long phase of erosion and deep weathering prior to deposition of Cooper Basin strata (Schulz-Rojahn, 1991) and thus is unlikely to have provided much carbon, if any, during siderite precipitation in the Tirrawarra Sandstone.

Both the $\delta^{13}C$ compositions of S2 and S3 are consistent with a major source of carbon involving the thermal decarboxylation of organic matter that produces a strongly

^{12}C-enriched carbon (cf. Irwin et al., 1977; Hudson, 1977; Carothers & Kharaka, 1980; Kharaka et al., 1983). The same source of carbon was proposed by Morad et al. (1994) for Mg-rich siderites in fluvial Triassic sandstones from southern Tunisia.

5.5.4 Significance of Dissolution Events

Several dissolution phases occurred during precipitation of different generations of siderite cement. The dissolution boundaries almost certainly mark a time gap between the precipitation of each major generation of siderite cement, as is indicated by the different isotope compositions of the various cement generations.

The results from this investigation show that siderite can undergo repeated cycles of precipitation and dissolution during the diagenetic history of a basin, and that secondary porosity produced as a result of siderite leaching can be a temporary phenomenon in clastic provinces. Since it can not be determined how much siderite cement was dissolved during each dissolution event, it is uncertain whether the secondary porosity was volumetrically significant in the past. The rather subtle nature of the dissolution boundaries, however, would suggest relatively minor dissolution events. The dissolution boundaries almost certainly mark a substantial time gap between the precipitation of each major generation of siderite cement, as indicated by the different isotope compositions and fluid inclusion data of the various cement generations.

The first dissolution event (D1) occurred between the precipitation of S1 and S2, at reservoir temperatures probably between about ≤ 30 and 68°C as suggested by the stable isotope and fluid inclusion data. The second dissolution phase (D2) took place after the formation of S2 but before S3 cementation, in the temperature range of about 68-102°C (Fig. 4.12).

The origin of the dissolution events is uncertain but the first dissolution event (D1) may be related to invasion of low-pH meteoric pore waters during kaolinite precipitation (cf. Bjørlykke & Brendsdal, 1986). The presence of oil at the dissolution boundary between S2 and S3 may point toward the role of organic processes in triggering carbonate cement dissolution, prior to, or synchronous with petroleum migration. The second dissolution phase (D2) broadly coincides with the temperature window for peak hydrocarbon generation (cf. Tissot & Welte, 1978). It is possible that organic acids which accompanied kerogen maturation (Schmidt & McDonald, 1979;

Surdam et al., 1984; Burley, 1986) triggered the dissolution event. According to Curtis (1983), maturing kerogen can generate Al-bearing acidic pore water that produces late-generation kaolinite. In the Tirrawarra Sandstone, either meteoric invasion or source-rock maturation probably accounts for the association of authigenic kaolinite patches with siderite spar displaying dissolution (Plate 10 E).

5.5.5 Paragenetic Sequence

Three main generations of siderite cement precipitated during the diagenetic history of the Tirrawarra Sandstone, each separated by at least one dissolution event that probably was short-lived (Plates 10A-C, 11A, 19A & 19G). The siderite cementation and dissolution events occurred between, and synchronous with other diagenetic processes, including quartz cementation, feldspar dissolution and kaolinisation, and illitisation (Fig. 4.18). An early Fe-rich siderite precipitated during methanogenesis whilst later, Mg-rich cement generations formed at elevated temperatures from carbon produced mainly from maturing source rocks.

5.6 CONCLUSIONS

Multi-generation siderite in the Tirrawarra Sandstone of the Moorari and Fly Lake Fields highlights the important role of differential cement development on bulk-rock isotope signatures. The results of this study show that caution must be exercised in the interpretation of bulk-rock isotope signatures even when only a single carbonate cement phase is indicated by semi-quantitative bulk XRD analysis. Failure to recognise isotopically heterogeneous samples may lead to erroneous interpretations of bulk-rock isotope results. Only the end-member isotope compositions of the different cement generations should be taken into consideration when interpreting the genesis of multi-generation siderite cements. Generally, the different generations of siderite cement are not readily identifiable under the optical microscope, highlighting the importance of back-scattered electron image analysis for siderite characterisation. In particular, the integrated use of video-imaging and image analysis software provides an efficient means of quantifying the different siderite cement generations seen under the BSE. Since the method can be semi-automated, the technique provides a potentially powerful

tool for improved bulk-rock isotope interpretations in clastics containing multi-generation carbonate cements. The method enables the determination of end-member $\delta^{18}O$ and $\delta^{13}C$ compositions of individual cement generations in cases where pure, or nearly pure samples of end-member carbonate cement generations are not available for isotope analysis, provided (1) a statistically representative number of BSE images is analysed, and (2) the various cement generations have different chemical compositions. The bulk isotopic composition of samples with multi-generation/phase cement has a direct linear relation with the relative proportion and $\delta^{18}O$ of each generation/phase of cement in the samples. This relation can be expressed with the $\delta^{18}O_{(sample)} = \Sigma^{1}_{n}(V_S * \delta^{18}O_S)$ equation.

In the Tirrawarra Sandstone of the Moorari and Fly Lake Fields, application of the BSE image analysis technique, together with bulk-rock isotope and fluid inclusion studies has led to the identification of three main generations of siderite cement. The first and second siderite cements were each followed by at least one dissolution event. The first generation of siderite cement is an homogeneous, Fe-rich siderite with a $\delta^{13}C$ signature of +1.45‰, which probably formed during low-temperature methanogenic processes ($\leq$ 30°C). The second generation of siderite cement is a Mg-rich, inhomogeneous siderite characterised by complex zoning, with a $\delta^{13}C$ signature of -8.5‰. This siderite cement is thought to have formed mainly by the decarboxylation of organic matter at temperatures between 64 and 76°C. The third and final siderite precipitation event produced a Mg-rich, regularly banded then homogeneous, pore-filling siderite with a $\delta^{13}C$ character of -11‰. This siderite is also interpreted to have formed during kerogen maturation, albeit at more elevated temperatures (98-110°C). The results from this study show that organic processes controlled siderite cementation over a range of different burial conditions in the study area.

CHAPTER SIX

Tectonic Fingerprints in Siderite Cement

6.1 Introduction

Compositional zoning and dissolution in cement is a direct response to fluctuations of the pore water chemistry, the variation of which during burial can be controlled by many factors, including the interaction between pore water and rock-forming minerals and the mixing of fluids from different origins. This study suggests that tectonic activity can, by altering the hydraulic gradient, also influence pore water chemistry and lead to dissolution of cement, made clear by zoning within siderite crystals.

Three different stages of siderite cement have been described from the Tirrawarra Sandstone in the Moorari and Fly Lake Fields, here referred to as early (S1), middle (S2), and (S3) late. Ragged dissolution surfaces separate the main phases, occurring after precipitation of S1 and S2 with incipient dissolution suggested within S2. Back scattered electron (BSE) images and electron microprobe analyses clearly differentiate each main phase of siderite. S1 is an homogenous, iron-rich siderite whereas S2 displays patchy compositional zoning associated with several minor dissolution stages and S3 commences with even compositional banding and grades into a thick homogenous phase in the terms of composition.

Isotope analyses and fluid inclusion studies indicate that S1 formed at a temperature around 30°C, S2 precipitated at a minimum temperature of 68°C and S3 formed around 102°C. The heterogenous, pitted and zoned S2 is thought to have formed during a time of active tectonism in the Cooper Basin whereas the evenly banded nature of S3 suggests that it precipitated during a quiet tectonic period when pore waters largely remained relatively constant (Rezaee et al., 1997). It appears that siderite cements in the Tirrawarra Sandstone record tectonic activity in the form of irregular growth and dissolution highlighted by compositional zoning with stages of strong dissolution recording particularly active times when pore waters changed composition dramatically. Some zoning could be related in part to tectonic pulses.

The temperature recorded by each of the siderite stages allows their precipitation to be tied to a burial history curve, and by making some simple assumptions about that history, the timing of cementation can be estimated. This can be a additional tool for calibrating the thermal history of an area.

6.2 Tectonic events influencing the Cooper Basin

Several tectonic events occurred during and after deposition of the Tirrawarra Sandstone. Some of the tectonic events are minor, such as the one which occurred during the Tirrawarra Sandstone deposition (here labelled T0a), and some of them are major tectonic events (T1 to T3) (Fig. 2.3). Apak et al., (1993) documented another weak composite tectonic event within the Patchawarra Formation (here referred to as T0b). This event is seen as local truncation of section over the GMI Trend but fades towards the depocentres, including into the study area. The main tectonic events are highlighted in a seismic section near the study area (Figs. 6.1 & 2.3) and a regional cross section, Figure 6.2 modified from Kreig et al., (1995).

The first main tectonic event after deposition of the Tirrawarra Sandstone (T1) occurred in the form of uplift and erosion after deposition of the Daralingie Formation (Thornton, 1979). Compressive forces reactivated basement thrusts, resulting in an angular contact between the Toolachee Formation and various underlying formations (Wopfner, 1966; Kapel, 1972; Pyecroft, 1973; Thornton, 1979). The erosion is particularly apparent over the GMI trend (Apak et al., 1993) and is strong enough to be present in the study area in the middle of the Patchawarra Trough (Hill & Gravestock, 1995) but may be less prominent in the deeper Nappamerri Trough to the east of the GMI ridge. A hiatus in sedimentation of about 12 Ma at the end of Early Permian is recorded by palynological studies (Thornton, 1979).

Cooper Basin deposition terminated before the end of the Triassic when widespread folding, regional uplift and erosion, here referred to as event T2, occurred (Battersby, 1976). Compression again reactivated the main basement faults (Apak et al., 1993) but the main effect of this event was to tilt the basin to the northeast, thereby dramatically separating the Permian and Triassic depocentres. Up to 500 m erosion of sediments has been recognised in the southern parts of the basin (Kantsler et al., 1983; Gray &

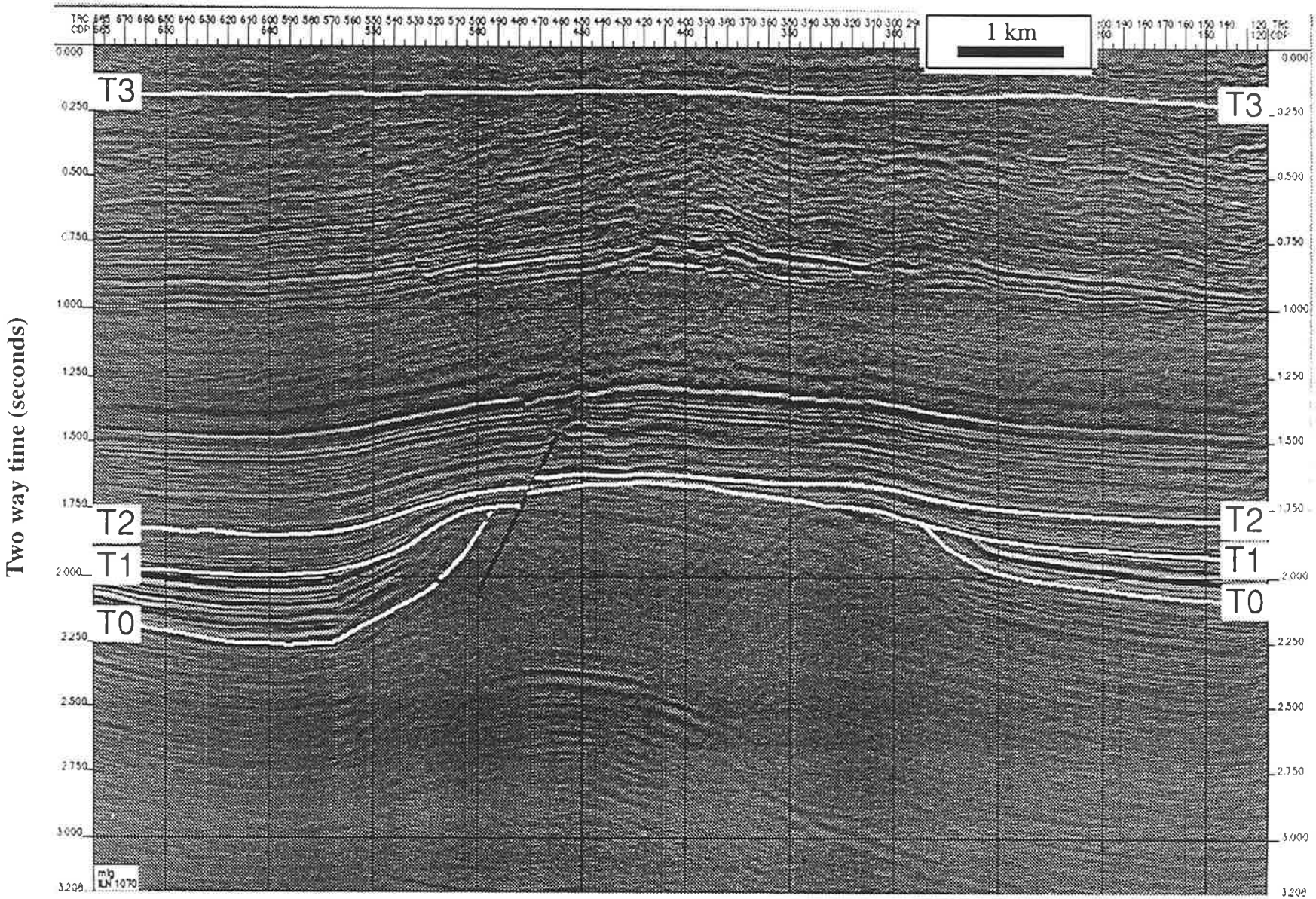

Figure 6.1 - Interpreted seismic section from near study area, highlighting tectonic events. T0 is a minor tectonic event occurred during Tirrawarra Sandstone deposition and T1, T2 and T3 are major tectonic events which occurred after deposition of the Tirrawarra Sandstone and led to uplift and erosion of sediments.

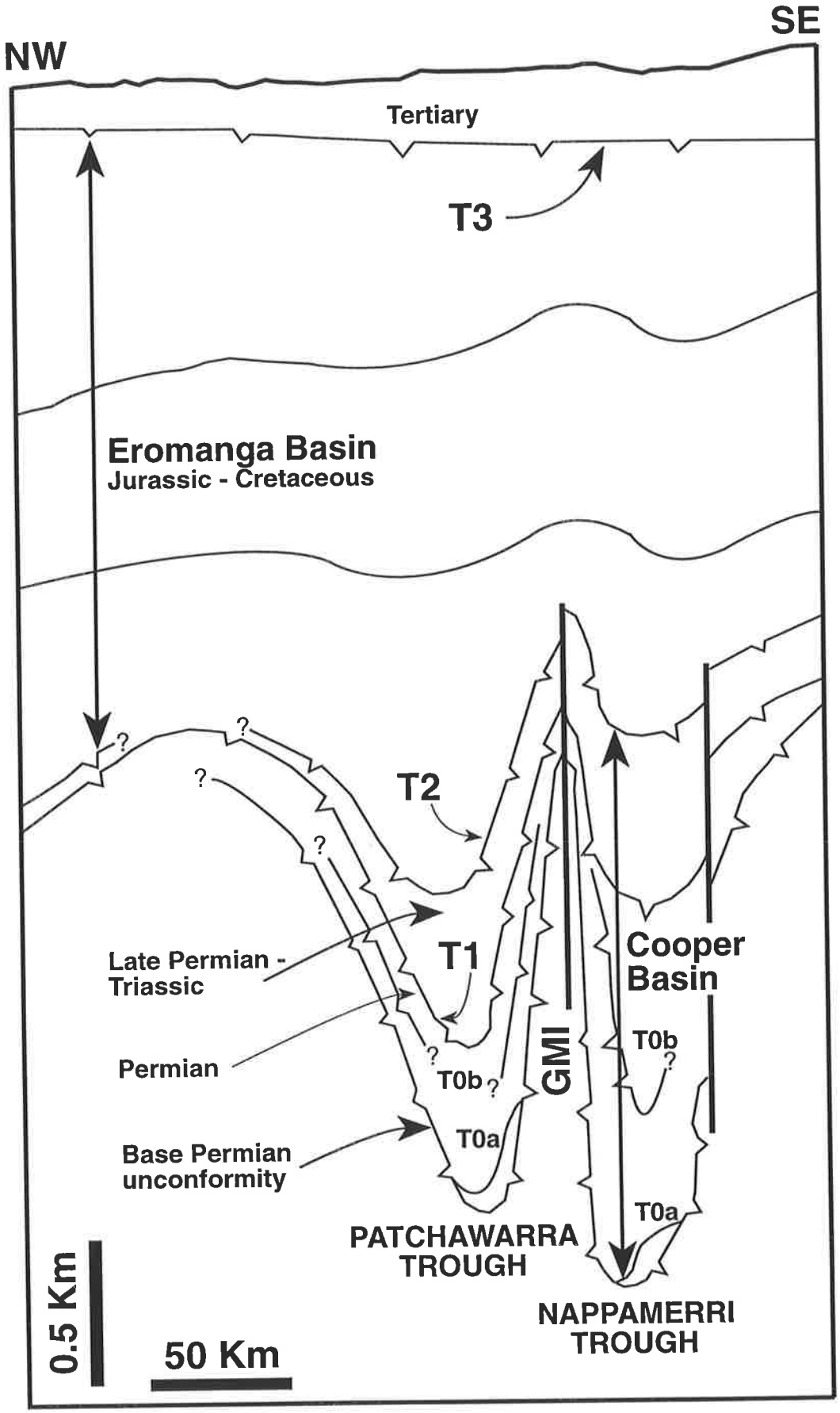

Figure 6.2 - Schematic cross section from the Patchawarra Trough, over the GMI Ridge and into the Nappamerri Trough illustrating the position of the main unconformities in the area. GMI is Gidgealpa - Merrimelia - Innamincka Ridge. (modified from Kreig et al., 1995).

Roberts, 1984) and although the effect diminished to the north, erosion is still evident in the study area.

Deposition of Eromanga Basin sediments (Jurassic - Cretaceous) commenced on the erosion surface of the Cooper Basin (Kantsler et al., 1983; Heath, 1989). After rapid subsidence which allowed deposition of the Cretaceous section, another tectonic event (T3) resulted in folding and faulting (Heath, 1989).

6.3 Thermal history modelling and the timing of siderite cements

Thermal modelling based on vitrinite data was carried out in order to constrain the timing of the siderite cements in the Tirrawarra Sandstone. Figure 6.3 is a simple thermal model without erosion at unconformities. The temperatures from this simple model have been transferred onto Figure 6.4 and shown as the solid line. Model vitrinite values are close to those measured at the level of the Tirrawarra Sandstone.

Figure 6.4 shows a schematic time-temperature path for the Tirrawarra Sandstone based upon thermal modelling. In this history, erosion occurred prior to 200 Ma but the maximum temperature was not achieved at that time. Near maximum temperatures are suggested to have occurred prior to Late Cretaceous erosion. As there is no known recent subsidence, the present maximum temperature of 130° C indicates a recent increase in geothermal gradient to 36° C/km (Russell & Bone, 1989). This is large enough to have brought previously immature hydrocarbon source rocks to a situation of generation and expulsion.

The three main tectonic events which resulted in uplift and erosion in the Cooper Basin area are illustrated on the time-temperature path of the Tirrawarra Sandstone as T1, T2, and T3 (Fig. 6.4). The grey lines indicate the constraints implied by the homogenisation temperatures of each siderite phase with two possibilities for timing of S2. Time B is based on a simple history with no uplift and time A takes account of event T2.

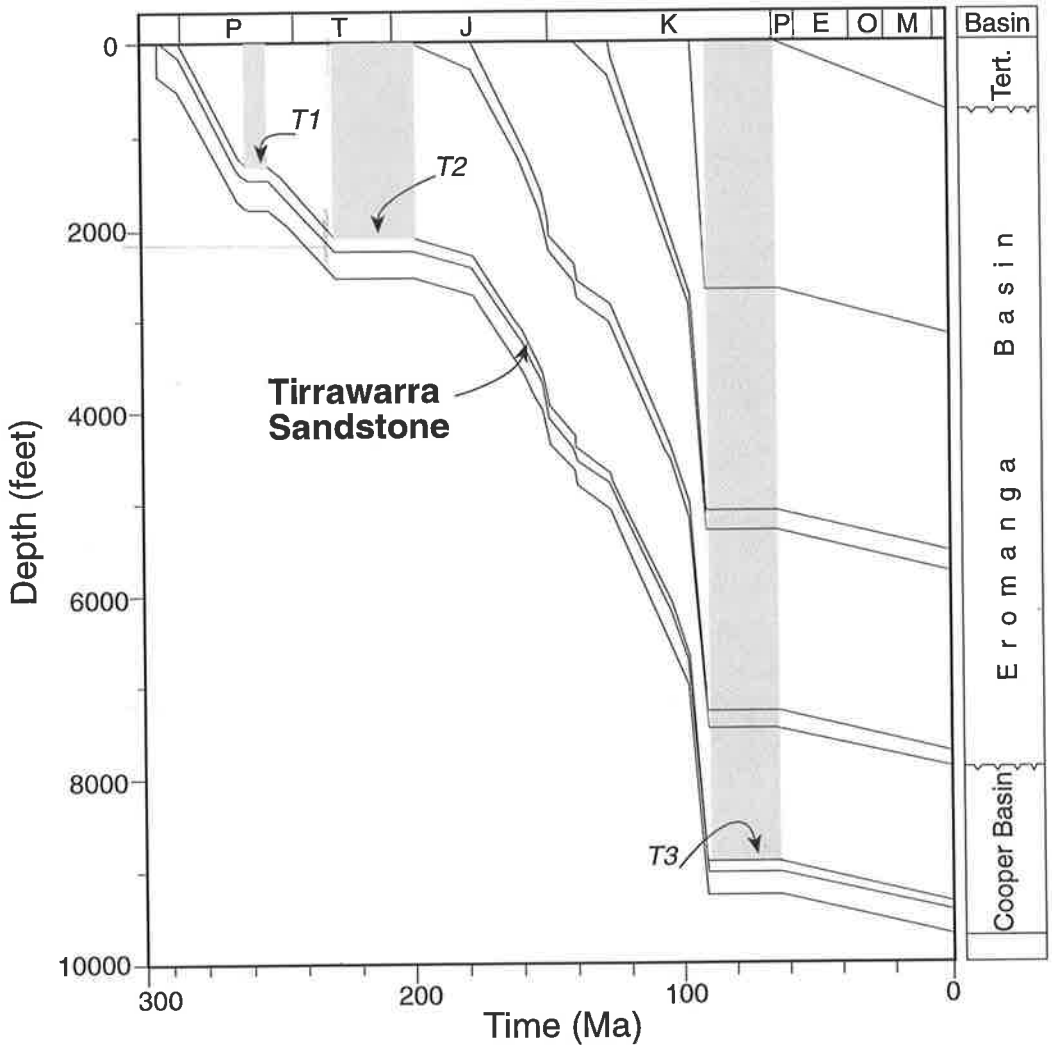

Figure 6.3 - Burial history plot of Fly Lake-1 generated using BasinMod software. This is a simple plot with no erosion. Time breaks in the Mid Permian, late Triassic and late Cretaceous are shown as flat zones of non-deposition.

6.4 Discussion

Results from the present investigation show that the pore-filling siderite precipitated in three main stages in the Moorari-Fly Lake area. An early, homogeneous Fe-rich siderite (S1) was followed by a generally more extensive cement stage characterised by a complex compositional zoning (S2), and in turn was engulfed by a late-stage homogeneous siderite cement (S3) (Plates 10B, 19G).

Detailed observation of BSE images of S2 and S3 indicate two different hydraulic conditions in the reservoir. S2 shows irregular compositional zoning (Plate 19E), which indicates fluctuation in pore fluid chemistry. Minor dissolution evident between the patchy zonation (Plate 19 E), shows that fluctuations in pore water chemistry were significant. Waves of varying geochemical concentration may be unrelated to tectonic activity but complex zoning with incipient dissolution suggests more severe fluctuation in what may be termed a hydraulically active porous medium. S3, however, displays a relatively consistent composition with simple zoning and no internal dissolution (Plate 19C & 19G). This indicates a more constant pore fluid chemistry suggestive of a hydraulically stable system.

6.4.1 Burial history and siderite cement stages

Plotting different stages of siderite cement on the time-temperature path of the Tirrawarra Sandstone (Fig. 6.3), constrains the timing of cement precipitation and dissolution, points to the influence of tectonic activity, and allows the burial history to be further refined.

The grey lines on Figure 6.4 illustrate the constraints implied by the cement precipitation temperatures. S1 was precipitated prior to the uplift T1. S2, with precipitation temperatures from 66 - 72°C, would fall on the time - temperature curve around 110Ma (position B on Figure 6.4) if the burial history was a simple one with no uplift. This would place S2 very close to S3 with no obvious reason for the dissolution event between them. It is suggested that S2 was emplaced prior to the main uplift of T2, position A on Figure 6.4. This implies that additional section was deposited to allow the Tirrawarra Sandstone to reach around 70 °C prior to at least 550 metres of uplift and erosion.

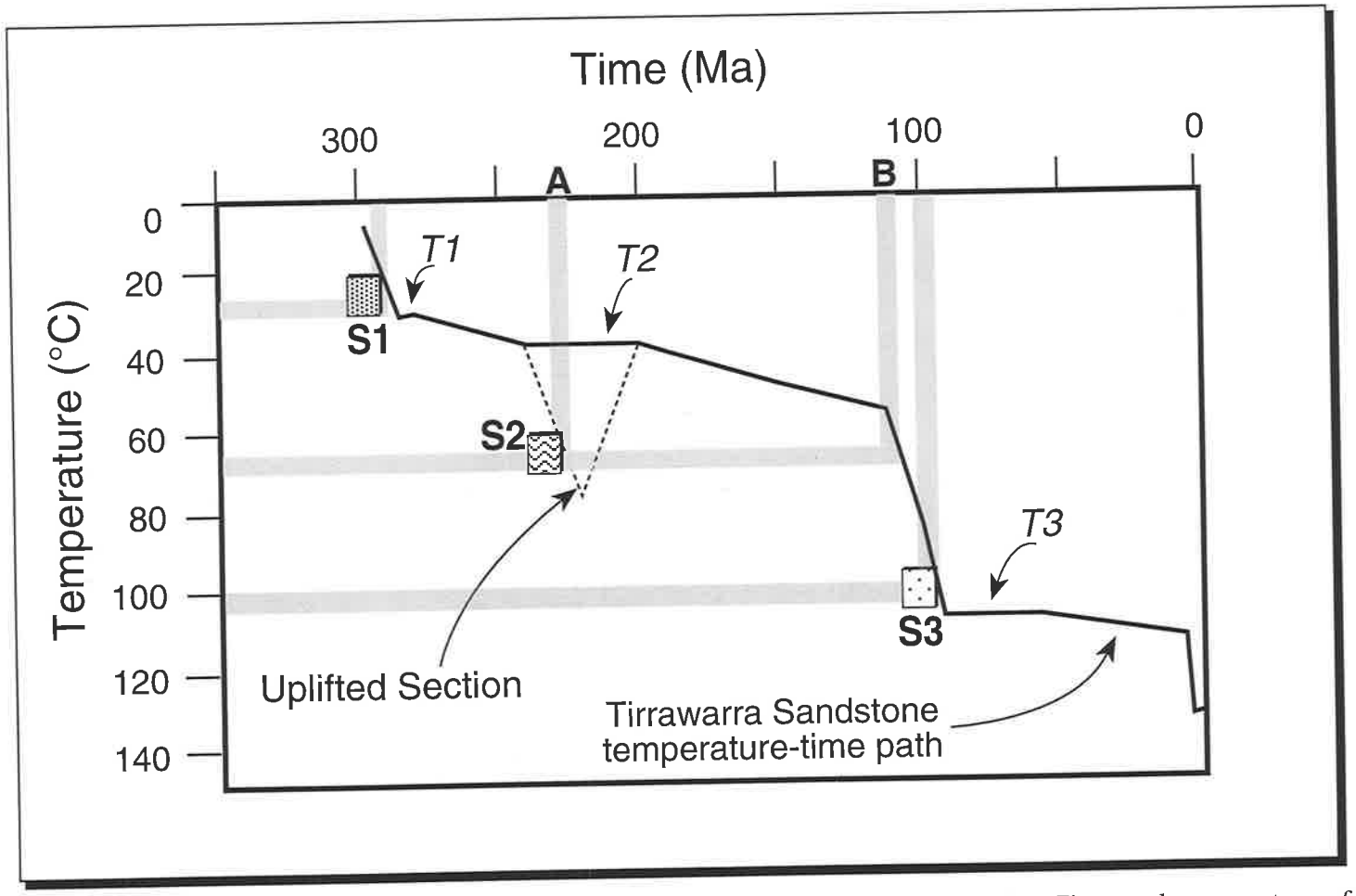

Figure 6.4 - Schematic thermal history of the Tirrawarra Sandstone, Fly Lake field. Time and temperature of formation of different generations of siderite cement and three main tectonic events which are resulted in uplift and erosion in the Cooper - Eromanga Basins are illustrated on time-temperature path of the Tirrawarra Sandstone. T1 = the first tectonic event, T2 = the second tectonic event and T3 = the third tectonic event, S1 = early stage of siderite cement; S2 = middle stage of siderite cement; S3 = late stage of siderite cement. A is the time of S2 precipitation taking into acount the uplift and erosion during T2 and B is the time of S2 precipitation on the default curve which does not take uplift into account.

The presence of minor dissolution phases between different zones within S2 and the relatively rapid compositional zoning in this stage of siderite cement suggest that the formation of S2 occurred during unstable conditions, possibly during the onset of T2.

The precipitation temperature of the late stage of siderite cement (S3) shows that it formed around 100 Ma, probably before T3 (Fig. 6.4). S3 formed during relatively stable hydraulic conditions in the Cooper Basin as indicated by the regular zoning then thick homogenous stage (Plate 19 C & G). This could be synchronous with the rapid burial stage in the mid Cretaceous.

The first phase of dissolution (D1), which occurred at temperatures between 30 and 68°C, is most likely have occurred during first tectonic event (T1) which may have allowed invasion of low-pH meteoric water into the reservoir. The second dissolution phase has occurred between 68 and 102°C. The presence of dead oil at the dissolution boundary between S2 and S3 may point toward the role of organic processes in triggering S2 dissolution, prior to or synchronous with petroleum migration.

6.5 Conclusions

In the Tirrawarra Sandstone of the Cooper Basin, three stages of siderite cement have formed under different tectonic conditions:

-The early stage (S1) which formed about 30°C is an Fe-rich structureless cement. S1 precipitated before the first tectonic event after deposition of Tirrawarra Sandstone.

-The middle stage of siderite cement (S2) which formed about 68°C, was formed under tectonically-active conditions in the Cooper Basin, probably in the lead up to T2. This stage of siderite cement is characterised with relatively rapid and irregular compositional zoning and minor dissolution phases.

-The late stage siderite cement (S3) which formed about 102°C, is a cement formed under tectonically-stable conditions in the Cooper Basin.

With the knowledge of precipitation temperature and timing of S2, it is possible to estimate the amount of erosion during T2. Assuming the current thermal gradient for the Patchawarra Trough of about 36°C/km (Russell & Bone, 1989) was valid for T2 time, at least 550 meters uplift and erosion would have been required in the Late Triassic in the study area.

CHAPTER SEVEN

POROSITY AND PERMEABILITY

7.1 Introduction

The nature of porosity in the Cooper Basin has been studied by many workers (Steveson & Spry, 1973; Stanley & Halliday, 1984; Martin & Hamilton, 1981; Heath, 1989; Schulz-Rojahn & Phillips, 1989; Schulz-Rojahn, 1991 Tingate & Luo, 1992; Rezaee & Griffiths, 1996a; Rezaee & Lemon, 1996c). Some of the workers mentioned that porosity in the Cooper Basin is mostly secondary (Steveson & Spry, 1973; Stanley & Halliday,1984), whereas some indicated the presence of different types of porosity including, primary, secondary and microporosity porosity in different formations of the Cooper Basin (Martin & Hamilton, 1981; Heath, 1989; Schulz-Rojahn & Phillips, 1989; Schulz-Rojahn, 1991, Hamlin et al., 1996). Rezaee & Lemon (1996c) indicated the presence of primary, secondary and microporosity in the Tirrawarra Sandstone in the Moorari and Fly Lake Fields and mentioned that the distribution of different types of porosities is controlled by sandstones composition which is in turn is depositional facies dependant parameter and they found a close relationship between pore geometry and permeability. Rezaee & Griffiths (1996a) divided the Tirrawarra Sandstone core samples to eight classes based on their porosity type.

In this chapter, based on integration of different data including, petrography point count, image analysis, mercury injection and core analysis data, the nature of porosity is closely investigated and parameters which control porosity and permeability are discussed. Based on porosity type, Tirrawarra Sandstone samples are divided into eight classes.

7.2 Data Availability

Data available for this study include:

- point count data of 130 studied thin sections,
- image analysis data including pore area size, mean pore diameter, pore perimeter of 66 carbon-coated polished thin sections,

- mercury injection capillary pressures data of 31 samples and,
- a total of 650 ambient core porosity, permeability, grain density, bulk density and fluid saturation measurements of 14 wells in the Moorari and Fly Lake Fields,
- Data from special core analysis for the determination of cementation exponent (m), tortuosity (a) and saturation exponent (n) in the Tirrawarra Sandstone from the Overton and Hamilton (1986) report for the Cooper Basin.

For porosity measurements, the helium injection technique was mainly used, but in some samples, summation of fluids was used for porosity measurement. In some samples both helium and summation of fluids porosity were available. The plot of helium porosity versus summation of fluids porosity (Fig. 7.1) indicates the following relationship between them:

$$helium\ porosity = 0.81 * fluid\ sum\ porosity + 0.85 \qquad (1)$$

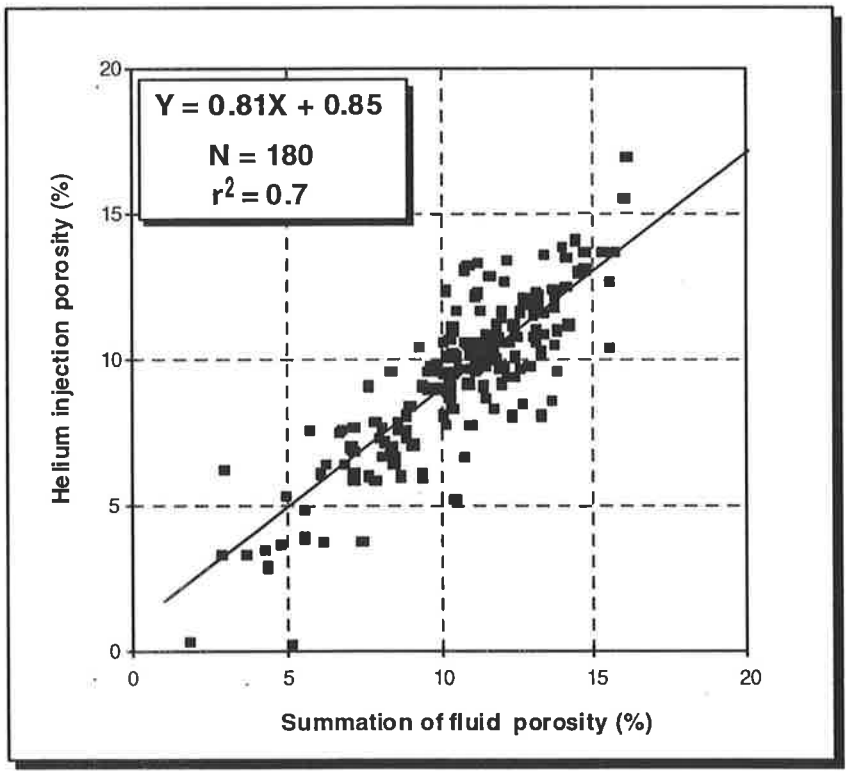

Figure 7.1 - Summation of fluid porosity plotted against helium injection porosity.

As the helium injection technique gives a more reliable value for porosity, all porosity values obtained from the summation of fluids method were converted to helium porosity using the above equation.

A porosity reduction of 5% between conventional (ambient pressure) and reservoir (overburden pressure) core analysis for the Cooper Basin has been derived by Morton (1989) as:

$$\phi_{overburden} = \phi_{ambient} * 0.95 \qquad (2)$$

All core porosity data are corrected for overburden pressure using equation 2. All core data are listed in Appendix 10.

Measured core porosities of the Tirrawarra Sandstone range up to 20 percent (Fig. 7.2), associated permeabilities may be as high as 340 mD (Fig. 7.3). On average, however, the Tirrawarra Sandstone is characterised by low porosity and permeability. Core porosity is mostly between 10 to 12 percent (Fig. 7.2) and permeability values are mostly less than 5 mD (Fig. 7.3).

7.3 Porosity Types

Three types of porosity were observed in the Tirrawarra Sandstone samples. The types of porosity include primary intergranular porosity, secondary porosity and microporosity.

7.3.1 Primary Porosity

Primary intergranular porosity was present between the euhedral faces of quartz overgrowths (Plates 20 & 21). SEM microscopy reveals that, even in samples which are tightly cemented by quartz overgrowth, there is a gap between cement faces (Plates 4H, 4B & 21H). The dimensions of primary pore spaces depend on the rate of cement growth, and ranges from 0.02 to 0.15 mm. The amount of primary porosity in the samples, indicated by point counting, ranges from zero to 10%. Primary porosity mostly occurs in quartz-rich sandstones where early quartz cementation has led to a strengthened grain framework to limit subsequent compaction and preserve porosity. Such sandstones are characterised by prominent euhedral quartz cement that grew into primary pores, reducing but not occluding initial porosity (Plate 21). In sandstones rich

Plate 20

Micrographs of Primary Porosity (I)

A - Medium-grained aeolian sandstone with dominant intergranular primary porosity. Early quartz cementation is responsible for helping prevent porosity destruction by mechanical compaction in quartz -rich sandstones. Porosity and permeability for this sample are 15 percent and 340 mD respectively. Sample M3-9412, Moorari-3, 2823.6 m. Scale bar = 1000 μm.

B - Close-up view of (**A**). It can be seen some of the pores are secondary (right lower corner) formed from dissolution of labile grains. Note good sorting and very well-rounded quartz grains. Sample M3-9412, Moorari-3, 2823.6 m. Scale bar = 100 μm.

C - Medium-grained, point bar sandstone which has dominantly primary intergranular porosity and some dissolution secondary porosity. Porosity and permeability for this sample are 16 percent and 154 mD respectively. Sample F6-9388, Fly Lake-6, 2816 m. Scale bar = 500 μm.

D - Another view of (**C**). Note the presence of relatively good connectivity between pore spaces. Scale bar = 1000 μm.

E - In most of the quartz-rich sandstones primary intergranular porosity is associated with some secondary porosity formed by dissolution. In this example both small primary porosity and enlarged secondary porosity can be seen. Note that in this sample the quartz cement can only be recognised by its euhedral faces. Sample F2-9569, Fly Lake-2, 2870.7 m. Scale bar = 250 μm.

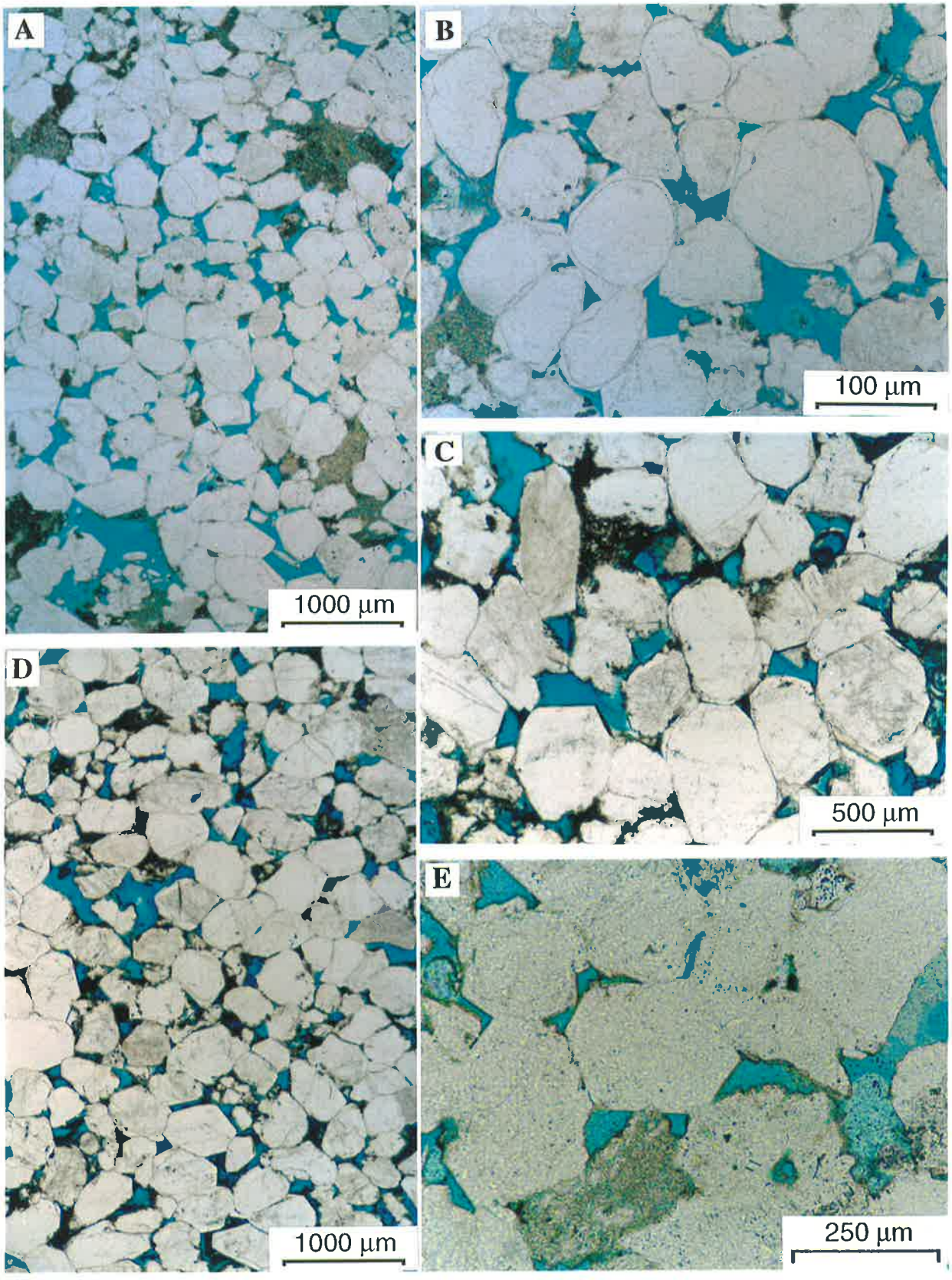
A
1000 µm
B
100 µm
C
500 µm
D
1000 µm
E
250 µm

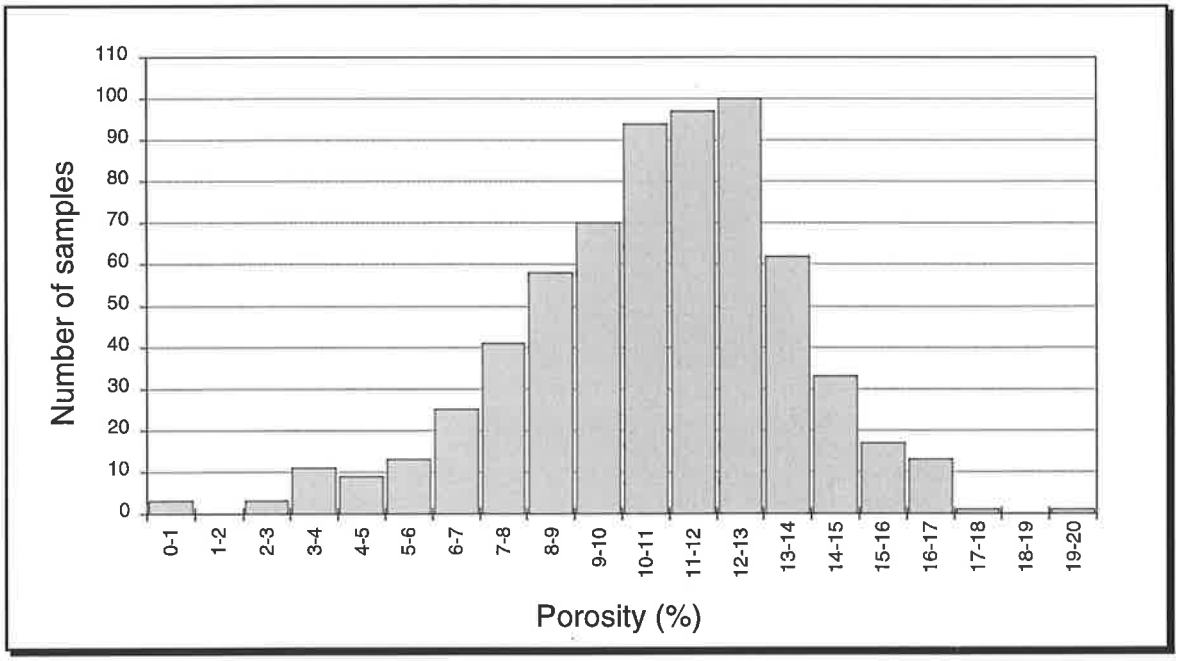

Figure 7.2 - Frequency histogram of porosity distribution in the Tirrawarra Sandstone in the Moorari and Fly Lake Fields.

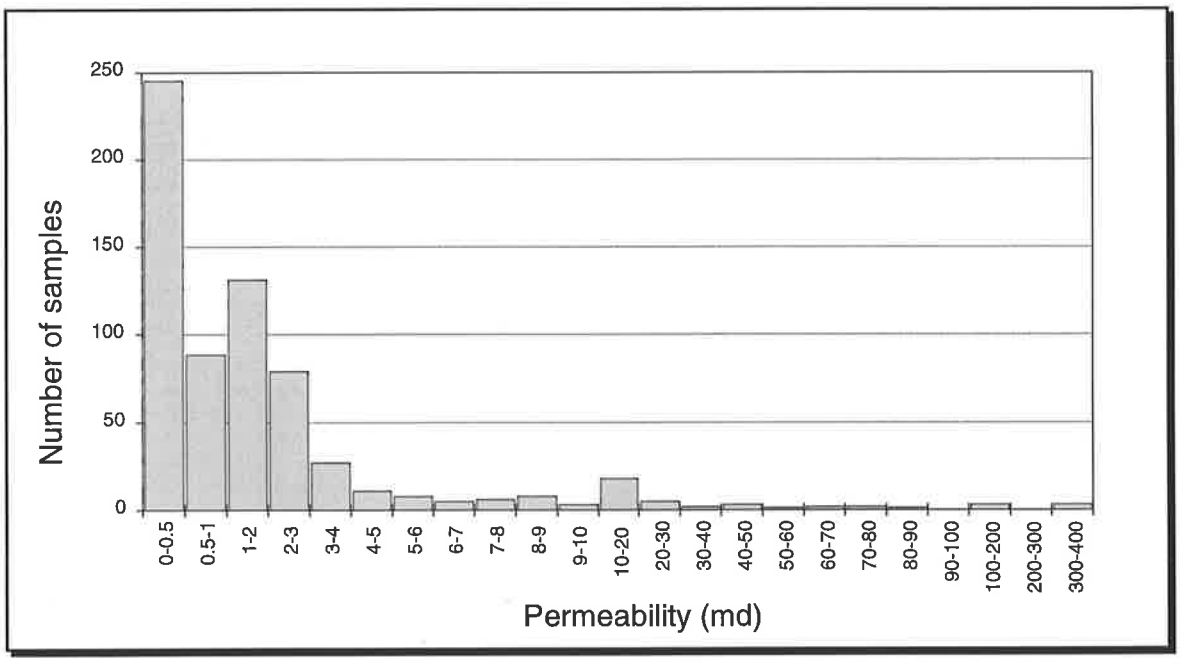

Figure 7.3 - Frequency histogram of permeability distribution in the Tirrawarra Sandstone in the Moorari and Fly Lake Fields.

in rock fragments in which compaction is intense, primary porosity is not present (Plate 2D). Primary porosity is the dominant porosity in the aeolian, point bar, and beach barrier environments of the Tirrawarra Sandstone.

7.3.2 Secondary Porosity

Secondary porosity, consisting of relatively large pores, was either the product of unstable-grain dissolution (Plate 22A-D); or the enlargement of pre-existing porosity by dissolution of the grain margins. Secondary porosity can be recognised in the samples by the presence of irregular, oversized and elongate pore spaces (Plate 22A). The size of these pores is very variable, and ranges from 0.02 to 0.3 mm. The amount of secondary porosity in the samples as indicated by point counting, ranges from zero to 11%.

7.3.3 Microporosity

The third type of porosity, microporosity, was present mainly in kaolinite masses (Plate 22E), and was abundant in the kaolinite-rich sandstones of the Tirrawarra Sandstone. Neasham (1977), Pittman & Thomas (1978), introduced the concept of microporosity within clay minerals and Hamilton & Wilson (1981), Tieh et al. (1986) defined microporosity as any pores with pore throat size less than 0.5 μm. "Kaolin-framework porosity" was coined by Tingate and Luo (1992) for larger micropores and was described as significant in gas reservoirs. In the present study, microporosity is used for pore spaces associated with clay minerals.

7.4 Quantification of Porosity by BSE image analysis

As mentioned by Ehrlich et al. (1991), the first two steps of petrographic image analysis are image digitising and porosity identification. Back-scattered electron images of carbon-coated polished sections from scanning electron microscopy provide a digitised image that is composed from a 512 × 512 pixels (2.4 × 2.4 micrometer) array with 256 grey levels for each pixel. The grey-level intensity from the matrix, which in this case is mostly quartz grains, is very different from the grey-level of pores which are impregnated with blue-dye epoxy. After changing the grey-level image to a binary image (black and white image in which values 0-127 are mapped to 0 and values 128-256 to 1) porosity can be differentiated from matrix. In a binary image, each pixel is

Plate 21

Micrographs of Primary Porosity (II)

A - SEM view of a medium-grained quartz-rich aeolian sandstone. Note that the dominant porosity is primary intergranular which is well connected. Porosity and permeability for this sample are 15 percent and 340 mD respectively. Sample M3-9412, Moorari-3, 2823.6 m. Scale bar = 500 μm.

B - Close-up view of (**A**), showing a big primary pore with a wide pore throat. Scale bar = 200 μm.

C - A close-up view of a medium grained, quartz-rich, well cemented sandstone with dominant primary intergranular porosity. Note the excellent connectivity between pore spaces. Sample M3-9405, Moorari-3, 2821.5 m. Scale bar = 200 μm.

D - A SEM close-up view of primary porosity retained between euhedral faces of quartz overgrowth. Sample M3-9412, Moorari-3, 2823.6 m. Scale bar = 200 μm.

E - Intergranular primary porosity survives between quartz overgrowths. Note the mechanical compaction of a rock fragment squeezing into the porosity at the lower left of the image. Sample M4-9563.7, Moorari-4, 2869 m. Scale bar = 200 μm.

F - SEM view of a primary pore surrounded with euhedral faces of quartz cement. Note that quartz cements are growing into the porosity. Sample M3-9405, Moorari-3, 2821.5 m. Scale bar = 100 μm.

G & H- Even in samples with a significant degree of quartz cementation, the probability of some primary porosity surviving is high. In these two examples it can be seen that, in spite of significant quartz development, small primary pores occur between euhedral faces of quartz overgrowths (arrows). Samples M3-9405, Moorari-3, 2821.5 m. Scale bar = 50 microns and M6-9733.2, Moorari-6, 2920 m. Scale bar = 200 μm.

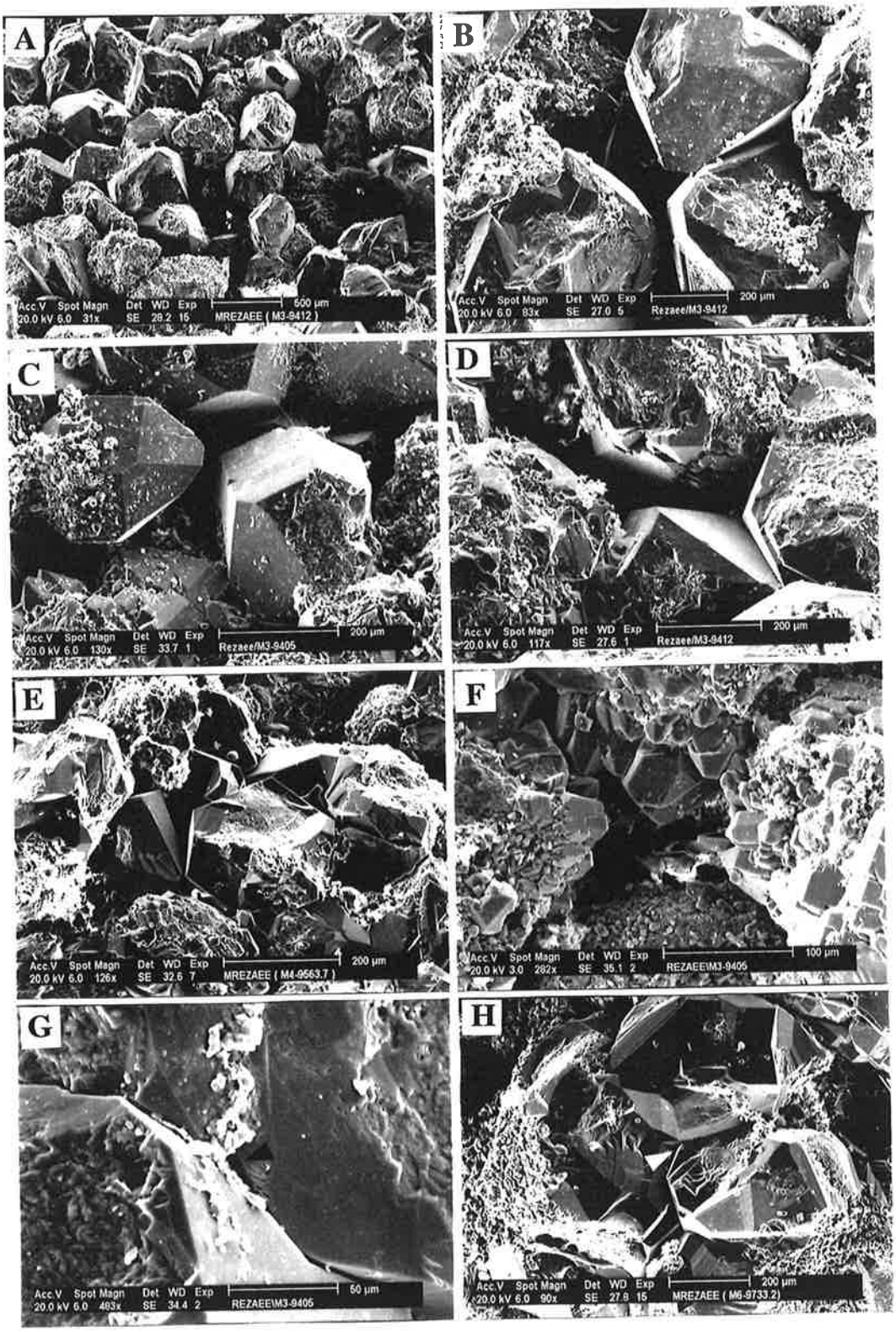
A
Acc.V Spot Magn Det WD Exp
20.0 kV 6.0 31x SE 28.2 15 MREZAEE (M3-9412)
500 µm
B
Acc.V Spot Magn Det WD Exp
20.0 kV 6.0 83x SE 27.0 5 Rezaee/M3-9412
200 µm
C
Acc.V Spot Magn Det WD Exp
20.0 kV 6.0 130x SE 33.7 1 Rezaee/M3-9405
200 µm
D
Acc.V Spot Magn Det WD Exp
20.0 kV 6.0 117x SE 27.6 1 Rezaee/M3-9412
200 µm
E
Acc.V Spot Magn Det WD Exp
20.0 kV 6.0 126x SE 32.6 7 MREZAEE (M4-9563.7)
200 µm
F
Acc.V Spot Magn Det WD Exp
20.0 kV 3.0 282x SE 35.1 2 REZAEE\M3-9405
100 µm
G
Acc.V Spot Magn Det WD Exp
20.0 kV 6.0 493x SE 34.4 2 REZAEE\M3-9405
50 µm
H
Acc.V Spot Magn Det WD Exp
20.0 kV 6.0 90x SE 27.8 15 MREZAEE (M6-9733.2)
200 µm

assigned a value of either 1 or 0. Pixels representing porosity have a darker grey level and are made black (1) and matrix, which is lighter in BSE images, is made white (0).

Erosion (thinning of an object) and dilation (thickening of an object) of images, a process used for pattern recognition, have been recently used for analysis of petrographic images (Rink, 1976; Fabbri, 1980; Ehrlich et al., 1984). Erosion is a technique that leads to a smooth and simple image by removing the outer layer of pixels (cf. Ehrlich et al., 1984), whereas dilation adds a layer of pixels to the object (Young, 1981). During erosion, small pores and small irregularities are lost completely and during the next dilation do not appear (Young, 1981). Erosion and dilation process for creating pore complex spectra were described by Ehrlich et al. (1984, 1991). As during this process, smaller pores and pore roughness and irregularities are eliminated, the resulting porosity spectrum represents information about the size distribution of pores (Ehrlich et al., 1984).

Successive cycles of erosion-dilation were used to construct pore complex spectra for some representative samples of the Tirrawarra Sandstone (Figs. 7.4a-b). In samples with high porosity and permeability, such as M3-9412 (ϕ = 15% and K = 328 mD), the pore complex spectrum (Fig. 7.4a) is different from those with less porosity and permeability; for example M5-9461 (ϕ = 13% and K = 15 mD) (Fig. 7.4b). The reduction of pore surface area after each erosion-dilation cycle, is more in samples with less porosity and permeability. This is due to the fact that samples with less porosity and permeability more likely have smaller pores and pore throats and subsequently, after each erosion-dilation cycle, they lose more pore spaces.

7.4.1 Macroporosity Quantification

A total of 61 polished sections were analysed by petrographic image analysis. For each polished section eight fields of view were observed and analysed. All of the measured parameters from eight fields of view of each sample were pooled in one file for further processing. Several characteristics of the pore spaces such as area, mean diameter and perimeter of each visible pore were measured.

Plate 22

Micrographs of Secondary Porosity and Microporosity

A - A fine-grained, point bar sandstone with dominant secondary dissolution porosity. Secondary porosity can be recognised in the samples by the presence of irregular, oversized and elongate pore spaces. The porosity and permeability for this sample are 14 percent and 62 mD respectively. Sample F2-9568, Fly Lake-2, 2870.4 m. Scale bar = 500 μm.

B - Close-up view of a large dissolution pore. Note the irregular and oversized nature of this pore. Sample M2-10127.6, Moorari-2, 3038.3 m. Scale bar = 250.

C - Secondary dissolution porosity formed from nearly complete dissolution of rock fragments. Note the presence of smaller primary porosity between quartz cemented grains. Sample M7-9618, Moorari-7, 2885.4 m. Scale bar = 500.

D - Very large, isolated secondary pores formed from dissolution of the labile detrital components of a sandstone. Sample F1-9431.4, Fly Lake-1, 2829.5 m. Scale bar = 500 μm.

E - Abundant microporosity associated with kaolinite booklets. In kaolinite-rich samples, this kind of porosity is dominant. Scale bar = 100 μm.

F - Another type of porosity which rarely can be seen in the Tirrawarra Sandstone, is micropores formed from dissolution of labile components of rock fragments. In this example, the rock fragment in the centre of micrograph is a very fine-grained sandstone which carbonate cement has dissolved. Sample M9-9732, Moorari-9, 2919.6 m. Scale bar = 1000 μm.

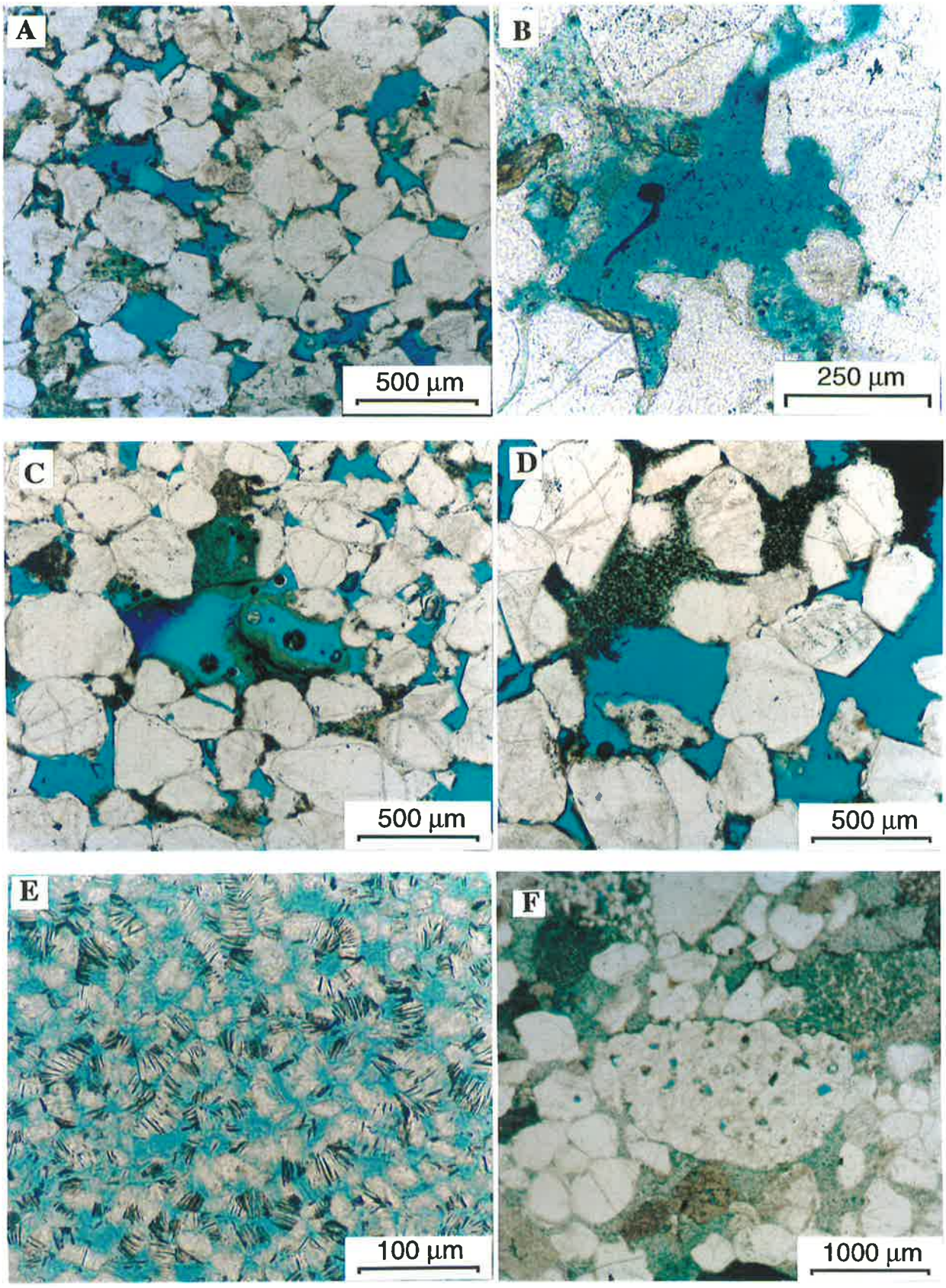
A
500 µm
B
250 µm
C
500 µm
D
500 µm
E
100 µm
F
1000 µm

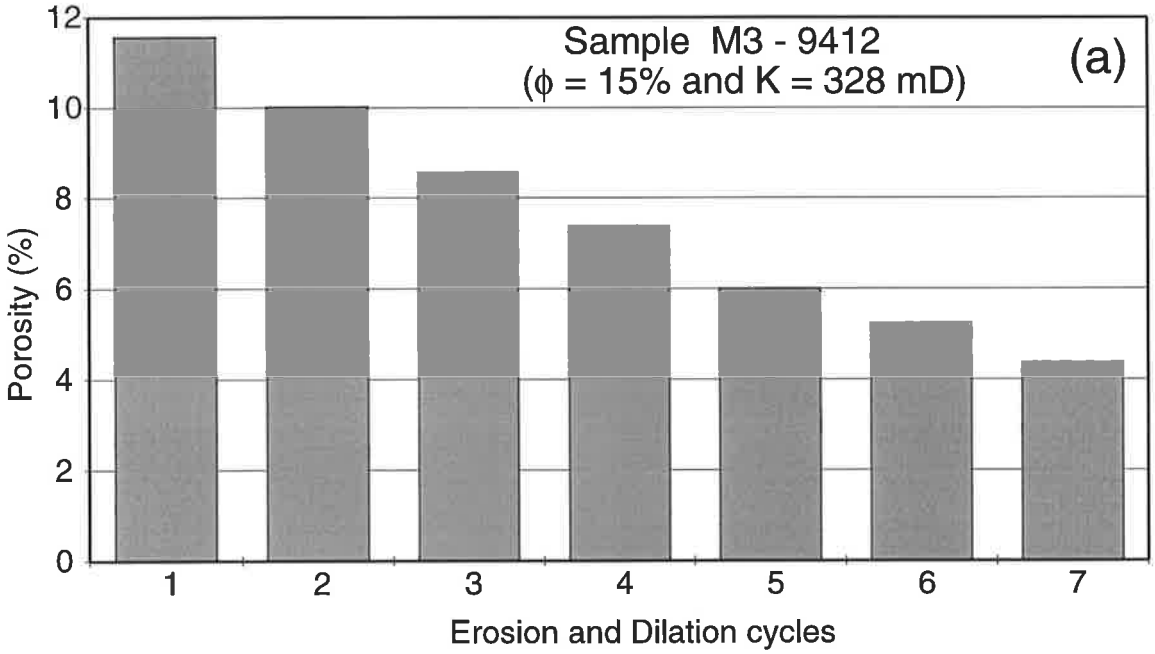

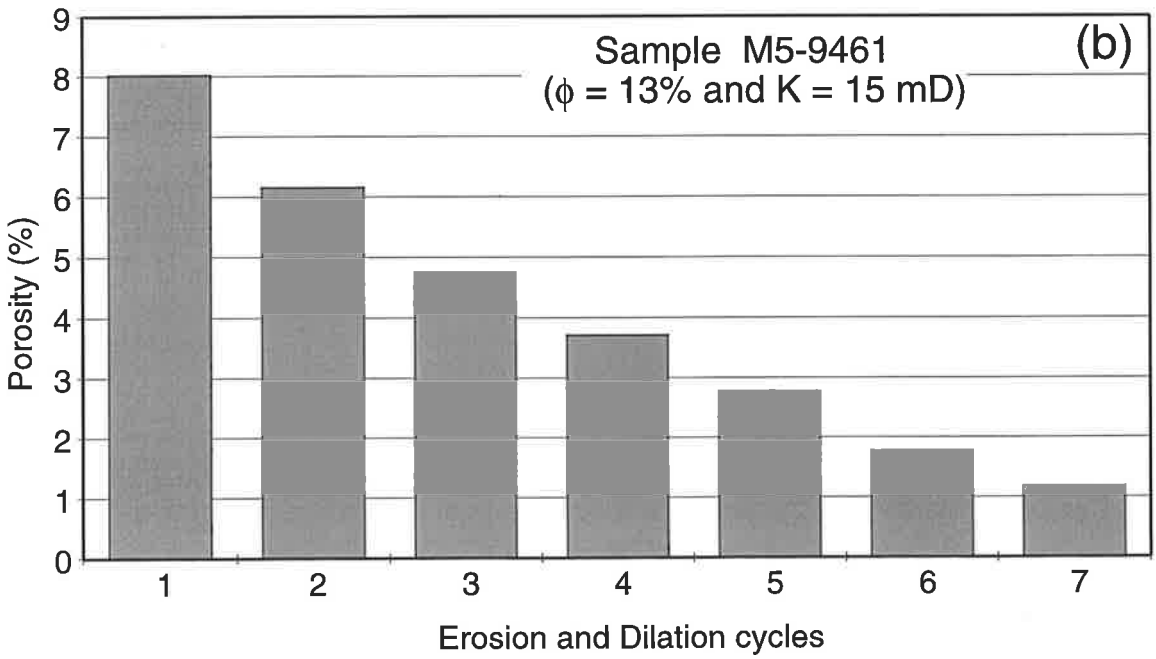

Figure 7.4a-b - Histograms illustrating pore complex spectra for samples with relatively high (**a**) and low (**b**) porosity and permeability.

7.4.2 Microporosity Quantification

In 44 carbon-coated polished sections that were impregnated by blue-dye epoxy, microporosity within kaolinite booklets was measured using a windows-based image analysis system added to a scanning electron microscope (SEM) with a back-scattered electron (BSE) detector. Kaolinite booklets in a BSE image appear light, whereas pore spaces among them are dark. A BSE image of kaolinite patches can be converted to a binary image including only the kaolinite booklets and the pore spaces among them (microporosity) (Fig. 7.5). The measurement of microporosity in clay minerals using BSE image analysis was developed by Nadeau & Hurst (1991) and Hurst & Nadeau (1995). The amount of microporosity within kaolinite flakes of the Tirrawarra Sandstone varies widely (Appendix 11). On average, the amount of microporosity is about 20%.

Total thin section porosity in this study is considered as macroporosity plus microporosity associated with kaolinite. This can be expressed as:

$$\text{Total thin section porosity} = \text{Macroporosity} + 0.2 \times \text{Volume of kaolinite}$$

The variation of microporosity within kaolinite is related to the size of kaolinite booklets by Nadeau & Hurst (1991) and Schulz-Rojahn (1991). In the present investigation, a close relationship is found between sandstone composition and the amount of microporosity associted with kaolinite booklets. In quartz-rich sandstones, the amount of microporosity is more than that in rock-fragment-rich sandstones (Fig. 7.6). The only explanation is that, in quartz-rich sandstones due to better development of quartz cement, the intensity of compaction reduces and there is a better chance for early kaolinite to protect the internal pore spaces from compaction. Figure 7.6 shows that, with increasing amounts of rock fragments, microporosity decreases. With increasing in amount of rock fragments, the amount of quartz cement decreases and consequently compaction index increases and this led to a reduction of microporosity.

7.5 Permeability

Permeability, which indicates the capacity of a reservoir to deliver hydrocarbons, is one of the most important parameter for a petroleum geologist. In the Tirrawarra Sandstone,

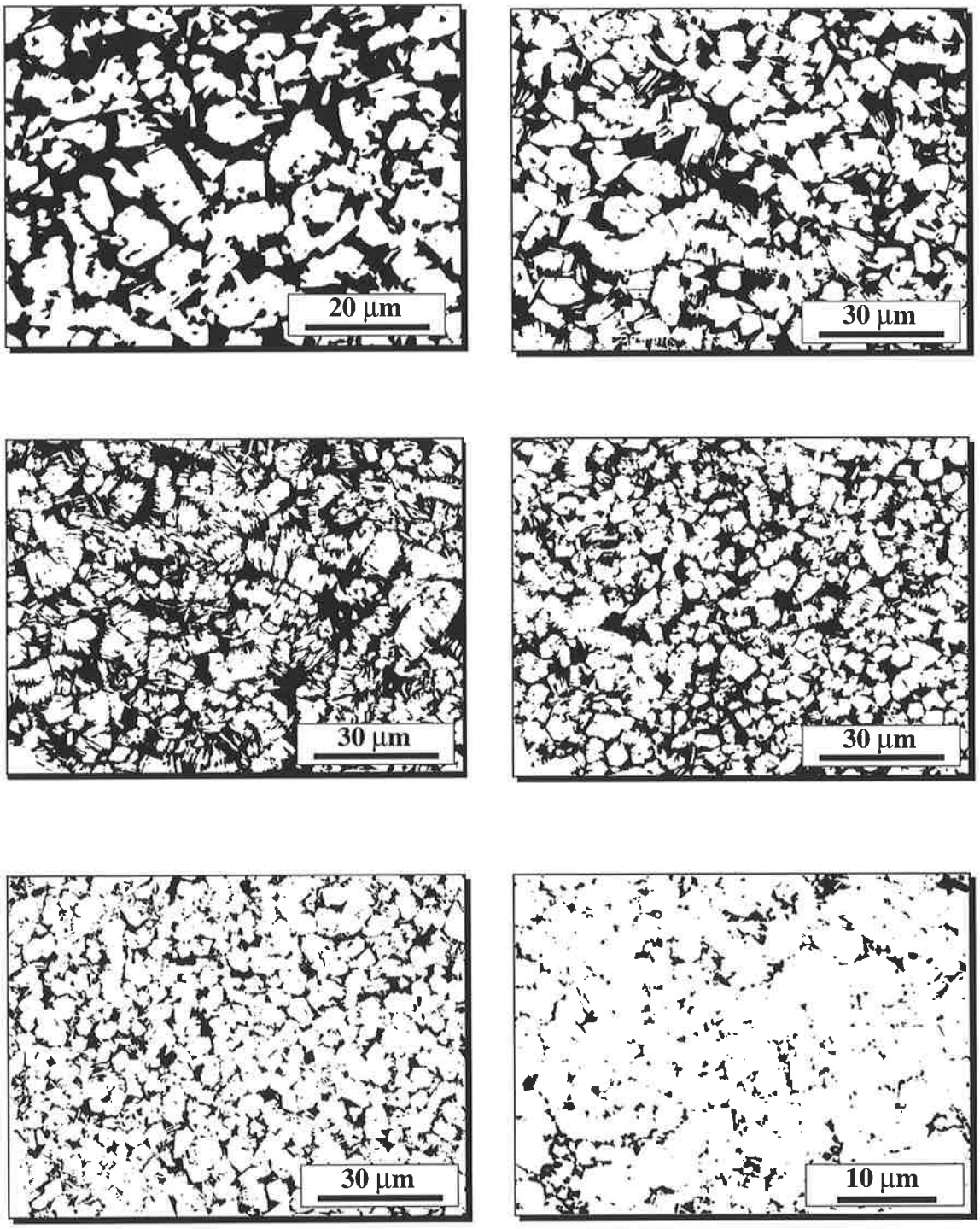

Figure 7.5 - Binary images of kaolinite masses in different samples of the Tirrawarra Sandstone. The proportion of microporosity in kaolinite masses varies in each sample.

permeability is very variable and ranges from near to zero to 340 (mD) and, in general, permeability values are mostly less than 5 mD (Fig. 7.3). In this section, important factors which control permeability in the Tirrawarra Sandstone are discussed.

7.5.1 Factors Controlling Permeability

The variation of permeability is related to a series of factors and there have been many efforts to establish a relationship between the different factors and permeability. McGowen & Bloch (1985), Atkinson et al., (1990) and Bloch (1991) noted the relationship between depositional facies and permeability. They showed that sandstones with initially high permeabilities were deposited in high energy environments. The influence of sandstone composition on porosity and permeability is reported by several workers (Seeman & Scherer, 1984; Scherer, 1987; Pittman & Larese, 1987; Marion et al., 1989; Smosna, 1989; Ahmed et al., 1991). They indicated that sandstone composition controls mechanical and chemical compaction which effects porosity and permeability during burial diagenesis. Dutton & Diggs (1992) indicated that in the Cretaceous Travis Peak Formation of East Texas, permeability decreases significantly with depth. The reduction of permeability with depth is attributed to increasing quartz cement, decreasing secondary porosity, and increasing overburden pressure that leads to occlusion of pore throats. The influence of textural parameters and sedimentary structures on permeability was studied by Chilingar (1964); Berg, (1970); Beard and Weyl (1973); Bloch (1991), Panda & Lake (1994) and Hurst and Rosvoll (1991). Beard and Weyl (1973) mentioned that permeability in unconsolidated sands is controlled by grain size and sorting. As grain size increases and sorting improves, permeability increases, whereas porosity depends on sorting. Many attempts have been made to establish a relationship between porosity and permeability (Berg, 1970; Bloch, 1991). Other parameters which have been used to estimate permeability include surface area of the grain spaces (Carmen, 1937; Johnson et al., 1987; Schwartz & Banavar, 1989), formation factor (Archie, 1942; Katz & Thompson, 1986), capillary pressures (Dullien, 1979; Swanson, 1981; Pittman, 1992), nuclear magnetic resonance relaxation time (Ahmed et al., 1991), sonic transit time (Iverson, 1990; Vernik & Nur, 1991) and pore and pore throat characteristics derived from image analysis of thin sections (Doyen, 1988, Ehrlich et al., 1991; Rezaee & Griffiths, 1996a; Rezaee & Lemon 1996c).

7.5.2 Parameters Controlling Permeability in the Tirrawarra Sandstone

7.5.2.1 Depth

As the variation in depth of the Tirrawarra Sandstone is not significant between different wells in the studied area, the influence of overburden pressure on the Tirrawarra Sandstone samples cannot be assessed. The maximum variation of depth of burial of the Tirrawarra Sandstone in the 14 wells of the Moorari and Fly Lake fields is about 200 m. Figure 4.22 shows there is no significant variation in the permeability with depth.

7.5.2.2 Porosity

A linear relationship exists between core porosity and permeability in the Tirrawarra Sandstone. This relationship is not very strong and data on the plot are rather scattered (Fig. 7.7). For example, for samples with porosity of about 12 percent, permeability ranges from 0.2 to 20 mD. The low correlation between porosity and permeability suggests that other parameters may be involved in controlling permeability. Regarding porosity, as noticed by Dutton & Digga (1992) for Lower Cretaceous Travis Peak Formation, East Texas, one of the reasons for scattered data on the porosity - permeability plot, is the fact that porosity from helium injection includes primary, secondary and microporosity types. Primary porosity has better interconnection between pore spaces than secondary porosity, so primary porosity contributes more to permeability than secondary porosity. In samples with various proportions of different types of porosity, the porosity and permeability trend will not be tight.

7.5.2.3 Diagenetic Parameters

7.5.2.3.1 Cementation

The relation between quartz cementation and permeability in the Tirrawarra Sandstone is not very significant. It seems that samples with less quartz cement (e.g. less than 10%) show higher permeability than samples with higher proportion of quartz cement (e.g. more than 10%). This relationship can be explained by the fact that in sandstones with less than 10% quartz cement, quartz cement prevents compaction, whereas in

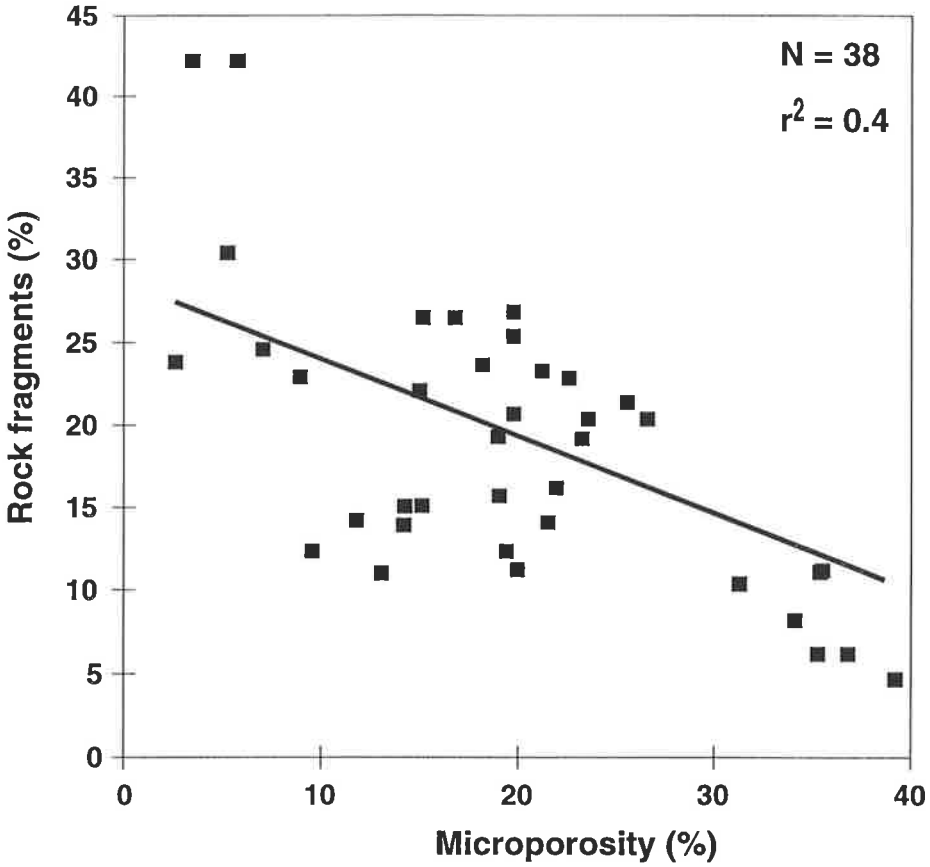

Figure 7.6 - Microporosity measured through BSE image analysis in kaolinite masses plotted against rock fragment percentage (%).

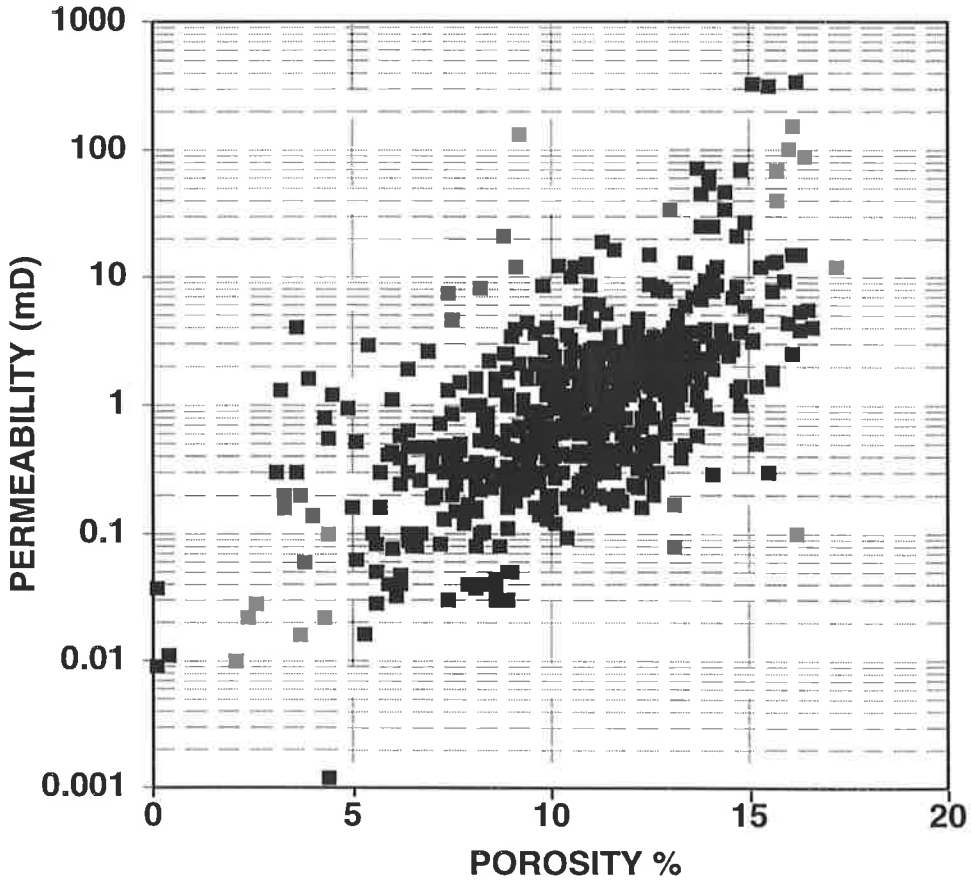

Figure 7.7 - Semi log cross-plot of core porosity (%) versus air core permeability (mD) for about 650 core data points from the Tirrawarra Sandstone.

sandstones with more than 10% quartz cement, the increased cement occludes pore spaces and pore throats.

Pore-filling kaolinite has a significant influence on the permeability of the Tirrawarra Sandstone. The precipitation of pore-filling kaolinite has changed macroporosity to microporosity with smaller pore throats. This process has led to the reduction of permeability. In samples with the same porosity, permeability is much ~~more~~ higher in samples with more macroporosity.

7.5.2.3.2 Compaction

There is a correlation, although scattered, between Compaction Index and permeability (Fig. 7.8). With increasing compaction index, permeability decreases. Compaction index is high in rock fragment-rich sandstones. In these sorts of sandstones, mechanical compaction has led to occlusion of pore spaces and pore throats.

7.5.2.4 Textural Parameters

An increase in grain size and improved sorting in the Tirrawarra Sandstone, increases permeability, but this relation is not significant. According to Beard and Weyl (1973) with increasing grain size and improving sorting, permeability should increase. Departure from this law in the Tirrawarra Sandstone is due to the fact that most of the coarse-grained intervals were deposited in braid-delta environments which are rich in rock fragments and during burial, their permeability decreases due to occlusion of pore throats by plastic deformation of the ductile rock fragments.

7.5.2.5 Sandstone Composition

Sandstone composition in the Tirrawarra Sandstone has a significant influence on the permeability. Figure 7.9 shows that permeability decreases with increasing amounts of rock fragments. The reduction of permeability with increasing the amount of rock fragments is due to the fact that in rock fragment rich sandstones the compaction is higher which leads to porosity reduction and pore throat sealing.

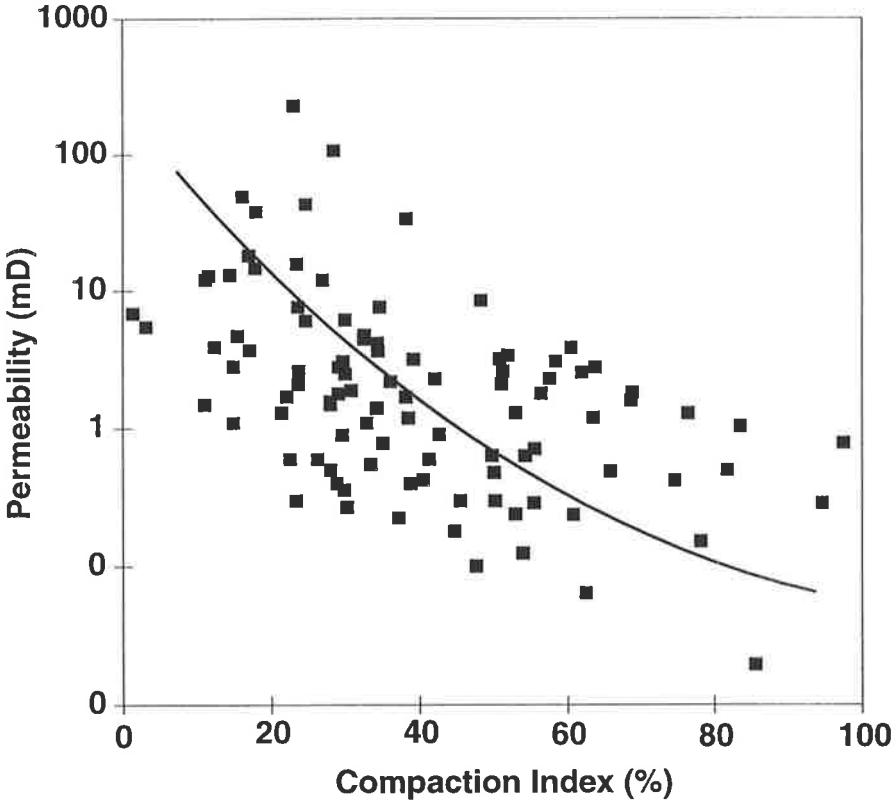

Figure 7.8 - Semi-log cross-plot of Compaction Index (%) versus air core permeability (mD). Permeability decreases with an increase in the Compaction Index.

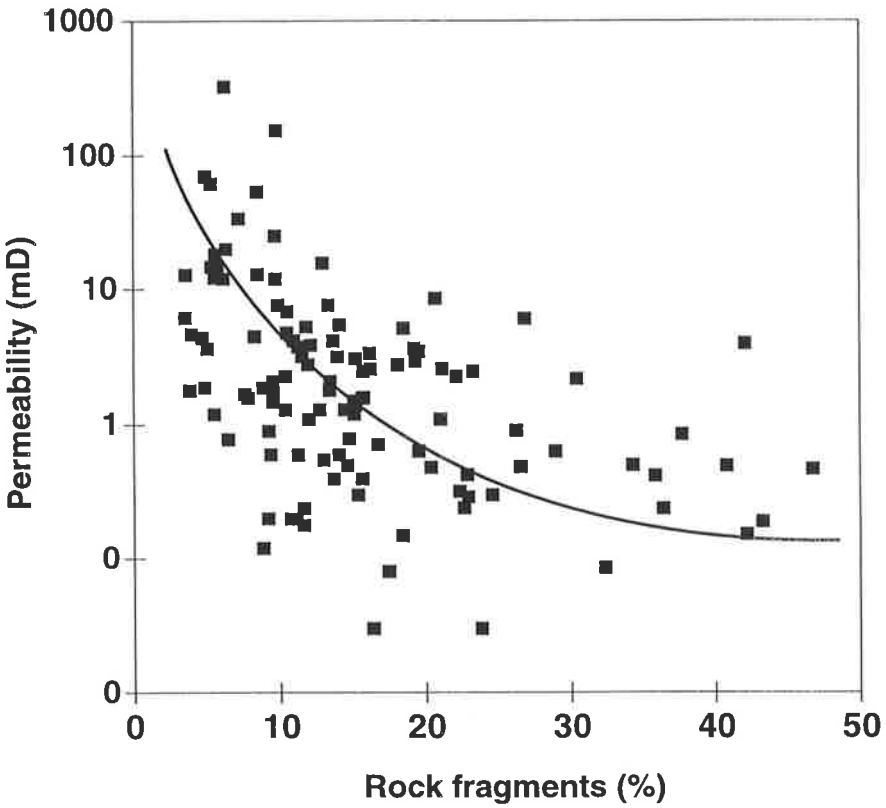

Figure 7.9 - Semi-log cross-plot of rock fragments (%) versus air core permeability (mD). Permeability decreases with increasing proportions of rock fragments.

7.5.2.6 Pore Throat Size

The mercury injection capillary pressures from 31 representative samples are used to indicate the relationship between pore throat sizes and permeability in the Tirrawarra Sandstone.

Washburn (1921) expressed the relationship between mercury capillary pressures and pore throat radii as:

$$P_C = -2\gamma\, Cos\theta / r_c \qquad (3)$$

where P_C is capillary pressures, γ is mercury surface tension, θ is contact angle and r_c is the radius of the pore throat being intruded by mercury. Considering $\gamma = 480$ (dynes/cm), $\theta = 140°$ for mercury/air, the equation becomes

$$P_C = 107/r_c \qquad (4)$$

where P_C is in psi and r_c is in micrometers. In this equation, the contact angle commonly used is 140° (Ritter and Drake, 1945; Juhola and Wiig, 1949).

Swanson (1977) noticed that the complete saturation of effectively interconnected pore spaces with a non-wetting phase (Wood's metal) corresponded to the apex of the hyperbola of a log-log mercury injection capillary pressures curve. Swanson (1981) empirically expressed the relationship between permeability and hyperbola of the log-log mercury injection capillary pressures curve by the equation

$$K_{air}=339(S_{HG}/P_C)_{apex}^{1.691} \qquad (5)$$

where K_{air} is air permeability (mD), S_{HG} is mercury saturation (%) corresponding with the apex of the hyperbola, and P_C is capillary pressures (psi).

Winland developed an empirical relationship between porosity, air permeability and throat size corresponding to a mercury saturation of 35% (r_{35}). This relationship published by Kolodzie (1980) as:

$$Logr_{35} = 0.732 + 0.588LogK_{air} - 0.864Log\phi \qquad (6)$$

where r_{35} is the pore throat corresponding to 35th percentile, K_{air} is uncorrected air permeability (mD) and ϕ is porosity (%).

Pittman (1992) extended the Winland work and introduced a series of equations extracted from multi-regression analysis of mercury injection, permeability and porosity data of 202 sandstone samples. He pointed out that equation 7 yields the best correlation coefficient among permeability, porosity and mercury injection data.

$$LogK = -1.221 + 1.415Log\phi + 1.512Logr_{25} \qquad (7)$$

where K is the uncorrected air permeability (mD), ϕ is porosity (%) and r_{25} is the pore throat corresponding to the 25th percentile of saturation on a cumulative mercury injection plot.

Permeability estimated from the Winland and Pittman equations for the Tirrawarra Sandstone show an excellent correlation with core permeability (Figs. 7.10a-b). Permeability from the Winland equation using *r35* has a correlation coefficient (r^2) of about 0.99 and permeability from the Pittman equation using *r25* has a correlation coefficient (r^2) of about 0.97.

7.6 The Effect of Sedimentary Environments on Porosity and Permeability

Figure 4.17 shows that permeability increases from deposits of the braided system to those of the aeolian environment. This increase corresponds with increasing effective porosity as measured by point counting in thin sections. The relationship between core porosity (total porosity) and permeability, however, is not simple. Although some samples from the braid-delta environment have a higher porosity than those from the aeolian environment, their permeability is lower. This is related to the presence of microporosity, which is more abundant in the sediments from the braided system than in the aeolian sandstones.

The trends of increase in permeability and effective porosity and the reduction of microporosity, in samples from braided to aeolian environments are explicable in terms of the processes in each environment which control diagenetic events such as compaction and cementation. Quartz overgrowths lead to porosity and permeability

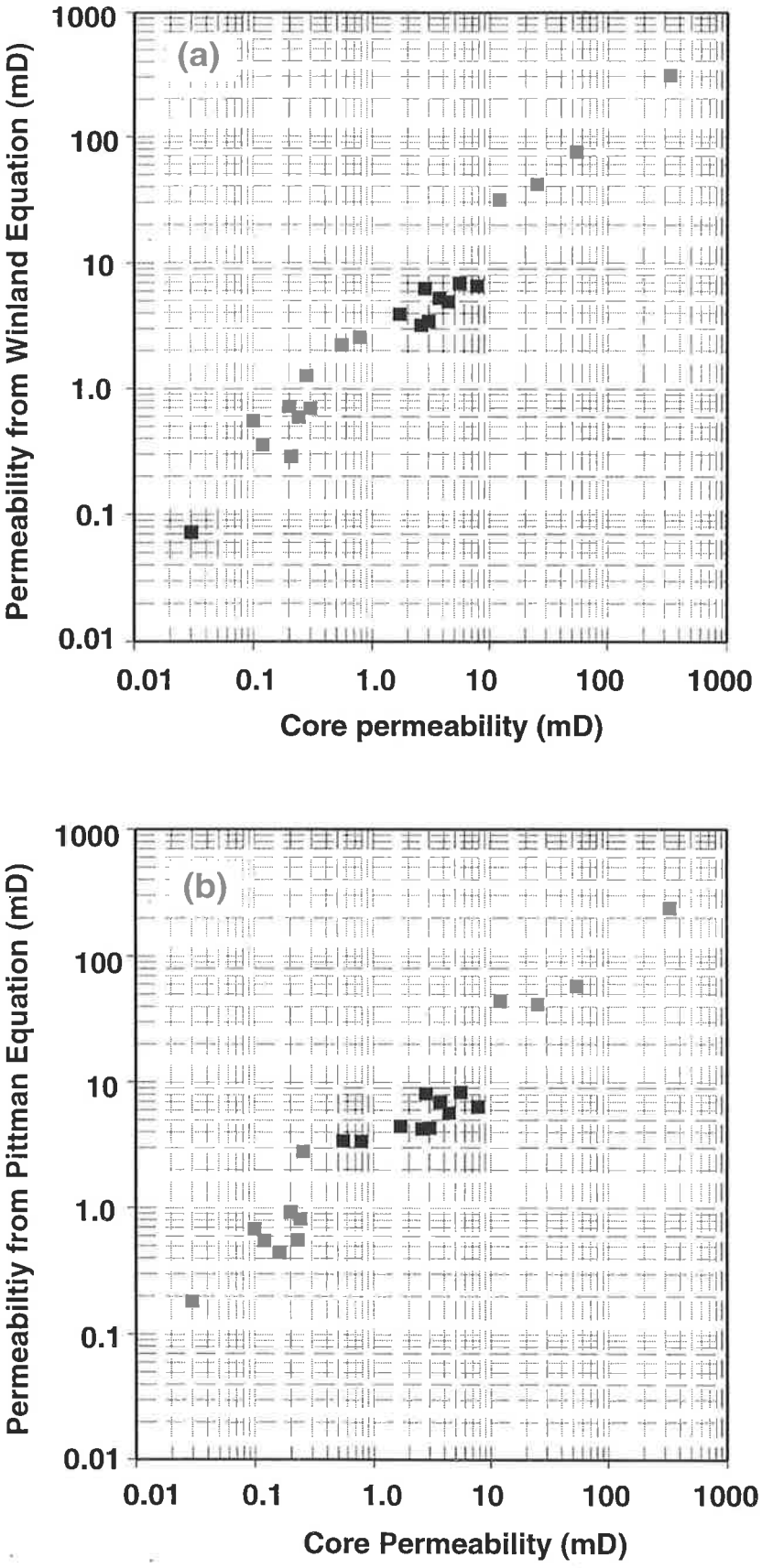

Figure 7.10a-b - Permeability calculated from the Winland (**a**) and Pittman (**b**) methods versus core permeability (mD).

reduction, but cementation has a smaller effect than compaction on porosity and permeability reduction. This is related to the presence of remnant intergranular porosity between cement crystal faces, even in samples with a high rate of quartz cementation (Plate 21). Porosity reduction in sandstones by cementation has been studied by many authors to quantify this diagenetic process (Leder and Park, 1986; Bloch et al., 1990). In the Tirrawarra Sandstone, the effect of early cementation on preservation of intergranular volume is very clear. In the aeolian and meandering depositional environments, which are relatively cleaner than the other facies, early quartz cementation is pervasive. In these depositional facies, IGV is greater than in the medial and distal parts of the braid-delta. IGV preservation in samples from the aeolian and meandering environments is due to inhibition of later compaction by early quartz cementation. As described by Rezaee and Tingate (1996a), quartz cementation in the Tirrawarra Sandstone has both positive and negative effects on reservoir quality. Thus, early quartz cementation prevents porosity loss by compaction, whereas late quartz cement occludes the remaining porosity.

Mechanical compaction has had a significant influence on porosity and permeability reduction. As the intensity of compaction increases, indicated by Compaction Index, porosity and permeability decreases. The reduction of porosity and permeability by compaction is due to occlusion of pore spaces and the closing of pore throats by plastic deformation of rock fragments.

7.7 CONCLUSIONS

Three types of porosity were identified in the Tirrawarra Sandstone, including primary intergranular, secondary and microporosity. Primary porosity is dominant in quartz-rich sandstones and microporosity was present mainly in kaolinite masses. Core porosities measured in the Tirrawarra Sandstone range up to 20 percent while associated permeabilities may be as high as 340 mD. On average, however, the Tirrawarra Sandstone is characterised by low porosity and permeability. Core porosity is mostly between 10 to 12%. Quantification of porosity by BSE image analysis indicates an average value of about 20% microporosity for kaolinite masses in the Tirrawarra Sandstone.

In the Tirrawarra Sandstone, permeability is very variable and in general permeability values are mostly less than 5 mD. Parameters controlling permeability in

the Tirrawarra Sandstone at a given depth, are mechanical compaction and quartz cementation which, in turn, are controlled by sandstone composition.

The results of this study indicate that permeability can be estimated for the Tirrawarra Sandstone with high precision ($r^2 = 0.99$) using mercury injection capillary pressure followed by Winland and Pittman equations. Only small chips of samples are needed for mercury injection analysis, so that it is possible to estimate the permeability of intervals where no core is available.

CHAPTER EIGHT

CONTROLS ON PORE GEOMETRY

8.1 Introduction

Reservoir properties such as porosity and permeability are controlled by the size and arrangement of pores and pore throats (Wardlaw, 1976; McCreesh et al., 1991; Pittman, 1992; Ehrenberg & Boassen, 1993; Bliefnick & Kaldi, 1996). Detailed study of pore geometry is needed to give a better understanding of reservoir rocks and how they are likely to perform during production. To find new ways to predict the pore geometry of reservoir formations, the factors which control pore geometry (depositional fabrics or/and post depositional events) should also be quantitatively studied. Petrographic image analysis procedures (Ehrlich et al., 1984; Ehrlich et al., 1991) enable the quantitative evaluation of characteristics such as pore surface area, pore diameter and pore perimeter. The Mercury injection (Purcell, 1949) can provide the pore throat sizes of the samples.

The role of diagenetic events on pore geometry is indicated by many workers (e.g. Pittman, 1979; Tingate & Luo, 1992; Rezaee & Lemon, 1996c) and several workers in the Cooper Basin have studied the influence of diagenetic events on the porosity and permeability of the Permian reservoir rocks (Farrow, 1989; Schulz-Rojahn & Phillips, 1989; Stuart et al., 1990; Rezaee, 1994). There is, however, a lack of a quantitative approach in the literature to evaluate the influence of depositional environments and post-depositional events on the pore geometry in sandstone reservoirs.

In the present work, pore space characteristics of the Tirrawarra Sandstone were evaluated with petrographic image analysis and mercury injection to indicate the size and distribution of pore throats. These data were then integrated with petrographic point count data, depositional facies information and core porosity and permeability values. The results show that, in the Tirrawarra Sandstone, depositional facies influence

sandstone texture and composition and composition controls diagenetic events such as mechanical compaction and cementation which in turn control pore geometry.

8.2 Classification of the Tirrawarra Sandstone

Petrographical observations of 130 thin sections of the Tirrawarra Sandstone enabled me to separate the samples based on their porosity types and texture. Initially, I separated the samples to 3 groups. Group 1 was samples with dominantly primary porosity, group 2 dominantly secondary porosity and group 3, microporosity. By further observations, I divided the samples to eight classes as follows:

- Class 1: samples dominated by well-connected primary porosity,
- Class 2: same as Class 1 but pores and grain size are smaller,
- Class 3: primary porosity and microporosity, nearly in the same proportion, are the dominant pores,
- Class 4: secondary porosity and microporosity are dominant,
- Class 5: primary porosity extensively reduced by quartz cementation is dominant pore spaces,
- Class 6: microporosity is dominant,
- Class 7: microporosity plus minor secondary porosity are dominant,
- Class 8: minor microporosity associated with highly-compacted kaolinite patches is dominant.

After classification of all samples, I selected some representatives from each class for more detailed examination, including image analysis and mercury injection. In the following sections all characteristics of each class are described in detail. Petrographic point count data for each of the eight classes are presented in Table 8.1, along with average porosity and permeability data.

Table 8.1 - Averaged core porosity, permeability and point count data for each class.

	Class 1	Class 2	Class 3	Class 4	Class 5	Class 6	Class 7	Class 8
Core porosity (%)	14.6	11.1	13.9	11.3	9.7	13.3	10.9	7.4
Permeability (mD)	66.2	15.6	3.6	2.5	3.3	0.9	0.4	0.3
Quartz (%)	88.3	89.8	79.7	77.7	87.7	83.4	80.3	67.5
Total rock fragment (%)	11.7	10.2	20.3	22.3	12.3	16.6	19.7	32.5
Quartz cement (%)	10.5	9.1	8.9	9.2	14	10.2	10.9	6.1
Macroporosity (%)	13.3	11.6	6.7	6.4	6.4	1.3	2.8	0.7
Microporosity (%)	1.4	2.4	4.7	3.8	1.2	9.1	5.4	3.6
Compaction Index (%)	22.2	18.4	36.8	43.0	27.6	47.7	38.3	59
Grain size (mm)	0.37	0.26	0.44	0.42	0.48	0.31	0.36	0.6
Sorting (σ)	0.35	0.51	0.57	0.65	0.54	0.6	0.69	1.4

8.2.1 Class Characteristics

Class 1 contains mostly primary intergranular porosity with a successive decrease in primary porosity towards Class 8 with a corresponding increase in the relative proportions of secondary porosity and microporosity (Plates 23-30). Petrographic image analysis and mercury injection data (Appendix 8) indicate that each class has different pore space and pore throat characteristics. In general, as porosity changes from dominantly macroporosity to dominantly microporosity from Class 1 to Class 8, pore size and pore throat size decrease. The reduction of pore throat size reduces permeability.

In this classification, macropores refer to any pore spaces that can be detected optically and microporosity is restricted to pore spaces among kaolinite booklets.

8.2.1.1 Pore area and pore throat characteristics

Class 1: Pore spaces of Class 1 samples are dominantly primary macroporosity, preserved between the euhedral faces of quartz cement (Plate 23A-E). Average point count porosity is about 13.3 percent. A pore throat curve displays very good sorting and in most cases the throat sizes are more than 10 microns (Plate 23). As seen in the binary

Plate 23

Micrographs, Image Analysis & Mercury Injection Data of Class 1

A - Black and white binary image of a representative sample from Class 1 (black = porosity & white = grain). There is lack of microporosity and macropores are mostly primary and are relatively well connected. Sample M3-9412, Moorari-3, 2823.6 m. Scale bar = 500 μm.

B - Photomicrograph of a representative sample from Class 1 containing dominantly primary macroporosity which survives between the euhedral faces of quartz cement. Compositionally, Class 1 samples have relatively a low ductile rock fragment content and are mostly medium-grained, well sorted and well rounded quartzarenites. Sample M3-9412, Moorari-3, 2823.6 m. Scale bar = 1000 μm.

C - Close-up of view of (**B**). Note that some of the pore spaces are oversized secondary porosity. Sample M3-9412, Moorari-3, 2823.6 m. Scale bar = 500 μm.

D - SEM view of a Class 1 sample. Dominant porosity is intergranular porosity. Sample M3-9412, Moorari-3, 2823.6 m. Scale bar = 200 μm.

E - Close-up of view of (**D**). Intergranular porosity is well preserved between quartz overgrowths. Sample M3-9412, Moorari-3, 2823.6 m. Scale bar = 200 μm.

F - In Class 1 samples, the size of pore areas exhibits a multimodal distribution. The pore area size varies from about 6000 to more than 33000 micron^2. Small pore sizes reflect smaller intergranular pores. Large pores are mainly caused by enlarged secondary pore spaces.

G - Pore diameters for typical Class 1 have a broad distribution and the pore perimeters are bimodal. Mean pore diameter and mean pore perimeter are 210 and 670 μm respectively.

H - Mercury injection capillary pressure curve of Class 1 representative sample.

I - The pore throat curve displays a good sorting and the size of most of pore throats are more than 10 μm.

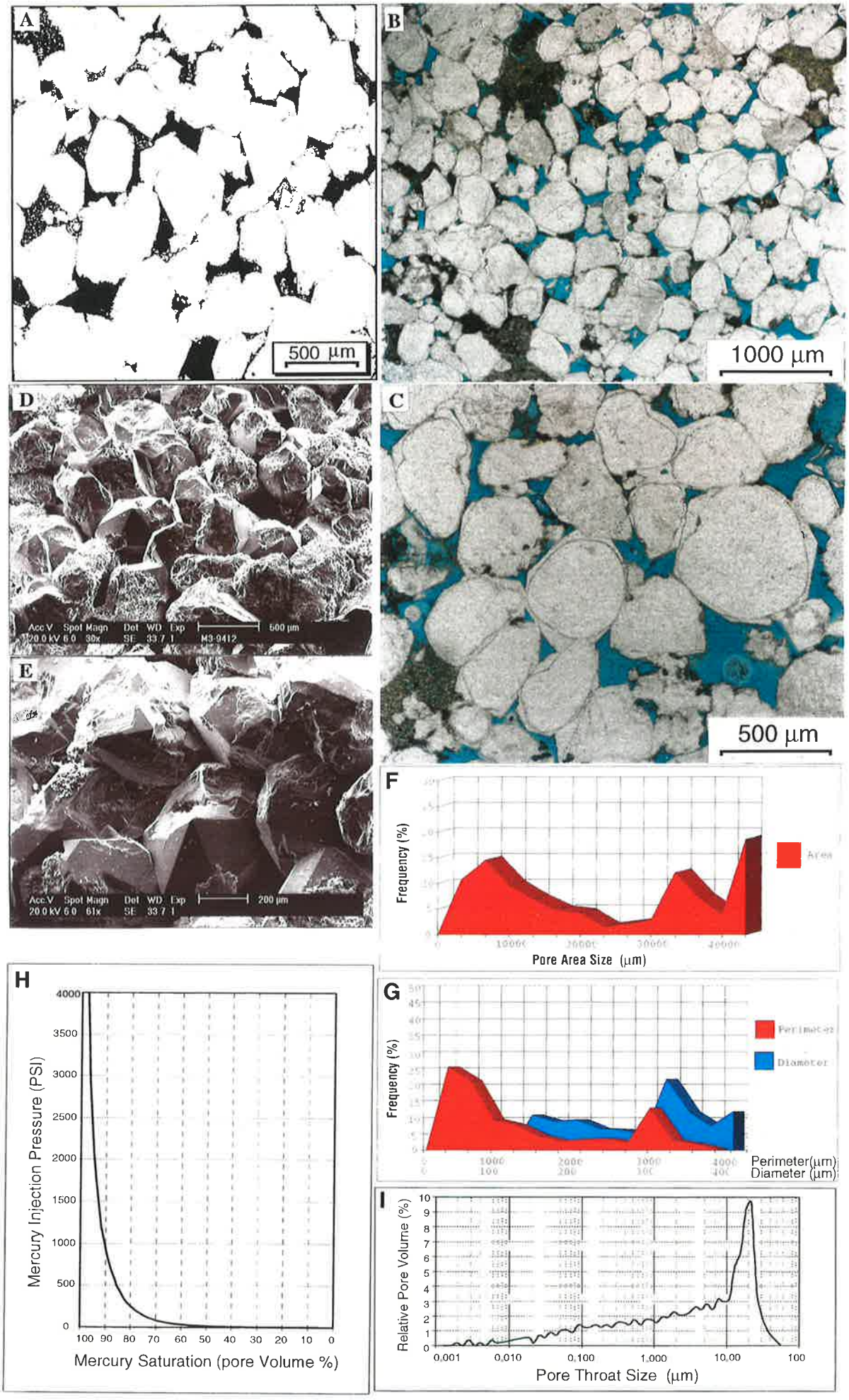
A
500 µm
B
1000 µm
D
Acc.V Spot Magn Det WD Exp
20.0 kV 6.0 30x SE 33.7 1 M3-9412
500 µm
C
500 µm
E
Acc.V Spot Magn Det WD Exp
20.0 kV 6.0 61x SE 33.7 1
200 µm
F
Frequency (%)
Area
Pore Area Size (µm)
H
Mercury Injection Pressure (PSI)
4000
3500
3000
2500
2000
1500
1000
500
0
100 90 80 70 60 50 40 30 20 10 0
Mercury Saturation (pore Volume %)
G
Frequency (%)
Perimeter
Diameter
Perimeter(µm)
Diameter (µm)
I
Relative Pore Volume (%)
10
9
8
7
6
5
4
3
2
1
0
0,001 0,010 0,100 1,000 10,00 100
Pore Throat Size (µm)

image (Plate 23A), there is lack of microporosity while macropores are relatively well connected and mostly primary in origin. Mean pore area in two dimensions is relatively large, about 36000 micron^2 (Plate 23). Mean pore diameter and mean pore perimeter are 210 and 670 microns respectively.

Class 2: Macroporosity is dominant in Class 2 samples (Plate 24A-E) but the pores are smaller than those in Class 1 (Plate 24A-E). Average point count porosity is about 11.6 percent. Pore spaces show relatively good connection through pore throats which in turn display good sorting, mostly about 2 microns (Plate 24). Mean pore space area is about 30860 micron^2 (Plate 24). Mean pore diameter and mean pore perimeter are 172 and 352 microns respectively (Plate 24).

Class 3: Pore spaces of the Class 3 samples include both macro and microporosity in nearly equal proportions (Plate 25A-E). Macroporosity in these samples includes mainly intergranular porosity and minor secondary pores formed from the dissolution of labile detrital grains. Average point count porosity is about 6.7 percent and average microporosity is about 4.7 percent. Pore throats are mostly about 2 microns and display moderate sorting with a tendency towards smaller pore throats (Plate 25). Mean pore space area is relatively large and is about 12720 micron^2. Mean pore diameter is 130 microns and mean pore perimeter is 420 microns.

Class 4: Primary and secondary macroporosity and microporosity are in nearly equal proportions in Class 4 samples (Plate 26A-E) with secondary porosity more abundant than primary porosity. Primary porosity includes relatively small pores remaining after incomplete development of quartz cement. Larger secondary pores formed from dissolution of unstable grains. Average point count porosity is about 6.4 percent and average microporosity is about 3.8 percent. The pore throat curve is biased towards finer throat sizes (Plate 26) with the skewness related to presence of small pores with smaller pore throats. Most of the pore throat sizes are around 1.5 microns (Plate 26). Mean pore space area is about 7890 micron^2 (Plate 26). Mean pore diameter and mean pore perimeter are 102 and 327 microns respectively (Plate 26).

Class 5: In this class, macroporosity is dominant but consists of mostly relatively small primary pores left after extensive quartz cementation (Plate 27A-E). This extensive quartz cement reduces original pore sizes from those in Class 1. The average point count porosity is about 5.4 percent and mean pore space area is about 2870 micron^2 (Plate 27). Mean pore diameter and mean pore perimeter are 204 and 658

Plate 24

Micrographs, Image Analysis & Mercury Injection Data of Class 2

A - Black and white binary image of a representative sample from Class 2 (black = porosity & white = grain). Pores in this class are smaller than those of Class 1. Sample F6-9398, Fly Lake-6, 2819.5 m. Scale bar = 500 μm.

B - Macroporosity is the dominant pore spaces in Class 2 samples. Sample F6-9398, Fly Lake-6, 2819.5 m. Scale bar = 1000 μm.

C - Close-up of view of (**B**). Macroporosity in Class 2 samples include both primary and secondary porosity.

D - SEM view of a Class 2 sample. Sample F6-9398, Fly Lake-6, 2819.5 m. Scale bar = 500 μm.

E - Close-up of view of (**D**).

F - Pore space area due to presence of small primary porosity and relatively larger secondary porosity is nearly bimodal. Mean pore space area is about 30860 micron^2.

G - In Class 2 samples, mean pore diameter and mean pore perimeter are respectively 172 and 352 μm.

H - Mercury injection capillary pressure curve of Class 2 representative sample.

I - Pore throats display a good sorting and are mainly about 2 μm.

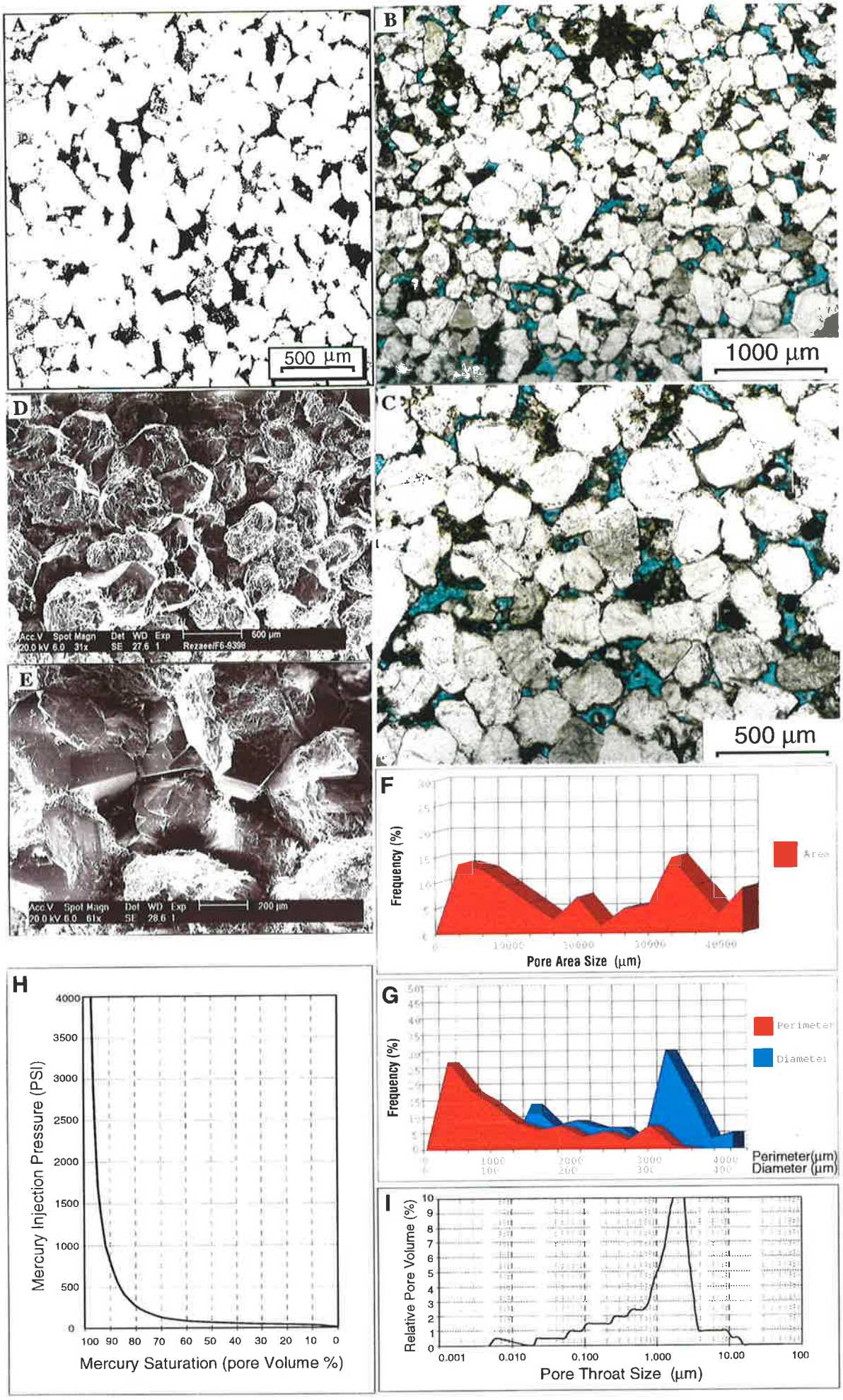
A
500 µm
B
1000 µm
C
500 µm
D
Acc.V Spot Magn Det WD Exp
20.0 kV 6.0 31x SE 27.6 1
500 µm
Rezaee/F6-9399
E
Acc.V Spot Magn Det WD Exp
20.0 kV 6.0 61x SE 28.6 1
200 µm
F
Frequency (%)
Area
Pore Area Size (µm)
G
Frequency (%)
Perimeter
Diameter
Perimeter(µm)
Diameter (µm)
H
Mercury Injection Pressure (PSI)
4000
3500
3000
2500
2000
1500
1000
500
0
100 90 80 70 60 50 40 30 20 10 0
Mercury Saturation (pore Volume %)
I
Relative Pore Volume (%)
10
9
8
7
6
5
4
3
2
1
0
0.001 0.010 0.100 1.000 10.00 100
Pore Throat Size (µm)

microns respectively (Plate 27). The pore throat curve shows relatively good sorting with pore throat sizes around 1.5 microns (Plate 27).

Class 6: Apart from a few very small macropores, microporosity is dominant in this class (Plate 28A-E). Mean pore space area is about 340 micron^2 (Plate 28). Mean pore diameter and mean pore perimeter are 21 and 57 microns respectively (Plate 28). The pore throat curve shows poor sorting with throat sizes between 0.2 and 0.7 microns (Plate 28).

Class 7: Pore spaces are dominantly micropores with some isolated secondary porosity generated from unstable grain dissolution (Plate 29A-E). Microporosity is relatively more important than macroporosity. Mean pore space area is about 11240 micron^2 (Plate 29). Mean pore diameter and mean pore perimeter are 121 and 396 microns respectively (Plate 29). Pore throat size is about 0.4 microns (Plate 29) and the throat curve is skewed toward smaller pore sizes.

Class 8: Micropores are the dominant porosity in this class (Plate 30A-E) which can be separated from Class 7 by a higher Compaction Index and less microporosity among kaolinite booklets. Mean pore space area is about 430 micron^2 (Plate 30). Mean pore diameter and mean pore perimeter are 24 and 75 microns respectively (Plate 30). The pore throat curve shows poor sorting with throat sizes mostly from 0.1 to 0.5 microns (Plate 30).

Mean pore area, mean pore perimeter and mean pore diameter and pore throat size of each of the eight classes are summarised in Table 8.2.

Table 8.2 - Average of pore characteristics and dominant pore throat size for each class.

	Pore area (μm^2)	Pore diameter (μm)	Pore perimeter (μm)	Pore throat (μm)
Class 1	36000	210	670	>10
Class 2	30860	172	352	2
Class 3	12720	130	417	2
Class 4	7890	102	327	1.5
Class 5	2870	204	658	1.5
Class 6	343	21	57	0.2-0.7
Class 7	11240	121	396	0.4
Class 8	430	24	75	0.1-0.5

Plate 25

Micrographs, Image Analysis & Mercury Injection Data of Class 3

A - Black and white binary image of a representative sample of Class 3 (black = porosity & white = grain).

B - Macroporosity and microporosity nearly in the same proportion form pore spaces of the Class 3 samples. Macroporosity includes both intergranular and secondary porosity formed from dissolution of labile detrital grains. Texturally, Class 3 samples are medium to fine-grained, moderately-sorted sandstones. Compositionally, they are mostly sublitharenitic.

C - Close-up of view of (**B**).

D - SEM view of a representative sample Class 3.

E - Close-up of view of (**D**). Kaolinite masses contain an average of 20% microporosity.

F - Pore space area is bimodal in Class 3 samples. The smaller pores have an area of about 5000 micron^2 and the bigger ones about 33000 micron^2. Mean pore space area is relatively large about 12720 micron^2.

G - Pore diameter show a bimodal distribution and ranges from 150 to 350 μm. Mean pore diameter is 130 and mean pore perimeter is 420 μm.

H - Mercury injection capillary pressure curve of Class 3 representative sample.

I - Pore throats are mostly about 2 microns and display moderate sorting with a tendency towards smaller pore throats

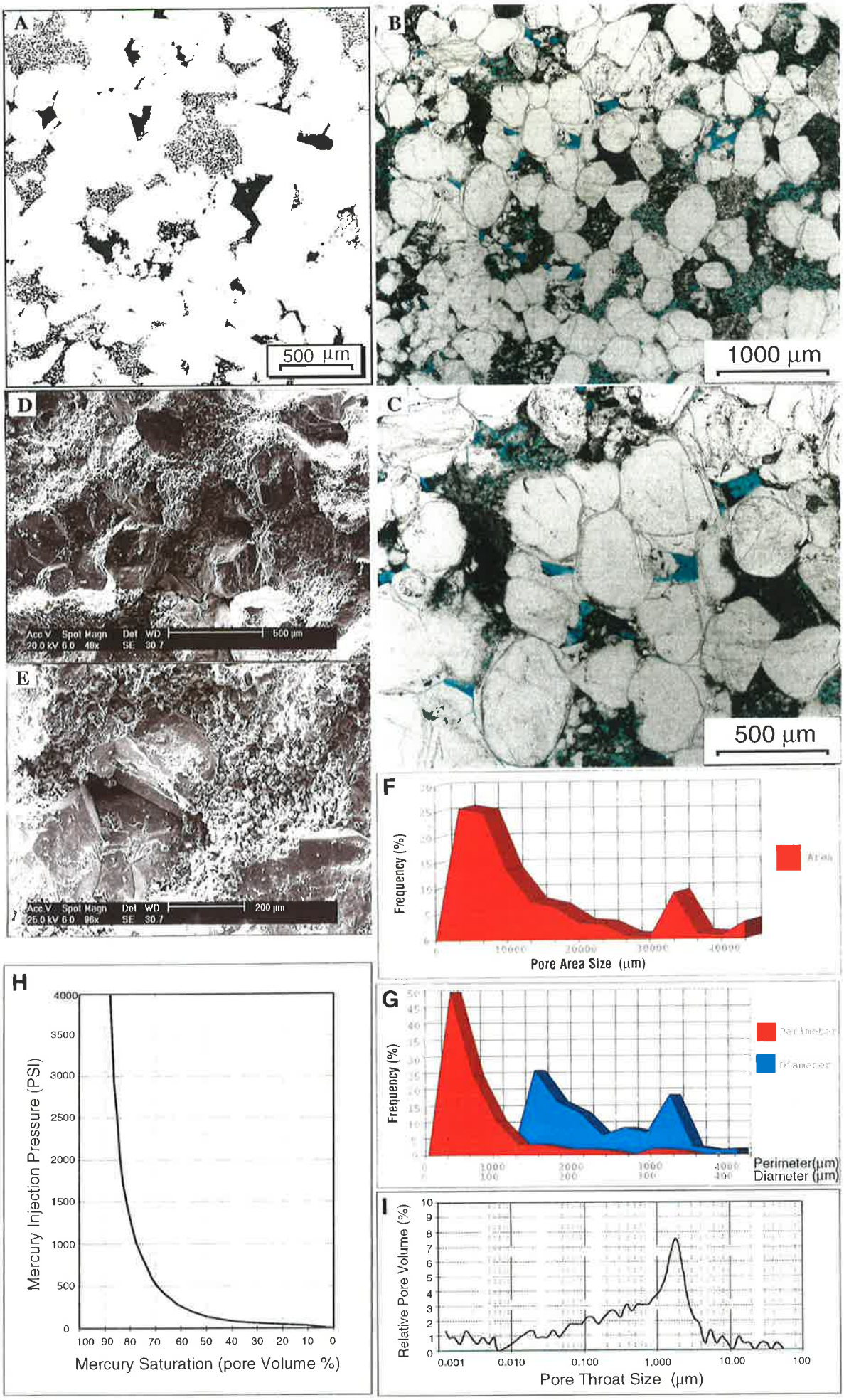
A
500 µm
B
1000 µm
C
500 µm
D
Acc.V Spot Magn Det WD
20.0 kV 6.0 48x SE 30.7
500 µm
E
Acc.V Spot Magn Det WD
25.0 kV 6.0 96x SE 30.7
200 µm
F
Frequency (%)
Area
Pore Area Size (µm)
G
Frequency (%)
Perimeter
Diameter
Perimeter(µm)
Diameter (µm)
H
Mercury Injection Pressure (PSI)
4000
3500
3000
2500
2000
1500
1000
500
0
100 90 80 70 60 50 40 30 20 10 0
Mercury Saturation (pore Volume %)
I
Relative Pore Volume (%)
10
9
8
7
6
5
4
3
2
1
0
0.001 0.010 0.100 1.000 10.00 100
Pore Throat Size (µm)

8.2.1.2 Porosity and Permeability Characteristics

While the porosity-permeability cross-plot appears as a continuum, ambient core porosity and permeability within each class exhibit a distinct range and the samples of each class plot as a relatively distinct area on that cross-plot (Fig. 8.1a). Samples which belong to Class 1 occupy the relatively high porosity and high permeability area, whereas Class 8 samples occupy the lowest part of the diagram in the area with low porosity and low permeability. In this regard it is possible to divide Figure 8.1a into eight parts as HH, MH, HM, MM, LM, HL, ML, and LL (Fig. 8.1b). The first letter of this nomenclature refers to porosity, from relatively High (H) to Medium (M) and Low (L) and the second letter stands for permeability, from relatively High (H) to Medium (M) and Low (L), (e.g. LH refers to samples with low porosity and high permeability). The Class 1 samples are the best parts of the Tirrawarra Sandstone reservoir and have the highest porosity and permeability (HH). The average ambient core porosity and permeability of Class 1 are 14.6 percent and 66.2 millidarcies (mD).

Class 2 samples are the second best Tirrawarra Sandstone reservoir type, with moderate porosity and high permeability (MH). Average ambient core porosity of the samples of this class is 11.1 percent and average ambient core permeability is 15.6 mD.

The samples of Class 3 show high porosity and moderate permeability (HM) with average ambient porosity of 13.9 percent and permeability of 3.6 mD. Class 4 samples with moderate porosity and permeability occupy the MM area of Figure 8.1a. Average ambient core porosity is 11.3 percent and average ambient core permeability is 2.5 mD. Class 5 samples have low porosity and moderate permeability (LM) with an average ambient core porosity and permeability of 9.7 percent and 3.3 mD respectively.

The samples which belong to Class 6 show moderate to high porosity and low permeability and plot in the HL area of the Figure 8.1a. Average ambient core porosity and permeability of the samples of Class 6 are 14.3 percent and 0.9 mD respectively. Class 7 samples present moderate porosity and low permeability (ML) with average ambient core porosity and permeability of 10.9 percent and 0.4 mD respectively. Class 8 samples have the lowest porosity and permeability (LL) with average ambient core porosity 8.4 percent and permeability 0.3 mD.

Plate 26

Micrographs, Image Analysis & Mercury Injection Data of Class 4

A - Black and white binary image of a representative sample of Class 4 (black = porosity & white = grain). There is a large amount of microporosity associated with kaolinite (stippled areas). Sample M1-9637, Moorari-1, 2891 m. Scale bar = 500 μm.

B - In Class 4 samples, pore spaces are primary and secondary macroporosity and microporosity nearly in the same proportion. Primary porosity include relatively small pores which are retained between euhedral faces of quartz cement. Larger secondary porosity formed from dissolution of chemically unstable grains. Class 4 samples are medium to coarse-grained, moderately-sorted sandstones. Compositionally, they are sublitharenites. Sample M1-9637, Moorari-1, 2891 m. Scale bar = 1000 μm.

C - Close-up of view of (**B**). Scale bar = 500 μm.

D - SEM view of Class 4 representative sample. Sample M1-9637, Moorari-1, 2891 m. Scale bar = 500 μm.

E - Close-up of view of (**D**).

F - The variation of pore area size in Class 4 samples is due to presence of different pores with different pore area sizes. Mean pore space area is about 7890 micron^2.

G - Mean pore diameter and mean pore perimeter are 102 and 327 μm respectively.

H - Mercury injection capillary pressure curve of Class 4 representative sample.

I - Most of pore throat sizes for Class 4 samples are around 1.5 μm. The pore throat curve skewed towards finer pore throat sizes between the small pores.

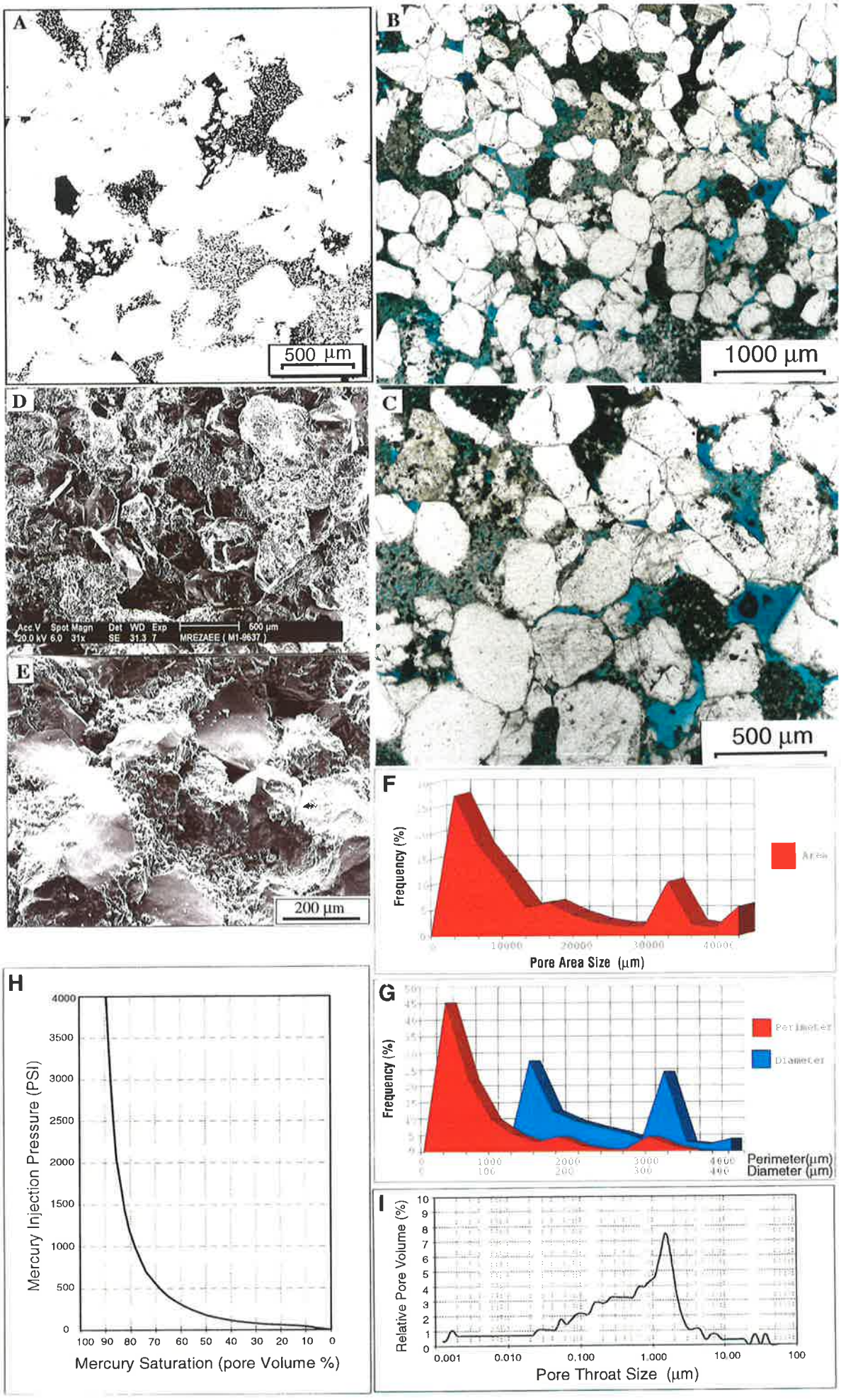
A
500 µm
B
1000 µm
D
Acc.V Spot Magn Det WD Exp 600 µm
20.0 kV 6.0 31x SE 31.3 7 MREZAEE (M1-8637)
C
500 µm
E
200 µm
F
Frequency (%)
Area
Pore Area Size (µm)
H
Mercury Injection Pressure (PSI)
4000
3500
3000
2500
2000
1500
1000
500
0
100 90 80 70 60 50 40 30 20 10 0
Mercury Saturation (pore Volume %)
G
Frequency (%)
Perimeter
Diameter
Perimeter(µm)
Diameter (µm)
I
Relative Pore Volume (%)
10
9
8
7
6
5
4
3
2
1
0
0.001 0.010 0.100 1.000 10.00 100
Pore Throat Size (µm)

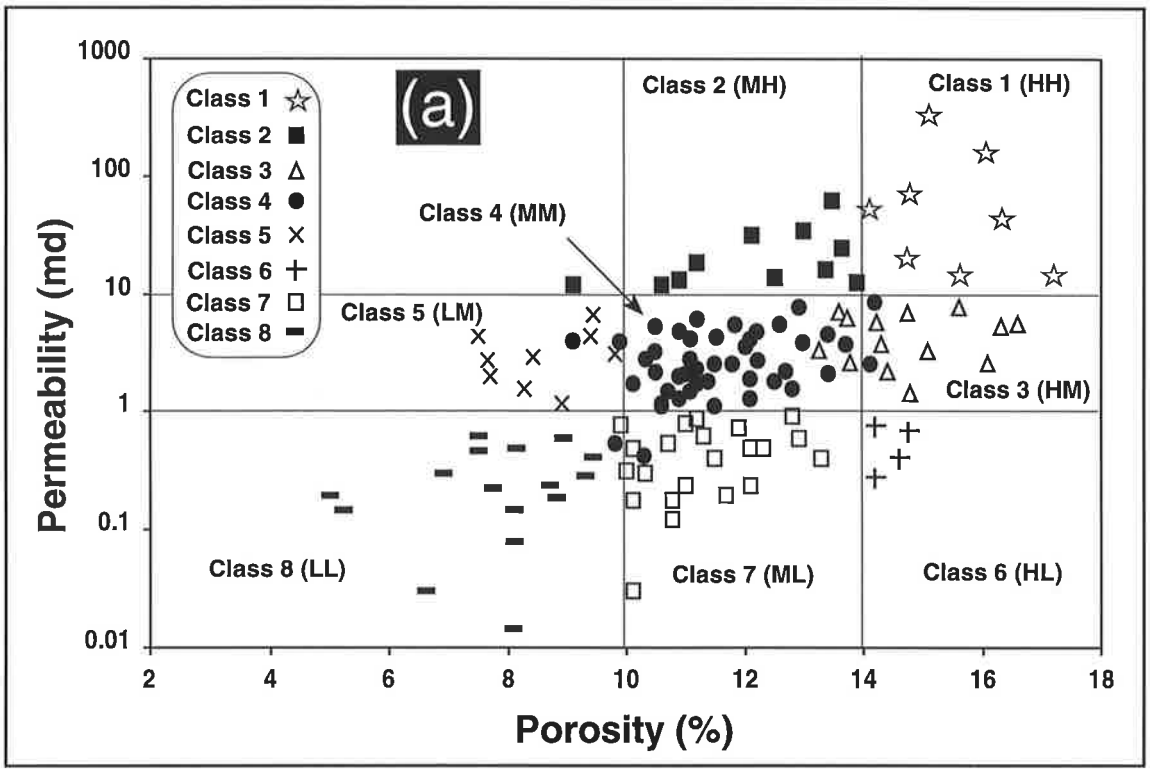

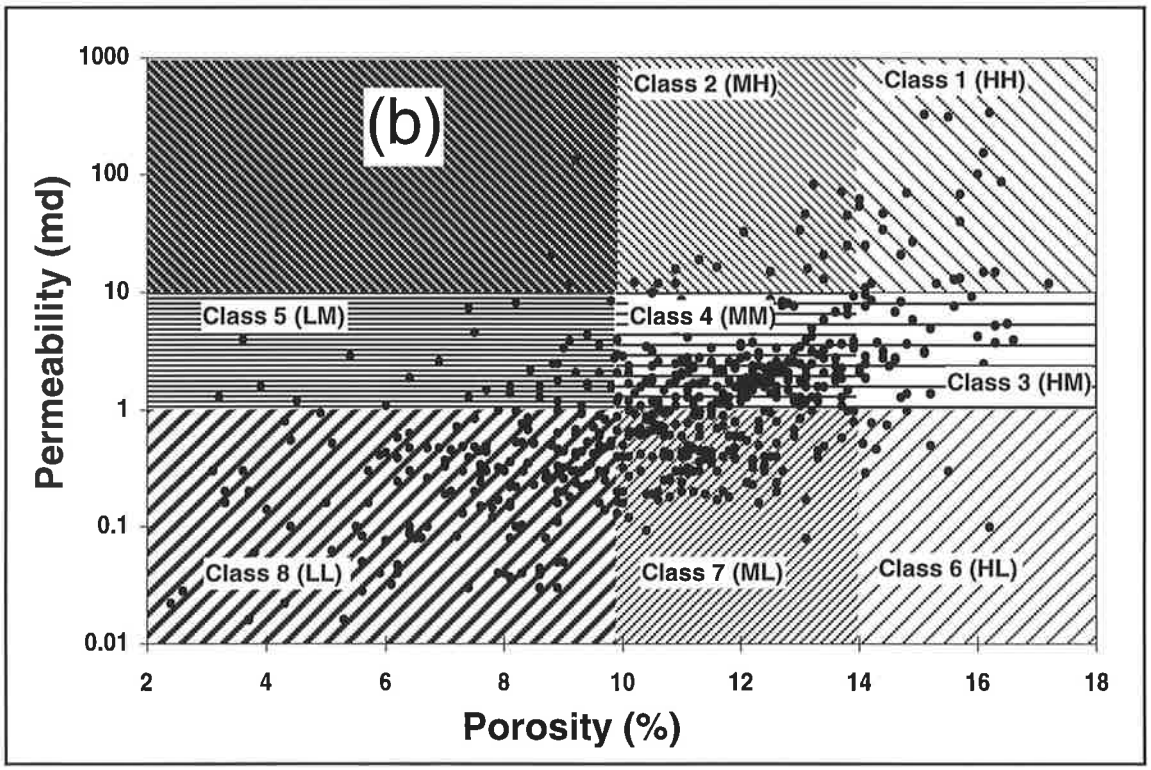

Figures 8.1a-b - Semi-log cross plot of porosity versus permeability. **a**) semi-log cross plot of porosity versus permeability for about 130 Tirrawarra Sandstone samples. The samples of each class occupy reasonably well-defined parts of the plot. Class 1 samples mainly occupy areas with relatively high porosity and permeability (HH) while class 8 samples mainly occur within areas of relatively low porosity and permeability (LL). **b**) Semi-log cross plot of porosity versus permeability of about 500 Tirrawarra Sandstone samples which is overlapped with classified area.

8.2.1.3 Textural and Environmental Characteristics

Texturally, Class 1 samples are medium-grained, well sorted and well rounded. Compositionally, Class 1 samples are relatively low in ductile rock fragments and are mostly quartzarenite. The Compaction Index of this class is relatively low with an average of 22 percent. The low compaction of Class 1 samples is related to early quartz cement development which prevents porosity loss by providing framework support against subsequent compaction. Class 1 samples were mostly deposited in aeolian (E), meandering system (M) and beach barrier (BS) environments.

Class 2 samples are medium- to fine-grained, well-sorted sandstones. Like Class 1, the samples of this class are quartz -rich and the average Compaction Index is small (18.4%). Class 2 samples were mostly deposited in the meandering system (M) and beach barrier (BS) environments.

Texturally, Class 3 samples are medium to fine-grained, moderately-sorted sandstones of mostly sublitharenite composition. High porosity and moderate permeability of these samples is caused by the presence of both macroporosity and microporosity. Class 3 samples were mostly formed in the distal part of the braid-delta (BD) and in the beach barrier bar (BS) environments.

Class 4 samples are medium to coarse-grained, moderately-sorted sublitharenites. The samples of this class were mostly deposited in meandering river (M), beach barrier bar (BS) and distal braid-delta (BD) environments.

Samples from Class 5 are medium-grained, well-sorted quartzarenites. These samples show significant development of quartz cement leading to reduction of pore spaces. The resultant moderate permeability is related to limited interconnection between primary pores. Most of the Class 5 samples were formed in meandering river (M) and beach barrier (BS) environments.

Class 6 samples are medium to fine-grained, moderately to poorly sorted sandstones. They are now relatively quartz-rich, but originally they were relatively rich in feldspar grains at the depositional surface before alteration of feldspar to kaolinite. Samples of this class were mostly formed in the distal and medial parts of the braid-delta (BD & BM) and beach barrier (BS) environments.

Class 7 samples are fine-grained, moderately- to poorly-sorted litharenites, usually showing depositional characteristics of the medial and distal parts of the braid-delta (BD & BM).

Plate 27

Micrographs, Image Analysis & Mercury Injection Data of Class 5

A - Black and white binary image of a representative sample of Class 5 (black = porosity & white = grain). The dominant porosity is macroporosity.

B - In this class, small primary porosity which are surrounded by quartz overgrowth faces are dominant porosity. Extensive development of quartz cement has reduced the original pore sizes much more than in Class 1. Class 5 sample are texturally medium-grained, well-sorted, quartzarenitic sandstones.

C - Close-up of view of (**B**).

D - SEM view of Class 5 representative sample.

E - Close-up of view of (**D**). Note the significant development of quartz overgrowth which has led to extensive reduction of pore spaces.

F - Mean pore space area for the samples of this class is about 2870 micron^2 and is relatively unimodal.

G - Mean pore diameter and mean pore perimeter are 204 and 658 μm respectively for samples of this class.

H - Mercury injection capillary pressure curve of Class 5 representative sample.

I - Pore throats curve show a relatively good sorting and most of pore throat sizes are around 1.5 μm.

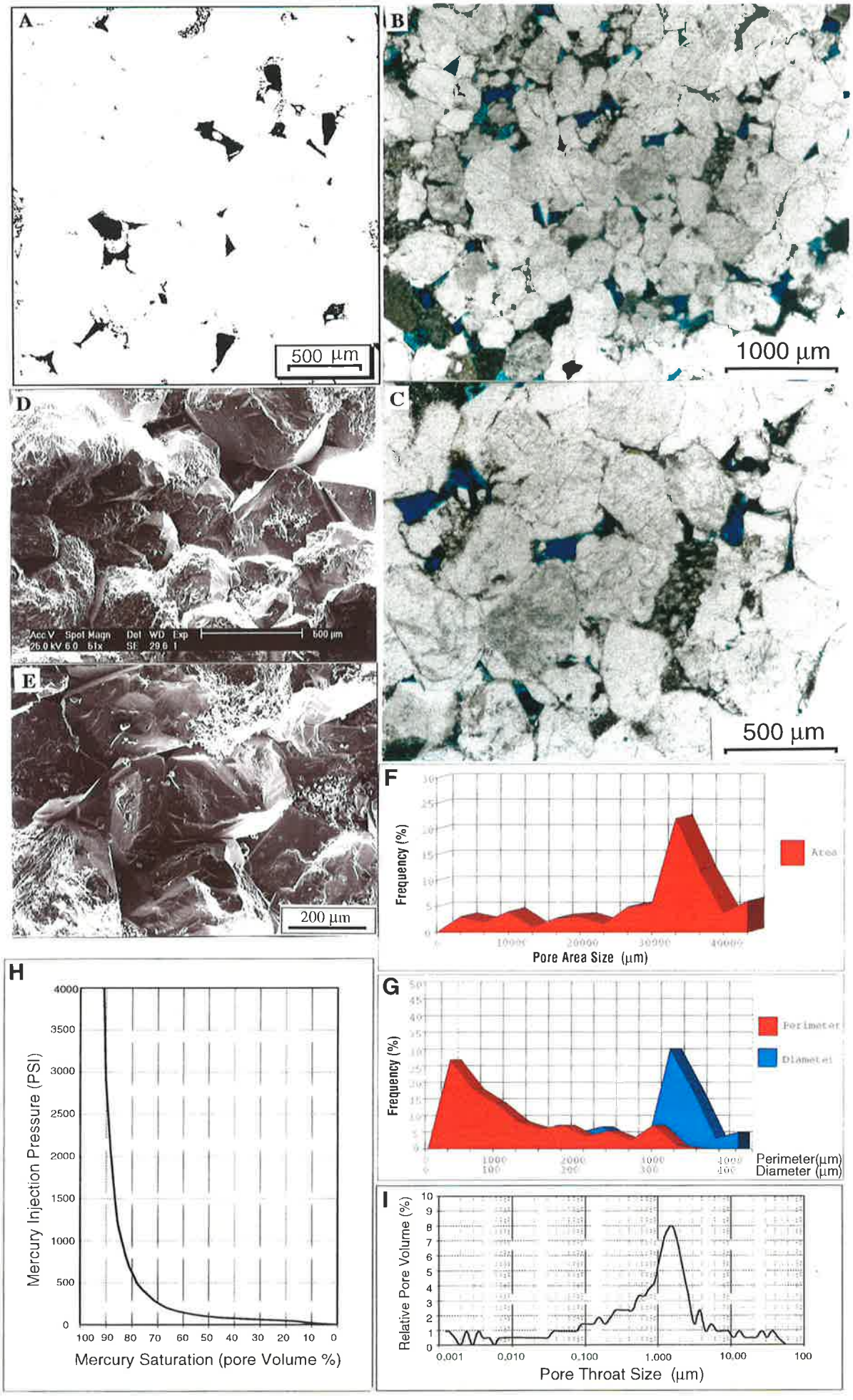
A
500 µm
B
1000 µm
C
500 µm
D
Acc.V Spot Magn Det WD Exp
26.0 kV 6.0 51x SE 29.6 1
500 µm
E
200 µm
F
Frequency (%)
Area
Pore Area Size (µm)
G
Frequency (%)
Perimeter
Diameter
Perimeter(µm)
Diameter (µm)
H
Mercury Injection Pressure (PSI)
4000
3500
3000
2500
2000
1500
1000
500
0
100 90 80 70 60 50 40 30 20 10 0
Mercury Saturation (pore Volume %)
I
Relative Pore Volume (%)
10
9
8
7
6
5
4
3
2
1
0
0,001 0,010 0,100 1,000 10,00 100
Pore Throat Size (µm)

Texturally, Class 8 samples are coarse to fine-grained, very poorly sorted litharenites with abundant ductile rock fragments. Average Compaction Index is about 59%, indicating that a high proportion of pores were lost during compaction. Class 8 samples were mostly deposited in the medial part of the braid-delta environment (BM).

Textural, compositional and environmental characteristics of different classes of the Tirrawarra Sandstone are summarised in Table 8.3

Table 8.3 - Depositional, textural and compositional characteristics of different classes of the Tirrawarra Sandstone.

Class	Depositional Environment	Texture		Composition
		Size	Sorting	
1	E & M & BS	medium-grained	well-sorted	quartzarenites
2	M & BS	medium- to fine-grained	well-sorted	quartz -rich
3	BS & BD	medium- to fine-grained	moderately-sorted	sublitharenites
4	BS & BD & M	medium- to coarse-grained	moderately-sorted	sublitharenites
5	BS & M	medium-grained	well-sorted	quartzarenites
6	BD & BM & BS	medium- to fine-grained	moderately- sorted	Kaolinite-rich
7	BD & BM	fine-grained	poorly-sorted	litharenites
8	BM	coarse-grained	very poorly-sorted	litharenites

8.3 Pore geometry controls on the porosity and permeability

The cross-plot of porosity and permeability (Fig. 7.7) does not show a straight and tight trend and the plotted data are very scattered. For example, the permeability of samples with 10% porosity, ranges from 0.1 to more than 10 mD. This indicates that the amount of porosity is not the only factor which controls permeability and it is more likely that pore geometry is the other parameter which controls permeability. In Figures 8.1a-b, the area with relatively high porosity and high permeability (HH) is populated by Class 1 samples which have the biggest pore area, pore diameter and pore throat sizes while the area with relatively low permeability and low porosity contains the Class 8 samples which have the smallest pore area, pore diameter and pore throat sizes. The conclusion

Plate 28

Micrographs, Image Analysis & Mercury Injection Data of Class 6

A - Black and white binary image of a representative sample of Class 6 (black = porosity & white = grain).

B - Apart from a few very small macropores, microporosity is the dominant pore type in this class

C - Close-up of view of (**B**). Note microporosity as the dominant pore spaces associated with kaolinite.

D - SEM view of representative sample of Class 6. These are abundant kaolinite masses in this example.

E - Close-up of view of (**D**).

F - Mean pore space area is about 340 micron^2 for Class 6 samples.

G - In this class, mean pore diameter and mean pore perimeter are 21 and 57 μm respectively.

H - Mercury injection capillary pressure curve of a representative Class 6 sample.

I - Pore throat curve shows poor sorting with the majority of pore throat sizes between 0.2 and 0.7 μm.

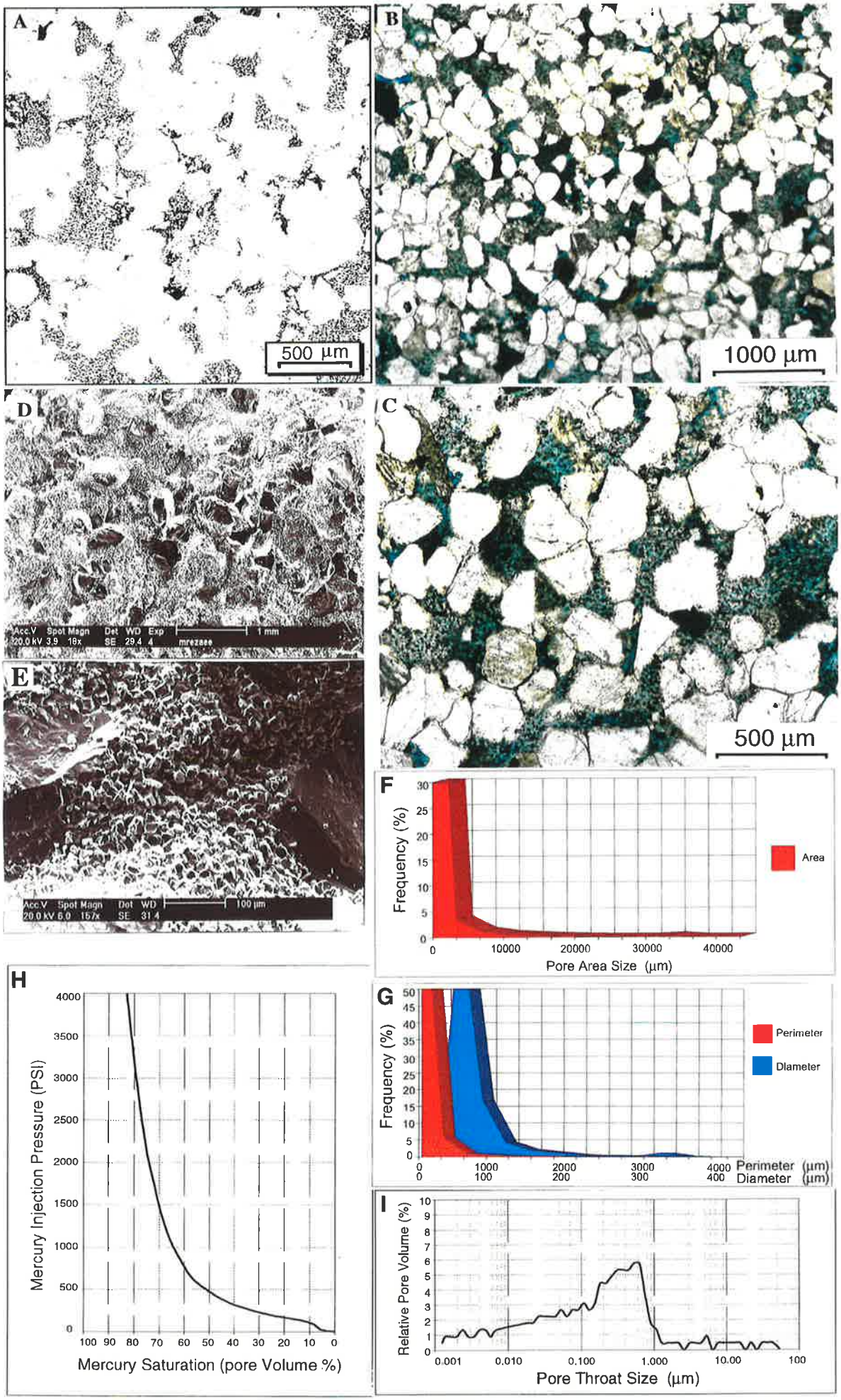
A
500 µm
B
1000 µm
C
500 µm
D
Acc.V Spot Magn Det WD Exp
20.0 kV 3.9 18x SE 29.4 4 mrezaee
1 mm
E
Acc.V Spot Magn Det WD
20.0 kV 6.0 157x SE 31.4
100 µm
F
Frequency (%)
0 5 10 15 20 25 30
0 10000 20000 30000 40000
Pore Area Size (µm)
Area
G
Frequency (%)
0 5 10 15 20 25 30 35 40 45 50
0 1000 2000 3000 4000
0 100 200 300 400
Perimeter (µm)
Diameter (µm)
Perimeter
Diameter
H
Mercury Injection Pressure (PSI)
0 500 1000 1500 2000 2500 3000 3500 4000
100 90 80 70 60 50 40 30 20 10 0
Mercury Saturation (pore Volume %)
I
Relative Pore Volume (%)
0 1 2 3 4 5 6 7 8 9 10
0.001 0.010 0.100 1.000 10.00 100
Pore Throat Size (µm)

reached is that pore and pore throat characteristics in the Tirrawarra Sandstone have a great influence on the permeability and porosity of the samples. Pore throat sizes decrease in a regular manner from Class 1 to Class 8 (Fig. 8.2) with a consequent decrease in permeability although pore area and pore diameter do not vary in the same regular way. An increase in pore area and pore diameter does not necessarily lead to an increase in permeability due to presence of large secondary macroporosity.

One application of this study is the prediction of pore geometry and porosity type from core data. In Figure 8.1a, the samples of each class show a distinct range of porosity and permeability and, as each class indicates a particular pore geometry and pore throat size, it is possible to predict pore geometry of unknown samples with the help of core analysis data (Fig. 8.1b).

8.4 Discussion

8.4.1 Control by depositional environment on pore geometry

The results show that classes are largely limited to specific depositional environments. For example, samples of Class 1 mostly occur in aeolian (E), meandering (M) and beach barrier (BS) environments, whereas samples belonging to Class 8 occur mostly in the medial braid-delta.

Each sedimentary environment is recognised by its characteristic texture, composition and diagenetic events. Reservoir quality, measured with respect to porosity and permeability, is highest in the aeolian sandstones and decreases through the meandering fluvial and beach barrier sandstones to the beds associated with the braided system. The most likely sedimentary factors which control pore geometry, and subsequent reservoir quality, are texture and composition of the sediments.

8.4.1.1 Textural Characteristics of Depositional Environments

Grain size and sorting of the samples belonging to the different sedimentary environments of the Tirrawarra Sandstone show a wide spectrum. As it discussed in Chapter 4, the textural characteristics of the Tirrawarra Sandstone have no significant influence on porosity and permeability. Therefore, these parameters can also be considered as an unimportant factors for controlling pore geometry in the Tirrawarra Sandstone.

Plate 29

Micrographs, Image Analysis & Mercury Injection Data of Class 7

A - Black and white binary image of a representative sample of Class 7 (black = porosity & white = grain). Sample M7-9606, Moorari-7, 2881 m. Scale bar = 500 μm.

B - A plain light thin section micrograph shows that porosity is dominantly micropores and some isolated secondary porosity generated from labile grain dissolution. There is a higher proportion of microporosity than macroporosity. Sample M7-9606, Moorari-7, 2881 m. Scale bar = 1000 μm.

C - Close-up of view of (**B**). Note the isolated small macroporosity.

D - SEM view of representative sample of Class 7. Sample M7-9606, Moorari-7, 2881 m. Scale bar = 500 μm.

E - Close-up of view of (**D**).

F - In this class, mean pore space area is about 11240 micron^2.

G - Mean pore diameter and mean pore perimeter are 121 and 396 μm respectively fro samples of Class 7.

H - Mercury injection capillary pressure curve of Class 7 representative sample.

I - Most of the pore throats sizes are about 0.4 μm. Pore throat curve is skewed towards smaller pore throats.

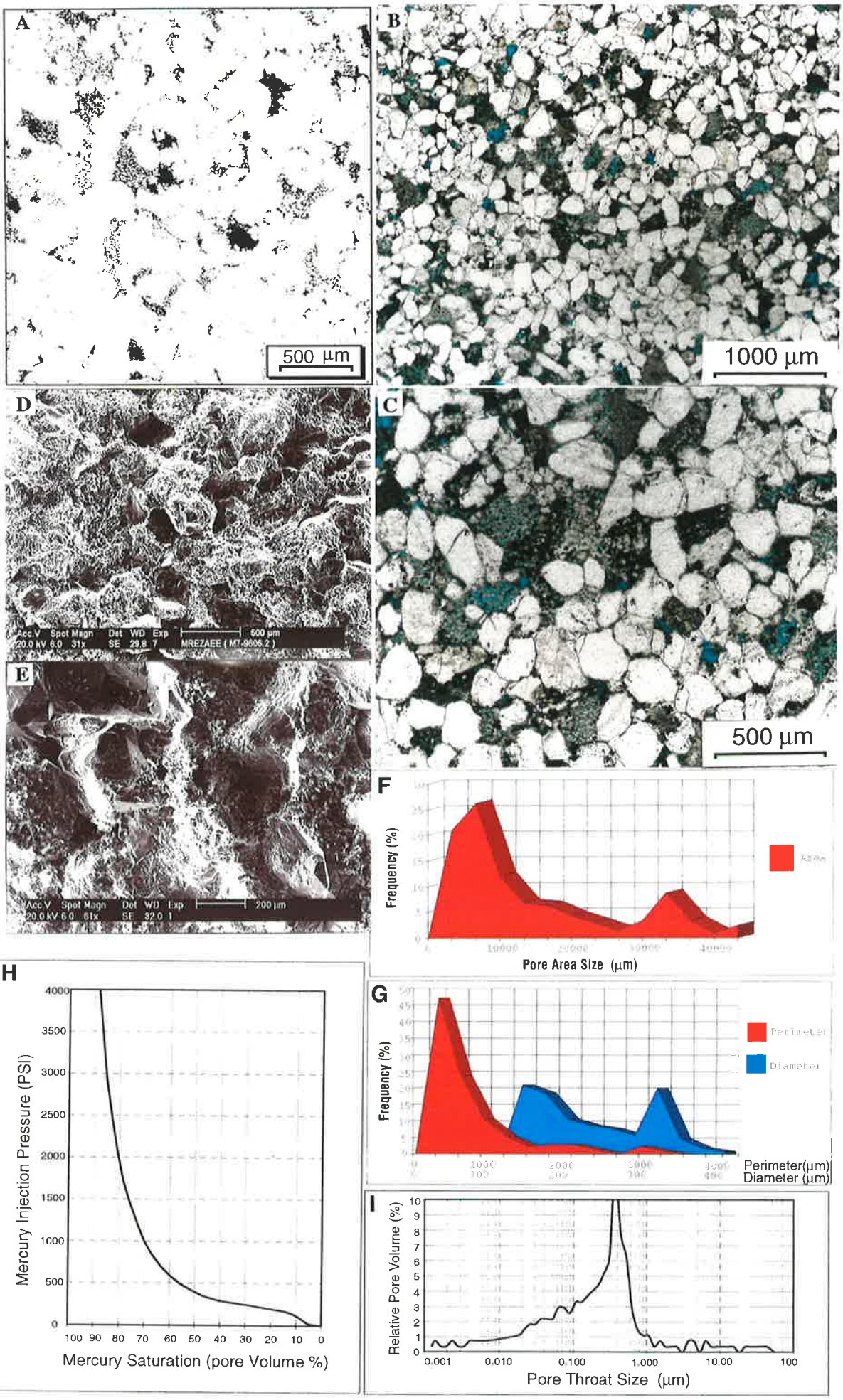
A
500 µm
B
1000 µm
D
Acc.V Spot Magn Det WD Exp 500 µm
20.0 kV 6.0 31x SE 29.8 7 MREZAEE (MT-9606.2)
C
500 µm
E
Acc.V Spot Magn Det WD Exp 200 µm
20.0 kV 6.0 61x SE 32.0 1
F
Frequency (%)
Area
Pore Area Size (µm)
G
Frequency (%)
Perimeter
Diameter
Perimeter(µm)
Diameter (µm)
H
Mercury Injection Pressure (PSI)
4000
3500
3000
2500
2000
1500
1000
500
0
100 90 80 70 60 50 40 30 20 10 0
Mercury Saturation (pore Volume %)
I
Relative Pore Volume (%)
10
9
8
7
6
5
4
3
2
1
0
0.001 0.010 0.100 1.000 10.00 100
Pore Throat Size (µm)

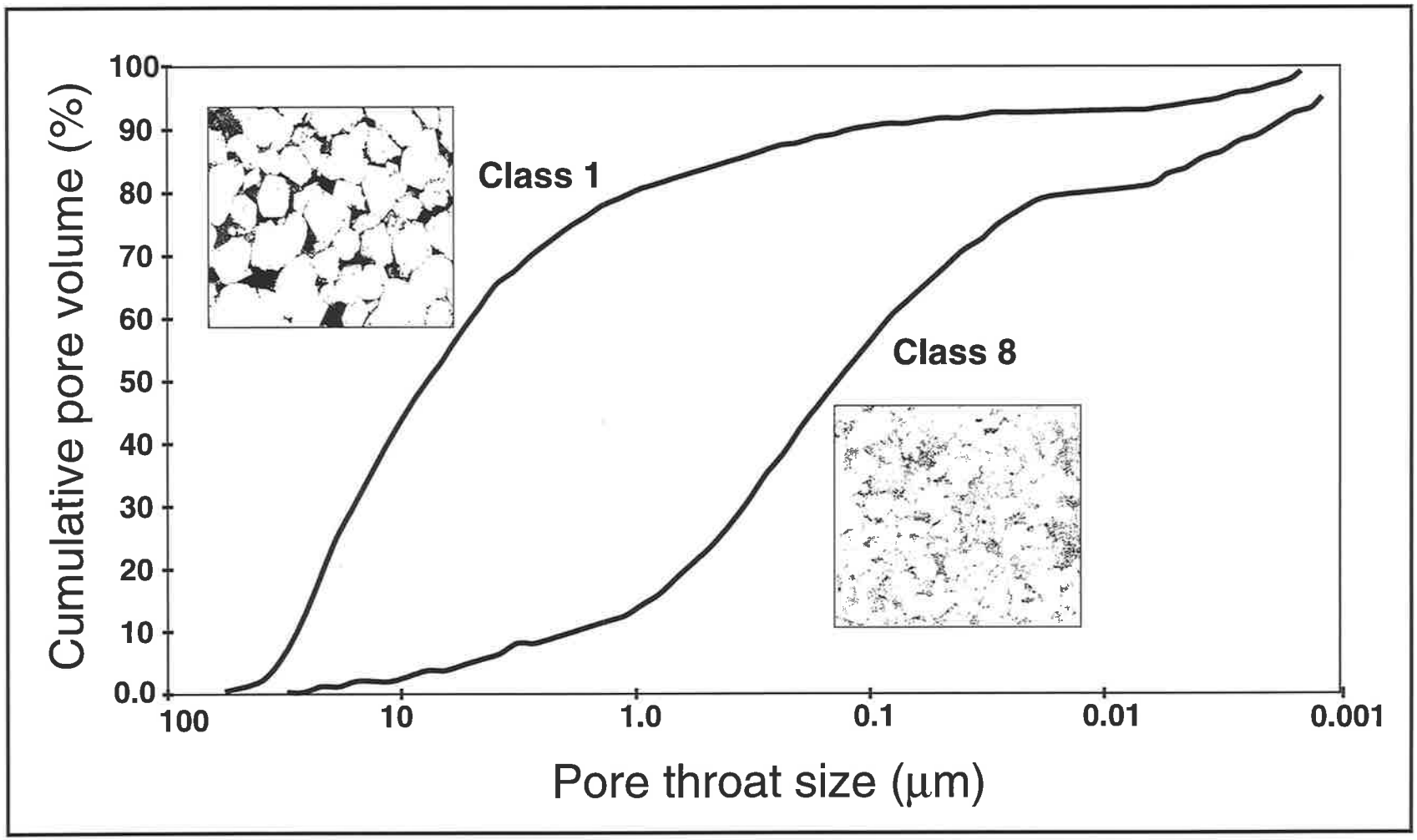

Figure 8.2 - Comparison between the pore throat curves of representative samples of classes 1 and 8. Class 1 has the larger pore throat size (~10 µm) with relatively good sorting, whereas calss 8 has smaller (~0.1 µm) and less well sorted pore throats.

8.4.1.2 Compositional Characteristics

In the Tirrawarra Sandstone, the composition of sands significantly varies in different sedimentary environments and each environment has a its own set of compositional characteristics. The intensity of mechanical compaction shows a strong relationship with the composition of the sandstones. Quartz cementation is also controlled by the composition of the sandstone. In samples with a high proportion of rock fragments, the development of quartz cement is slight, whereas in quartz-rich sandstones, the early precipitation of quartz cement is pervasive. The development of quartz cement has had a great influence on preventing subsequent compaction, thereby preserving pore spaces and pore throats.

Thin-section and SEM observations show that intergranular pores in quartz-rich samples with early quartz cement and subsequently with less compaction, are preserved and relatively good connectivity exists among the pores. With increasing amounts of rock fragments in the samples, pore space decreases and pore-throat occlusion increases, mostly by plastic deformation of rock fragments.

It is concluded that, in the Tirrawarra Sandstone, depositional environments control sandstone composition, and sandstone composition controls compaction and cementation. These are the two most important factors controlling pore geometry in the Tirrawarra Sandstone. In quartz-rich depositional facies, such as the aeolian and meandering systems, compaction is slight and quartz cementation is relatively extensive, with widespread preservation of primary pore spaces and pore throats. On the other hand, in the braid-delta environments which are rich in rock fragments, mechanical compaction is greater and subsequently most of the intergranular primary porosity is lost and pore throats are sealed by mechanical compaction.

8.5 CONCLUSIONS

Tirrawarra Sandstone core samples in the studied area can be grouped in eight classes based on pore geometry and texture. Each class occupies a well-defined part of the porosity-permeability cross-plot. This indicates that pore geometry is a significant control on petrophysical characteristics of the Tirrawarra Sandstone.

The association of each class with a given depositional environment of the Tirrawarra Sandstone suggests that pore geometry was controlled by the initial

Plate 30

Micrographs, Image Analysis & Mercury Injection Data of Class 8

A - Black and white binary image of a representative sample of Class 8 (black = porosity & white = grain). Sample M4-9506.6, Moorari-7, 2852 m. Scale bar = 500 μm.

B - In Class 8, microporosity is the dominant porosity. In this class, microporosity associated with kaolinite is less due to higher compaction. Sample M4-9506.6, Moorari-7, 2852 m. Scale bar = 1000 μm.

C - Close-up of view of (**B**).

D - SEM view of Class 8 representative sample.

E - Close-up of view of (**D**).

F - Mean pore space area of this class is about 430 micron^2.

G - In Class 8 samples, pore diameter and mean pore perimeter are 24 and 75 μm respectively.

H - Mercury injection capillary pressure curve of a representative sample from Class 8.

I - Pore throat curve shows poor sorting with pore throat size ranges mostly falling in the range from 0.1 to 0.5 μm.

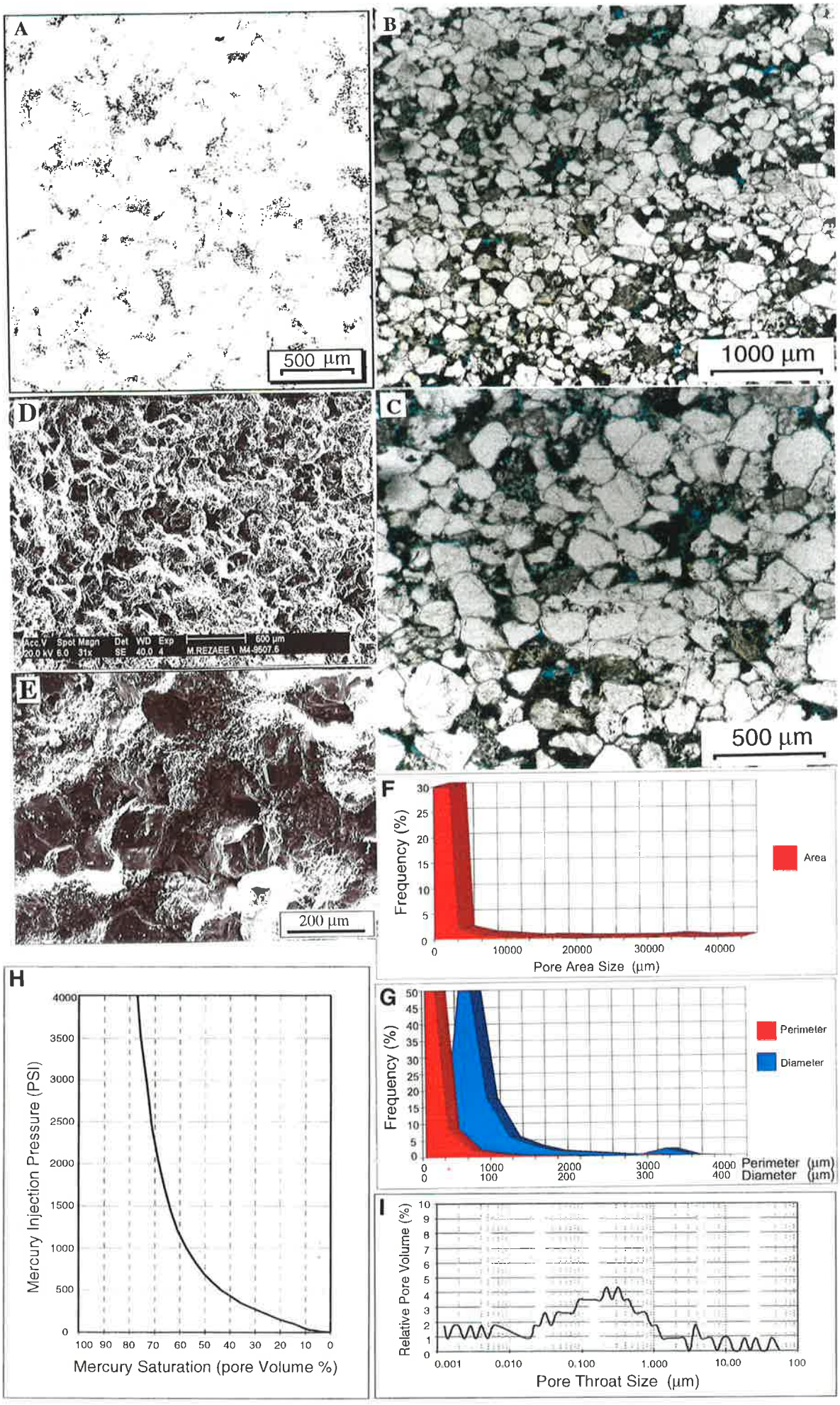
A
500 µm
B
1000 µm
D
Acc.V Spot Magn Det WD Exp 600 µm
20.0 kV 6.0 31x SE 40.0 4 M.REZAEE \ M4-9607.6
C
500 µm
E
200 µm
F
Frequency (%)
Pore Area Size (µm)
Area
G
Frequency (%)
Perimeter
Diameter
Perimeter (µm)
Diameter (µm)
H
Mercury Injection Pressure (PSI)
Mercury Saturation (pore Volume %)
I
Relative Pore Volume (%)
Pore Throat Size (µm)

depositional environment and process. The Tirrawarra Sandstone depositional environments dictate sandstone texture and composition and sandstone composition effectively controls diagenetic events such as mechanical compaction and quartz cementation. In turn these diagenetic events control pore geometry.

CHAPTER NINE

PETROPHYSICAL EVALUATION

9.1 Introduction

In the 14 studied wells from the Moorari and Fly Lake Fields, log suites generally comprised the gamma-ray (*GR*), spontaneous potential (*SP*), deep laterolog (*LLD*), shallow laterolog (*LLS*), micro-spherically focused log (*MSFL*), induction log (*ILD*) and caliper log. Neutron, density and litho-density (*PEF*) logs are also available in a small number of the wells. Most wells show some adverse hole conditions, so *DRHO* is high, indicating that density and neutron logs, which are sensitive to hole conditions are not reliable. The sonic log the most common tool in the Cooper Basin, is less sensitive to hole conditions and is used for porosity determination.

For this part of the study, all data, including wireline logs (Appendix 12), core analyses (Appendix 10) and petrographic point count data (Appendix 2) were converted to a digital format required for the *Geolog* log analysis software. Cross-plots were used to find the relationship between different variables and to derive empirical relationships. Environmental corrections were performed on the *GR* and resistivity logs.

9.2 Volume of shale (V_{sh}) from Gamma-ray (GR)

9.2.1 Introduction

The gamma-ray tool is sensitive to natural gamma-rays emitted from the potassium ^{40}K isotope and from the radioactive elements, uranium (*U*) and thorium (*Th*) (Schlumberger, 1987). Potassium 40 most commonly occurs in illitic clay minerals and mica which are rich in potassium (Table 9.1). The isotope ^{40}K also occurs in K-feldspars and glauconite. Uranium mostly concentrates in organic material and heavy minerals while *Th* occurs in some heavy minerals such as monazite (Hurst & Milodowski, 1996) and adsorbed on the surface of clays. Natural gamma-ray spectrometry (*NGS*) is a tool that can indicate the source of emitted gamma-rays (Gilchrist et al., 1982). In the studied area, *NGS* has not been run but petrographical studies indicated that heavy minerals,

feldspar and organic material are minor to very minor components of the Tirrawarra Sandstone and can be ignored as a source of gamma-rays. Alteration of mica to kaolinite, with associated rare earth element (REE) phosphate, anatase, sphalerite and pyrite, are sources of *Th* (Milodowski & Hurst, 1989), but alteration of mica to kaolinite in the Tirrawarra Sandstone is minor and only can be seen in a few samples and cannot be considered as source for *Th*. The most likely possible gamma-ray source in the samples studied is K-bearing clay minerals such as illite which exist in most of the Tirrawarra Sandstone samples as a alteration product of labile grains and sometimes as matrix.

9.2.2 Gamma-ray responses in the Tirrawarra Sandstone

Gamma-ray values have a close relationship with the composition of Tirrawarra Sandstone. With increasing amounts of quartz in the sandstones, gamma-ray values decrease (Fig. 9.1). On the other hand, gamma-ray increases with an increase in rock fragments (Fig. 9.2). The latter relationship is due to the fact that most of the detrital rock fragments are altered in part to illite and some of the metamorphic rock fragments are rich in mica.

Kaolinite is the most dominant clay mineral as determined by point counting in 130 studied thin sections. Although the plot of kaolinite percentage versus gamma-ray values is very scattered (Fig. 9.3), the trend of the plot displays gamma-ray decrease with increasing amounts of kaolinite. There is also a moderately close relationship between gamma-ray and grain size. With an increase in the grain size, gamma-ray increases (Fig. 9.4). An increase in the proportion of rock fragments with grain size increase (Fig. 9.5) explains this relationship. The gamma-ray log cannot therefore be a reliable tool for estimation of clay content in the Tirrawarra Sandstone. This is supported by Hurst (1987) who pointed out that the gamma log is a poor indicator of shaliness of reservoir rocks and other tools such as MSFL and neutron log give the most realistic correlation with the actual clay mineralogy.

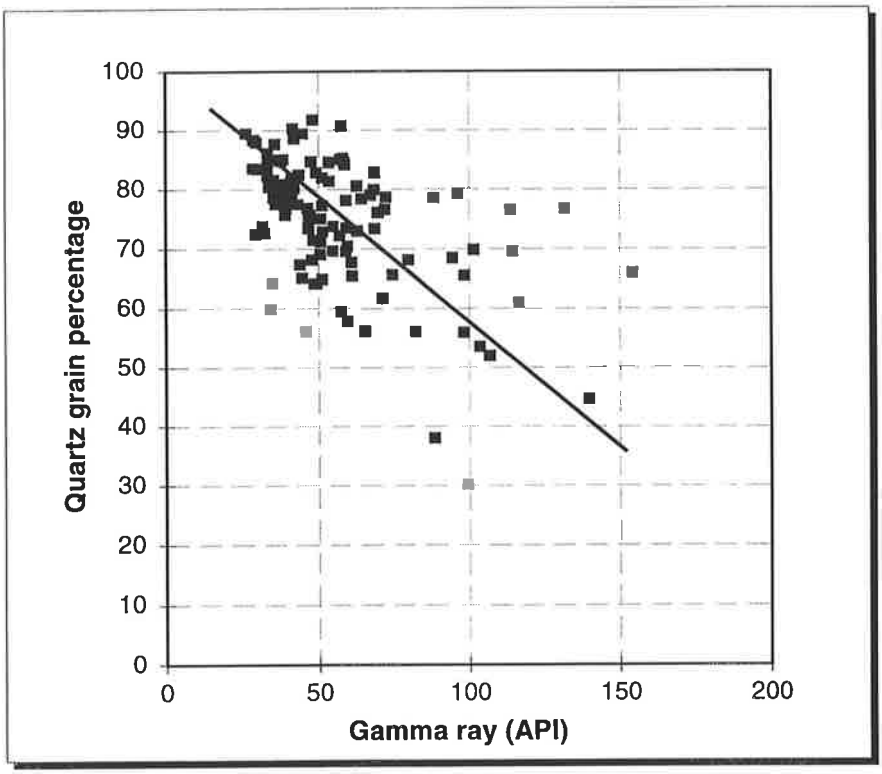

Figure 9.1 - Quartz grain percentage plotted against gamma-ray values.

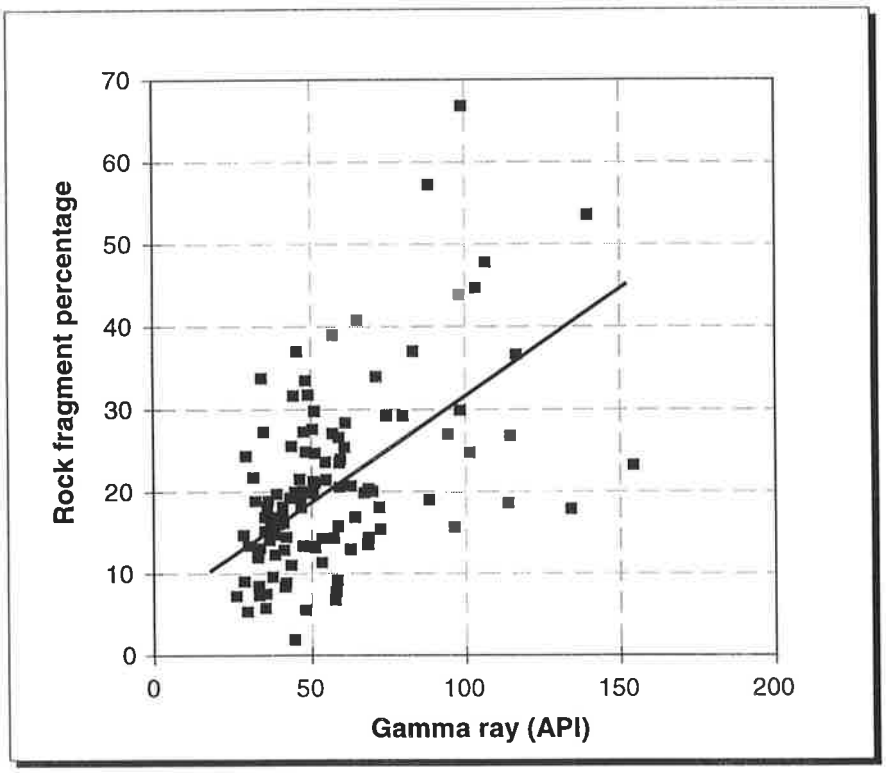

Figure 9.2 - Rock fragment percentage plotted against gamma-ray values.

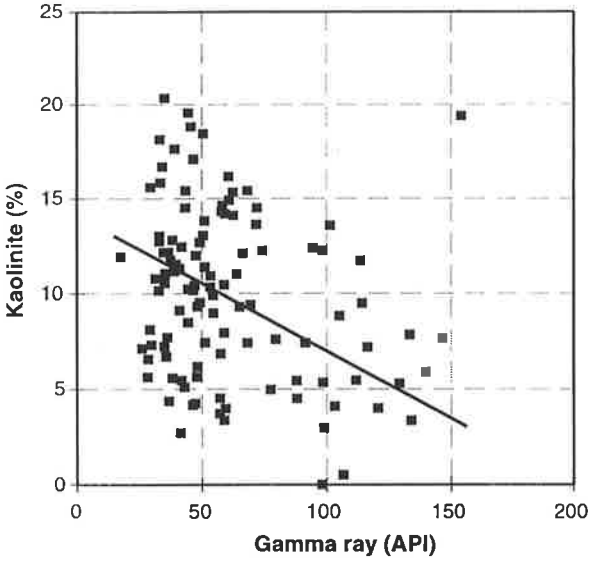

Figure 9.3 - Gamma-ray values plotted against kaolinite percentage.

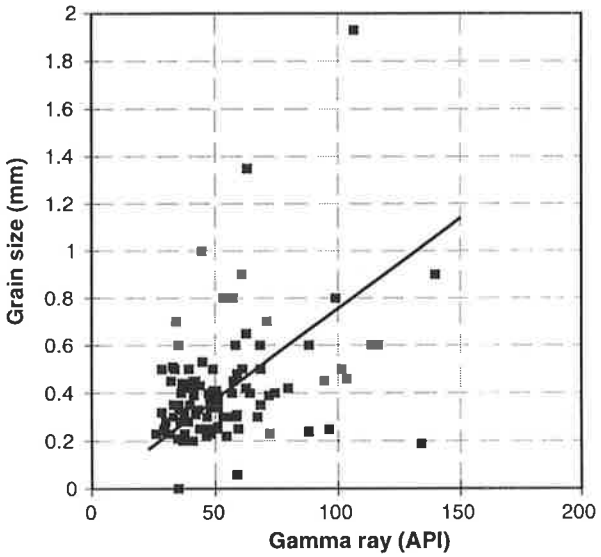

Figure 9.4 - Gamma-ray values plotted against mean grain size of the samples.

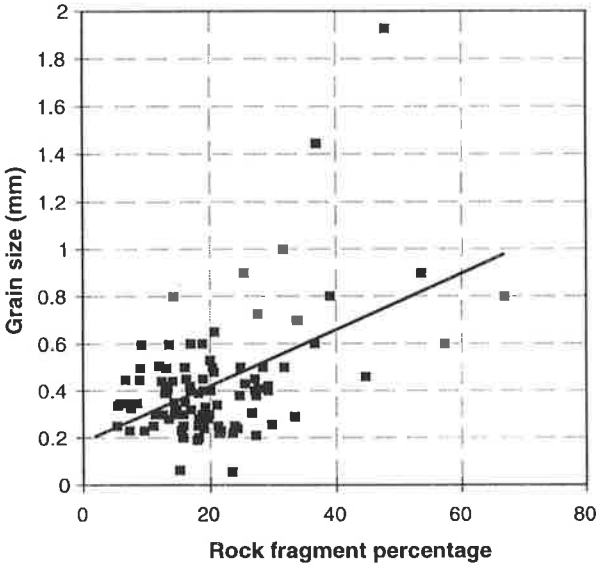

Figure 9.5 - Rock fragment percentage plotted against mean grain size.

Table 9.1 Gamma-ray signature (*API*) and Potassium (*K*), Uranium (*U*), and Thorium (*Th*) concentrations in three types of clay minerals (% by weight).

Clay	*GR*	*K*	*U*	*Th*
Kaolinite	80-130	0.5	4.4-7	6-19
Illite	250-300	3.5-8.3	8.7-12.7	10-25
Smectite	150-200	0.0-1.5	4.3-7.7	14-24

(Data from Dresser Atlas (1983)).

9.3 Porosity from Sonic Log

9.3.1 Summary

Many equations have been introduced for the estimation of porosity from sonic log in shaly sand formations. In most of the equations the volume of shale is introduced to compensate for the reduction of acoustic velocity due to presence of clay minerals. In the present study, petrographic point count and image analysis data from 130 samples, together with porosity data from about 650 core samples are combined with sonic transit times from the kaolinite-bearing Tirrawarra Sandstone reservoir in the Moorari and Fly Lake Fields.

Plots of petrographic-point-count data versus acoustic transit time show that acoustic transit time is a function of several factors including porosity, mineral composition, cementation and compaction (Rezaee & Lemon, 1997). Porosity measured in thin-section using point-count methods includes macroporosity (primary intergranular porosity and secondary dissolution porosity), and microporosity associated with kaolinite booklets.

New empirical equations are introduced for the Tirrawarra Sandstone in the Moorari and Fly Lake Fields. The plot of sonic porosity derived from the new equations and core porosity shows an r^2 value of 0.8.

The results of this study suggest that rock parameters such as composition, cementation and clay content have a clear and measurable effect on acoustic transit time. The rock parameters which affect transit time also influence porosity but, for sandstones

with a given composition, the most important parameter controlling acoustic transit time is porosity.

9.3.2 Introduction

The time required for a sonic wave to travel a given distance in a formation is measured by sonic log. This travel time depends on many factors, including porosity, pore geometry, pore fluid type, pore fluid transit time, matrix transit time, fluid saturation, pore pressure, clay content, and consolidation. Many workers, over the years, have tried to find a universal equation to translate sonic transit time to porosity.

The Wyllie time average equation (Wyllie et al., 1958) has been used for many years to determine porosity from logs, where:

$$\phi = \frac{\Delta t - \Delta t_{ma}}{\Delta t_{fl} - \Delta t_{ma}} \qquad (1)$$

Δt is rock transit time (μs/ft), Δt_{ma} is the transit time of the rock matrix, and Δt_{fl} is the pore fluid transit time.

Many other equations have been proposed to improve the Wyllie equation for translating sonic transit time to porosity. Most of the proposed equations show a linear relationship between transit time and porosity in the following form:

$$\Delta t = a\phi + b \qquad (2)$$

Equations of this form directly reflect the Wyllie transit time equation in which a and b are empirical coefficients and can be defined as:

$$a = \Delta t_{fl} - \Delta t_{ma} \qquad (3)$$

$$b = \Delta t_{ma} \qquad (4)$$

In further studies, other parameters such as clay content, pressure and temperature were also added to the general equation:

$$\Delta t = a\phi + b + c \tag{5}$$

The coefficients a, b, and c are usually determined by linear regression.

Pickett (1963) introduced a linear relationship between acoustic wave transit time and porosity in the form

$$\Delta t = a\phi + b \tag{6}$$

where Δt is rock transit time in (μs/ft), and a and b are empirical coefficients.

Raymer et al., (1980) indicated that the Wyllie time-average equation underestimated porosity in the 5 to 25 % porosity range and overestimated porosity in the greater than 30% range. They indicated that the Wyllie time-average equation only correctly predicted porosity in the range between 25 and 30%. Raymer et al., (1980) proposed a new, non-linear equation for transferring sonic transit time to porosity on an empirical basis. Their equation for the 0 to 37% porosity range is:

$$V = (1 - \phi)^2 V_{ma} + V_{fl} \tag{7}$$

where V_{ma} matrix acoustic velocity and V_{fl} pore fluid acoustic velocity.

Tosaya and Nur (1982) studied the acoustic velocity in 18 sandstone samples with different proportions of clay to find the effect of clay on sonic velocity. They found a linear relationship between compressional velocity, porosity and clay content.

$$V_p = -8.6\phi + 5.8 - 2.4C \tag{8}$$

where V_P is velocity of compressional wave (km/sec) and ϕ porosity (fraction) and C is the volume of clay (fraction). They mentioned that the P-wave velocity is more sensitive to porosity than clay content.

Kowallis et al., (1984) measured compressional wave velocities in 14 sandstone samples. They showed that the velocity variation with clay content is due to

microporosity associated with clay minerals. They introduced the following equation with a clay content term

$$V_p = -9.2\phi + 5.6 - 5.7\,C \tag{9}$$

Han et al., (1986) measured compressional and shear wave velocities in 75 sandstone samples with different porosities and different clay contents. They showed that clay content has a great effect on the reduction of compressional (V_P) and shear wave velocities (V_s). They introduced the following equations with a clay term:

$$V_p = -6.93\phi + 5.59 - 2.18C \tag{10}$$

$$V_s = -4.91\phi + 3.52 - 1.89C \tag{11}$$

A multivariate analysis to investigate the influence of effective pressure (P_e), porosity (ϕ) and clay content (C) on compressional (V_P) and shear wave velocities (V_s) on 64 different sandstones was conducted by Eberhart-Phillips et al., (1989). They introduced the same-style equation with clay content and effective pressure terms:

$$V_p = -6.94\phi + 5.77 - 1.73\sqrt{C} + 0.446(P_e - e^{-16.7P_e}) \tag{12}$$

$$V_s = -4.94\phi + 3.70 - 1.57\sqrt{C} + 0.361(P_e - e^{-16.7P_e}) \tag{13}$$

Raiga-Clemenceau et al., (1988) proposed an equation for transferring sonic transit time to porosity. The equation is for clean sandstones and includes the concept of Formation Factor (F) and is named Acoustic Formation Factor (AFF):

$$\phi = 1 - \left(\frac{\Delta t_{ma}}{\Delta t}\right)^{1/x} \tag{14}$$

where Δt_{ma} is matrix transit time and x is the slope of the regression line produced from a cross-plot of log ($1/t$) versus log($1-\phi$). For a silica matrix with matrix transit time equal to 55.5 (μs/ft), x is about 1.6.

Vernik (1994) studied compressional velocity-porosity trends in siliciclastic and carbonate rocks. Instead of considering the volume of clay in various lithlogies, he defined four major petrophysical groups which range from clean arenites with less than two percent clay to shales with 35 percent clay content. By cross-plotting compressional velocity versus porosity for the different groups, he introduced four empirical equations with the same style for each lithology.

$$V_p = a\phi + b \tag{15}$$

From clean arenites to shales, a ranges from -6.91 to -9.03 and b ranges from 6.07 to 4.93.

In the present study, an empirical equation is introduced for translating sonic wave transit time to porosity for the Tirrawarra Sandstone. The equation, which has a Wyllie equation style, estimates total porosity (macroporosity and microporosity) with high precision. To estimate macroporosity alone a new equation is introduced, in which the reduction of sonic wave velocity in shaly sand formations is attributed to microporosity associated with kaolinite. In general, macroporosity estimated through this equation is 2 porosity units less than total porosity.

9.3.3 Sonic Porosity Equations Introduced for use in the Cooper Basin

Many workers in the Cooper Basin have tried to establish an appropriate equation for transformation of acoustic transit time to porosity. Their empirical equations are presented below:

Porter and Crocker (1972) introduced an empirical equation as

$$\phi = \frac{\Delta t - 56}{1.5} \qquad \text{for } Vsh_{GR} < 15\% \tag{16}$$

$$\phi = \frac{\Delta t - 59}{1.63} \qquad \text{for } Vsh_{GR} \geq 15\% \tag{17}$$

$$V_{sh} = \frac{GR - GR_{min}}{GR_{max} - GR_{min}} \tag{18}$$

Porter, in 1976, introduced another equation for porosity determination in the Cooper Basin.

$$\phi = \frac{88.3(\Delta t - 54.5)}{GR + 111.16} \tag{19}$$

Northcott (1982) introduced another equation for the Cooper Basin as

$$\phi = \frac{\Delta t - 53}{\{192.71 + (0.841GR)\} - 53} \tag{20}$$

Overton and Hamilton (1986) introduced an empirical equation for the determination of porosity from sonic log in the Cooper Basin. They used the Wyllie equation but instead of using a unique value for pore-fluid transit time, they found an empirical relationship between gamma-ray and fluid transit time for different formations in the Cooper Basin. For the Tirrawarra Sandstone, pore fluid transit time was is defined as:

$$\Delta t_{fl} = 0.31GR + 195 \tag{21}$$

The equation for the Tirrawarra Sandstone becomes:

$$\phi = \frac{\Delta t - \Delta t_{ma}}{(0.31GR + 195) - \Delta t_{ma}} \tag{22}$$

They considered matrix transit time as equal to 55.5 (μs/ft).

Morton (1989) introduced another modified Wyllie equation for porosity determination from sonic log in the Cooper Basin. He considered matrix transit time as:

$$\Delta t_{ma} = \Delta t_{ss} + [V_{sh}(\Delta t_{sh} - \Delta t_{ss})] \quad (23)$$

and pore fluid transit time as

$$\Delta t_{fl} = (S_w \Delta t_{water}) + [(1 - S_w)\Delta t_{gas}] \quad (24)$$

With values of acoustic transit time in sandstones, shale, water and gas respectively as 56, 65, 189, and 240 (μs/ft), the Morton equation then becomes:

$$\phi = \frac{\Delta t - [56 + 9(V_{sh})]}{[(189 S_w) + 240(1 - S_w)] - [56 + 9(V_{sh})]} \quad (25)$$

Most of the equations used in the Cooper Basin are linear and have the same style of

$$\phi = \frac{\Delta t - b}{a} \quad (26)$$

in which b and a are coefficients which depend on matrix and pore fluid transit time and shaliness of sandstones. In fact, b and a are derived from regression lines of core porosity versus sonic log transit time. To correct for the effect of shale and the presence of gas, other parameters such as gamma-ray values (Porter & Crocker, 1972; Porter, 1976; Northcott, 1982; Overton & Hamilton, 1986) and water saturation terms are also added (Morton, 1989).

9.3.4 The Results of Previous studies on the Sonic Porosity for the Tirrawarra Sandstone

About 650 core porosity values from the Tirrawarra Sandstone in the studied area are cross-plotted against sonic porosity as determined from various equations (Appendix 13).

The cross-plot from the Porter and Crocker equation (Porter & Crocker, 1972) is widely scattered (Fig. 9.6a) with correlation coefficient of about 0.62. This equation underestimates porosity by about 1.5 porosity units. Core porosity versus sonic porosity from the Porter equation (Porter, 1976) also displays a wide scatter (Fig. 9.6b) with

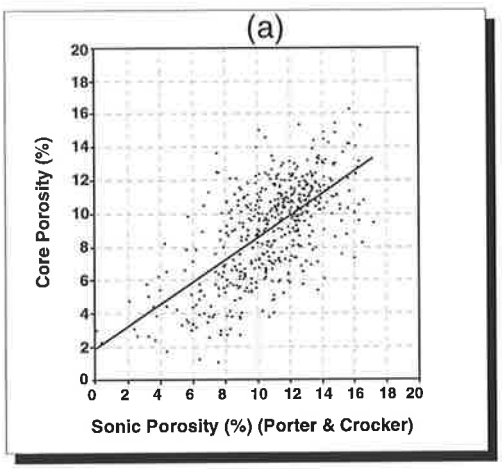

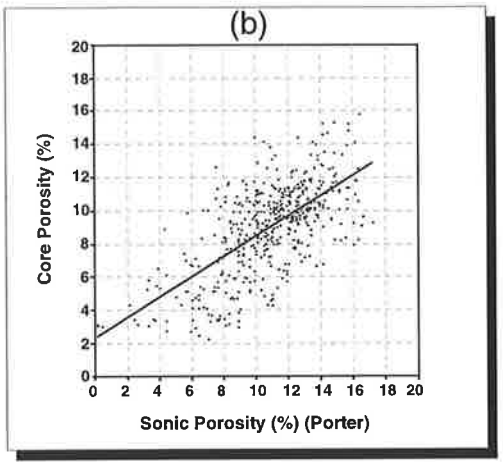

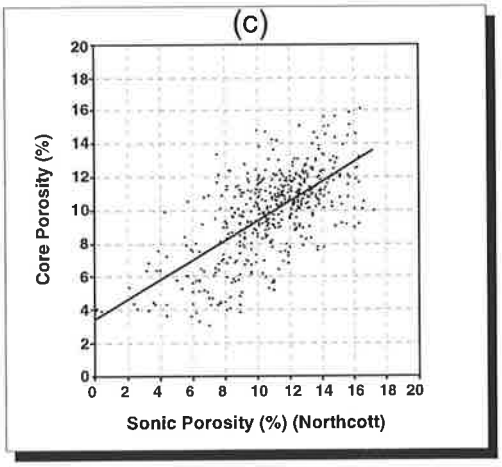

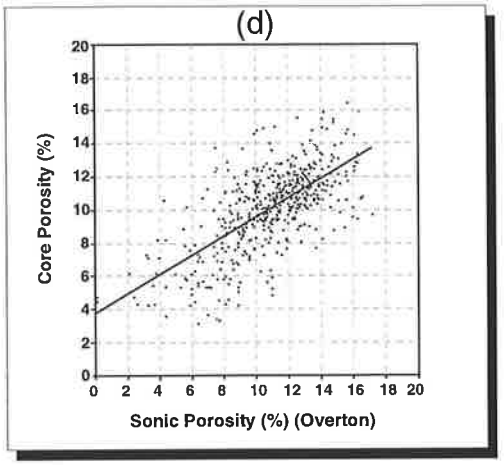

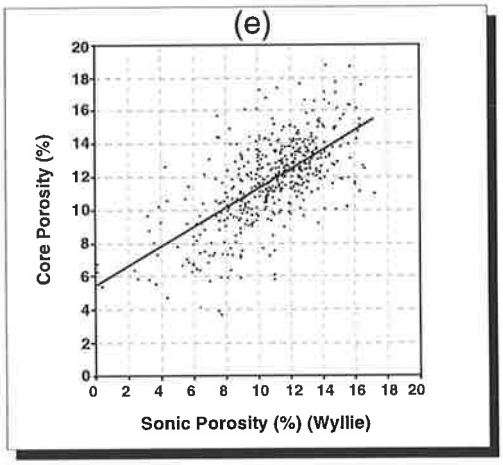

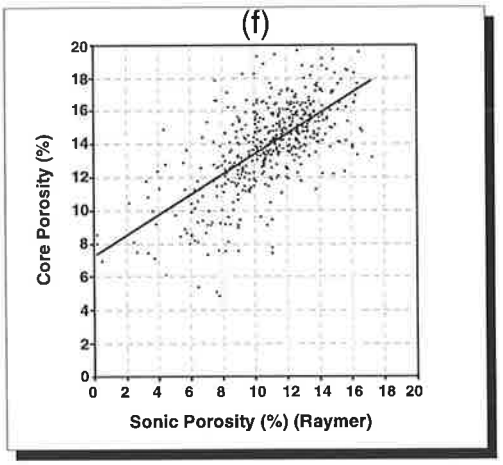

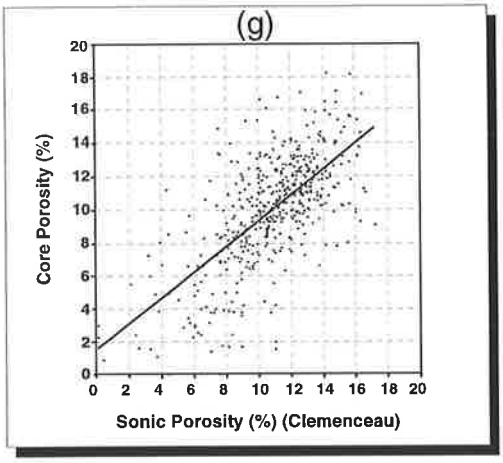

Figures 9.6a-g - Plots of core porosity versus sonic porosity calculated by various equations. (**a**) Porter & Crocker, (**b**) Porter, (**c**) Northcott, (**d**) Overton & Hamilton, (**e**) Wyllie et al., (**f**) Raymer et al. and (**g**) Clemenceau. Correlation coefficient of each plot is around 0.6.

correlation coefficient about 0.66. The Porter equation (Porter, 1976) underestimates core porosity by about 1.5 porosity units. Sonic porosity from the Northcott equation (Northcott, 1982) also underestimates core porosity by about 1 porosity unit. Core porosity versus sonic porosity from the Northcott equation displays a wide scatter (Fig. 9.6c) with a correlation coefficient of about 0.66. Sonic porosity from the Overton and Hamilton equation (Overton & Hamilton, 1986) also does not match well with core porosity (Fig. 9.6d) with a correlation coefficient of about 0.67. This equation also underestimates core porosity by about 0.8 porosity unit.

In general, it can be concluded that sonic porosity from the equations introduced for the Cooper Basin does not closely match with Tirrawarra Sandstone core porosity data. All of the equations underestimate core porosity.

Cross-plots of porosity from the Wyllie equation (Wyllie et al., 1958), Raymer equation (Raymer et al., 1980) and Clemenceau equation (Raiga-Clemenceau et al., 1988) versus core porosity (Fig. 9.6e-g), which use a matrix transit time of 55.5 and a fluid transit time of 189.5 (μs/ft), also show very scattered data.

9.3.5 *Introducing A New Empirical Equation*

A new empirical equation is presented which can translate sonic transit time to porosity (Appendix 14) for the Tirrawarra Sandstone (Rezaee & Griffiths, 1996b) with a higher degree of correlation than those presented above. To derive this equation, several corrections have been applied to the data, including:

- zonation of sonic log data and core porosity: One of the important problems that makes comparison of core and log measurements difficult is the different in volume investigated by log and core plugs (Marion & Pellerin, 1994). In order to reduce this problem, log data and core porosity were averaged for the intervals with the same lithological properties. During core logging, the Tirrawarra Sandstone was divided into eleven classes based on visual grain size, porosity, sorting, clay content and consolidation. This visual classification on core was established by Sneider et al., (1984). Zonation of the core and sonic data were carried out within each interval which displays similar lithological properties.
- deletion of problematic core data: During core logging, great care was taken to separate core plugs which were not appropriate for core analysis. Many plugs were

found to be completely unsuitable for core analysis due to the presence of microfractures, surface bedding and pebbles in the plugs (Plate 31). Some plugs were from very thin unrepresentative intervals. These sorts of data points were deleted during this approach.

- precise core and log depth matching: Several methods were used for core and log depth matching including: core gamma scan; comparison of lithology and gamma-ray and comparison of sonic log and core porosity.

The new empirical equation has the same style as previous equations:

$$\Delta t = a\phi + b$$

in which empirical coefficients, *a* and *b*, refer to apparent matrix and pore-fluid transit time. Apparent matrix and pore-fluid transit time are determined from the relationship between core porosity and sonic transit time (Fig. 9.7 a-b). Apparent matrix transit time is the intersection of a regression line at zero percent porosity and apparent pore fluid transit time is the intersection of regression line at 100% porosity. The apparent matrix transit time and apparent pore fluid transit time in Moorari Field are 58 and 175 (μs/ft), and in the Fly Lake Field are 58 and 180 (μs/ft), respectively.

The equation relating sonic transit time to porosity in the Moorari Field is

$$\phi = \frac{\Delta t - 58}{117} \qquad (27)$$

and for Fly Lake Field is

$$\phi = \frac{\Delta t - 58}{122} \qquad (28)$$

The cross-plot of measured sonic porosity from the above equations and core porosity show a good correlation ($r^2 = 0.8$) (Fig. 9.8).

Plate 31

Micrographs of Problematic Core Plugs

Many core plugs during core logging were found to be completely unsuitable for core analysis (porosity and permeability). The problems include the presence of microfractures, surface bedding and gravels in the plugs. Furthermore, some of the plugs were taken from intervals which were not representative of the dominant lithology. In this plate some of the core plugs features which make the measurements of porosity and permeability questionable are shown.

A - Some of the core plugs were taken along surface bedding. These sorts of plugs obviously will show higher porosity and permeability.

B - In many instances core plugs were selected from intervals which were not representative of the whole interval. In these examples it can be seen that core plugs were taken from thin intervals which are finer-grained than the whole interval and also have abundant dissolution seams. The core data from these sorts of plugs erroneously provide pessimistic porosity and permeability.

C - The presence of pebbles in the core plugs can cause problems in porosity and permeability measurements. In these examples it can be seen that core plugs are taken from thin gravel-rich intervals.

D - In these two examples core plugs are taken from fractured intervals. Obviously these sorts of plugs will erroneously provide higher porosity and permeability.

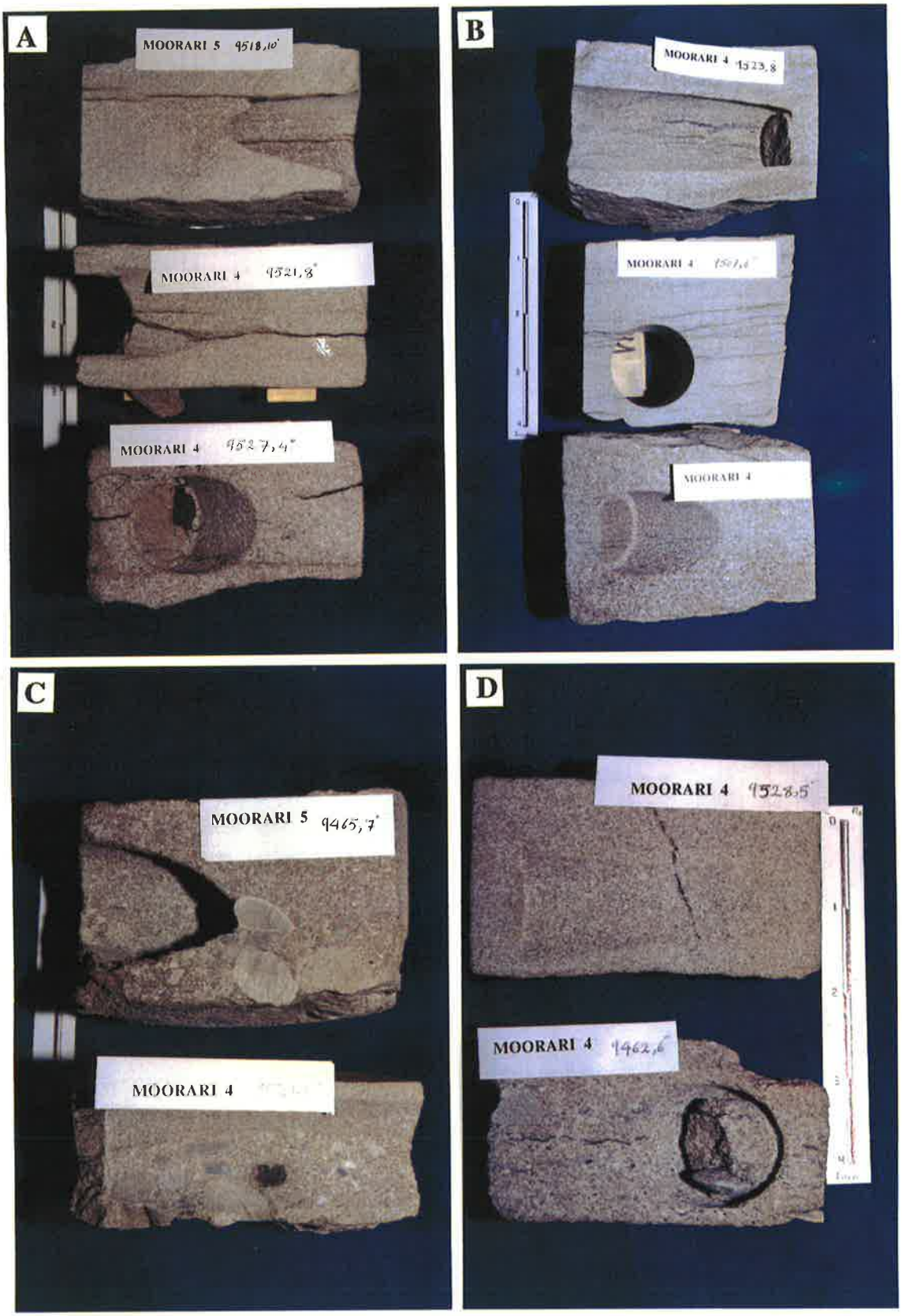
A
MOORARI 5 9518,10'
MOORARI 4 9521,8'
MOORARI 4 9527,4'
B
MOORARI 4 1523,8
MOORARI 4
MOORARI 4
C
MOORARI 5 9465,7'
MOORARI 4
D
MOORARI 4 9528,5'
MOORARI 4 9462,6'

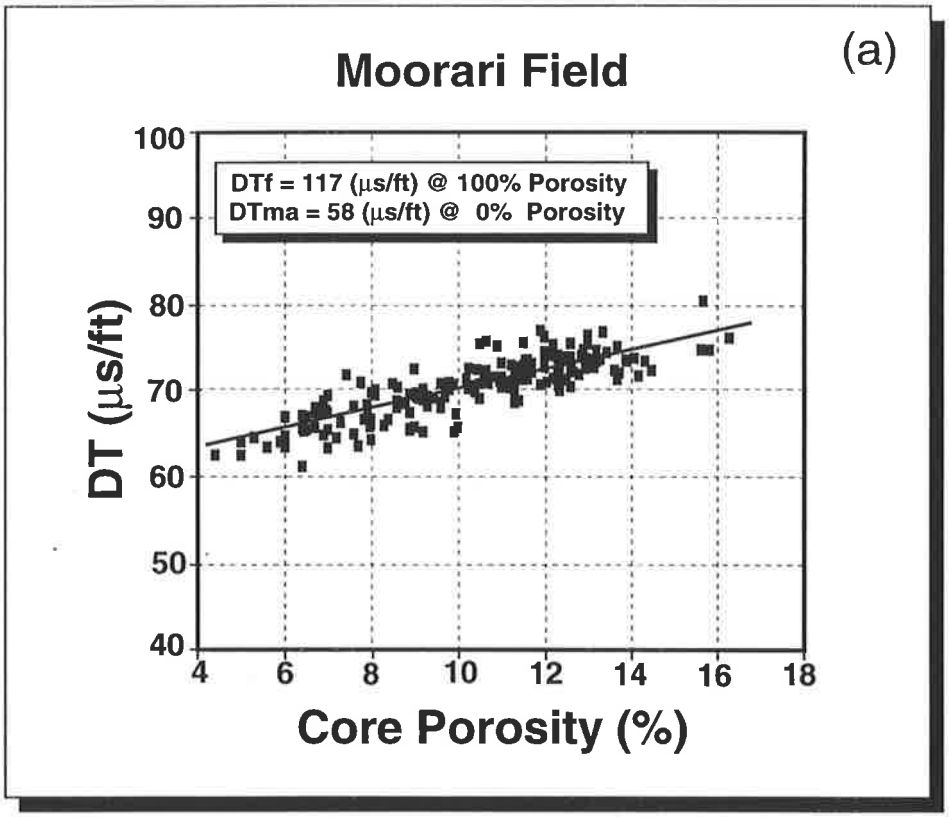

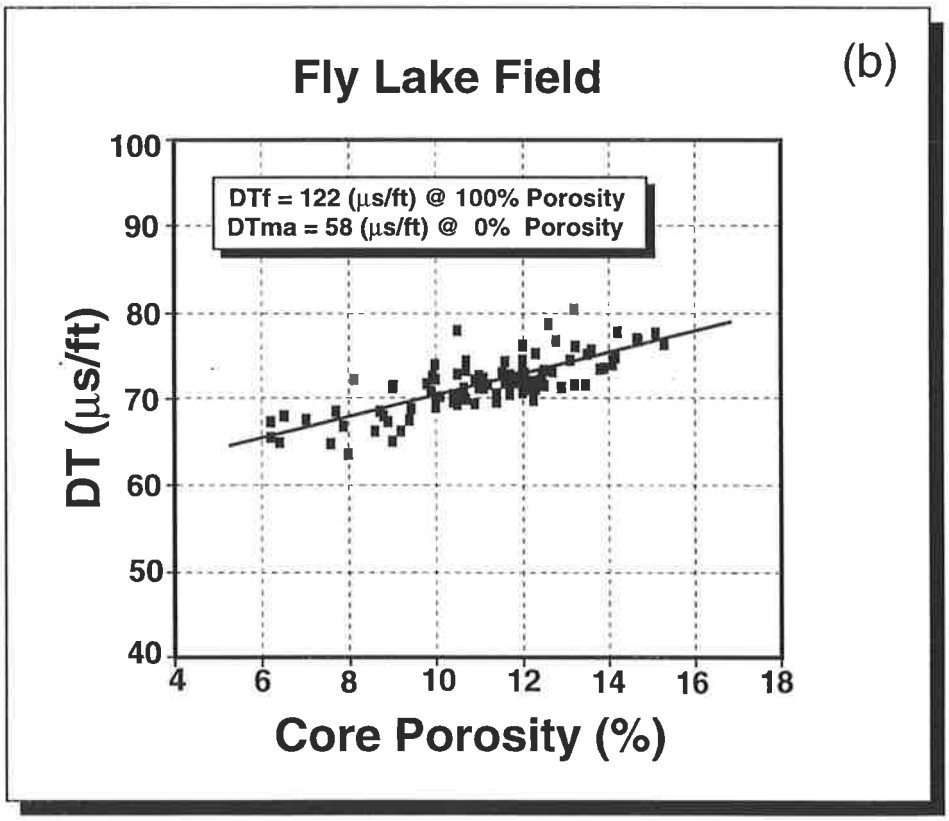

Figure 9.7a-b - Core porosity (%) plotted against sonic wave transit time (µs/ft) in the (a) Moorari and (b) Fly Lake Fields. DT_f = pore fluid transit time, DT_{ma} = matrix transit time.

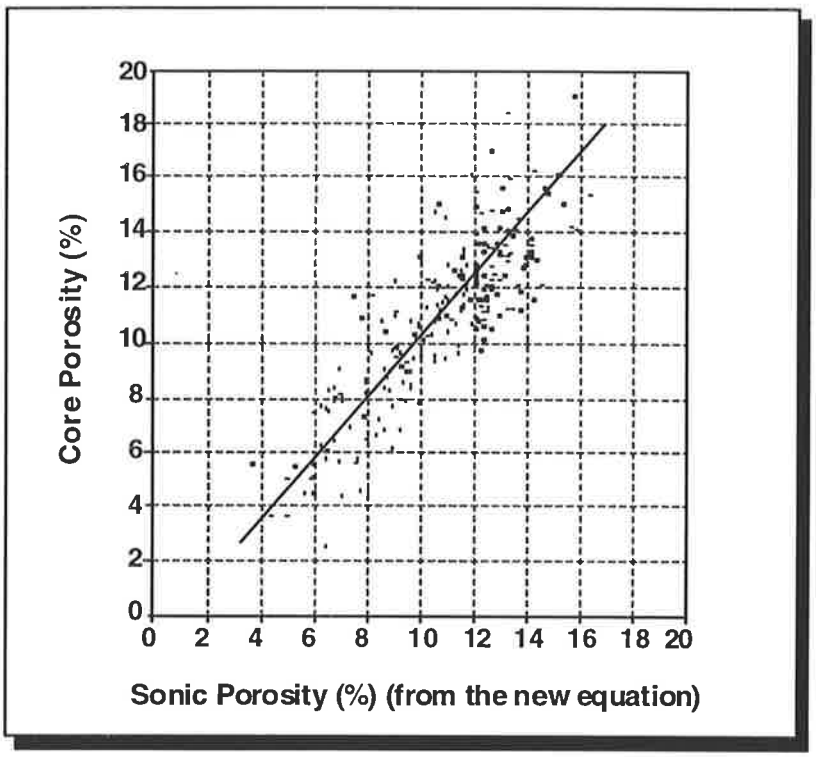

Figure 9.8 - A cross-plot of porosity calculated using the new equation shows good correlation ($r^2 = 0.8$) with measured core porosity.

9.3.6 Estimation of Effective Porosity

The reduction of acoustic wave velocity is attributed by Kowallis et al., (1984) to the presence of microporosity associated with clay minerals (Neasham, 1977; Pittman & Thomas, 1978). As will be discussed later, the present work also supports Kowallis et al., (1984) that the presence of microporosity reduces acoustic wave velocity. With this assumption, sonic porosity includes both microporosity and macroporosity. Helium injection core porosity also measures total porosity. The relation between total porosity and effective macroporosity can be expressed by equation (29):

$$\phi_t = \phi_e + \phi_{mic} \qquad (29)$$

where ϕ_t is total porosity, ϕ_e is effective porosity and ϕ_{mic} is microporosity associated with clay minerals.

As sonic porosity is equal to total porosity, and Back-Scattered Electron (BSE) image analysis of the clay minerals in the Tirrawarra Sandstone indicates an average of 20% microporosity in the kaolinite, equation (29) will become:

$$\phi_e = \phi_{sonic} - 0.2V_k \quad (30)$$

where ϕ_{sonic} is sonic porosity and V_k is the volume fraction of kaolinite.

Knowledge of the volume fraction of clay, allows determination of the amount of effective porosity for the Tirrawarra Sandstone.

Petrographic point count data were used to evaluate equation (30). Point count intergranular porosity is considered as effective porosity and sonic porosity is estimated from equations (27) and (28). On average, the estimated effective porosity is 2 porosity units less than the total porosity, with a correlation coefficient of about 0.9 (Appendix 15). To find a better estimation of effective porosity with less variation of values, different subsets were tried. The best subsets were those classified according to depositional environment where variations of effective and sonic porosity were less, thereby suggesting a better estimation of effective porosity. The statistics of the different porosity in each sedimentary environment are shown in Table 9.2. The difference between effective and total porosity in each sedimentary environment (Table 9.3) indicates that the volume of kaolin is different in each environment.

Table 9.2 - Statistics of the variation of porosities (%) in the different environments. Aeolian (E) due to very small sample size is not included. BM=medial part of braid-delta, BD=distal part of braid-delta, BS=beach barrier , M=meandering, r^2 = correlation coefficient between total and effective porosity.

	BM			BD			BS			M		
	ϕ_t	ϕ_e	ϕ_{mic}	ϕ_t	ϕ_e	ϕ_{mic}	ϕ_t	ϕ_e	ϕ_{mic}	ϕ_t	ϕ_e	ϕ_{mic}
Average	9.8	7.9	1.8	12.6	10.3	2.3	13.5	11.2	2.2	12.0	10.2	1.7
Max.	15.5	14.9	3.9	16.1	13.8	4.1	18.1	16.1	3.5	17.0	15.2	3.9
Min.	4.6	3.2	0.0	9.2	6.4	0.5	10.4	7.9	1.0	8.6	6.2	0.2
Stdev.	2.3	2.4	1.1	1.6	1.9	1.0	2.3	2.5	0.6	2.2	2.3	1.0
r^2	0.87			0.86			0.94			0.88		

The cross-plots of sonic porosity versus effective porosity for samples from each sedimentary environment (Fig. 9.9a-e) show a good correlation. The equations from the

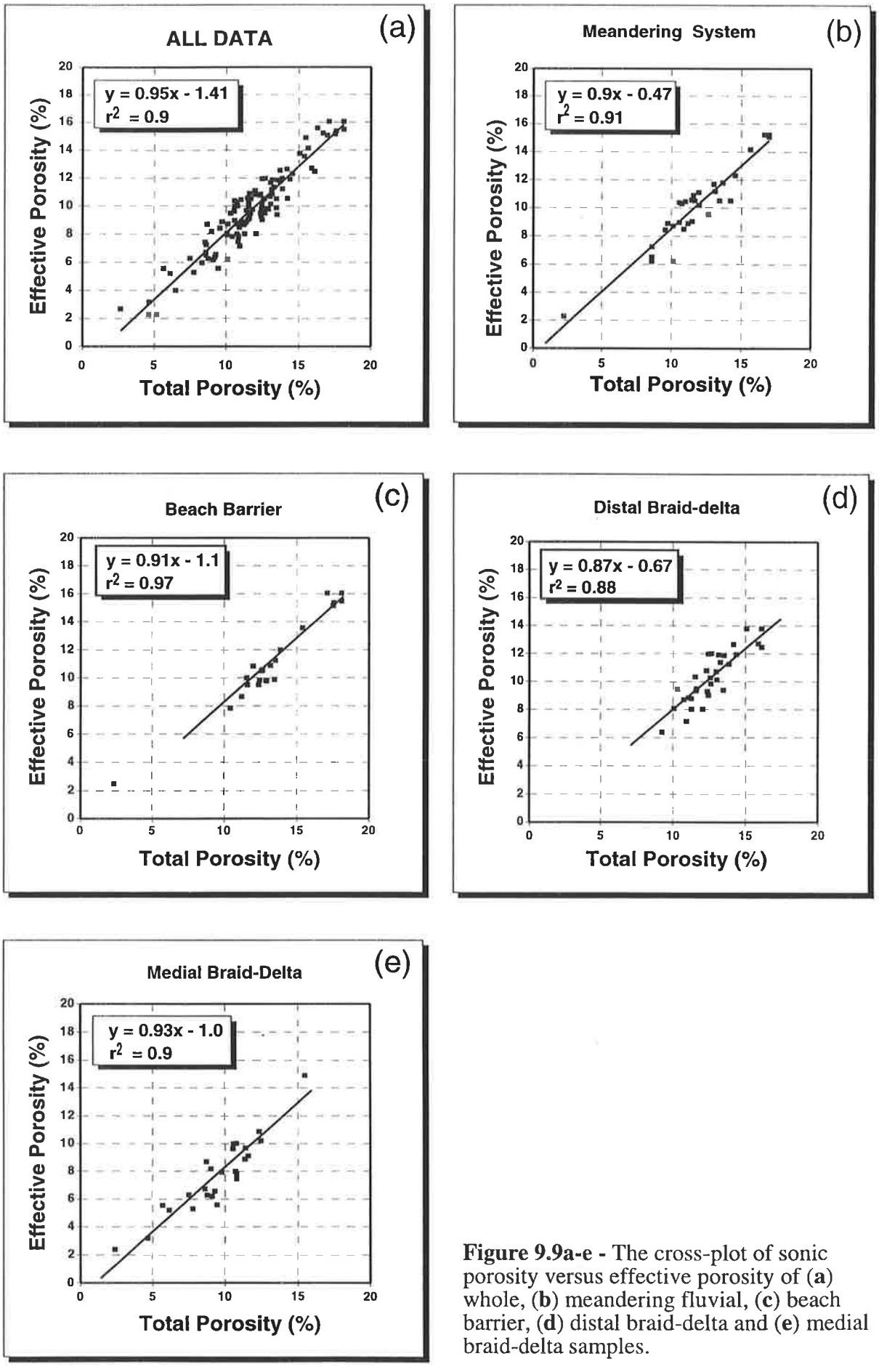

Figure 9.9a-e - The cross-plot of sonic porosity versus effective porosity of (**a**) whole, (**b**) meandering fluvial, (**c**) beach barrier, (**d**) distal braid-delta and (**e**) medial braid-delta samples.

regression lines of the cross-plots can be used for each sedimentary environments to estimate effective porosity.

Table 9.3 - The difference between total and effective porosity (%) in different depositional facies (D. facies).

D. Facies	BD	BS	BM	M	E
$\phi_t - \phi_e$	2.3	2.2	1.8	1.7	1.1

For all samples, the relation between effective and sonic total porosity is:

$$\phi_e = 0.95\phi_t - 1.41 \quad (31)$$

The relation between sonic total porosity and effective porosity in the medial part of braid-delta (BM) is equal to:

$$\phi_e = 0.93\phi_t - 1.0 \quad (32)$$

For distal part of braid-delta (BD) the relation between sonic total porosity and effective porosity is equal to:

$$\phi_e = 0.87\phi_t - 0.67 \quad (33)$$

For barrier beach environment (BS) equation is:

$$\phi_e = 0.91\phi_t - 1.1 \quad (34)$$

The meandering system (M) relationship can be expressed as:

$$\phi_e = 0.9\phi_t - 0.47 \quad (35)$$

As the determination of kaolinite from wireline data for the present wells is difficult and not reliable, the above equations will allow estimation of effective porosity for the Tirrawarra Sandstone in the Moorari and Fly Lake Fields.

9.4 Controls on Sonic Transit Time

Several factors control the sonic transit time in the Tirrawarra Sandstone samples, including porosity, sandstone composition, type of pore fluid, cementation, compaction and clay content.

9.4.1 Porosity

The most important factor which controls sonic travel time in a given matrix, is porosity. As the amount of porosity increases, the time required for an acoustic wave to travel through a given distance will increase. Figure 9.10 shows that, for Tirrawarra Sandstone samples, sonic transit time increases with increasing core porosity. The presence of pore spaces results in a longer distance or more tortuous course for sonic

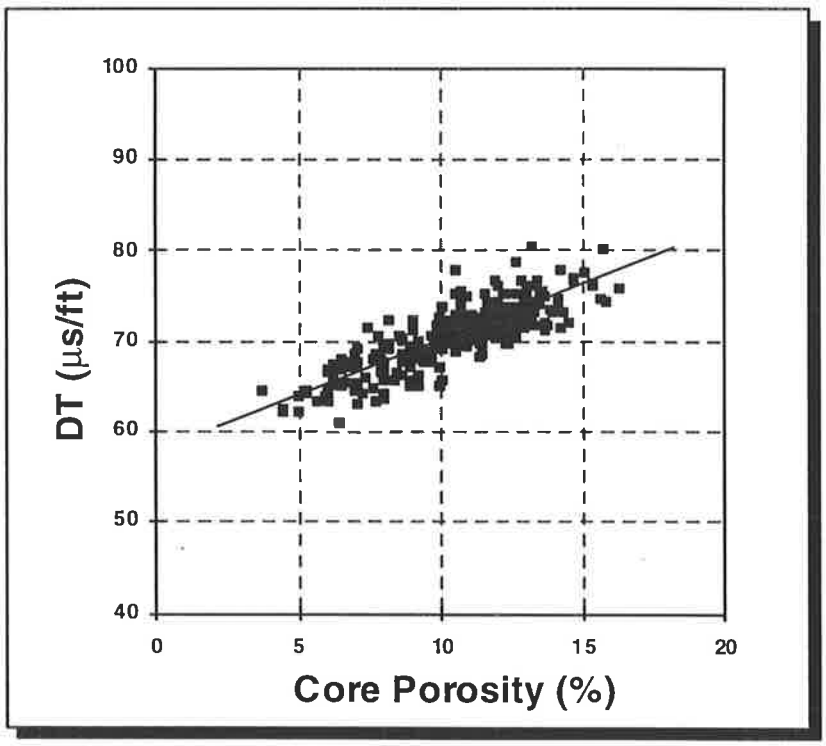

Figure 9.10 - Sonic transit time (µs/ft) plotted against core porosity (%).

waves to travel through a media. Pore spaces include all types of porosity which may exist in the rocks. In the Tirrawarra Sandstone, porosity is macroporosity plus microporosity associated with clay minerals (kaolinite). With an increase in either macroporosity or microporosity, sonic transit time should increase, i.e. sonic transit time measures total porosity. Core porosity also includes all pore spaces which are accessible to helium injection. In most of the studied thin sections most of the microporosity associated with kaolin is readily impregnated with blue-dyed epoxy, indicating the accessibility to the fluids. Helium injection porosity, measured on dried samples, therefore also indicates total porosity for these rocks. Many authors have noted that the presence of clay decreases sonic wave velocity (e.g. Tosaya and Nur 1982; Wilkens et al., 1986; Han et al., 1986; Marion et al., 1989; Eberhart-Phillips, 1989; and Vernik, 1994). Reduction of sonic wave velocity is attributed to a reduction of the elastic moduli in clay-bearing sandstones (Vernik and Nur, 1991 and 1992). Kowallis et al., (1984) attributed the reduction of sonic wave velocity to the microporosity within clays.

Cross-plots of sonic porosity versus point count macroporosity (Fig. 9.11) and point count total porosity (macroporosity plus microporosity associated with kaolinite) (Fig. 9.12) show that a better correlation exists between sonic porosity versus petrographically determined total porosity. This may suggest that sonic porosity includes both macroporosity and microporosity.

9.4.2 Sandstone Composition

Composition of the Tirrawarra Sandstone ranges from quartzarenite to litharenite. In a sandstone with zero porosity, the velocity of a sonic wave depends on the sandstone components. In quartz-rich sandstones, the matrix transit time should be around 55.5 (μs/ft) (Serra, 1984). With increasing rock fragments, in this case mostly of metamorphic, sedimentary and volcanic rock origin, the matrix transit time should vary from that of quartz-rich sandstones. Figure 9.13 shows that, with increasing amounts of rock fragments, sonic transit time decreases. It seems that a sonic wave travels faster in rock fragments than in quartz grains. The reduction of sonic transit time with increasing rock fragment content, however, is related more to the reduction in porosity with increasing rock fragments, resulting in a reduction of sonic transit time. An increase in rock fragments, increases the Compaction Index and Figure 9.14 shows that relationship with sonic velocity.

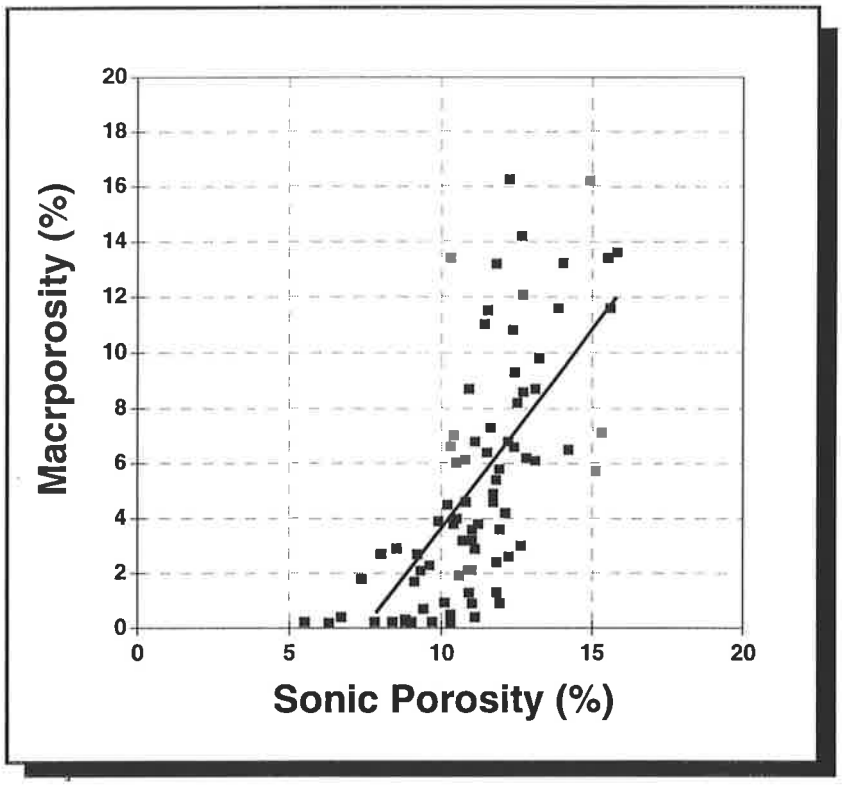

Figure 9.11 - Sonic porosity plotted against point count macroporosity.

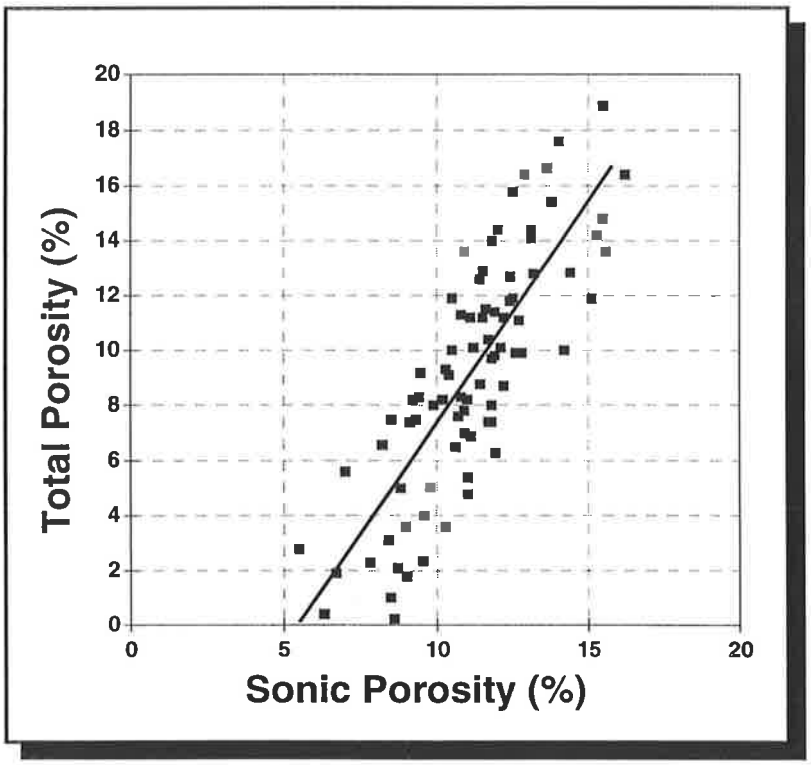

Figure 9.12 - Sonic porosity plotted against total point count porosity.

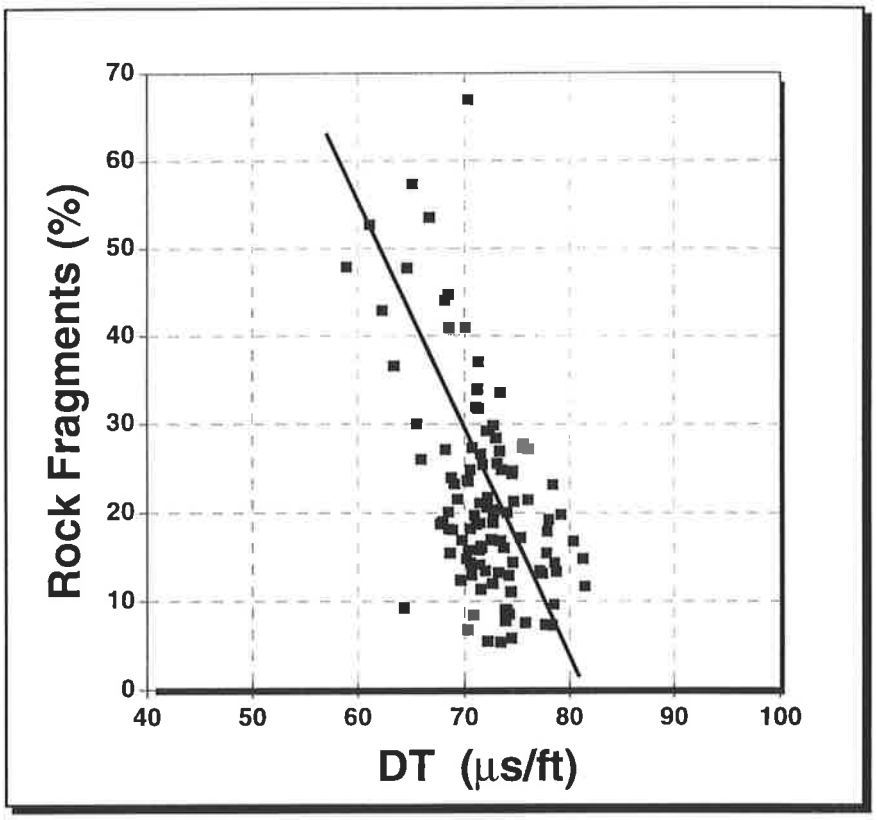

Figure 9.13 - Sonic transit time (µs/ft) plotted against total rock fragment percentage determined by point counting.

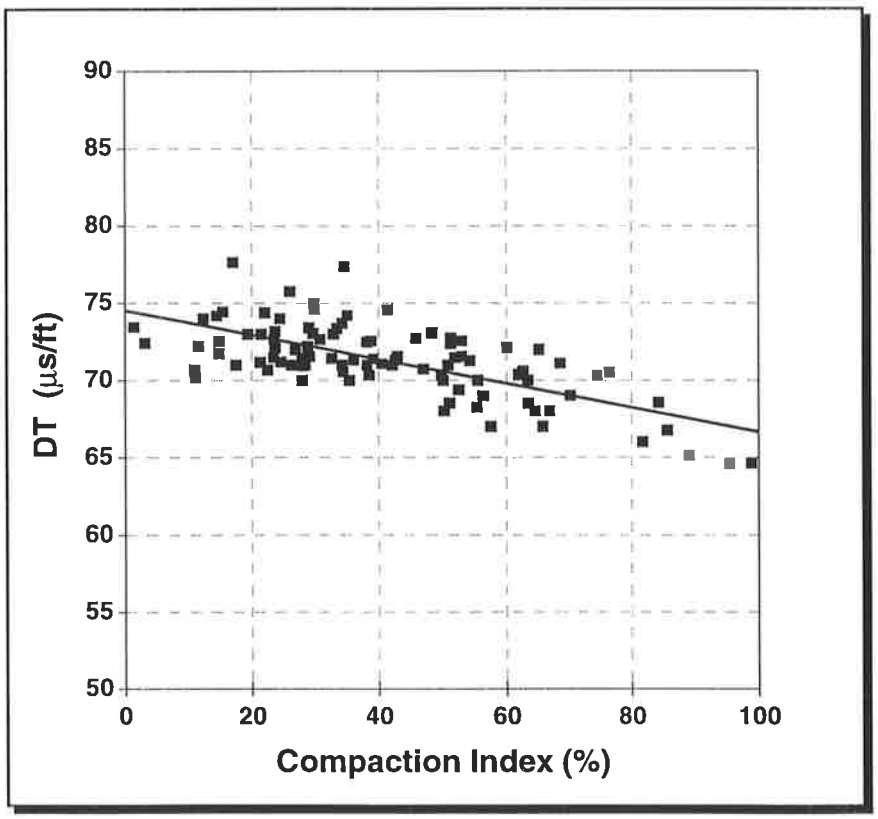

Figure 9.14 - Compaction Index (%) plotted against sonic transit time (µs/ft).

9.4.3 Type of Pore Fluids

The type of pore fluid can affect sonic wave velocity. Gas in a pore fluid dramatically reduces sonic wave velocity. The Tirrawarra Sandstone in the Moorari and Fly Lake Fields is an oil reservoir and most of the cored intervals are in the oil zone. A difference in water saturation will not affect sonic transit time in an oil-bearing interval. According to Wang et al., (1988) (Fig. 9.15), at a temperature of more than 90°C, sonic wave velocity in brine- or oil-saturated samples is the same, so this parameter has no effect on the variation of sonic transit time for the Tirrawarra Sandstone in the Moorari and Fly Lake Fields.

9.4.4 Cementation

Point count petrographic evidence shows that sonic transit time is controlled in part by diagenetic parameters, especially quartz cementation. In general, sonic transit time decreases with increasing cementation (Vernik and Nur, 1991 and 1992). The reduction of sonic transit time is a result of occlusion of pore spaces and the consequent increase in solid contacts among quartz grains, thereby providing a faster route for the sonic wave. Sandstones with little or no cement should have higher porosity and looser contacts between the grains, leading to an increase in sonic transit time. The apparent relationship between sonic transit time and quartz cement looks simple and straightforward and is common in quartz-rich sandstones. The effect of cement on the sonic log in the Tirrawarra Sandstone, however, is relatively complex. The quartz cement and sonic transit time cross-plot is not linear (Fig. 9.16). The polynomial regression of the cross-plot shows a reversal in trend at 10% quartz cement. When quartz cement is less than 10%, the relationship between sonic transit time and quartz cement is positive, but where quartz cement is more than 10%, the trend is negative.

Quartz cement provides a basis to divide samples into two groups. The first group (*Group I*) contains the samples with quartz cement less than 10% and the second group (*Group II*) samples with more than 10% quartz cement. *Group I* shows a positive correlation between quartz cement and sonic transit time (Fig. 9.17). *Group II* shows a negative correlation between quartz cement and sonic transit time (Fig. 9.18). In *Group I*, porosity increases with increasing quartz cement leading to an increase in sonic transit time. The role of quartz cement for this group is the prevention of compaction and

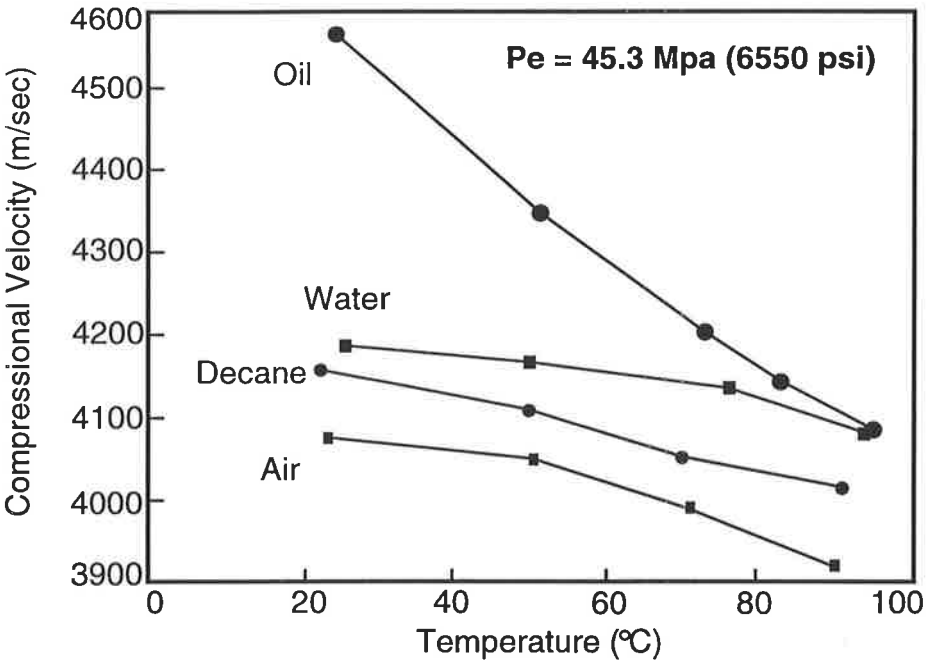

Figure 9.15 - Influence of pore fluid properties and temperature on the compressional velocity in the Berea Sandstone (from Wang et al., 1988).

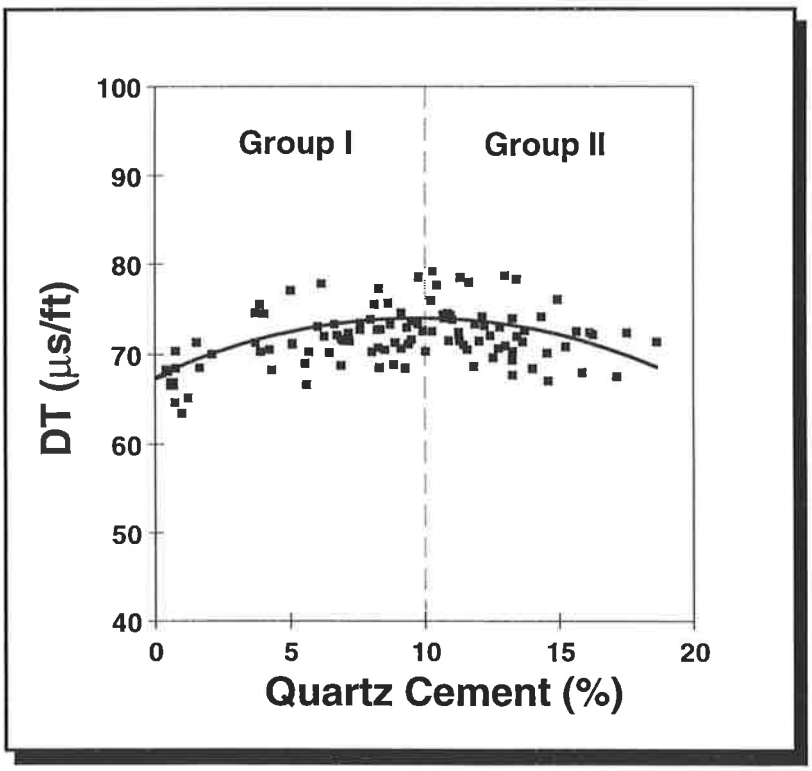

Figure 9.16 - Quartz cement (%) plotted against sonic transit time (ms/ft).

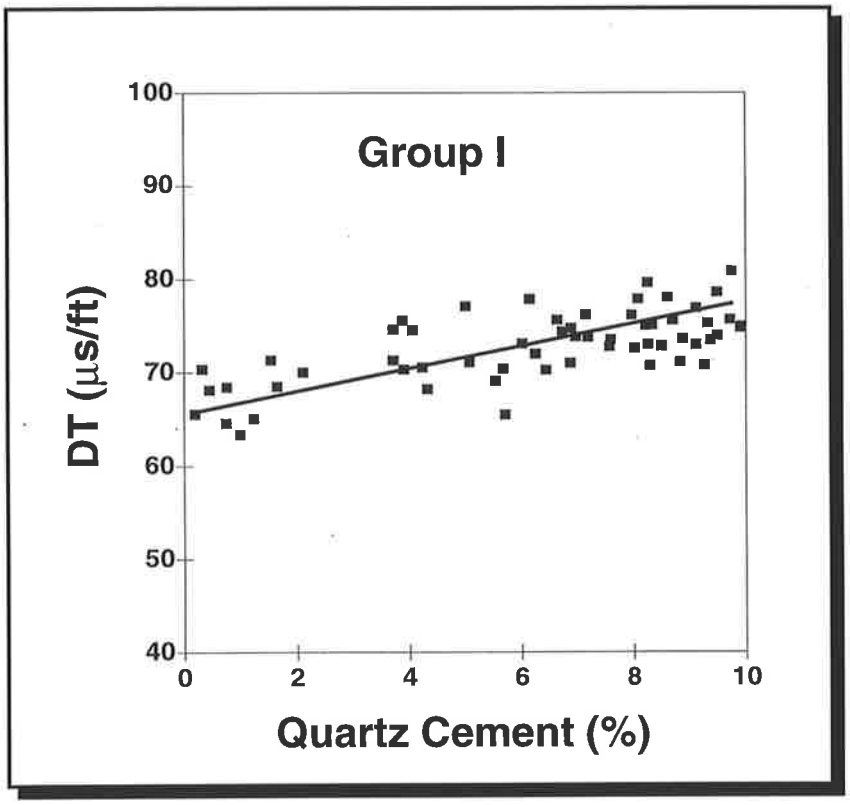

Figure 9.17 - Quartz cement percentage from point counting plotted against sonic transit time (µs/ft) for samples with less than 10% quartz cement (*Group I*).

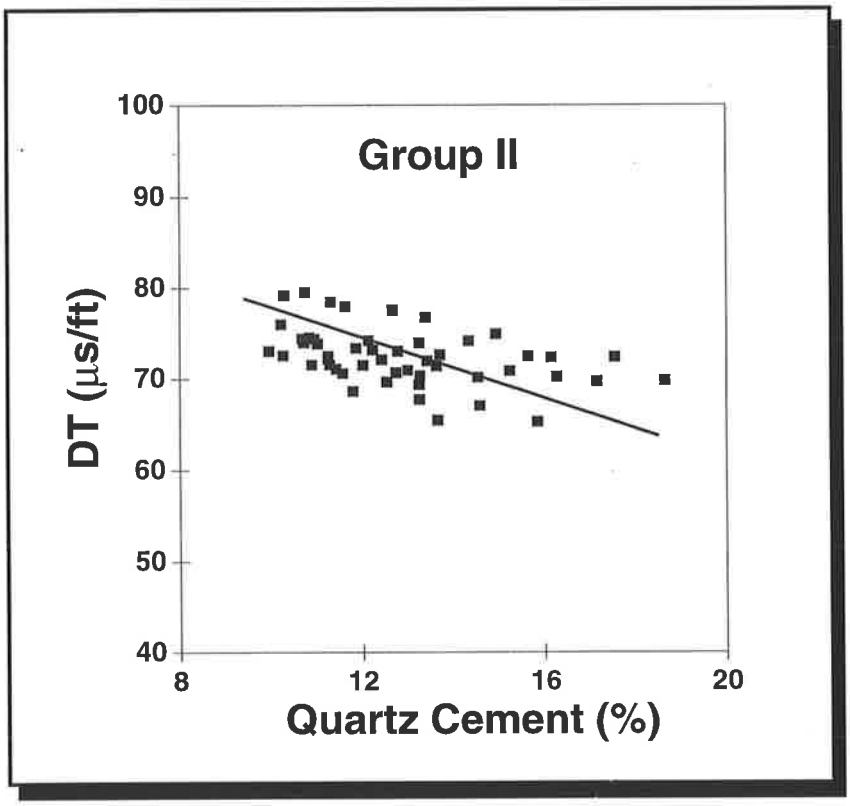

Figure 9.18 - Quartz cement percentage from point counting plotted against sonic transit time (µs/ft) for samples with more than 10% quartz cement (*Group II*).

consequently preservation of porosity. In *Group II*, quartz cement occludes porosity and as it increases, more occlusion of pore spaces occurs, resulting in reduction of porosity and consequently a reduction of sonic transit time.

Comparing average values of different parameters for these two groups (Table 9.4) indicates a significant difference between sandstone composition and Compaction Index values. *Group II* sandstones are more quartz rich and show less compaction. *Group I* has more rock fragments and a higher compaction Index value.

Table 9.4 - Average values of quartz cement (Cqtz), detrital quartz (Qtz), rock fragments (RF) and Compaction Index in samples with less than 10% (I) and samples with more than 10% (II) quartz cement.

	Cqtz (%)	**Qtz (%)**	**RF (%)**	**Comp. Index (%)**
Group I	6.2	70	26	50.2
Group II	13	80	15	30.5

9.4.5 Compaction

Compaction leads to reduction of porosity and may lead to a significant reduction of sonic transit time. In the Tirrawarra Sandstone, compaction is one of the important factors responsible for the reduction of intergranular porosity. Figure 9.14 shows sonic transit time increases with increasing Compaction Index, supporting the notion that compaction in the Tirrawarra Sandstone greatly effects sandstone porosity.

9.4.6 Clay Content

Many authors suggest that the presence of clay in sandstones increases sonic transit time (Tosaya & Nur, 1982; Kowallis, 1984; Wilkens et al., 1986; Han et al., 1986; Marion et al., 1989; Eberhart-Phillips, 1989; Vernik & Nur, 1992; and Vernik, 1994). Reduction of sonic wave velocity is attributed to a reduction of elastic moduli in clay-bearing sandstones or the presence of microporosity within clays.

Clay minerals in the Tirrawarra Sandstone (kaolinite) have a clear influence on the sonic wave transit time. With increasing amounts of kaolinite, sonic wave transit

time increases. This increase, as discussed in section 9.4.1, is related to microporosity associated with kaolinite.

Gamma-ray values plotted against sonic transit time in the Tirrawarra Sandstone show that, with an increasing gamma-ray response, sonic transit time reduces (Fig. 9.19). Gamma-ray log responses basically indicate the presence of illitised rock fragments or mica-rich metamorphic rock fragments in the Tirrawarra Sandstone. The reduction of sonic transit time in the Tirrawarra Sandstone with increasing gamma-ray is related to an increase in the amount of rock fragments which in turn leads to more compaction and consequently to porosity reduction.

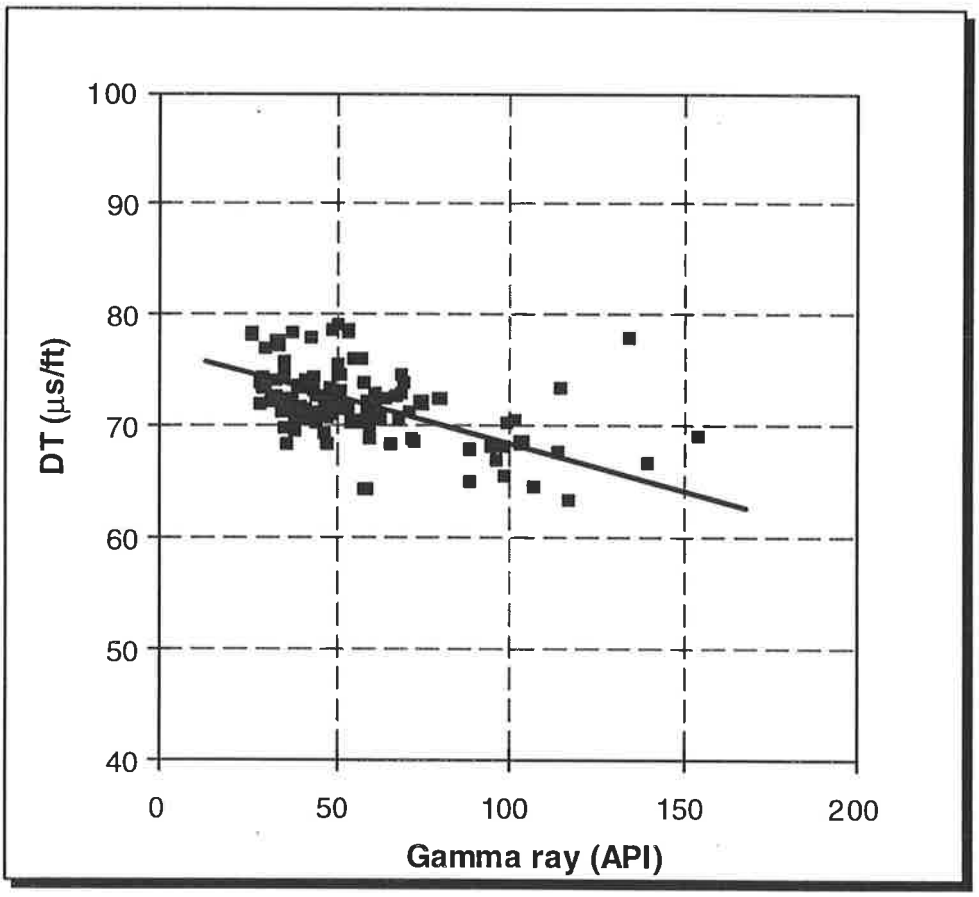

Figure 9.19 - Gamma-ray values plotted against sonic transit time (µs/ft).

9.5 Water saturation (S_w)

9.5.1 Introduction

Water saturation (S_w) in shaly sand formations is a parameter of fundamental economic importance and has been the subject of debate for many years. In clean sandstones, estimation of water saturation is rather simple due to the lack of electrically-conductive materials such as clays. The presence of clays in the shaly sandstones which display high conductivity (Winsauer & McCardell, 1953) makes estimation of water saturation complicated. In this section, factors effecting conductivity of shaly sandstones are reviewed and some of the common equations which are used for calculation of water saturation are applied to the Tirrawarra Sandstone and a new equation to estimate water saturation in kaolinite-rich sandstones is introduced.

The results from the Archie and Waxman-Smits equations display a good correlation with measured core water saturation and core oil saturation. Plots of water saturation from the Archie equation with water saturation from the other equations show that the Archie and Waxman-Smits equations are approximately the same (r^2=98%). As can be expected from the low cation exchange capacity (CEC) of the Tirrawarra Sandstone, the second part of the Waxman-Smits equation concerning shale conductivity is very small. As a consequence, the values of S_w from the Waxman-Smits equation are very close to those from the Archie equation. Petrographic studies indicated that kaolinite patches in the Tirrawarra Sandstone are water wet. In this case, the formation resistivity is a function of formation water in macroporosity and irreducible water associated with kaolinite microporosity. In other words, when kaolinite is electrically inert, the whole rock can be considered as a clean sandstone which obeys the Archie law. Because resistivity logs cannot recognise free water within the macroporosity from bound water associated with clay minerals, calculated water saturation includes both free and irreducible water. As the irreducible water associated with kaolinite minerals is not expelled during production, some intervals of kaolinite-rich sandstones, which may never produce water, may be bypassed as non-productive zones.

A new equation is introduced for the estimation of effective water saturation. The equation is based on the integration of resistivity and sonic log with image analysis data for wells in the Moorari and Fly Lake Fields, where obtaining the volume of clay is

difficult and unreliable (Rezaee & Lemon, 1996a; Rezaee & Griffiths, 1996c). This equation, which reduces calculated water saturation by about 10% for the Tirrawarra Sandstone, is likely to be applicable to other kaolinite-bearing sandstones.

9.5.2 Basic Concepts

Electrical conductivity of a rock depends on several variables including, conductivity of rock components, conductivity of pore fluid, fluid saturation and formation resistivity factor (F). In clean sandstones, the conductivity of the rock components is zero and electrical conductivity is a function of conductivity of pore fluid, fluid saturation and formation factor. In shaly sand formations, the electrical conductivity of rock components cannot be considered zero, as clay minerals provide additional conductivity (Winsauer & McCardell, 1953). In shaly sand formations, conductivity of the clay minerals should also be estimated.

9.5.2.1 Formation Factor

Formation factor was first introduced by Archie (1942) and defined as the ratio of the conductivity of brine to the conductivity of fully saturated clean sandstone:

$$F = \frac{C_w}{C_o} = \frac{R_o}{R_w} \tag{36}$$

where C_w is brine conductivity, C_o is conductivity of fully-saturated reservoir rock, and R_w and R_o are corresponding resistivities.

In clean sandstones F is a variable which is controlled by pore geometry and was expressed by Archie (1942) as:

$$F = \frac{a}{\phi^m} \tag{37}$$

where a is tortuosity factor, m is cementation exponent and ϕ is total porosity. As is shown by Porter and Carothers (1970), variation of a and m can be very significant across a field. The possible variations of a and m are shown by Keelan (1982) and Keelan & Marschall, (1989) (Fig. 9.20a-b).

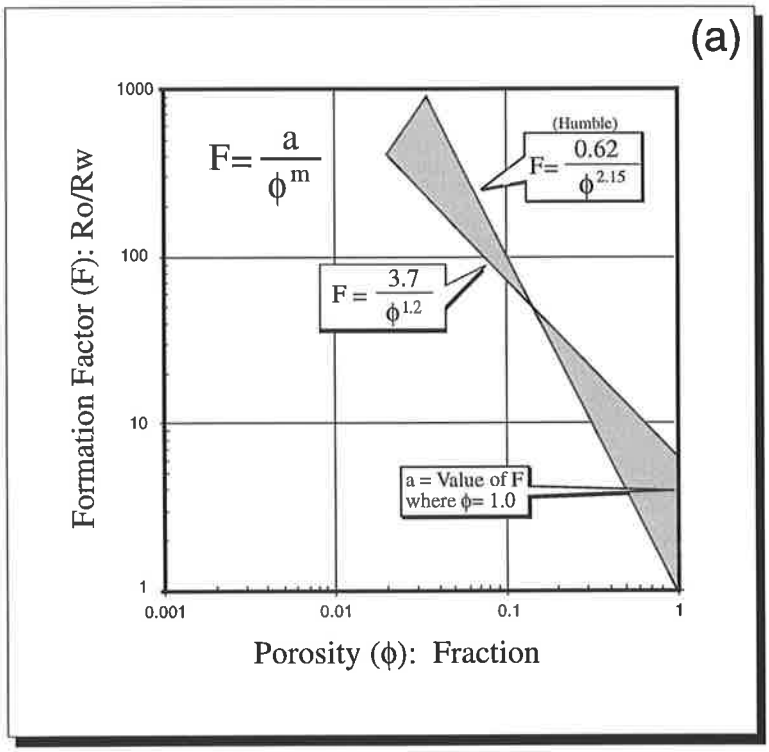

Figure 9.20 a - Formation factor versus porosity, illustrating variation in intercept (*a*) (Keelan, 1982).

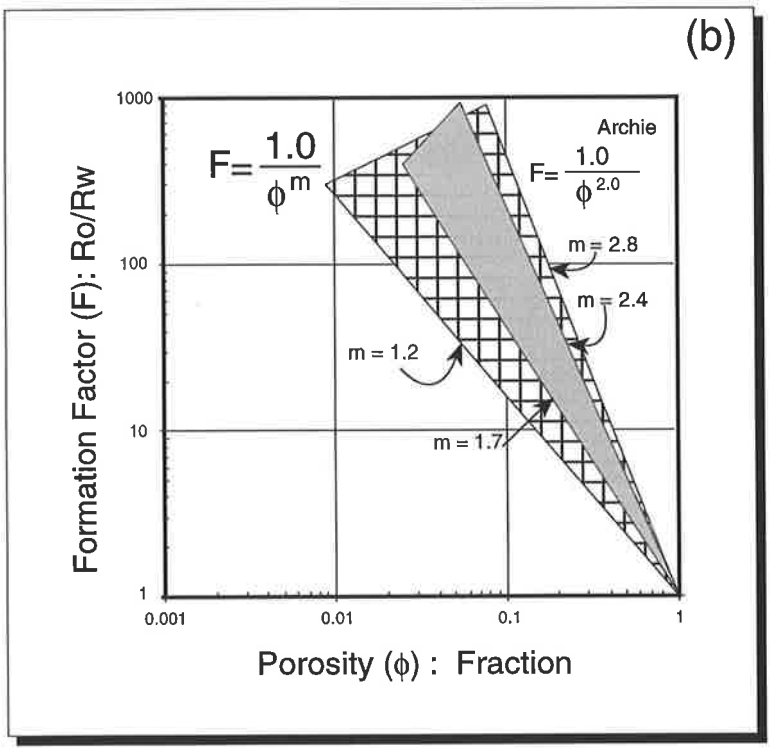

Figure 9.20 b - Formation factor versus porosity, for a range of measured cementation factor (*m*). The grey-shaded area show the most common values for *m* (from Keelan & Marschall, 1989).

As reviewed by Worthington (1985), F is not constant in shaly sandstones and decreases with increasing shale volume. The reduction of F, which is an intrinsic parameter and depends on pore geometry, is due to the presence of clay minerals which produce higher than normal conductivity in the rock. It should be noticed that F in shaly sands is an apparent F and is less than an intrinsic F.

9.5.2.2 Electrical Conductivity of rock components

Rock components can be classified into two parts with respect to electrical conductivity. The first part is non-conductive. Framework grains which are the main components of the rocks and mostly composed from quartz, feldspar and rock fragments in sandstones, belong to the non-conductive part (excluding shaly rock fragments). The second part includes any other component which has the ability to conduct electricity. The most abundant conductive materials in sandstones are the clays. Depending on the type, form and location, clays can have a significant influence on the conductivity of rocks (King, 1992).

9.5.2.3 Electrical Conductivity of Clay Minerals

Clay minerals are hydrous aluminium silicates composed of sheets of silica tetrahedra and alumina octahedra (Wilson, 1987). Clay minerals are classified by the number of tetrahedral and octahedral sheets (Wilson & Pittman, 1977). The most common known clay minerals in reservoir rocks are kaolin, illite, smectite and chlorite (Wilson & Pittman, 1977). The type, form and location of clay minerals controls the character of reservoir rocks (Hurst & Archer, 1986a and 1986b; King, 1992). Clay particles with their internal crystallographic reasons and small size (surface effect), have surface ions with unsatisfied charge (Faure, 1991). Charge imbalance in clay minerals is due to isomorphous substitution within the mineral structure (Wilson, 1987). Substitution of trivalent aluminium for quadrivalent silicon in the tetrahedral sheets gives rise to charge imbalance which causes adsorption of cations on the surface of the clays. Cations on the surface of clay minerals can be exchanged with the surrounding water. This phenomenon is termed cation exchange capacity (CEC) (Faure, 1991). CEC depends at least on the charge imbalance that originated from within the crystal lattice (Faure, 1991). In kaolinite, isomorphous substitution within the mineral structure is not very

significant and cation exchange capacity is limited to broken bonds which result in unsatisfied charge (Pittman, 1988). The smectite and illite groups have more isomorphous substitution within their mineral structure which gives rise to a negative charge which needs to be balanced by cations. This situation provides an electrical ionic double layer around clay mineral surfaces. These cations can be exchanged with pore fluid cations, resulting in an increase in pore fluid conductivity. The CEC of different clay minerals is shown in Table 9.5. Kaolinite has the lowest CEC, suggesting that the members of this clay mineral group have little significant contribution to the electrical conductivity of the rock matrix in terms of their cation exchange capacity.

Table 9.5 - Cation exchange capacity (CEC) of clay minerals.

Mineral	**CEC (meq/100g)**
Kaolinite	2-15
Halloysite	5-50
Illite	10-40
Chlorite	0-40
Allophane	25-50
Montmorillonite	60-150
Vermiculite	100-150

(Data from Garrels & Christ, 1965; Grim, 1968; Johnson & Linke, 1978).

The conductivity of clay minerals in reservoir sands can be attributed to either their associated bound water or their cation exchange capacity or both. There are two different approaches to estimate the conductivity of clay minerals in sandstones. The first is from calculation of clay volume in the samples (cf. Hossin, 1960; Simandoux, 1963; Poupon & Leveaux, 1971) and the second is from evaluating the electrical activity of the clay minerals by considering their CEC (cf. Waxman & Smits, 1968; Clavier et al., 1977 and 1984).

9.5.2.4 Concepts for estimation of water saturation (S_w)

In clean sandstones, conductivity of fully water-saturated rock obeys the Archie equation (Archie, 1942):

$$C_o = \frac{C_w}{F} \tag{38}$$

The presence of clay minerals introduces an excessive conductivity (X) into sandstones (Fig. 9.21) (Winsauer & McCardell, 1953):

$$C_o = \frac{C_w}{F} + X \tag{39}$$

As reviewed by Worthington (1985), two concepts exist for the calculation of excessive conductivity of shaly sands:

In the first concept, the volume of shale is considered to add to the conductivity in shaly sandstones by the associated bound waters, regardless to the type of clay mineral (cf. Hossin, 1960; Simandoux, 1963; Poupon & Leveaux, 1971). The second concept considers electrical conductivity of clay minerals regardless of their volumetric significance (cf. Waxman & Smits, 1968; Clavier et al., 1977 and 1984). The second concept is based on an electrical double layer in the solution adjacent to clay surfaces in shaly sands as discussed by Winsauer and McCardell (1953). These authors consider that excessive conductivity in shaly sands is due to adsorption of ions on the charged clay surfaces.

The advantage of the first concept is that all information can be obtained through wireline log data but the role of electrical conductivity of clay minerals, which depends on the type of clays, is ignored. The advantage of second concept is the scientific approach to the problem but some of the rock parameters need to be obtained in the laboratory (Worthington, 1985). Juhasz (1981) tried to establish a relationship between CEC and ϕ_t and ϕ_N in an effort to obtain all requisite information from logs.

9.5.2.4.1 Shaly sand conductivity from Vsh concept

In the first concept, excessive conductivity (X) is considered as a function of volume of shale (V_{sh}) and shale conductivity (C_{sh}).

Hossin (1960) proposed that the conductivity of a fully brine-saturated shaly sand is as follows:

$$C_o = \frac{C_w}{F} + V_{sh}{}^2 * C_{sh} \tag{40}$$

and in the hydrocarbon zone:

$$Ct = \frac{C_w}{F} S_w^n + V_{sh}{}^2 * C_{sh} \tag{41}$$

Simandoux (1963) introduced an alternative equation based on experimental work on a mixture of a clay mineral (montmorillonite) and sand grains. He proposed that the excessive conductivity of shaly sands is a function of shale volume and the conductivity of shale components:

$$C_o = \frac{C_w}{F} + V_{sh} * C_{sh} \tag{42}$$

and in the hydrocarbon-bearing shaly sands:

$$Ct = \frac{C_w}{F} S_w^n + V_{sh} * C_{sh} \tag{43}$$

Poupon and Leveaux (1973) developed an equation for calculation of water saturation of fresh water formations in Indonesia:

$$\sqrt{C_o} = \sqrt{\frac{C_w}{F}} + V_{sh}{}^{1-\frac{V_{sh}}{2}} * \sqrt{C_{sh}} \tag{44}$$

and in the hydrocarbon-bearing shaly sands:

$$\sqrt{C_t} = \sqrt{\frac{C_w}{F}} S_w^{\frac{n}{2}} + V_{sh}^{1-\frac{V_{sh}}{2}} * \sqrt{C_{sh}} S_w^{\frac{n}{2}} \quad (45)$$

9.5.2.4.2 Shaly sand conductivity from the double layer concept

Waxman and Smits (1968) proposed an equation for the conductivity of shaly sandstones based on CEC of the shale component:

$$C_t = \frac{C_w}{F^*} S_w^n + \frac{BQ_v}{F^*} S_w^{n-1} \quad (46)$$

where Q_v is the CEC per unit pore volume expressed as follows:

$$Q_v = \frac{CEC*(1-\phi_t)\rho_{ma}}{\phi_t} \quad (47)$$

where F^* is the intrinsic formation factor for shaly sands and B is the equivalent conductance of sodium clay exchange cations as a function of C_w and temperature (Juhasz, 1979) and is expressed as:

$$B = \frac{-1.28 + 0.225t - 0.0004059t^2}{1 + R_w(0.045t - 0.27)} \quad (48)$$

Clavier et al., (1977, 1984) noticed that F^* in the W-S equation cannot be achieved through a multiple salinity test as it is under the influence of clay-surface-bound water. They introduced an equation with another term for the conductivity of clay-bound water (dual-water model):

$$C_t = \frac{C_w}{F_o} S_w^n + \frac{(C_{tw} - C_w)V_Q Q_v}{F_o} S_w^{n-1} \quad (49)$$

9.6 Water saturation (S_w) in the Tirrawarra Sandstone

Apart from down-hole resistivity data, several parameters should also be available to estimate water saturation. These include formation water resistivity (R_w), formation factor (F), saturation exponent (n), volume of shale (V_{sh}), shale conductivity (C_{sh}), and CEC.

9.6.1 Formation water resistivity

Formation water resistivity (R_w) is one of the important parameters necessary for calculation of water saturation. There are several ways to determine R_w, including calculation from logs (Resistivity and SP logs) and direct acquisition from a drill stem test (DST).

In the Cooper Basin, water analyses from Tirrawarra Sandstone DSTs show that formation water is mostly sodium chloride water with resistivity about 0.5 (ohm-m) @ 75°F. Measured water resistivity in the Tirrawarra Sandstone from different fields show nearly the same value, suggesting a possible representative Tirrawarra Sandstone formation water (Table 9.6). R_w from resistivity logs in the wet zone, calculated by the ratio method (Schlumberger, 1989) is very variable but the average is about the same as the DST measurements. An average value of 0.51 (ohm-m) @ 75°F is adopted for the Tirrawarra Sandstone. Figure 9.22 shows representative Stiff Plot for the Tirrawarra Sandstone.

Table 9.6 - Formation water R_w from the Tirrawarra Sandstone in different fields in Cooper Basin.

Field	R_w @ 75°F, ohm-m
Fly Lake	0.5
Moorari	0.5
Tirrawarra	0.63
Gidgealpa	0.43
Merrimelia	0.52
Mudrangi	0.52
Average	**0.51**

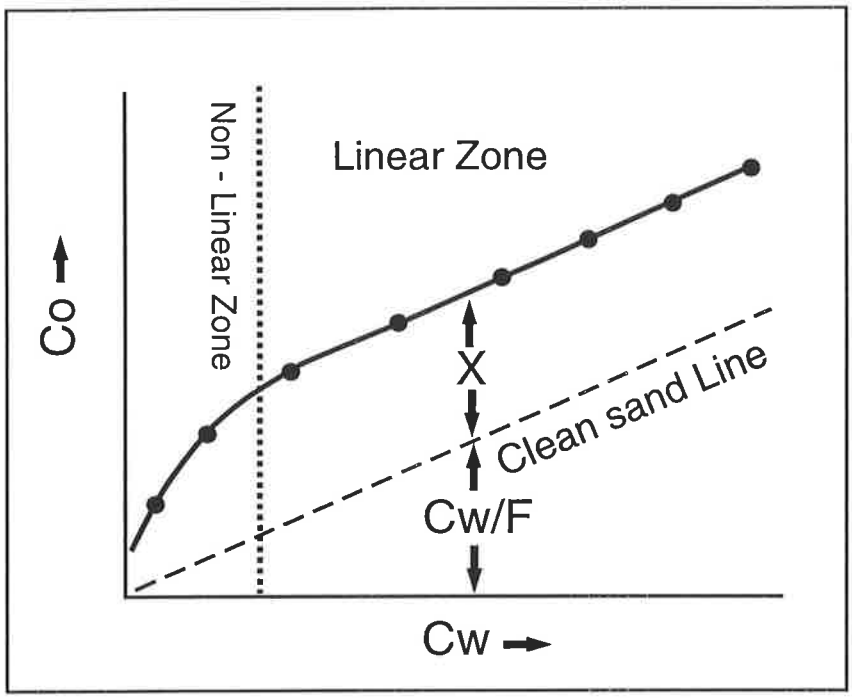

Figure 9.21 - Co versus Cw in water saturated shaly sandstone. Cw is brine conductivity (1/Rw) and Co is saturated rock conductivity (1/Ro), (from Worthington, 1985).

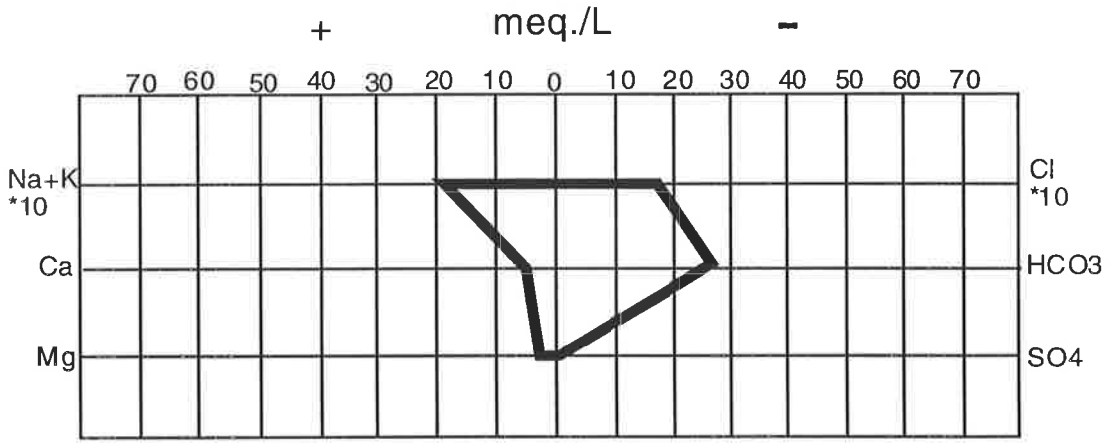

Figure 9.22 - Representative Stiff diagram of water from the Tirrawarra Sandstone. Fly Lake 3, DST 7, Rec.900' GCW. 100'WM, Rw = 0.50 @ 75°F.

9.6.2 Formation Factor (F)

A total of 26 special core analyses under overburden pressure for the Tirrawarra Sandstone in different fields provided information about formation factor and saturation exponent (Santos database) (Table 9.7). The plot of porosity versus formation factor provides the cementation exponent (m) and tortuosity factor (a) values for the Tirrawarra Sandstone (Fig. 9.23). Cementation exponent (m) and tortuosity factor (a), are about 1.88 and 1.22 respectively. The average saturation exponent (n) for the analysed samples is about 1.9.

Table 9.7 - The results of special core analysis under overburden pressure for Tirrawarra Sandstone.

Well	Depth (ft)	Porosity (%)	Formation factor (F)	Saturation Exponent (n)
Fly Lake 2	9552.5	10.9	74.7	1.95
Fly Lake 2	9566.5	8.7	103	1.91
Gidgealpa 16	7259.5	16.4	31.1	1.90
Gidgealpa 16	7262	15.2	33	1.86
Gidgealpa 16	7264	14	40.8	1.93
Packsaddle 2	8587.5	12	65.9	1.90
Packsaddle 2	8598	10.6	87.6	1.91
Tirrawarra 2	9806.5	11.6	80.7	2.00
Tirrawarra 2	9832.5	10.4	92	2.07
Tirrawarra 9	9635.5	12.9	53.1	1.92
Tirrawarra 9	9657.5	12.5	56.8	1.93
Tirrawarra 9	9684.5	10.7	74.7	1.92
Tirrawarra 18	9814	11.2	76.4	2.02
Tirrawarra 18	9850	11.3	92.7	1.98
Tirrawarra 20	9598	10.4	89.1	1.98
Tirrawarra 20	9631	12.6	92	2.01
Tirrawarra 20	9688	11	66.8	1.94
Tirrawarra 22	9715	13.4	44.2	1.96
Tirrawarra 22	9840	12.9	61.3	2.03
Tirrawarra 35	9626.5	13.2	67	1.79
Tirrawarra 35	9636	10.9	83.7	1.89
Tirrawarra 35	9646	8.7	134	1.82
Tirrawarra 39	9650	11	124	1.60
Tirrawarra 39	9708	8.4	79	1.87
Tirrawarra 39	9790.5	10.7	94	1.80

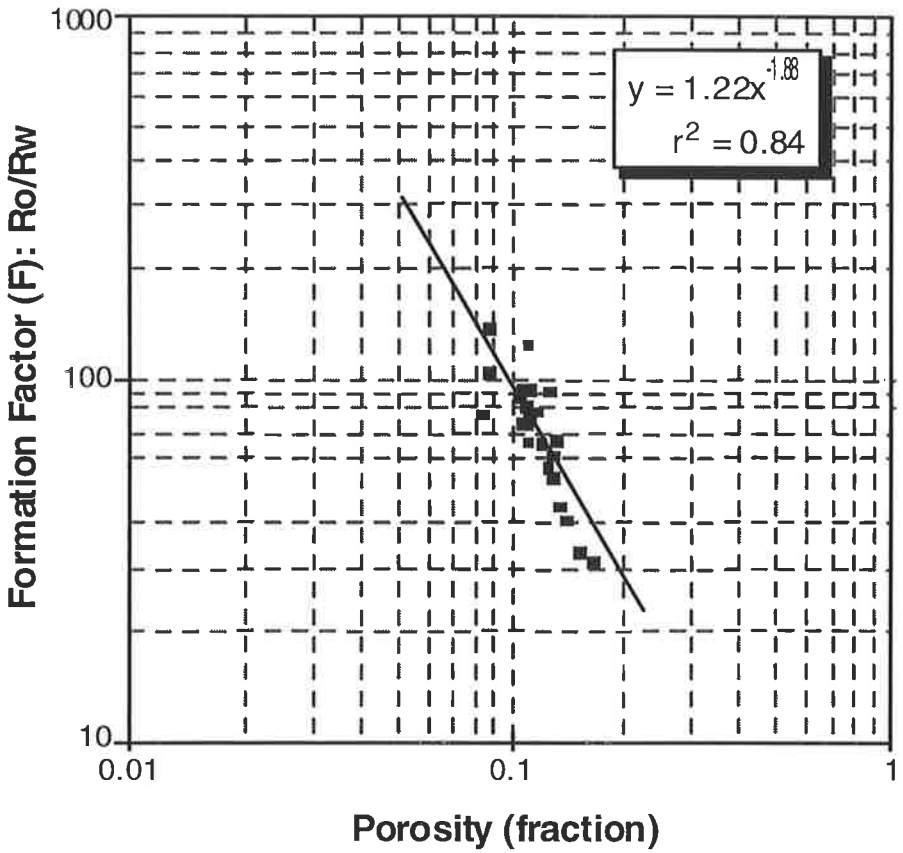

Figure 9.23 - Log - log plot of formation factor versus porosity values of the Tirrawarra Sandstone used for determination of *m* and *a*.

For the Waxman-Smits water-saturation equation, a shaliness-independent saturation exponent (n^*) and shaliness-independent cementation exponent (m^*) are adopted from the work of Morton (1989). Following multiple salinity tests of Tirrawarra Sandstone samples, he assigned a value of 1.93 and 2.06 for m^* and n^* respectively.

9.6.3 Volume of shale (V_{sh})

V_{sh} is required for the estimation of water saturation from the first concept. The only tool to estimate volume of shale in the Tirrawarra Sandstone is gamma-ray (GR). Since kaolinite with its minimal K content is the major clay mineral in the Tirrawarra Sandstone, the determination of V_{sh} is not reliable by using gamma-ray.

9.6.4 Shale conductivity (C_{sh})

Shale conductivity was determined from adjacent shale intervals. It ranges from 13 to 29 Siemens/meter (S/m) with average of 19 (S/m) for the Tirrawarra Sandstone in different wells in the Moorari and Fly Lake fields. An average of 19 (S/m) is adopted for C_{sh}, although it may not be representative of shale conductivity within the reservoir as the detrital clays in the shales may be quite different from the authigenic clays developed in a sandstone.

9.6.5 Cation Exchange Capacity (CEC)

A total of 33 samples were used to find the CEC of the different lithologies from different depositional environments recognised in the Tirrawarra Sandstone (Appendix 9). Cation exchange capacity derived from wet chemistry of the samples indicated that CEC ranges from 0.4 to 1.3 (meq/100g). Average CEC values were adopted for each depositional environment (Table 9.8).

Table 9.8 - The average of CEC for different depositional facies of the Tirrawarra Sandstone.

Depositional facies	CEC (meq/100g)
Beach barrier	0.63
Meandering fluvial	0.70
Distal braid-delta	0.74
Medial braid-delta	0.98

9.6.6 Determination of S_w for the Tirrawarra Sandstone

Some of the most common equations in the literature were applied to the Tirrawarra Sandstone in order to find the best equation for this formation, considering that the Tirrawarra Sandstone is a kaolinite-rich sandstone.

The Archie (Archie, 1942), Hossin (Hossin, 1960), Simandoux ((Simandoux, 1963) and Indonesia (Poupon & Leveaux, 1981) equations using the V_{sh} concept and the Waxman-Smits equation (Waxman & Smits, 1968) using the ionic double layer concept were applied (Appendix 16).

Although the cross-plots of core water saturation and water saturation calculated from the above mentioned equations show widely scattered plots (Fig. 9.24a-e), the results from the Archie and Waxman-Smits equations display better correlation with core water saturation. The correlation coefficient of the regression line from core water saturation and water saturation calculated from the Archie and Waxman-Smits equations is about 0.6 whereas for the remaining is about 0.4.

The better correlation between core water saturation and water saturation calculated from the Archie and Waxman-Smits equations may suggest that these two equations can better estimate water saturation in the Tirrawarra Sandstone than other equations which use a shale volume term in the equation.

The cross-plots of water saturation from the Archie equation with water saturation from the other equations (Fig. 9.25a-d) show that the Archie and Waxman-Smits equations are approximately the same ($r^2 = 0.98$). As can be expected, from the low CEC values of kaolinite-rich sandstones of the Tirrawarra Sandstone, the second part of the Waxman-Smits equation, which considers conductivity of shale, is very small. This results in the values of S_w from the Waxman-Smits equation are very close to those from the Archie equation.

9.6.7 A new approach to determination of S_w

Low CEC values indicate that clay minerals in the Tirrawarra Sandstone do not significantly increase the bulk electrical conductivity of the samples. In most of the studied thin sections of the reservoir samples from the oil zone of the Moorari and Fly Lake Fields, most of the kaolinite patches are not invaded by oil. This indicates that microporosity associated with kaolinite is water wet by trapping of water in capillary pore spaces in kaolinite booklets. Formation resistivity in this situation is a function of formation water in macroporosity and irreducible water associated with kaolinite microporosity. When kaolinite is electrically inert in terms of CEC, the whole rock can be considered as a clean sandstone which obeys Archie law. As resistivity logs cannot

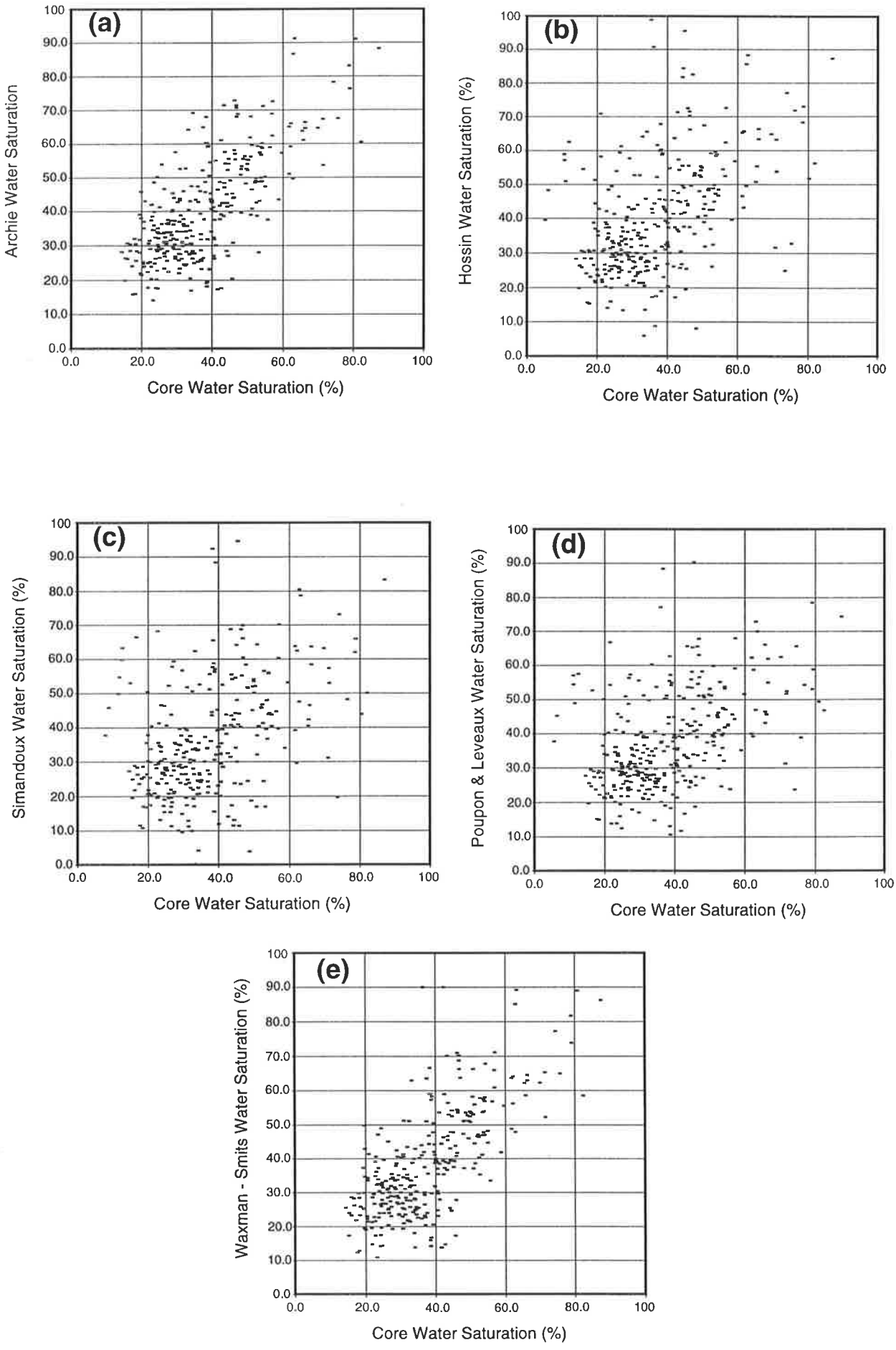

Figures 9.24a-e - Core water saturation plotted against water saturation calculated by the (**a**) Archie, (**b**) Hossin, (**c**) Simandoux, (**d**) Poupon & Leveaux and (**e**) Waxman-Smits equations.

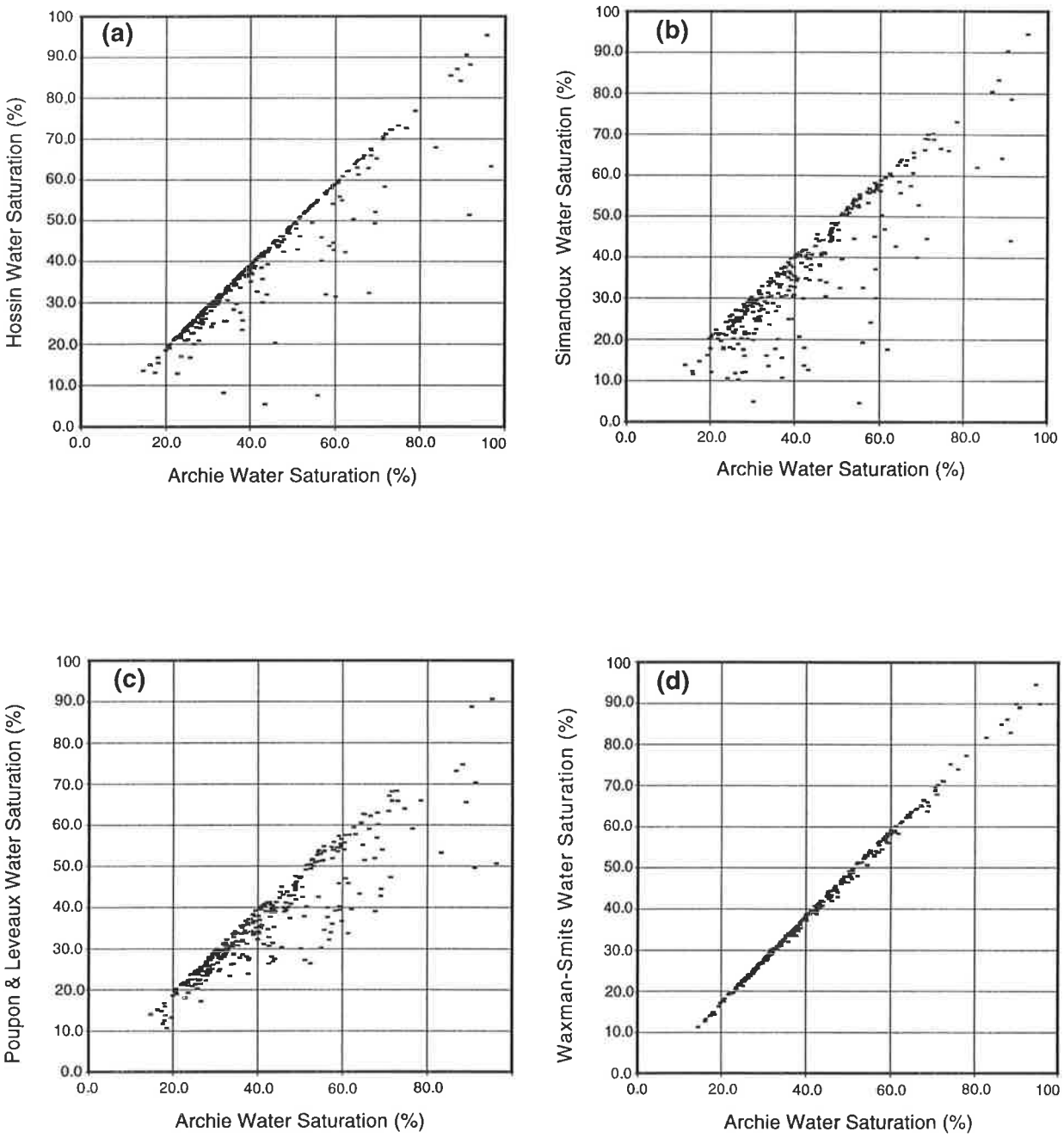

Figures 9.25a-d - Water saturation from the Archie equation plotted against water saturation determined by the (**a**) Hossin , (**b**) Simandoux , (**c**) Poupon & Leveaux and (**d**) Waxman-Smits equations.

distinguish free water within the macroporosity from bound water associated with clay minerals (Pittman, 1988), calculated water saturation must include both free and irreducible waters. As the irreducible water associated with kaolinite minerals is not expelled during production, some intervals of kaolinite-rich sandstones which may never produce water may be bypassed as non-productive zones.

Back-scattered electron (BSE) image analysis of the kaolinite in the Tirrawarra Sandstone indicates a wide range of microporosity in the kaolinite with an average of 20% (Chapter 7). The measurement of microporosity in clay minerals using BSE image analysis was developed by Nadeau and Hurst (1991) and Hurst and Nadeau (1995). Since in the Tirrawarra Sandstone the kaolinite is water wet, appreciation of the volume fraction of kaolinite will allow estimation of the free water saturation as follows:
The total water saturation (S_{w_t}) can be defined by the Archie equation in the Tirrawarra Sandstone:

$$S_{w_t}^{n} = \frac{FR_w}{R_t} \tag{50}$$

The total water volume (V_{tw}) is expressed as:

$$V_{tw} = \phi_t * S_{w_t} \tag{51}$$

The volume of clay-bound water (V_{bw}) within capillary pore spaces of kaolinite can be determined by:

$$V_{bw} = V_k * \phi_{mic} \tag{52}$$

and as the average of microporosity (ϕ_{mic}) in kaolinite is indicated to be about 20% and they are water wet, the volume of clay bound water can be expressed by:

$$V_{bw} = 0.2V_k \tag{53}$$

where V_k is volume fraction of kaolinite.

The volume of free water is equal to:

$$V_{fw} = V_{tw} - V_{bw} \tag{54}$$

so the free water saturation ($S_{w_{fw}}$) can be expressed as

$$S_{w_{fw}} = \frac{V_{fw}}{\phi_e} = \frac{V_{tw} - V_{bw}}{\phi_e} = \frac{\phi_t [\frac{FR_w}{R_t}]^{1/n} - 0.2V_k}{\phi_e} \tag{55}$$

where ϕ_e is effective porosity and ϕ_t is total porosity.

The advantage of this equation is that there is no need to obtain shale conductivity (C_{sh}) from the adjacent shale intervals where the conductivities are likely to be different from those in the sandstones.

9.6.8 Evaluation of the new equation

The point count data of the studied thin sections were used to evaluate the new equation for Tirrawarra Sandstone. The point count values include intergranular porosity or effective porosity (ϕ_e) and volume fraction of kaolinite (V_k). Free water saturation ($S_{w_{fw}}$) calculated from the new equation has a very close correlation with total water saturation (S_{w_t}) from the Archie equation (r^2=0.92) (Fig. 9.26). In general, it seems that $S_{w_{fw}}$ is approximately 10% less than S_{w_t}.

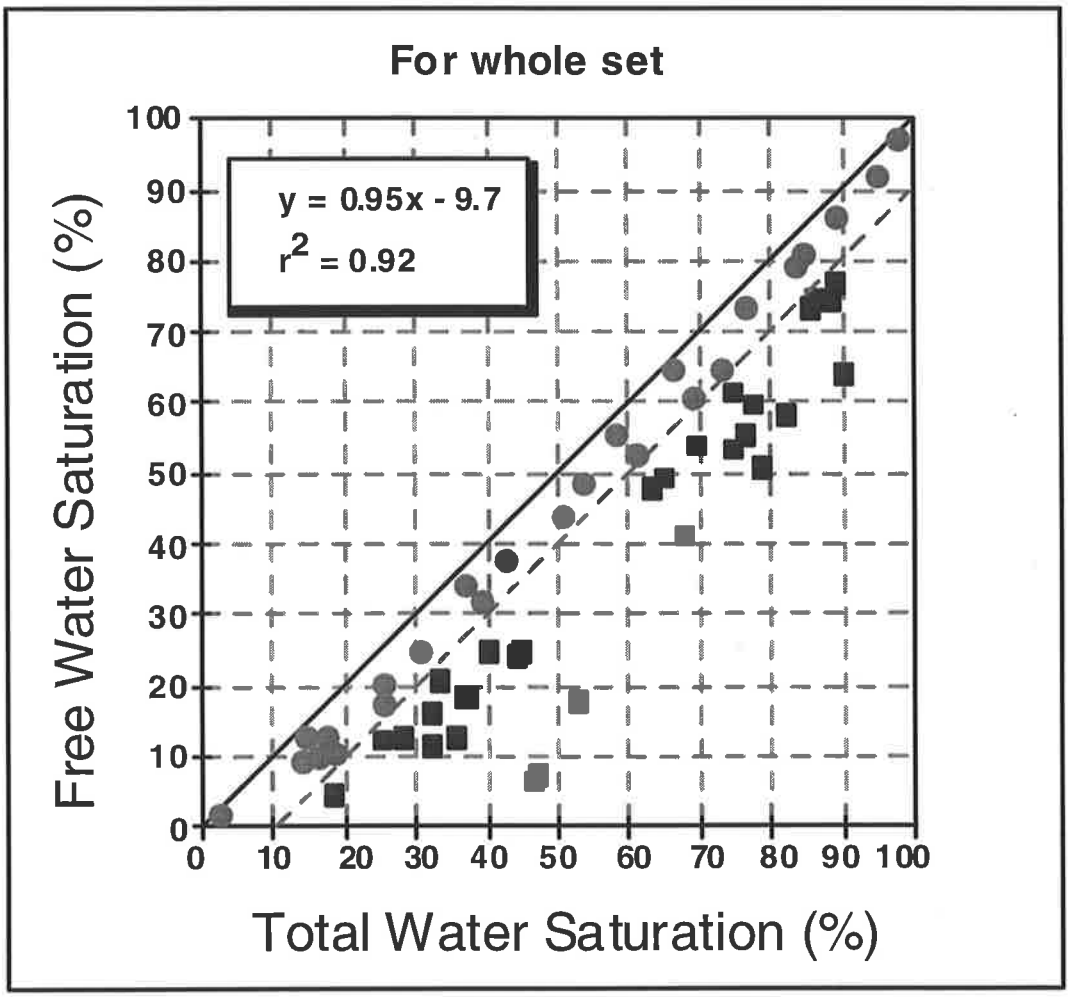

Figure 9.26 - Total water saturation plotted against free water saturation for all of the samples. In some of the samples the difference between $S_{w_{fw}}$ and S_{w_t} is relatively low (circles) whereas for the others (squares), $S_{w_{fw}}$ is considerably less than S_{w_t}.

Based on the regression line of the $S_{w_{fw}}$ and S_{w_t} cross-plot (Fig. 9.26), the relation between $S_{w_{fw}}$ and S_{w_t} can be established as:

$$S_{w_{fw}} = 0.95\, S_{w_t} - 9.7 \qquad (56)$$

Although $S_{w_{fw}}$ is generally 10% less than S_{w_t}, $S_{w_{fw}}$ in some samples may vary above or below this estimate with different amounts of kaolinite. As the estimation of kaolinite content in the Tirrawarra Sandstone is difficult and unreliable, free water saturation should be estimated without counting the volume fraction of kaolinite. Figure

9.26 shows that some of the samples are relatively close to 1:1 line (circles) whereas for the others (squares), $S_{w_{fw}}$ is quite smaller than S_{w_t}. Samples close to 1:1 line are those which have less kaolinite content, thus the difference between $S_{w_{fw}}$ and S_{w_t} is small (less than 10%). While the other samples (squares) have higher content of kaolinite and show larger difference between $S_{w_{fw}}$ and S_{w_t} (more than 10%). Wireline log data of these two groups, showed that they can be well separated on the basis of their sonic transit times. Samples close to 1:1 line, have a sonic transit time more than 73 (μs/ft) and the other group show sonic transit time less than 73 (μs/ft). Regression lines from the $S_{w_{fw}}$ - S_{w_t} cross-plots for samples above and below a sonic transit time of 73 (μs/ft) show very close correlation. The correlation coefficient of the regression line for samples with a sonic transit time more than 73 (μs/ft) is about 0.94 and is about 0.9 for samples with sonic transit time less than 73 (μs/ft) (Fig. 9.27a-b). A better relationship between $S_{w_{fw}}$ and S_{w_t} can be written as:

$$S_{w_{fw}} = 0.99\, S_{w_t} - 8.9 \qquad (57)$$

for intervals with a sonic transit time more than 73 (μs/ft), and

$$S_{w_{fw}} = 0.95\, S_{w_t} - 11.3 \qquad (58)$$

for intervals with sonic transit time less than 73 (μs/ft).

Estimating the volume of clay in the present wells in the Moorari and Fly Lake fields is difficult and unreliable so equations 57 and 58 may be useful for estimation of water saturation which influence production. These equations reduce water saturation by about 9% and 13.5% for intervals with sonic transit time above and below 73 (μs/ft) respectively, and should result in better estimation of reserves in the Tirrawarra Sandstone in the Moorari and Fly Lake fields.

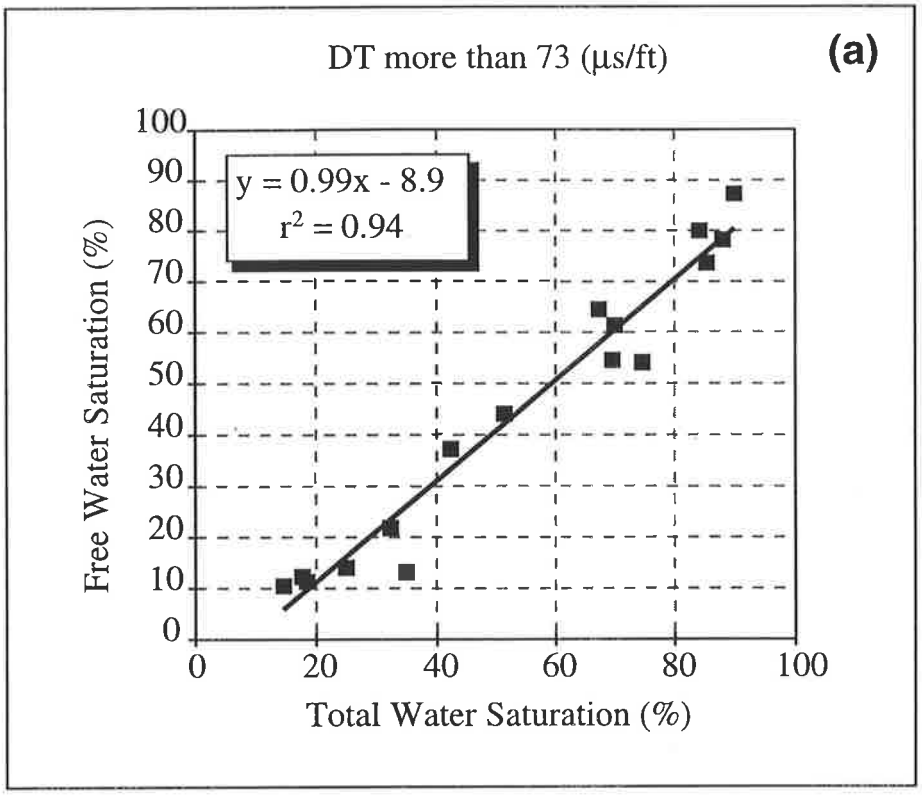

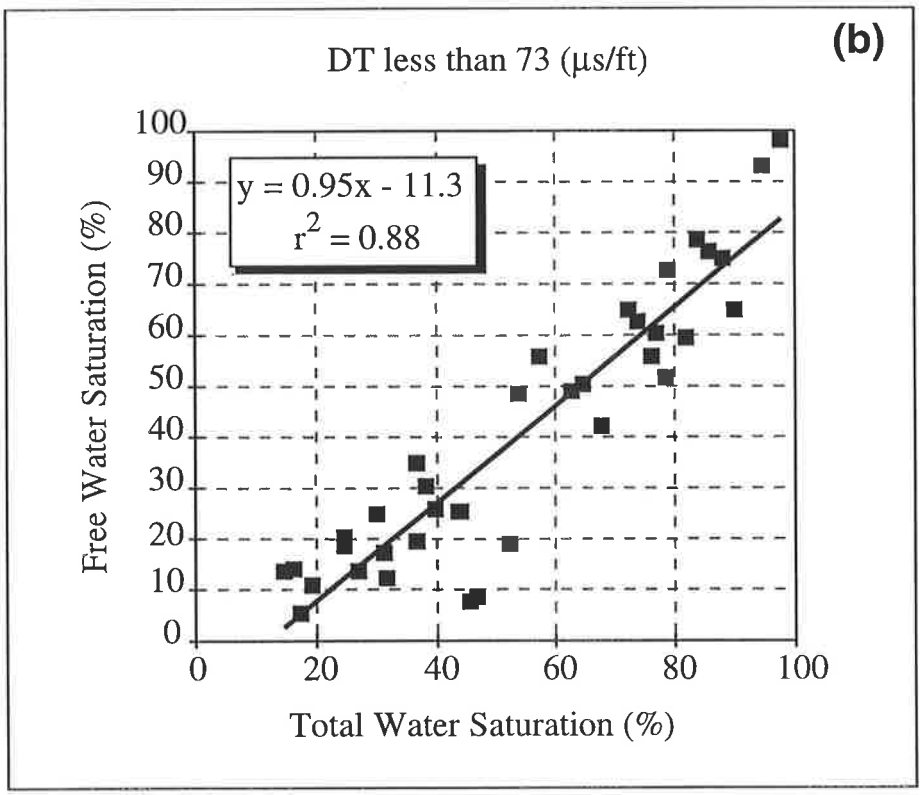

Figures 9.27a-b -Total water saturation versus free water saturation for samples with sonic transit time more than 73 (**a**) and less than 73 (µs/ft) (**b**).

9.7 Discussion and Conclusions

9.7.1 Volume of shale

In the Cooper Basin, the shale volume calculation is routinely carried out by using equation 59:

$$V_{sh} = \frac{GR - GR_{min}}{GR_{max} - GR_{min}} \qquad (59)$$

where GR_{min} is minimum gamma-ray log value (API) for clay-free intervals and GR_{max} is maximum gamma-ray log value for 100% shale intervals (Rider, 1986; Bowler, 1988). As the gamma-ray in the Tirrawarra Sandstone mainly represents the presence of illitised rock fragments, it does not show the abundance of kaolinite which is the dominant clay in the Tirrawarra Sandstone so this method cannot be suitable for the estimation of shale volume in the studied area.

9.7.2 Sonic porosity

Plots of petrographic point count data versus acoustic transit time show that acoustic transit time is a function of several factors including porosity, mineral composition, cementation and compaction.

Previous sonic porosity equations used in the Cooper Basin reservoirs have had limited success. The problem with the previous equations is that most of them calculated clay fraction volume from the gamma response without considering that kaolin, which has a minimal gamma response, is the major clay mineral in the Tirrawarra Sandstone. The reduction of acoustic velocity, however, in the kaolinite-bearing Tirrawarra Sandstone is probably due to microporosity among kaolinite booklets. Sonic porosity, therefore, includes both macroporosity and microporosity. New empirical equations are introduced for the Tirrawarra Sandstone in the Moorari and Fly Lake Fields.

The plot of sonic porosity derived from the new equations and core porosity show an r^2 value of 0.8 i.e. 80% of the porosity variation is explained by the equation. Remember that total porosity is being calculated using this equation. However, knowing

the amount of microporosity, it is possible to estimate macroporosity. The relation between total porosity and macroporosity can be expressed by:

$$\phi_t = \phi_e + \phi_{mic}$$

As the sonic porosity is equal to total porosity, and Back-Scattered Electron (BSE) image analysis of the clay minerals in the Tirrawarra Sandstone indicates that, on average, 20% of the total kaolinite volume can be considered microporosity, the equation will be:

$$\phi_e = \phi_{sonic} - 0.2V_k$$

Knowing the volume fraction of clay, it is then possible to determine the amount of macroporosity in a Tirrawarra Sandstone.

Quartz cementation in the Tirrawarra Sandstone has a complex effect on acoustic transit time. The plot of quartz cement percentage versus transit time shows a non-linear trend. For samples with less than 10% quartz cement (*Group I*), acoustic transit time increases with increasing quartz cement , whereas in samples with more than 10% quartz cement (*Group II*) transit time increases as the quartz cement decreases. The samples of *Group I* are more lithic and quartz cement is less developed, but the role of quartz cement in this group acts to prevent compaction and consequently preserve porosity. In *Group II* samples, which have less rock fragments, the development of quartz cement leads to occlusion of pore spaces and acoustic transit time reduction.

Compaction in the Tirrawarra Sandstone results in a reduction of porosity, especially in rock-fragment-rich sandstones. Plots of compaction index versus acoustic transit time show that, with increasing compaction index, transit time decreases.

These results suggest that rock parameters such as composition, cementation and clay content have a clear effect on sonic wave transit time because these parameters indirectly control porosity. For sandstones with a given composition, the most important parameter which controls sonic wave transit time is porosity.

9.7.3 Water saturation

CEC values for the Tirrawarra Sandstone samples obtained from the wet chemistry method (Appendix 9), indicate a low CEC of the samples. Although the wet chemistry method is thought not to be a reliable CEC determination (Mian & Hilchie, 1982; de Waal, 1989), and Morton (1989) indicated that CEC from wet chemistry showed values too high in Cooper Basin samples, the low CEC values for the Tirrawarra Sandstone samples agrees with petrographic studies. The major clay mineral in the Tirrawarra Sandstone is kaolinite with only minor amounts of illite. As the CEC of kaolinite is relatively low (Table 9.5), the low value CEC from the Tirrawarra Sandstone samples is expected. Clay minerals in the Tirrawarra Sandstone are largely electrically inactive in terms of their cation exchange capacity. This suggests that an equation like the Waxman-Smits equation (Waxman-Smits, 1968), which considers the influence of the double layer model of clay minerals, is not necessary. Figure 9.25d shows that the cross-plot of water saturation from the Archie and Waxman-Smits equations are the same, because Q_v term in the Waxman-Smits equation is very low. Other equations for water saturation which consider the volume of shale (Hossin, 1960; Simandoux, 1963 and Poupon and Leveaux, 1981) are also not appropriate for the studied area because, with the present logging suite, the calculation of the volume fraction of kaolinite in the Tirrawarra Sandstone is not possible and leads to erroneous results. The Archie equation, which estimates both free and bound water together, gives a better total water saturation. With the knowledge of the amount of microporosity it will be possible to determine the free water saturation and so more accurately predict the location of potential reservoirs.

9.8 Nomenclature

a = tortuosity factor

B = equivalent conductance of sodium clay exchange cations as a function of C_w and temperature

C = clay content term

CEC = Cation Exchange Capacity, (meq/100g).

C_o = conductivity of fully saturated reservoir rock, (S/m)

C_{sh} = shale conductivity, (S/m)

C_w = brine conductivity, (S/m)

F = formation resistivity factor (R_o/R_w)

F^* = intrinsic formation factor for shaly sands

GR = gamma-ray (API)

GR_{max} = maximum GR log value for 100% shale intervals

GR_{min} = minimum GR log value for clay-free intervals

m = cementation exponent

m^* = shaliness-independent cementation exponent

n = saturation exponent

n^* = shaliness-independent saturation exponent

P_e = effective pressure

Q_v = the CEC per unit pore volume

S_w = water saturation

S_{Wfw} = free water saturation

S_{Wt} = total water saturation

V_{bw} = volume of clay-bound water

V_{fl} = pore fluid acoustic velocity (km/sec)

V_k = volume fraction of kaolinite

V_{ma} = matrix acoustic velocity (km/sec)

V_P = compressional wave velocities (km/sec)

V_s = shear wave velocities (km/sec)

V_{sh} = volume of shale

V_{tw} = total water volume

X = excessive conductivity

ϕ_e = effective porosity

ϕ_{mic} = microporosity associated with clay

ϕ_{sonic} = sonic porosity

ϕ_t = total porosity

Δt = whole rock transit time (μs/ft)

Δt_{fl} = pore fluid transit time (μs/ft)

Δt_{ma} = rock matrix transit time (μs/ft)

CHAPTER TEN

CONCLUSIONS

10.1 Introduction

The following topics were tackled as part of this thesis:

- Interpretation of the depositional environments of the Tirrawarra Sandstone,
- A detailed study of diagenetic events of the sediments using the following techniques:
    - * optical petrography
    - * bulk-rock and clay-fraction XRD analyses,
    - * scanning electron microscopy,
    - * cathodoluminescence microscopy,
    - * electron microprobe analysis,
    - * oxygen and carbon isotopes,
    - * fluid inclusion microthermometry,
    - * image analysis.
- Combination of sedimentology and petrographic data with burial history curves provided the most substantial diagenetic history of the Tirrawarra Sandstone to date,
- The use of image analysis for quantification of multi-generation of siderite cement for enhancement of oxygen and carbon stable isotope interpretation,
- Development of a new concept regarding the influence of tectonic events on siderite cement precipitation in the Tirrawarra Sandstone,
- Incorporation of petrographical information with petrophysical data to enhance log analysis of the Tirrawarra Sandstone.

10.2 Depositional Facies

Following detailed sedimentological logging of all available relevant cores, deposition of the Tirrawarra Sandstone was described in terms of the following depositional facies:

- Lacustrine environment with upper and lower shoreface deposits

- Parallel beach barrier
- Back barrier marsh with outwash beds
- Distal part of a braid-delta with lingoiud bars, inter-channel bay, and splay deposits
- Medial part of a braid-delta with longitudinal bars
- Meandering system, dominated by point bar deposits
- Aeolian deposits

Vertical succession of these facies association indicates three depositional units for the Tirrawarra Sandstone in the Moorari and Fly Lake fields. The vertical succession records progradation and retreat of a braid-delta into a lacustrine environment.

Each sedimentary environment has a characteristic detrital composition controlled by the distance from the sedimentary source and the energy of the depositional environment. The relative proportions of quartz grains and rock fragments vary considerably between each sedimentary environment.

10.3 Diagenesis

Mechanical compaction and quartz cementation are recognised as the principal diagenetic processes which significantly modified porosity in the Tirrawarra Sandstone. The absolute and relative intensity of these diagenetic events is controlled by the composition of the sandstones. Mechanical compaction is more pronounced in lithic sandstones, whereas, in quartz-rich sandstones, the precipitation of quartz cement is more developed. Now that the sandstone composition range in each sedimentary environment is more fully understood, it is possible to quantitatively estimate the intensity of these two important diagenetic events in the Tirrawarra Sandstone to predict reservoir quality.

A variety of authigenic minerals are recognised for Tirrawarra Sandstone, including syntaxial quartz overgrowths, siderite, patchy kaolinite, and minor illite.

Quartz is the dominant pore-filling cement in most samples. Quartz cementation was initiated prior to major compaction, as evident by the loose grain packing of detrital grains, but probably continued until relatively recent times. CL observations show three main zones of quartz cement which fluid inclusions show were precipitated at different temperatures. The zones of quartz cement are:

◊ an inner-most zone of brown-luminescing cement (Z1),

◊ a middle zone of bright-blue-luminescing cement (Z2) and

◊ an outer zone of brown-luminescing cement (Z3).

Dead oil or bitumen is trapped between Z2 and Z3, indicating that Z3 formed after oil migration commenced. Homogenisation temperature measurements from fluid inclusions within quartz overgrowths indicate that quartz cement precipitated over a temperature range of 65° to 130°C. Z1 quartz cement formed between 65° and 80°C, Z2 cement between 80° and 100°C, Z3 quartz cement formed later at temperatures around 130°C.

The best reservoir lithologies are composed of sandstones containing mainly Z1 and Z2 quartz cements. They are typically well-sorted, quartz-rich sandstones that formed in aeolian and point bar environments and the higher porosities encountered (14-17%).

Integration of petrographic, stable isotope and fluid inclusion results have led to the identification of the following siderite cementation events:

⇒ an early, homogeneous Fe-rich siderite with a $\delta^{13}C$ signature of +1.45‰, indicative of low-temperature methanogenic processes (≤ 30°C);

⇒ an Mg-rich inhomogeneous siderite characterised by complex zoning, with a $\delta^{13}C$ signature of -8.5‰ that was produced mainly by the decarboxylation of organic matter at temperatures between 64 and 76°C;

⇒ an Mg-rich, relatively homogeneous pore-filling siderite with a $\delta^{13}C$ character of -11‰ that was produced during kerogen maturation, at more elevated temperatures (98-110°C). Both the first and second generation of siderite cement were followed by a period of cement dissolution. The first dissolution event probably is related to low-pH meteoric water interaction during which early dissolution of feldspar grains occurred. The second siderite dissolution phase probably related to acidic fluids generated from kerogen maturation. Z1 and Z2 quartz cement precipitation coincided with the dissolution phases of siderite cement. Z1 formed during meteoric water flushing that led to silica release from early feldspar dissolution and also led to S1 dissolution. Z2 quartz cement precipitated during kerogen maturation, when generated fluid led to dissolution of feldspar grains and S2 siderite.

Two types of clay minerals as kaolinite and illite were recognised. Pore-filling euhedral and vermiform kaolinite booklets are common, and are sometimes intergrown with the outer margin of quartz overgrowths. The kaolinite is believed to have formed mainly as a replacement product of feldspars, and, to a lesser extent, micas. Most of the kaolinite patches appear water-wet and they had a great influence on porosity modification. The pore-filling kaolinite converted macroporosity to microporosity associated with kaolinite booklets. The authigenic nature of illite is evident from its rare fibrous, lath-like habit. The mineral is thought to have formed as a replacement product of chemically-unstable rock fragments and therefore most of them act as structural clay in Tirrawarra Sandstone with no great influence on permeability reduction.

10.3.1 A new approach for determination of silica sources for quartz cement

Electron microprobe analysis shows a consistent variation in aluminium between each of quartz cement zone. The average aluminium content for Z1, Z2 and Z3 is respectively 237, 538 and 58 ppm. Fluid inclusion homogenisation temperatures and aluminium content have been used to help identify the silica sources for different zones of cement. The cement zones with high Al_2O_3 content (Z1 and Z2) are thought to be related to discrete episodes of feldspar dissolution and kaolinite precipitation. These discrete episodes can be matched with tectonic events and organic acid generation during burial history of the Tirrawarra Sandstone. The pore fluids during these episodes had high Al contents and low pH. Low pH pore fluid helps dissolution of feldspar grains and also leads to the conversion of octahedrally coordinated Al to tetrahedrally coordinated Al complexes which are preferentially substituted into silicate lattices. Low pH pore fluids for Z1 and Z2 occurred via flushing of acidic meteoric water or later generation of organic acid from kerogen maturation. Considering the temperature of precipitation, very low aluminium content, and the occurrence of Z3 cement in facies prone to stylolitisation, the silica source for the cement is likely to have been pressure solution of detrital quartz at stylolites and grain contacts.

10.3.2 Introduction a new method for enhancement of stable isotope interpretation

A new method to improve the interpretation of bulk-rock oxygen and carbon isotope data in isotopically heterogeneous samples is presented. In the Tirrawarra Sandstone, volumetric estimation of individual cement generations of siderite is accomplished using image analysis techniques in conjunction with electron microprobe data. Results show that bulk-rock isotope values are controlled by the relative proportions of three main siderite cement generations. The variation in $\delta^{18}O$ can be expressed by the equation $\delta^{18}O_{(bulk)} = (V_{S1}*\delta^{18}O_{S1})+(V_{S2}*\delta^{18}O_{S2})+(V_{S3}*\delta^{18}O_{S3})$. The variation in $\delta^{13}C$ can be expressed by the same type of equation, but the correlation coefficient is lower (0.64) than that for $\delta^{18}O$ (0.82). Both $\delta^{18}O$ and $\delta^{13}C$ end-member values for each cement generation fall within a narrow range, enabling a precise definition of the conditions under which the individual cement generations formed. The technique presented has particular applications in cases where pure, or nearly pure samples of end-member siderite cement generations are not available for isotope analysis, provided the various cement generations have different chemical compositions. The findings illustrate the need for a detailed understanding of cement stratigraphy and the isotope character of individual cement stages before bulk-rock isotope signatures can be confidently interpreted in rocks containing multi-stage cements. Non-recognition of the heterogenous nature of bulk-rock isotope data can lead to erroneous interpretations of the diagenetic sequence. The results from this investigation show that caution must be exercised in the interpretation of bulk-rock isotope signatures even when only a single carbonate cement phase is indicated by semi-quantitative bulk XRD analysis. Only the end-member isotope compositions of the different cement generations should be taken into consideration when interpreting the genesis of multi-generation siderite cements. Generally, the different generations of siderite cement are not readily identifiable under the optical microscope, highlighting the importance of back-scattered electron image analysis for siderite characterisation. In particular, the integrated use of video-imaging and image analysis software provides an efficient means of quantifying the different siderite cement generations seen under BSE images. Since the method can be semi-automated, the technique provides a potentially powerful tool for improved bulk-rock isotope interpretations in clastics containing multi-generation carbonate cements. The method enables the determination of end-member $\delta^{18}O$ and $\delta^{13}C$ compositions of

individual cement generations in cases where pure, or nearly pure samples of end-member carbonate cement generations are not available for isotope analysis, provided (1) a statistically representative number of BSE images is analysed, and (2) the various cement generations have different chemical compositions.

10.3.3 A new concept for tectonic fingerprinting of siderite cements

This study indicates that authigenic minerals formed during burial diagenesis may record tectonic activity of a basin. In the Tirrawarra Sandstone, three stages of siderite cement have formed under different tectonic conditions: S1 formed before the first major tectonic event after deposition of the Tirrawarra Sandstone; S2 precipitated under tectonically-active conditions and is characterised with complex compositional zoning and minor dissolution phases; S3 which commences with even compositional banding and grades into a thick homogenous phase in the terms of composition, formed under tectonically-stable conditions in the Cooper Basin.

With the knowledge of precipitation temperatures and timing of S2, it is possible to estimate the amount of erosion during T2. Assuming the current thermal gradient for the Patchawarra Trough of about 36°C/km was valid for T2 time, at least 550 meters uplift and erosion would have occurred in the Late Triassic in the area.

10.4 Oil Migration

Both S2 and S3 siderite and Z1 and Z2 quartz cements have bitumen trapped between them. With the knowledge of precipitation temperatures of different generations of siderite and quartz cement, hydrocarbon migration was indicated to be occurred at temperature range between 80°C and 102°C. This temperature range indicates that the occurrence of oil in the Tirrawarra Sandstone happened during Cretaceous burial.

10.5 Tirrawarra Sandstone Classification

Tirrawarra Sandstone samples are separated to eight classes according to the relative proportions of different kinds of porosity (microporosity, and primary and secondary macroporosity). The reservoir quality increases from class eight to class one and the classes have a predictable relationship to sedimentary environment. Pore geometry of

each class studied in detail by further examinations, including image analysis, and mercury injection capillary pressures, on the representative samples of each class.

Class one samples, associated with meander, aeolian or beach-barrier environments, have primary macroporosity with partial quartz cement. Pore throats usually exceed 10 microns, mean pore space area is about 36000 micron^2 and mean pore diameter and mean pore perimeter are 170 and 350 microns respectively. At the other end of the scale, Class 8, associated with a braid-delta environment, is dominated by microporosity and has a mean pore space area of about 430 micron^2 with mean pore diameter and mean pore perimeter 24 and 75 microns respectively. The pore throat distribution shows poor sorting, ranging from 0.1 to 0.5 microns.

10.6 Petrophysical Evaluation

10.6.1 Porosity from sonic log

Previous sonic porosity equations used in Cooper Basin reservoirs have had limited success. The problem with the previous equations is that most of them calculated clay volume from the gamma response without considering that kaolinite is the major clay mineral in the Tirrawarra Sandstone. The reduction of acoustic velocity in kaolinite-bearing Tirrawarra Sandstone, however, is more likely related to microporosity among kaolinite booklets, and sonic porosity thus includes both macroporosity and microporosity. In the present study, new equations are introduced for the Tirrawarra Sandstone in the Moorari and Fly Lake fields.

$$\phi = \frac{\Delta t - 58}{117} \qquad \text{Moorari Field}$$

$$\phi = \frac{\Delta t - 58}{122} \qquad \text{Fly Lake Field}$$

The plot of sonic porosity derived from the new equations and core porosity show an r^2 value of 0.8. These equations calculate total porosity. In this study, a new equation is suggested for kaolinite-rich sandstones to estimate macroporosity from sonic porosity.

$$\phi_{mac} = \phi_{sonic} - 0.2V_k$$

This study indicated that acoustic transit time is a function of several factors including porosity, mineral composition, cementation and compaction.

Quartz cementation in the Tirrawarra Sandstone has a complex effect on acoustic transit time. The plot of quartz cement percentage versus sonic transit time shows a non-linear trend. For samples with less than 10% quartz cement (*Group I*), acoustic transit time increases with increasing quartz cement , whereas in samples with quartz cement greater than 10% (*Group II*) transit time increases as the quartz cement decreases. The samples of *Group I* are more lithic and quartz cement is less developed, but the role of quartz cement in this group is to prevent compaction and consequently preserve porosity. In *Group II* samples, which have less rock fragments, the development of quartz cement leads to occlusion of pore spaces and acoustic transit time reduction.

Compaction in the Tirrawarra Sandstone results in a reduction of porosity especially in rock fragment-rich sandstones. Plots of compaction index versus acoustic transit time show that, with increasing compaction index, transit time decreases.

These results suggest that rock parameters such as composition, cementation and clay content have a clear and measurable effect on acoustic transit time. The rock parameters which effect transit time, also influence porosity, but for sandstones with a given composition, the most important parameter controlling acoustic transit time is porosity.

10.6.2 Water saturation (S_w)

This study indicated that in kaolinite-bearing sandstone water saturation (S_W) can be well estimated by Archie and Waxman-Smits equations. Plots of water saturation from the Archie equation with water saturation from the Waxman-Smits equation indicated that they are approximately the same (r^2=98%) because of the low cation exchange capacity values in the Tirrawarra Sandstone samples (average of 0.7 meq/100g).

In this study a new equation is introduced for Tirrawarra Sandstone to estimate effective water saturation.

$$S_{w_{fw}} = \frac{V_{fw}}{\phi_e} = \frac{V_{tw} - V_{bw}}{\phi_e} = \frac{\phi_t [\frac{FR_w}{R_t}]^{1/n} - 0.2V_k}{\phi_e}$$

The equation does not rely on shale conductivity (C_{sh}) from the adjacent shale intervals where the conductivities are likely to be different from those in the sandstones. This equation reduces calculated water saturation by about 9% and 13.5% for intervals with sonic transit time more than 73 and less than 73 (μs/ft) respectively, i.e. hydrocarbon reserves in the Tirrawarra Sandstone in the Moorari and Fly Lake Fields may be greater than previously estimated.

References

Ahmed, U., Crary, S., and Coates, G., 1991. Permeability estimation: the various sources and their interrelationship. *Journal of Petroleum Technology*, v. 43, p. 578-587.

Al-Aasm, I.S., Taylor, B.E., and South, B., 1990. Stable isotope analysis of multiple carbonate samples using selective acid extraction. *Chemical Geology*, v. 80, p. 119-125.

Alexander, R., Larcher, A.V., and Kagi, R.I., 1988. The use of plant-derived biomarkers for correlation of oils with source rocks in the Cooper/Eromanga Basin system, Australia. *Australian Petroleum Exploration Association Journal*, v. 28, p. 311-324.

Apak, N.S., 1994. Structural development and control on stratigraphy and sedimentation in the Cooper Basin, Australia. University of Adelaide, (unpublished Ph.D. thesis) 105 p.

Apak, S.N., Stuart, W.J., and Lemon, N.M., 1993. Structural-stratigraphic development of the Gidgealpa-Merrimelia-Innamincka Trend with implications for petroleum trap styles, Cooper Basin, Australia. *Australian Petroleum Exploration Association Journal,* v. 33, p. 94-104.

Archie, G.E., 1942. The electrical resistivity log as an aid in determining some reservoir characteristics. *Transactions of AIME*, v. 146, p. 54-62.

Armstrong, J.D., and Barr, T.M., 1986. The Eromanga Basin. An overview of exploration and potential. In: Contributions to the geology and hydrocarbon potential of the Eromanga Basin. *Geological Society of Australia Special Publication*, v. 12, p. 25-38.

Atkinson, G.D., Bloch, S., and Scheihing, M.H., 1990. Sedimentology and depositional environments of the Oligo-Miocene gas-bearing succession in the Yacheng 13-1 field, South China Sea, People's Republic of China. *AAPG Bulletin*, v. 74, p. 601.

Bahrig, B., 1989. Stable isotope composition of siderite as an indicator of the paleoenvironmental history of oil shale lakes. *Paleogeography, Paleoclimatology, Palaeoecology*, v. 70, p. 139-151.

Baker J.C., Kassan, J., and Hamilton, P.J., 1996. Early diagenetic siderite as an indicator of depositional environment in the Triassic Rewan Group, southern Bowen Basin, eastern Australia. *Sedimentology*, v. 43, p. 77-88.

Bathurst, R.G.C., 1987. Diagenetically enhanced bedding in argillaceous platform limestones: stratified cementation and selective compaction. Sedimentology, v. 34, p. 89-100.

Battersby, D.G., 1976. Cooper Basin oil and gas fields. *Australasian Institute of Mining and Metallurgy*, Monograph 7, p. 321-370.

Beard, D.C., and Weyl, P.K., 1973. Influence of texture on porosity and permeability of unconsolidated sand. AAPG Bulletin, v. 57, p. 349-369.

Beddoes, L.R.Jr., 1973. *Oil and gas fields of Australia, Papua New Guinea and New Zealand*. Tracer Petroleum and Mining Publications, Sydney, 391 p.

Berg, R., 1970. Method of determining permeability from reservoir rock properties. *Gulf Coast Association of Geologic Society Transaction*, v. 20, p. 303-317.

Bever, J.M., Carrol, P.G., Williams, B.P.J., and Wild, E.K., 1987. Petrography and core study, Tirrawarra Sandstone, Moorari and Tirrawarra Fields (2 volumes). Unpubl. report, SAGASCO Ltd. 138 pp.

Bever, J.M., Carroll, P.G., Wild, E., and Williams, B.P.J., 1988. Core facies, petrology, and permeability of Tirrawarra Sandstone, Moorari Field, Cooper Basin, South Australia. *AAPG Bull*etin, v. 72, p. 162.

Bjørkum, P.A., 1996. How important is pressure in causing dissolution of quartz in sandstones? *Journal of Sedimentary Research*, v. 66, p. 147-154.

Bjørkum, P.A., and Gjelsvik, N., 1988. An isochemical model for formation of authigenic kaolinite, K-feldspar and illite in sediments. *Journal of Sedimentary Petrology*, v. 58, p. 506-511.

Bjørlykke, K., 1984. Formation of secondary porosity: how important is it? *AAPG Memoir* 37, p. 217-224.

Bjørlykke, K., 1988. Sandstone diagenesis in relation to preservation, destruction and creation of porosity. in: G.V.,Chilingarian, and K.H., Wolf, (eds.), Diagenesis, 2. *Developments in Sedimentology*, 41. Elsevier Scientific Publications, Amsterdam, p. 555-588.

Bjørlykke, K., Aagaard, P., Dypvik, H., Hastings, A.S., and Harper, D.S., 1986. Diagenesis and reservoir properties of Jurassic sandstones from the Haltenbanken area, offshore mid-Norway, *in:* Spencer, A.M., Holter, E., Campell, C.J., Hanslien, P.H.H., Nysaether, E., Ormaasen, (eds.) Habitat of hydrocarbons on the Norwegian Continental Shelf: London, Graham and Trotman Ltd., p. 275-276.

Bjørlykke, K., and Brendsdal, A., 1986. Diagenesis of the Brent Sandstone in the Statfjord Field. *SEPM Special Publication,* 38, p. 157-167.

Bjørlykke, K., and Egeberg, P.K., 1993. Quartz cementation in sedimentary basins: *AAPG Bulletin*, v. 77, p. 1538-1548.

Bjørlykke, K.P., Aagaard, P., 1992. Clay minerals in North Sea sandstones. *SEPM Special Publication*, 47, p. 65-80.

Bliefnick, D.M., and Kaldi, J.G., 1996. Pore geometry: Control on reservoir properties, Walker Creek Field, Columbia and Lafayette Counties, Arkansas. *AAPG Bulletin*, v. 80, p. 1027-1044.

Bloch, S., 1991. Empirical prediction of porosity and permeability in sandstones. *AAPG Bulletin*, v. 75, p. 1145-1160.

Bloch, S., McGowen, J.H., Duncan, J.R., and Brizzolara, D.W., 1990. Porosity prediction, prior to drilling, in sandstones of the Kekiktuk Formation (Mississippian), North slope of Alaska. *AAPG Bull*etin, v. 74, p. 1371-1385.

Boles, J.R., and Franks, S.G., 1979. Clay diagenesis in Wilcox sandstones of southwest Texas: implication of smectite diagenesis on sandstone cementation. *Journal of Sedimentary Petrology*, v. 49, p. 55-70.

Boothroyd, J.C., and Ashley, G.M., 1975. Processes bar morphology, and sedimentary structures on braided outwash fans, Northeastern gulf of Alaska. *SEPM Special Publication* 23, p. 193-222.

Boothroyd, J.C., and Nummedal, D., 1978. Proglacial braided outwash: a model for humid alluvial fan deposit. In: Miall, A. D. (Ed.), Fluvial Sedimentology, *Canadian Society of Petroleum Geologists*, Memoir 5, p. 641-648.

Bowler, J., 1988. Wireline log evaluation for explorationists. Unpubl. course notes, Bowler Log Consulting Services Pty. Ltd., 73p.

Brooks, J.K., Hesp, W.R. and Rigby, D., 1971. The natural conversion of oil to gas in sediments in the Cooper Basin. *Australian Petroleum Exploration Association Journal*, v. 11, p. 121-5.

Brown, C.S., and Thomas, L.A., 1960. The effect of impurities on the growth of synthetic quartz: *Journal of Physics and Chemistry of Solids*, v. 13, p. 337-343.

Burley, S.D., 1986. The development and destruction of porosity within Upper Jurassic reservoir sandstonesof the Piper and Tartan Fields, Outer Moray Firth, North Sea. *Clay Mineralogy*, v. 21, p. 649-694.

Burley, S.D., and Kantorowicz, J.D., 1986. Thin section and SEM textural criteria for the recognition of cement-dissolution porosity in sandstones. *Sedimentology*, v. 33, p. 587-604.

Campbell, C.V., 1976. Reservoir geometry of a fluvial sheet sandstone. *AAPG Bulletin*, v. 60, p.1009-1020.

Carmen, P., 1937. Fluid flow through granular beds. *Institute of Chemical Engineers Transactions*, v. 15, p. 150-166.

Carothers, W.W., Adami, H.L., and Rosenbauer, R.J., 1988. Experimental oxygen isotope-fractionation between siderite-water and phosphoric acid liberated CO2-siderite: *Geochimica et Cosmochimica Acta*, v. 52, p. 2445-2450.

Carothers, W.W., and Kharaka, Y.K., 1980. Stable carbon isotopes of HCO3 in oil-field waters - implications for the origin of CO2. *Geochimica et Cosmochimica Acta*, v. 44, p. 323-332.

Carpenter, S.J., Erickson, J.M., Lohmann, K.C., and Owen, M.R., 1988. Digenesis of fossiliferous concretions from the Upper Cretaceous Fox Hills Formation, North Dakota. *Journal of Sedimentary Petrology*, v. 58, p. 706-723.

Chilingar, G., 1964. Relationship between porosity, permeability and grain size distribution of sands and sandstones. In: L. van Straaten, (ed.) Deltaic and shallow marine deposits: New York, Elsevier, p. 71-75.

Clavier, C., Coates, G., and Dumanoir, J., 1977. The theorical and experimental bases for the "dual water" model for the interpretation of shaly sands. *Society of Petroleum Engineers Paper* 6859.

Clavier, C., Coates, G., and Dumanoir, J., 1984. Theorical and experimental bases for the dual-water model for interpretation of shaly sands. *Society of Petroleum Engineers Journal*, v. 24, p.153-168.

Cohen, A.J., 1985. Amethyst color in quartz, the result of radiation protection involving iron. *American Mineralogist*, v. 70, p. 1180-1185.

Collinson, J.D., 1986. Alluvial sediments. In: Reading, H.G., (ed.), *Sedimentary environments and facies*, Oxford Blackwell Scientific Publication Ltd., p. 20-62.

Cooper, B.J., 1981. Carboniferous and Permian sediments in South Australia and their correlation. Quart. Geol. Notes No. 79, Geol. Survey of South Australia, p. 2-6.

Coplen, T.B., Kendall, C., and Hopple, J., 1983. Comparison of stable isotope reference samples. *Nature*, v. 302, p. 236-238.

Costello, W.R., and Walker, R.G., 1972. Pleistocene sedimentology, Credit River, southern Ontario; a new component of the braided river model. *Journal of Sedimentary Petrology*, v. 42, p. 389-400.

Craig, H., 1957. Isotope standards for carbon and oxygen and correction factors for mass spectrometric analysis of carbon dioxide. *Geochimica et Cosmochimica Acta,* v. 12, p. 133-149.

Craig, H., 1961. Standards for reporting concentrations of deuterium and oxygen-18 in natural waters. *Science*, v. 133, p. 1833-1834.

Curtis, C.D., 1983. Link between aluminum mobility and destruction of porosity: *AAPG Bulletin*, v. 63, p. 380-384.

Curtis, C.D., and Coleman, M.L., 1986. Controls on the precipitation of early diagenetic calcite, dolomite, and siderite concretions in complex depositional sequences, in: Gautier, D.L., (ed.), Roles of Organic Matter in Sediment Diagenesis: *SEPM Special Publication*, 38, p. 23-33.

Curtis, C.D., Pearson , M.J., and Somogyi, V.A., 1975. Mineralogy, chemistry, and origin of a concretionary siderite sheet (clay-ironstone band) in the Westphalian of Yorkshire. *Mineralogical Magazine*, v. 40, p. 385-393.

Dansgaard, W., 1964. Stable isotopes in precipitation. *Tellus*, v. 16, p. 436-468.

de Waal, J.A., 1989. Influence of clay distribution on shaly sand conductivity. *Society of Petroleum Engineers Formation Evaluation*, v. 4, p. 377-583.

Deer, W.A., Howie, R.A., and Zussman, J., 1992. An introduction to the rock-forming minerals. Longman Group Limited, London, 695p.

Deines, P., 1986. The isotopic composition of reduced organic carbon. In: P., Fritz, and J.Ch., Fontes, (eds.), *Handbook of environmental isotope geochemistry*, Elsevier Scientific Publishing Company, New York, 329-406.

Dennen, W.H., and Blackburn, W.H., 1970. Aluminum in quartz as a geothermometer. *Contributions to Mineralogy and Petrology*, v. 27, p. 332-342.

Desborough, G.A., 1978. A biogenic-chemical stratified lake model for the origin of oil shale of the Green River Formation: an alternative to the playa-lake model. *Geological Society of American Bulletin*, v. 89, p. 961-971.

Devine, S.B., and Gatehouse, C.G., 1977. Sandstone reservoir geometry of non-marine sediments in the Toolachee Gas Field. *Australian Petroleum Exploration Association Journal*, v. 17, p. 50-57.

Dickson, J.A.D., Smalley, P.C., Raheim, A., and Stijfhoorn, D.E., 1990. Intercrystalline carbon and oxygen isotope variations in calcite revealed by laser microsampling. *Geology*, v. 18, p. 809-811.

Doyen, P., 1988. Permeability, conductivity and pore geometry of sandstone. *Journal of Geophysical Research*, v. 93, p. 7729-7740.

Dresser Atlas, 1983. *Log interpretation charts*. Dresser Atlas Publication, 237p.

Dullien, F., 1979. *Porous media, fluid transport and pore structure*. New York, Academic Press, p. 42-65.

Durney, D.W., 1972. Solution-transfer, an important geological deformation mechanism. Nature, v. 235, p. 315-317.

Dutta, P.K., and Suttner, L.J., 1986. Alluvial sandstone composition and paloeclimate, II. Authigenic mineralogy. *Journal of Sedimentary Petrology*, v. 56, p. 346-358.

Dutton, S.P., 1993. Influence of provenance and burial history on diagenesis of Lower Cretaceous Frontier Formation sandstones, Green River Basin, Wyoming: *Journal of Sedimentary Petrology*, v. 63, p. 665-667.

Dutton, S.P., and Diggs, T.N., 1990, History of quartz cementation in the Lower Cretaceous Travis Peak Formation, East Texas: *Journal of Sedimentary Petrology*, v. 60, p. 191-202.

Dutton, S.P., and Diggs, T.N., 1992. Evolution of porosity and permeability in the Lower Cretaceous Travis Peak Formation, East Texas. *AAPG Bulletin*, v. 76, p. 252-269.

Eberhart-Phillips, D., Han, D.H., and Zoback, M.D., 1989. Empirical relationships among seismic velocity, effective pressure, porosity, and clay content in sandstone. *Geophysics* v. 54, p. 82-89.

Edward, A.J., 1989. Porosity and packing of Holocene river, dune and beach sands. Unpublished Master's thesis, 223p.

Ehrenberg, S.N., 1990. Relationship between diagenesis and reservoir quality in sandstones of the Garn Formation, Haltenbanken, Mid-Norwegian continental shelf. *AAPG Bulletin*, v. 74, p. 1538-1558.

Ehrenberg, S.N., and Boassen, T., 1993. Factor controlling permeability variation in sandstones of the Garn Formation in Trestakk Field, Norwegian continental shelf. *Journal of Sedimentary Petrology*, v. 63, p. 929-944.

Ehrlich, R., Crabtree, S.J., Horkowitz, K.O., and Horkowitz, J.P., 1991. Petrography and reservoir physics I: Objective classification on reservoir porosity. *AAPG Bulletin*, v. 75, p. 1574-1562.

Ehrlich, R., Kennedy, S.K., Crabtree, S.J., and Cannon, R.L., 1984. Petrographic image analysis, I. Anlysis of reservoir pore complexes. *Journal of Sedimentary Petrology*, v. 54, p. 1365-1378.

Embleton, B.J.J,. and McElhinny, M.W., 1982. Marine magnetic anomalies, palaeomagnetism and the drift history of Gondwanaland. *Earth Planet. Sci. Letters*, v. 58, p.1 41-50.

Engelder, T., Geiser, P.A., and Alvarez, W., 1981. Role of pressure solution and dissolution in geology. Geology, v. 9, p. 44-45.

Exon, N.F., & Senior, B.R., 1976. The Cretaceous of the Eromanga and Surat Basins. *BMR Jour. Aust. Geol. Geophys.*, v. 1, p. 33-50.

Fabbri, A.B. 1980. GIAPP: Geological image-analysis program package for estimating geometrical probabilities. *Computer and Geoscience*, v. 6, p. 153-161.

Fairburn, W.A., 1989. The geometry of Toolachee unit 'C' fluvial sand trends, Moomba Field, Permian Cooper Basin, South Australia. *Australian Petroleum Exploration Association Journal,* v. 29, p. 239-250.

Fanning, M., 1987. Ella-1. K-Ar dating of drill core at 4190 feet 10 inches. Unpubl. Amdel report for Delhi Petroleum Pty. Ltd., 4p.

Farrow, B.B., 1989. Permeability estimation from well logs using probabilities: The Cooper and Eromanga Basins, Australia. In: O'Neil, B.J. (Ed.), Proceeding of the Cooper and Eromanga Basins conferences, PESA, SPE AND SAEG, Adelaide, 1989, p.165-171.

Faure, G., 1986. *Principles of isotope geology*. 2nd edition, John Wiley & Sons, 589p.

Folk, R.L., 1974. *Petrology of Sedimentary rocks*: Austin, Texas, Hemphill publishing co., 182 p.

Fothergill, C.A., 1955. The cementation of oil reservoir sands and its origin: Proc. 4th World Petroleum Conference, Rome, 1955, p. 301-314.

Fritz, P., Binda, P.L., Folinsbee, F.E., and Krouse, H.R., 1971. Isotopic composition of diagenetic siderites from Cretaceous sediments in Western Canada. *Journal of Sedimentary Petrology*, v. 41, p. 282-288.

Füchtbauer, H., 1967. Influence of different types of diagenesis on sandstone porosity. Proc. *7th World Petroleum Congress*, v. 2, p. 353-369.

Füchtbauer, H., 1974. *Sediments and Sedimentary rocks*. New York, N.Y., Wiley, 464p.

Garrels, R.M., and Christ, C.L., 1965. *Solutions, Minerals and Equilibria*. Harper & Row, New York, 450pp.

Gatehouse, C.G., 1972. Formations of the Gidgealpa Group in the Cooper Basin. *Oil & Gas Journal,* v. 18, p. 10-15.

Gatehouse, C.G., 1986. The geology of the Warburton Basin in South Australia: *Australian Journal of Earth Science*, v. 33, p. 161-180.

Gautier, D.L., 1982. Siderite concretions: indicators of early diagenesis in the Gammon Shale (Cretaceous). *Journal of Sedimentary Petrology*, v. 52, p. 859-871.

Gilby, A.R. & Mortimore, I.R., 1989. The prospects for Eromanga oil accumulations in the northern Cooper Basin region, Australia. In: B.J. O'Neil (ed.), The Cooper and Eromanga Basins, Australia. Proceedings of the Cooper and Eromanga Basins Conference, Adelaide, 26-27 June 1989, p. 391-403.

Gilchrist, W.A., Quirein, Jr.J., Boutemy, Y., and Tabanou, J., 1982. Application of gamma-ray spectrometry to fromation evaluation. *SPWLA,* July 1982.

Glasmann, J.R., Clark, R.A., Larter, S., Briedis, N.A., and Lundegard, P., 1989. Diagenesis and hydrocarbon accumulation, Brent Sandstone (Jurassic), Bergen High area, North Sea. *AAPG Bulletin,* v. 73, p. 1341-1360.

Gleadow, A.J.W., Duddy, I.R., Green, P.F., and Lovering, J.F., 1988. Assessment of hydrocarbon resource potential in Australian sedimentary basins: development of fission track techniques: End of Grant Technical Report, National Energy Research and Development and Demonstration Cooperation Project 720, 116 p.

Goldstein, R.H., and Rynolds, T.J., 1994. Systematics of fluid inclusions in diagenetic minerals. *SEPM short course* 31, 199p.

Gostin, V., 1973. Lithological study of the Tirrawarra Sandstone. Unpubl. report for Delhi Int. Oil Corp. 21 p.

Gould, K.W. and Smith, J.W., 1979. The genesis and isotopic composition of carbonates associated with some Permian Australia coals. *Chemical Geology*, v. 24, p. 137-150.

Gray, R.J., and Roberts, D.C., 1984. A seismic model of faults in the Cooper Basin. *Australian Petroleum Exploration Association Journal*, v. 24, p. 421-428.

Grim, R.E., 1968. *Clay mineralogy*. New York McGraw-Hill, 596p.

Grund, R., 1966. The glacigene sediments of the Coopers Creek Basin. Unpubl. B.Sc. (Hons.) thesis, University of Adelaide, Australia, 197p.

Hamilton, J.R., and Wilson, J.S., 1981. Study of geopressured reservoir by drilling and producing a well in a limited geopressured water sand. Proc. 4th U.S. Gulf Coast Geopressured-Geothermal Energy Conference, Research and Development, 3: Centre for Energy Studies, University of Texas, Austin, p. 1137-1159.

Hamlin, H.S., Dutton, S.P., Seggie, R.J., Tyler, N., 1996. Depositional controls on reservoir properties in a braid-delta sandstone, Tirrawarra oil field, South Australia. AAPG Bulletin, v. 80, p. 139-156.

Han, D., Nur, A., and Morgan, D., 1986. Effects of porosity and clay content on wave velocities in sandstones. *Geophysics*, v. 51, p. 2093-2107.

Harland, W.B., Cox, A.V., Llewellyn, D.G., Pickton, C.A.G., Smith, A.G., and Walters, R., 1989. *A Geologic Time Scale*. Cambridge University Press.

Harms, J.C., Southard, J.B., Spearing, D.R., and Walker, R.G., 1975. Depositional environments as interpreted from primary sedimentary structures and stratification sequences. SEPM short course 2, Dallas Texas, 161p.

Haszeldine, R.S., and Osborne, M., 1993. Fluid inclusion temperatures in diagenetic quartz reset by burial: implications for oil field cementation. *in* Horbury, A.D., and Robinson, A.G., (eds.), Diagenesis and Basin Development: *American Association of Petroleum Geologists Studies in Geology*, v. 36, p. 35-46.

Hawkins, P.J., 1978. Relationship between diagenesis, porosity reduction, and oil emplacement in late Carboniferous sandstone reservoirs, Bothamsall Oilfield, E. Midlands. *Geological Society of London Journal* , v. 135, p. 7-24.

Heald, M.T., 1955. Stylolites in sandstones. *Journal of Geology*, v. 63, p. 101-114.

Heald, M.T., 1959. Significance of stylolites in permeable sandstone. *Journal of Sedimentary Petrology*, v. 29, p. 251-253.

Heath, R., 1989, Exploration in the Cooper Basin: *Australian Petroleum Exploration Association Journal*, v. 29, p. 366-378.

Henry, D.J., Toney, J.B., Suchecki, R.K., and Bloch, S., 1986. Development of quartz overgrowths and pressure solution in quartz sandstones: evidence from cathodoluminescence backscattered electron imaging and trace element analysis on electron microprobe (Abstract), *Geol. Soc. Am. Abstr. Prog.*, v. 18, p. 635.

Hibburt, J., 1993, *Petroleum exploration and development in Souht Australia.* South Australia Department of Mines and Energy, 161p.

Hill, A.J., and Gravestock, D.I., 1995. Cooper Basin. In: Drexel, J.F., and Preiss, W.V., (Eds.), The Geology of South Australia, Volume 2, The Phanerozoic. *South Australian Geological Survey, Bulletin,* 54, p. 78-87.

Hollingsworth, R.J.S., Barnes, R.G., Middleton, M.P., and Covil, M.W., 1976. Tooroopie seismic survey by Seismograph Service Ltd. S. Aust. Dept. Mines and Energy Confidential Env. 2523 (unpubl.), 62p.

Hollister, L.S., & Crawford, M.L., 1981. *Fluid inclusions: application to petrology.* Mineralogical association of Canada, Short Course Handbook 6.

Hossin, A., 1960. Calcul des saturation en eau par la methode du ciment argileux (formule d' Archie generalisee). *Bull. Assoc. Francaise Tech. Pet.,* 140, 31 March.

Houseknecht, D.W., 1984. Influence of grain size and temperature on intergranular pressure solution, quartz cementation, and porosity in a quartzose sandstone. Journal of Sedimentary Petrology, v. 54, p. 348-361.

Houseknecht, D.W., 1987. Assessing the relative importance of compaction processes and cementation to reduction of porosity in sandstones. AAPG. Bulletin, v. 71, p. 633-642.

Houseknecht, D.W., 1988, Intergranular pressure solution in four quartzose sandstones: *Journal of Sedimentary Petrology*, v. 58, p. 228-246.

Houseknecht, D.W., and Hathon, L.A., 1987. Petrographic constraints on models of intergranular pressure solution in quartzose sandstones. *Applied Geochemistry*, v. 2, p. 507-521.

Houseknecht, D.W., and Ross, L.M., 1992. Clay minerals in Atokan deep-water sandstone facies, Arkoma Basin: Origin and influence on diagenesis and reservoir quality. *SEPM, Special Pub*lication, 47, p. 227-240.

Howard, J.J., 1992. Influence of authigenic-clay minerals on permeability. *SEPM Special pub*lication, 47, p. 257-264.

Hower, J., Eslinger, E.V., Hower, M.E., and Perry, E.A., 1976. Mechanism of burial metamorphism of argillaceous sediments. 1 - Mineralogical and chemical evidence. *AAPG Bulletin*, v. 87, p. 725-737.

Huang, W.H., and Keller, W.D., 1970. Dissolution of rock-forming silicate minerals in organic acids: simulated first stage weathering of fresh mineral surfaces. *American Mineralogist*, v. 55, p. 2076-2094.

Hudson, J.D., 1977. Stable isotopes and limestone lithification. *Journal of Geological Society of London*, v. 133, p. 637-660.

Hunt, J.W., Heath, R.S., and Mckenzie, P.F., 1989. Thermal maturity and other geological controls on the distribution and composition of Cooper Basin hydrocarbons. *Australian Petroleum Exploration Association Journal*, v. 29, p. 509-523.

Hurst, A.R., 1980. Occurrence of corroded authigenic kaolinite in a diagenetically modified sandstone. *Clays & Clay Minerals*, v. 28, p. 393-396.

Hurst, A., 1987. Mineralogical analysis and the evaluation of the petrophysical parameter V_{shale} for reservoir description. *Marine and Petroleum Geology*, v. 4, p. 82-91.

Hurst, A., and Archer, J.S., 1986a. Sandstone reservoir description; an overview of the role of geology and mineralogy. *Clay Minerals*, v. 21, p. 791-809.

Hurst, A., and Archer, J.S., 1986b. Some application of clay mineralogy to reservoir description. *Clay Minerals*, v. 21, p. 811-826.

Hurst, A., and Irwin, H., 1982. Geological modelling of clay diagenesis in sandstones. *Clays & Clay Minerals*, v. 17, p. 5-22.

Hurst, A., and Milodowski, A.E., 1996. Thorium distribution in some North Sea sandstones: implication for petrophysical evaluation. *Petroleum Geoscience*, v. 2, p. 59-68.

Hurst, A., and Rosvoll, K.J., 1991. Permeability variations in sandstones and their relationship to sedimentary structures. In: Lake L.W., Carroll, H.B. Jr. and Wesson, T.C. (eds.), *Reservoir characterization; II*. p. 166-196.

Hurst, H., and Nadeau, P.H., 1995. Clay microporosity in reservoir sandstones: An application of quantitative electron microscopy in petrophysical evaluation. *AAPG Bulletin*, v. 79, p. 563-573.

Irwin, H., 1980. Early diagenetic carbonate precipitation and pore fluid migration in the Kimmeridge Clay of Dorset, England. *Sedimentology*, v. 27, p. 577-591.

Irwin, H., Curtis, C.D., and Coleman, M.L., 1977. Isotopic evidence for source of diagenetic carbonates formed during burial of organic-rich sediments. *Nature*, v. 269, p. 209-213.

Iverson, W., 1990. Permeability estimation from sonic versus porosity gradients. *Society of Exploration Geophysicists International Meeting*, v.1, paper BG5.2, p. 106-109.

Jain, H., and Nowick, A.S., 1982. Electrical conductivity of synthetic and natural quartz crystals. *Journal of Applied Physics*, v.53, p. 447-484.

Jenkins, C.C., 1989. Geochemical correlation of source rocks and crude oils from the Cooper and Eromanga Basins. In: O'Neil (ed.), The Cooper and Eromanga Basins, Australia. Proceedings of the Cooper and Eromanga Basins Conference, Adelaide, 26-27 June 1989, 525-39.

Johnson D., Koplik, J., and Dashen, R., 1987. Theory of dynamic permeability and tortuosity in fluid-saturated porous media. *Journal of Fluid Mechanics*, v. 176, p. 379-402.

Johnson, W.L., and Linke, W.A., 1978. Some practical applications to improve formation evaluation of sandstones in the Mckenzie Delta. *SPWLA 19th Annual Logging Symposium*, Paper C, 32 p.

Jourdan, A., Thomas, M., Brevart, O., Robson, P., Sommer, F., and Sullivan, M., 1987. Diagenesis as the control of the Brent Sandstone reservoir properties in the Greater Alwyn area (East Shetland Basin), *in* Brooks, J., and Glennie, K., (eds.), Petroleum Geology of North West Europe: London, Graham and Trotmann Ltd., p. 951-961.

Juhasz, I., 1979. The central role of Qv and formation-water salinity in the evaluation of shaly formations. *Trasactions of the SPWLA Twentieth Annual Logging Symposium*, AA1-AA26.

Juhasz, I., 1981. Normalised Qv - The key to shaly sand evaluation using the Waxman-Smits equation in the absence of core data. *SPWLA Twenty-Second Annual Logging Symposium*, 1-36.

Juhola, A.J., and Wiig E.O., 1949. Pore structure in activated charcoal. II. Determination of macro pore-size distribution. *Journal of American Chemical Society*, v. 71, p. 2078-2080.

Kantorowicz, J.D., 1985. The petrology and diagenesis of Middle Jurassic clastic sediments, Ravenscar Group, Yorkshire. *Sedimentology*, v. 32, p. 833-853.

Kantsler, A.J., Prudence, T.J.C., Cook, A.C., and Zwigulis, M., 1983. Hydrocarbon habitat of the Cooper/Eromanga Basin, Australia: *Australian Petroleum Exploration Association Journal*, v. 23 , p. 373-389.

Kapel, A.J., 1966. The Cooper's Creek Basin. *The Australian Petroleum Exploration Association Journal*, v. 6, p.71-75.

Kapel, A.J., 1972. The geology of the Patchawarra area Cooper Basin. *Australian Petroleum Exploration Association Journal*, v. 12, p. 53-57.

Katz, A., and Thompson, A., 1986. Quantitative prediction of permeability in porous rocks. *Physical Review B*, v. 34, p. 8179-8181.

Keelan, D.K., 1982. Core analysis for aid in reservoir description. *Proceeding International meeting on petroleum engineering*, v. 1, p. 221-230.

Keelan, D.K., and Marschall, D.M., 1989. *Fundamentals of core analysis*. Core Laboratories, Houston.

Keeling, C.D., 1958. The concentration and isotopic abundances of atmospheric carbon dioxide in rural areas. *Geochimica et Cosmochimica Acta*, v. 13, p. 322-334.

Keene, J.B., 1975. Cherts and porcelanites from the North Pacific, DSDP Leg 32, *in* Larson, R.L., et al., (eds.), Deep Sea Drilling Project, v. 32, p. 429-507.

Keltz, K., and Hsü, K.J., 1978. The mineralogy and related chemistry of lake sediments. In: A., Lerman, (ed.), Lakes, chemistry, geology, physics. Springer, Berlin, p. 179-236.

Kharaka, Y.K., Carothers, W.W., and Rosenbauer, R.J., 1983. Thermal decarboxylation of acetic acid: implications for origin of natural gas. *Geochimica et Cosmochimica Acta,* v. 47, p. 397-402.

King, E.K., 1992. Formation clays: Are they really a problem in production? *SEPM Special publication*, 47, p. 265-271.

Klemme, H.D., 1980. Petroleum basins - classifications and characteristics. *Journal of Petroleum Geology*, v. 3, p. 187-207.

Kolodzie, S.Jr., 1980. Analysis of pore throat size and use of the Waxman-smits equation to determine OOIP in Spindle Field, Colorado. *Society of Petroleum Engineers, 55th Annual Fall Technical Conference*, Paper 9382, 10p.

Kowallis, B.J., Jones, L.E.A., and Wang, H.F., 1984. Velocity-porosity-clay content systematics of poorly consolidated sandstones. *Journal of Geophysical Research*, v. 89, p. 10,355-10,364.

Kreig, G.W., Alexander, E.M. and Rogers, P.A., 1995. Eromanga Basin. In: Drexel, J.F. & Preiss, W.V., (Eds.), 1995. The Geology of South Australia, Volume 2, The Phanerozoic. *South Australian Geological Survey Bulletin*, 54, p. 101-105.

Kuang, K.S., 1985. History and style of Cooper-Eromanga basin structures. *Australian Society of Exploration Geophysics Bulletin*, v. 16, p. 245-48.

Laws, R.A., 1989, Preface. In: B.J. O'Neil (ed.), The Cooper and Eromanga Basins, Australia. Proceedings of the Cooper and Eromanga Basins Conference, Adelaide, 26-27 June 1989, v-vi.

Leder, F., and Park, W.C., 1986. Porosity reduction in sandstones by quartz overgrowth. *AAPG Bulletin*, v. 70, p. 1713-1728.

Leeder, M.R., 1973. Fluviatile fining-upwards cycles and the magnitude of paleochannels. *Geological Magazine*, v. 110, p. 265.

Lehmann, G., and Bambauer, H.U., 1973. Quartz crystals and their colors. *Angewandte Chemie*, International Edition, v. 12, p. 283-291.

Levey, R.A., 1978. Bed-form distribution and internal stratification of coarse-grained point bars, Upper Congaree River, S.C. In: Miall A.D., (ed.), Fluvial Sedimentology, *Canadian Society of Petroleum Geologists*, Memoir 5, p. 105-127.

Macaulay, C.I., Haszeldine, R.S., and Fallick, A.E., 1993. Distribution, chemistry, isotopic composition and origin of diagenetic carbonates: Magnus Sandstone, North Sea. *Journal of Sedimentary Petrology*, v. 63, p. 33-43

Marion D., Nur, A., and Albert F., 1989. Modelling the relationship between sonic velocity, porosity, permeability, and shaliness in sand, shale and shaly sand. *SPWLA Thirtieth Annual Logging Symposium Proceeding*, paper G, p. 1-22.

Marion, D.P., and Pellerin, F.M., 1994. Acoustic measurments on cores as a tool for calibration and quantitative interpretation of sonic logs. *Society of Petroleum Engineers Formation Evaluation*, p. 100-104.

Martin, C.A., 1967. The Gidgealpa and Merrimelia Formations in the Cooper's Creek Basin. *Australian Oil & Gas Journal*, v. 14, p. 29-35.

Martin, K.R., 1981. Petrology and diagenesis of the Tirrawarra Sandstone in Tirrawarra Field. Unpubl. report, Santos Ltd. 17p.

Martin, K.R., 1984. Petrology and diagenesis and reservoir quality of the Tirrawarra Sandstone in Tirrawarra , Fly Lake and Moorari Fields. Unpubl., report, Santos Ltd. 31p.

Martin, K.R., and Hamilton, N.J., 1981. Diagenesis and reservoir quality, Toolachee Formation, Cooper Basin. *Australian Petroleum Exploration Association Journal*, v. 21, p. 143-154.

Matsumoto, R., and Iijima, A., 1981. Origin and digenetic evolution of Ca-Mg-Fe carbonates in some coalfields of Japan. *Sedimentology*, v. 18, p. 239-259.

Matter, A., and Ramseyer, K., 1985. Cathodoluminescence microscopy as a tool for provenance studies of sandstones, *in:* Zuffa, G.G., (ed.), Provenance of Arenites: Reidel, Dordrecht, p. 191-211.

May, H.M., Helmke, P.A., & Jackson, M.L., 1979. Gibbsite solubility and thermodynamic properties of hydroxy-aluminium ions in aqeous solution at 25°C. *Geochimica et Cosmochimica Acta*, v. 43, p. 861-868.

McBride, E.F., 1989. Quartz cement in sandstones: a review. Earth-Science Reviews, v. 26, p. 69-112.

McCrea, J.M., 1950. On the isotopic chemistry of carbonates and a palaeotemperature scale. *Journal of Chemical Physics.*, v. 18, p. 849-857.

McCreesh, C.A., Ehrlich, R., and Crabtree, S.J., 1991. Petrography and reservoir physics II: Relating thin section porosity to capillary pressure, the association between pore types and throat size. *AAPG Bulletin*, v. 75, p. 1563-1578.

McElhinny, M.W., 1969. The palaeomagnetism of the Permian of southeast Australia and its significance regarding the problem of intercontinental correlation. *Geological Society of Australia Special Publication*, v. 2, p. 61-67.

McGowen, J H., and Bloch, S., 1985. Depositional facies, diagenesis and reservoir quality of Ivishak sandstone, Prudhoe Bay field (abs.). *AAPG Bulletin*, v. 69, p. 276.

McGowen, J.H., and Garner, L.E., 1970. Physiography features and stratification types of coarse-grained point bars: Modern and ancient examples. *Sedimentology*, v. 14, p. 77-111.

McKirdy, D.M., 1989. Geochemistry of oils and condensates associated with CO2-rich natural gas in the Otway and Cooper Basins. CSIRO Marine Laboratories, 1989 *Australian Organic Geochemistry Conference*, April 13-14, Hobart, Tasmania (abstract).

McLimans, R.K., 1987. The application of fluid inclusions to migration of oil and diagenesis in petroleum reservoirs. *Applied Geochemistry*, v. 2, p. 585-603.

McPherson, J.G., Shanmugam, G., and Moiola, R.J., 1987. Fan-deltas and braid deltas: Varieties of coarse-grained deltas. *Geological Society of American Bulletin*, v. 99, p. 331-340.

Merino, E., Harvey, C., and Murray, H.H., 1989. Aqueous-chemical control of the tetrahedral-aluminum content of quartz, halloysite, and other low-temperature silicates. *Clays and Clay Minerals*, v. 32, p. 135-142.

Miall, A. D., 1977. A review of the braided river depositional environment. *Earth Science Review*, v. 13, p. 1-26.

Miall, A.D., 1978. Lithofacies type and vertical profile models in braided river deposits: A summery: in A.D., Miall, (ed.), Fluvial Sedimentology, *Canadian Society of Petroleum Geologists Memoir* 5, p. 597-604.

Miall, A.D., 1985. Architectural -element analysis: a new method of facies analysis applied to fluvial deposits. *Earth Science Reviews*, v. 22, p. 261-308.

Miall, A.D., 1988. Reservoir heterogenities in fluvial sandstones: lessons from outcrops studies. *AAPG Bulletin*, v. 72, p. 682-697.

Mian, M.A., and Hilchie, D.W., 1982. Comparison of results from three cation exchange capacity (CEC) analysis techniques. *The Log Analyst*, v. 23, p. 10-16.

Middleton, H.A., and Nelson, C.S., 1996. Origin and timing of siderite and calcite concretions in late Palaeogene non- to marginal-marine facies of the Te Kuiti Group, New Zealand. *Sedimentary Geology*. v. 103, p. 93-115.

Milodowski, A.E., and Hurst, A., 1989. The authigenesis of phosphate minerals in some Norwegian hydrocarbon reservoirs; evidence for the mobility and redistribution of rare earth elements (REE) and *Th* during sandstone diagenesis. In: Miles Douglas (ed.), Water-rock interaction, *Proceedings - International Symposium on Water-Rock Interaction*, 6; p. 491-494.

Moore, S.E., Ferrell, R.E., and Aharon, P., 1992. Diagenetic siderite and other ferroan carbonates in a modern subsiding marsh sequence: *Journal of Sedimentary Petrology*, v. 62, p. 357-366.

Morad, S., and Aldahan A.A., 1987a. A SEM study of diagenetic kaolinization and illitization of detrital feldspars in sandstones. *Clay Minerals*, v. 22, p. 237-243.

Morad, S., and Aldahan A.A., 1987b. Diagenetic replacement of feldspars by quartz in sandstones. Journal of Sedimentary Petrology, v. 57, p. 488-493.

Morad, S., Ben Ismail, H.N., De Ros, L.F., Al-Aasm, I.S., and Serrhini, N.E., 1994. Diagenesis and formation water chemistry of Triassic reservoir sandstones from southern Tunisia. *Sedimentology*, v. 41, p. 1253-1272.

Morad, S., Bhattacharyya, A., Al-Aasm, I.S., and Ramseyer, K., 1991. Diagenesis of quartz in the upper Proterozoic Kaimur Sandstones, Son Valley, central India. *Sedimentary Geology*, v. 73, p. 209-225.

Morad, S., Ros, L.F., Al-Aasm, I.S., 1996. Origin of low $\delta^{18}O$, pre-compactional ferron carbonates in the marine Stø Formation (Middle Jurassic), offshore NW Norway. *Marine and Petroleum Geology*, v. 13, p. 263-276.

Moraes, M.A., and De Ros, L.F., 1990. Infiltrated clays in fluvial Jurassic sandstones of Reconcavo Basin, Northeastern Brazil. *Journal of Sedimentary Petrology*, v. 60, p. 809-819.

Morton, J.G.G., 1990. Cooper Basin core and log analysis for gas reserves assessment. National Energy Research and Development and Demonstration Cooperation Project, 237p.

Mozley, P.S., 1989. Relation between depositional environment and the elemental composition of early diagenetic siderite. *Geology*, v. 17, p. 704-706.

Mozley, P.S., and Carothers, W.W., 1992. Elemental and isotopic composition of siderite in the Kuparuk Formation, Alaska: effect of microbial activity and water/sediment interaction on early pore-water chemistry. *Journal of Sedimentary Petrology*, v. 62, p. 681-692.

Nadeau, P.H., and Hurst, A., 1991. Application of back-scattered electron microscopy to the quantification of clay mineral microporosity in sandstones. *Journal of Sedimentary Petrology*, v. 61, p. 921-925.

Nagtegaal, P.J.C., 1978. Sandstone framework instability as a function of burial diagenesis. *Journal of London Geological Society,* v. 135, p. 101-105.

Neashem, J.W., 1977. Application of scanning electron microscopy to the charactrization of hydrocarbon-bearing rocks. Scanninig Electron Microscopy, v. 1, p. 523-552.

Nordstorm, D.K.. and Munoz, J.L., 1986. *Geochemical thermodynamics*. Blackwel, Oxford, 477p.

Northcott, I., 1982. A new empirical technique for the determination of petrophysical parameters in the Cooper Basin, South Australia. South Australian Department of Mines and Energy (Unpublished report).

O'Driscoll, E.S.T., 1983. Deep tectonic foundations of the Eromanga Basin. *Australian Petroleum Exploration Association Journal,* v. 23, p. 5-17.

Oelkers, E.H., Bjørkum, P.A., and Murphy, W.M., 1996. A petrographic and computational investigation of quartz cementation and porosity reduction in North Sea sandstones. *American Journal of Science*, v. 296, p. 420-452.

Osborne, M., and Haszeldine, R.S., 1993. Evidence for resetting of fluid inclusion temperatures from quartz cements in oilfields. *Marine and Petroleum Geology*, v. 10, p. 271-278.

Overton, M., and Hamilton N., 1986. A petrophysical review of Unit Fields, Cooper Basin, South Australia. Unpublished SANTOS Report: SDRN 86/29, 63p.

Panda, M.N., and Lake, L.W., 1994. A physical model of cementation and its effect on single-phase permeability. *AAPG Bulletin*, v. 79, p. 431-443.

Papalia, N., 1969. The Nappamerri Formation. *Australian Petroleum Exploration Association Journal*, v. 9, p. 108-110.

Pavlishin, V.I., Mazykin, V.V., Matyash, I.V., and Voznyak, D.K., 1978. Variations in the proportion of substitutional aluminum during growth of a quartz crystal. *Geochem. Int.,* v. 15, p. 158-165.

Pearson, M.J., 1974a. Siderite concretions from the Westphalian of Yorkshire: a chemical investigation of the carbonate phase. *Mineralogical Magazine,* v. 39, p. 696-699.

Pearson, M.J., 1974b. Magnesian siderite in carbonate concretions of Yorkshire. *Mineralogical Magazine,* v. 39, p. 700-704.

Pearson, M.J., 1985. Some chemical aspects of digenetic concretions from the Westphalian of Yorkshire, England. *Chemical Geology*, v. 31, p. 225-244.

Perny, B., Eberhardt, P., Ramseyer, K., Mullis, J., and Pankrath, R., 1992. Microdistribution of Al, Li, and Na in a quartz: Possible causes and correlation with short-lived cathodoluminescence. *American Mineralogist*, v. 77, p. 534-544.

Pettijohn, F.J., Potter, P.E., and Siever, R., 1987. Sand and sandstone. NewYork, Springer- Verlag, 618p.

Pianalto, E.I., 1985. The Tirrawarra oil and gas field, Cooper Basin, South Australia. Postdepositional evolution and reservoir quality. Unpubl. B.Sc. (Hons.) thesis, Department of Earth Sciences, Monash University, Australia. 93 p.

Pickett, G.R., 1963. Acoustic character logs and their application in formation evaluation. *Journal of Petroleum Technology*, v. 15, p. 659-667.

Pittman, E.D., 1979. Porosity, diagenesis and productive capability of sandstone reservoirs, *in:* Scholle, P.A., and Schluger, P.R., (eds.), Aspects of diagenesis: *SEPM Special Publication* 26, p. 159-173.

Pittman, E.D., 1988. Problems related to clay minerals in reservoir sanstones. *AAPG studies in Geology*, 28, p. 237-244.

Pittman, E.D., 1992. Relation of porosity and permeability to various parameters derived from mercury injection-capillary pressure curves for sandstones. *AAPG Bulletin*, v. 76, p. 191-198.

Pittman, E.D., and Thomas, J.B., 1978. Some applications of scanning electron microscopy to the study of reservoir rock. Paper Society of Petroleum Engineers 7550.

Pittman, E.D., Larese, R.E., and Heald, M.T., 1992. Clay coats: Occurence and relevance to reservation of porosity in sandstones. *SEPM Special Publication*, 47, p. 241-255.

Pittman, ED., Larese, R.E., 1987. Experimental compaction of lithic sands. *SEPM Annual Midyear Meeting*, v. 4, p. 66.

Porter, C.R., 1976. An empirical approach to the determination of porosity, shale percentage, and permeability of Permian sandstones in the Cooper Basin, South Australia. *Australian Petroleum Exploration Association Journal*, v. 16 , p. 111-115.

Porter, C.R., and Crocker, H., 1972. Petrophysics of the Cooper Basin, South Australia. *Australian Petroleum Exploration Association Journal*, v. 12, p. 23-27.

Porter, C.R., Carothers, J.E., 1970. Formation factor-porosity relation derived from well log data. *SPWLA Logging Symposium Transactions*, p. A1-A18.

Porter, E.W., and James, W.C., 1986. Influence of pressure, salinity, temperature and grain size on silica diagenesis in quartzose sandstones. Chemical Geology, v. 52, p. 259-369.

Poupon, A., and Leveaux, J., 1971. Evaluation of water saturation in shaly formations. *Transactions of SPWLA 12th Annual Symposium*, O1-2.

Powell, C.McA., and Veevers, J.J., 1987. Namurian uplift in Australia and South America triggered the main Gondwana glaciation. *Nature*, v. 326, p. 177-179.

Powers, M.C., 1953. A new roundness scale for sedimentary particles. *Journal of Sedimentary Petrology,* v. 23, p. 117-119.

Powis, G.D., 1989. Revision of Triassic stratigraphy at the Cooper Basin to Eromanga Basin transition. *Australian Petroleum Exploration Association Journal*, v. 29, p. 265-277.

Prezbindowski, D.R., and Tapp, J.B., 1991. Dynamics of fluid inclusion alteration in sedimentary rocks: a reveiw and discussion. *Organic Geochemistry*, v. 17, p. 131-142.

Prezbindowski, DR., and Larese, R.E., 1987. Experimental stretching of fluid inclusions in calcite - Implications for diagenetic studies. *Geology*, v. 15, p. 333-336.

Pryor, W.A., 1973. Permeability-porosity patterns and variations in some Holocene sand bodies. *AAPG Bulletin*, v. 57, p. 162-189.

Purcell, W.R., 1949. Capillary pressure - their measurment using mercury and the claculation of permeability therefrom. *AIME Petroleum Transactions*, Februry 1949 p. 39-48.

Pyecroft, M., 1973. The Della Field, Cooper Basin, South Australia. *Australian Petroleum Exploration Association Journal*, v. 13, p. 58-67.

Raiga-Clemenceau, J., Martin, J.P., and Nicoletis, S., 1988. The concept of acoustic formation factor for more accurate porosity determination from sonic transit time data. *The Log Analyst*, January 1988, p. 54-59.

Railsback, L.B., 1993. Lithologic controls on morphology of pressure-dissolution surfaces (stylolites and dissolution seams) in Paleozoic carbonate rocks from the mideastern United States. *Journal of Sedimentary Petrology*, v. 63, p. 513-522.

Ramseyer, K., and Mullis, J., 1990. Factors influencing short-lived blue cathodoluminescence of α-quartz. *American Mineralogist*, v. 75, p. 791-800.

Raymer, L.L., Hunt, E.R., and Gardner J.S., 1980. An improved sonic transit time-to-porosity transform. *SPWLA 21 annual logging symposium*, July 1980, p. 1-10.

Reynolds, T.J., 1978. Fluid inclusion adapted U.S.G.S. gas flow heating/freezing instruction manual: Fluid Incorporated, Denver.

Rezaee, M.R., 1994. Influence of diagenetic alteration on the Tirrawarra Sandstone reservoir quality in the Moorari and Fly Lake Fields. Unpublished Report EDRN: 022/95, Santos Ltd.,25p.

Rezaee, M.R., and Griffiths, C.M., 1996a. Pore Geometry Controls on Porosity and Permeability in the Tirrawarra Sandstone Reservoir, Cooper Basin, South Australia. *AAPG Annual Convention, San Diego, May 19-22, 1996.*

Rezaee, M.R., and Griffiths, C.M., 1996b. Porosity from Sonic Log in Kaolin-bearing Sandstones: A case study in the Tirrawarra Sandstone reservoir, Cooper Basin, Australia. *17th European Formation Evaluation Symposium,* The Netherlands, 3 - 7 June 1996, paper E-17.

Rezaee, M.R., and Griffiths, C.M., 1996c. Water saturation (S_W) of Kaolin-bearing sandstones: A case study in the Tirrawarra Sandstone reservoir, Cooper Basin, Australia. *17th European Formation Evaluation Symposium,* The Netherlands, 3 - 7 June 1996, paper E-12.

Rezaee, M.R., and Lemon, N., 1996a. Petrophysical Evaluation of Kaolinite-bearing Sandstones: I: Water saturation (S_W), an example of the Tirrawarra Sandstone reservoir, Cooper Basin, Australia. *Society of Petroleum Engineers* paper 37023, p. 539-549.

Rezaee, M.R., and Lemon, N., 1996b. Influence of depositional environment on diagenesis and reservoir quality: Tirrawarra Sandstone reservoir, southern Cooper Basin, Australia. *Journal of Petroleum Geology*, v. 19, p. 369-391.

Rezaee, M.R., and Lemon, N., 1996c. Controls on Pore Geometry in the Tirrawarra Sandstone Reservoir, Cooper Basin, Australia. *Petroleum Exploration Society of Australia Journal,* v. 24, p. 125-146.

Rezaee, M.R., and Lemon, N., 1997. Estimation of Effective Porosity, Tirrawarra Sandstone, Cooper Basin, South Australia. *Australian Society of Exploration Geophysics Bulletin,* in press.

Rezaee, M.R., and Schulz-Rojahn, J.P., 1996. Application of quantitative back-scattered electron image analysis in isotope interpretation of siderite cement: Tirrawarra Sandstone reservoir, Cooper Basin (Australia), *in* Morad, S., (ed.), Carbonate Cementation in sandstones*: International Association of Sedimentologists Special Publication*, in press.

Rezaee, M.R., and Tingate, P.R., 1996a. Precipitation temperatures and origin of quartz cement and its influence on the Tirrawarra Sandstone reservoir quality, southern Cooper Basin, South Australia. *Geological Society Of Australia, Abstract No.41*, p.362. *13th Australian Geological Convention, Canberra, February, 1996.*

Rezaee, M.R., and Tingate, P.R., 1996b. Quartz Cement Trace Element Composition: A Key to Reveal the Origin of Silica?, *International Association of Sedimentologists Workshop* (Belfast), 13-14 May, 1996.

Rezaee, M.R., and Tingate, P.R., 1997. Origin of the quartz cement, Tirrawarra Sandstone, Southern Cooper Basin, South Australia. *Journal of Sedimentary Research,* v. 67, p. 168-177.

Rezaee, M.R., Lemon, N., and Seggie, R., 1996. Tectonic fingerprints in siderite cement, Tirrawarra Sandstone, southern Cooper Basin, South Australia. *Geological Magazine*, v. 133 (7), in press.

Riciputi, L.R., and Paterson, B.A., 1994. High spatial-resolution measurement of O isotope ratios in silicates and carbonates by ion microprobe. *American Mineralogist*, v. 79, p. 1227-1230.

Rider, M.H., 1986. *The geological interpretation of well logs*. John Wiley & Sons, New York, 175p.

Rink, M., 1976. A computerized quantitative image analysis procedure for investigating features and an adopted image process. *Journal of Microscopy*, v. 107, p. 267-386.

Rittenhouse, G., 1971. Mechanical compaction of sands containing different percentage of ductile grains: a theorical approach. *AAPG Bulletin*, v. 55, p. 92-96.

Ritter, H.L., and Drake, L.C., 1945. Pore-size distribution in porous materials; pressure porosimeter and determinations of complete macrpore-size distribution. *Industrial Engineering Chemical Analysis*, v. 17, p.782-786.

Rodda, J.S., and Paspaliaris, T.G.,1989. Tirrawarra and Moorari Oil Fields enhanced oil recovery schemes - further developments. *Australian Petroleum Exploration Association Journal,* v. 29, p. 121-130.

Roedder, E., 1979. Fluid inclusion evidence in the environments of sedimentary diagenesis, a review, *in:* Scholle, P.A., and Schluger, P.R., (eds.), Aspects of diagenesis: *SEPM Special Publication* 26, p. 89-108.

Roeder, E., 1984. Fluid inclusions. *Mineralogical society of America, Reviews in Mineralogy* 12, Washington.

Rosenbaum, J., and Sheppard, S.M.F., 1986. An isotopic study of siderites, dolomites and ankerites at high temperatures. *Geochimica et Cosmochimica Acta*, v. 50, p. 1147-1150.

Rosenfeld, W.D., and Silverman, S.R., 1959. Carbon isotope fractionation in bacterial production of methane. *Science*, v. 130, p. 1658-1659.

Russell, N.J., and Bone, Y., 1989. Palaeogeothermometry of the Cooper and Eromanga Basins, South Australia. In: O'Neil, B.J. (ed.), The Cooper and Eromanga Basins, Australia. Proceedings of the Cooper and Eromanga Basins Conference, Adelaide, 26-27 June 1989, p. 559-581.

Rust, B.R., 1972. Structure and process in a braided river. *Sedimentology*, v. 18, p. 221-245.

Scherer, M., 1987. Parameters influencing porosity in sandstones: a model for sandstone porosity prediction. *AAPG Bulletin*, v. 71, p. 85-491.

Schidlowski, M., Eichmann R., and Junge, C., 1976. Carbon isotope geochemistry of the Precambrian Lomagundi carbonate province, Rhodesia. *Geochimica et Cosmochimica Acta*, v. 40, p. 449-455.

Schidlowski, M., Eichmann, R., and Junge, C., 1975. Precambrian sedimentary carbonates: Carbon and oxygen isotope geochemistry and implication the terrestrial oxygen budget. *Precambrian Researchs*, v. 2, p. 1-69.

Schlumberger, 1987. *Log interpretation principles/applications*. 2nd edition. Schlumberger Educational Series.

Schmidt, V., and D. Mcdonald, A., 1979. The role of secondary porosity in the course of sandstone diagenesis. *SEPM Special Publication*, 26, p. 175-207.

Schulz-Rojahn, J.P., 1991. Origin, evolution and controls of Permian reservoir sandstones in the southern Cooper Basin, South Australia. Unpublished Ph.D. thesis, National Centre for Petroleum Geology & Geophysics, University of Adelaide, Australia. 187p.

Schulz-Rojahn, J.P., and Phillips, S.E., 1989. Diagenetic alteration of Permian reservoir sandstones in the Nappamerri Trough and adjacent areas, southern Cooper Basin. In: O'Neil, B. J., (ed.), *The Cooper and Eromanga Basins, Australia (Proceedings PESA/SPE/ASEG conference, Adelaide*, p. 629-645.

Schwartz, L., and Banavar, J., 1989. Transport properties of disordered continuum systems. *Physical Review B*, v. 39, p. 11965-11970.

Schwebel, D.A., Devine, S.B., and Riley, M., 1980. Source maturity and gas composition relationships in the southern Cooper Basin. *Australian Petroleum Exploration Association Journal*, v. 20, p. 191-200.

Seeman, U., and Scherer, M., 1984. Volcanoclastics as potential hydrocarbon reservoirs. *Clay Mineralogy*, v. 9, p. 457-470.

Seggie, R.J., Lansom, P.B., Hamlin, H.S., and Johnson, G.A., 1994. The Tirrawarra Oil Field: Field revitalisation through reservoir description and characterisation: *Australian Petroleum Exploration Association Journal*, v. 34, p. 33-54.

Senior, B.R., Mond, A., and Harrison, P.L., 1978. Geology of the Eromanga Basin. *BMR Bulletin* 167, 102p.

Serra, O, 1984. *Fundamental of well-log interpretation*. Elsevier Science Publisher, 423p.

Sibley, D.F., and Blatt, H., 1976. Intergranular pressure solution and cementation of the Tuscarora orthoquartzite. *Journal of Sedimentary Petrology*, v. 46, p. 881-896.

Siever, R., 1957. Pennsylvanian sandstones of the Eastern Interior Coal Basin. *Journal of Sedimentary Petrology*, v. 27, p. 227-250.

Siever, R., 1962. Silica solubility, 0-200 °C, and the diagenesis of siliceous sediments. *Journal of Geology*, v. 70, p. 127-150.

Simandoux, P., 1963. Dielectric measurements on porous media: application to the measurement of water saturation: study of behaviour of argillaceous formations. *Revue de l ' Institut Francais du Petrole*, v. 18, p. 193-215.

Singh, I.B., and Kumar, S., 1974. Mega and giant ripples in the Gang River, Utar Pradesh, India. *Sedimentary geology*, v. 12, p. 53-66.

Smalley, P.C., Maile, C.N., Coleman, M.L., and Rouse, J.E., 1992. LASSIE (laser ablation sampler for stable isotope extraction) applied to carbonate minerals. *Chemical Geology*, v. 101, p. 43-52.

Smith, J.V., and Steele, I.M., 1984. Chemical substitution in silica polymorphs. *Neus Jahrbuch fur Mineralogie Abhandlungen*, v. 3, p. 137-144.

Smith, N.D., 1970. The braided stream depositional environment : Comparison of the Platte River with some Silurian clastic rocks, North-Central Appalachians. *AAPG Bulletin*, v. 81, p. 2993-3014.

Smosna, R., 1989. Compaction law for Cretaceous sandstones of Alaska's North Slope. *Journal of Sedimentary Petrology*, v.59, p.572-584.

Smyth, M. 1979. Hydrocarbon generation in the Fly Lake-Brolga area of the Cooper Basin. *Australian Petroleum Exploration Association Journal,* v. 19, p. 108-114.

Smyth, M., 1983. Nature of source material for hydrocarbons in Cooper Basin, Australia. *AAPG Bulletin*, v. 67 p. 1422-1428.

Sneider, M., King, H.R., Hietala, R.W., and Connolly, E.T., 1984. Integrated rock-log calibration in the Elmworth Field, Alberta, Canada. *AAPG memoir,* 38, p. 205-282.

Soegaard, K., 1990. Fan-delta and braid-delta in pennsylvanian Sandia Formation, Taos Trough, northern New Mexico: Depositional and tectonic implications. *Geological Society of America Bulletin*, v. 102, p. 1325-1343.

Sommer, F., 1978. Diagenesis of Jurassic sandstones in the Viking Graben. *Journal of Geologcal Society of London*, v. 135, p. 63-67.

Spiro, B., Gibson, P.J., and Shaw, H.F., 1993. Eogenetic siderite in lacustrine oil shales from Queensland, Australia, a stable isotope. *Chemical Geology*, v. 106, p. 415-427.

Spötl, C., Matter, A., and Brevart, O., 1993. Diagenesis and pore water evolution in the Keuper Reservoir, Paris Basin (France). *Journal of Sedimentary Petrology*, v. 63, p. 909-928.

Sprigg, R.C., 1961. On the structural evolution of the Great Artesian Basin. *Australian Petroleum Exploration Association Journal*, v. 1, p. 37-56.

Sprunt, E.S., 1981. Causes of quartz luminescence colors. *Scanning Electron Microscopy*, v. 1, p. 525-535.

Staats, P.A., and Kopp, O.C., 1974. Studies on the origin of 3400 cm-1 region infrared bands of synthetic and natural a-quartz. *Journal of Physics and Chemistry of Solids*, v. 35, p. 1029-1033.

Stanley, D.J., and Halliday, G., 1984. Massive hydraulic fracture stimulation of Early Permian gas reservoirs, Big Lake Field, Cooper Basin. *Australian Petroleum Exploration Association Journal*, v. 24, p. 180-195.

Stanmore, P.J., 1989. Case studies of stratigraphic and fault traps in the Cooper Basin: *Australian Petroleum Exploration Association Journal*, v. 29, p. 361-369.

Stanmore, P.J., and Johnstone, E.M., 1988. The search for stratigraphic traps in the Southern Patchawarra Trough, South Australia. *Australian Petroleum Exploration Association Journal*, v. 28, p. 156-66.

Stephan, H.J., 1970, Diagenesis of the Middle Bunt sandstein in South Oldenburg, Lower Saxony: Meyniana, v. 20, p. 39-82.

Steveson, B.G. & Spry, A.H., 1973. Nature of porosity in some indurated Permian sandstones from the Cooper Basin. *Australian Petroleum Exploration Association Journal*, v. 13, p. 86-90.

Stuart, W.J., 1976. The genesis of Permian and Lower Triassic reservoir sandstones during phases of southern Cooper Basin development. *Australian Petroleum Exploration Association Journal*, v. 16, p. 37-47.

Stuart, W.J., Farrow, B.B., Lemon, N.M., and Phillips, S.E., 1990. Porosity and permeability in Permian sandstones: southern Cooper Basin. Final report, NERDDC Project No. 1175, National Centre for Petroleum Geology & Geophysics, University of Adelaide, Australia. 104p.

Stuart, W.J., Kennedy, S., and Thomas, A.D., 1988. The influence of structural growth and other factors on the configuration of fluviatile sandstones, Permian Cooper Basin. *Australian Petroleum Exploration Association Journal*, v. 28, p. 255-266.

Surdam, R.C., Boses, S.W., and Crossey, L.J., 1984. The chemistry of secondary porosity diagenesis, *in* McDonald, D.A., and Surdam, R.C., eds., Clastic Diagenesis. *AAPG Memoir,* 37, p. 127-150.

Swanson, B.F., 1977. Visualizing pores and non-wetting phase in porous rocks. *Society of Petroleum Engineers Annual Fall Technical Conference*, SPE Paper 6857, 10p.

Swanson, B.F., 1981. A simple correlation between permeabilities and mercury capillary pressures. *Journal of Petroleum Technology*, v. 33, p. 2498-2504.

Swineford, A., and Franks, P.C., 1959. Opal in the Ogallala Formation in Kansas: *in* Ireland, H.A., ed., Silica in Sediments. *SEPM Special Publication,* 7, p. 111-120.

Taylor, G.H., Liu, S.Y., and Smyth, M., 1988. New light on the origin of Cooper Basin oil. *Australian Petroleum Exploration Association Journal*, v. 28, p. 303-9.

Thomson, A., 1959. Pressure solution and porosity. In: H.A., Ireland, (ed.), Silica in sediments. *SEPM Special Publication,* 7, p. 92-111.

Thornton, R.C.N., 1973, Lithofacies study on the Toolachee Formation. Gidgealpa-Moomba-Big Lake area, Cooper Basin, South Australia. *Australian Petroleum Exploration Association Journal,* v. 13, p. 41-48.

Thornton, R.C.N., 1979. Regional stratigraphic analysis of the Gidgealpa Group, Southern Cooper Basin, Australia. *Geological Survey of South Australia, Bulletin* 49, 140 p.

Tieh, T.T., Berg, R.R., Popp, R.K., Brasher, J.E. and Pike, J.D., 1986. Deposition and diagenesis of Upper Miocene arkoses, Yowlumne and Rio Viejo Fields, Kern County, California. AAPG Bulletin, v. 70, p. 953-969.

Tingate, P.R., and Luo, P., 1992. Silica diagenesis and pore development in Permian sandstones, southern Cooper Basin. *Australian Petroleum Exploration Association Journal,* v. 32, p. 325-338.

Tissot, B.P., and Welte, D.H., 1978. *Petroleum formation and occurrence - a new approach to oil and gas exploration.* Springer Verlag, Berlin, 538p.

Tosaya, C., and Nur, A., 1982. Effects of diagenesis and clays on compressional velocities in rocks. *Geophysical Research Letters*, v. 9, p. 116-119.

Towe, K.M., 1962. Clay mineral diagenesis of a possible source of silica cement in sedimentary rocks. *Journal of Sedimentary Petrology*, v. 32, p. 26-28.

Tupper, N.P., and Burckhardt, D.M., 1990. Use of the methylphenanthrene index to characterise expulsion of Cooper and Eromanga Basin oils. *Australian Petroleum Exploration Association Journal*, v. 30, p. 373-385.

Veevers, J.J., 1984. *Phanerozoic earth history of Australia.* Oxford Geological Science Series, Oxford University Press, New York, 418p.

Vernik, L., 1994. Predicting lithology and transport properties from acoustic velocities based on petrophysical classification of siliciclastics. *Geophysics*, v. 59, p. 420-427.

Vernik, L., and A., Nur, 1992. Petrophysical classification of siliciclastics for lithology and porosity prediction from seismic velocities. *AAPG Bulletin*, v. 76, p. 1295-1309.

Vernik, L., and Nur, A., 1991. Lithology prediction and storage/transport properties evaluation in clastic sedimentary rocks using seismic velocities (abs.), *AAPG Bulletin*, v. 75, p. 384.

Walderhaug, O., 1990. A fluid inclusion study of quartz-cemented sandstones from offshore mid-Norway - possible evidence for continued quartz cementation during oil emplacement. *Journal of Sedimentary Petrology*, v. 60, p. 203-210.

Walderhaug, O., 1994. Temperatures of quartz cementation in Jurassic sandstones from the Norwegian continental shelf - evidence from fluid inclusions. *Journal of Sedimentary Research*, v. A64, p. 311-323.

Waldschmidt, W.A., 1941. Cementing materials in sandstones and their influence on the migration of oil. *AAPG Bulletin*, v. 25, p. 1839-1879.

Walker, T.R., 1960. Carbonate replacement of detrital crystalline silicate minerals as a source of authigenic silica in sedimentary rocks. *AAPG Bulletin*, v. 71, p. 145-152.

Wang, Z., Hirsche, W.K., Auman, J.B., 1989. Applications of acoustic velocity testing in petroleum exploration and production. *Canadian Society of Exploration Geophysics Recorder*, V. 14, p. 6-19.

Wardlaw, N.C., 1979. Pore geometry of carbonate rocks as revealed by pore casts and capillary pressure. *AAPG Bull*etin, v. 60, p. 245-257.

Washburn, E.W., 1921. Note on a method of determining the distribution of pore sizes in a porous material. *Procceding of the National Academy of Science*, v. 7, p. 115-116.

Waxman, M.H., and Smits, L.J.M., 1968. Electrical conductivities in oil-bearing shaly sands. *Society of Petroleum Engineers Journal*, v. 18, p. 107-122.

Webb, A.W., 1974. Geochronology of stratigraphically significant rocks from South Australia. Unpubl. progress report 7. S. Aust. Dept. Mines and Energy Open File Env. 1689, 5p.

Weyl, P.K., 1959. Pressure solution and the force of crystallisation - A phenomenological theory. *Journal of Geophysical Research*, v. 64, p. 2001-2005.

Whiticar, M.J., Faber, E., and Schoell, M., 1986. Biogenic methane formation in marine and fresh water environments: CO2 reduction vs. Acetate fermentation-isotope evidence. *Geochimica et Cosmochimica Acta*, v. 50, p. 693-709.

Wild, E.K., 1987. The sedimentology and reservoir quality of the Kinnerton Sandstone Formation, U.K. and the Tirrawarra Sandstone, South Australia (unpublished Ph.D. thesis) Department of Geology, University of Bristol, England, 370 p.

Wilkens, R.H., Simmons, G., Wissler, T.M., and Caruso, L., 1986. The Physical Properties of a set of sandstones - Part III. The effects of fine-grained pore-filling materials on compressional wave velocity. *Int. J. Rock Mech. Min. Sci. & Geomech. Abstr.*, v. 23, p. 313-325.

Williams, B.P.J., and Wild, E.K., 1984. The Tirrawarra Sandstone and Merrimelia Formation of the Southern Cooper Basin, South Australia- The sedimentation and evolution of a Glacio-fluvial system. *Australian Petroleum Exploration Association Journal*, v. 34, p. 377-392.

Williams, B.P.J., and Wild, E.K.,.1985. Late Carboniferous-Early Permian sandstone reservoir facies analysis in hydrocarbon exploration of the Gidgealpa Group, Southern Cooper Basin, Southern Australia. *Abstract-Geological society of Australia*, v. 12, p. 553.

Williams, B.P.J., Wild, E.K., and Suttill, R.J., 1985. Paraglacial aeolianites: potential new hydrocarbon reservoirs, Gidegalpa Group, southern Cooper Basin. *Australian Petroleum Exploration Association Journal*, v. 25, p. 291-310.

Williams, P.F., and Rust, B.R., 1969. The Sedimentology of a braided river. *Journal of sedimentary petrology*, v. 39, p. 649-679.

Wilson, J.C., and Mcbride, E.F., 1988. Compaction and porosity evolution of Pliocene sandstones, Ventura Basin, California. AAPG Bulletin, v. 72, p. 664-681.

Wilson, M.D., 1992. Inherited grain-rimming clays in sandstones from eolian and shelf environment: Their origin and control on reservoir properties. *SEPM Special Publication*, 47, p. 209-224.

Wilson, M.D., and Pittman, E.D., 1977. Authigenic clays in sandstone - Recognition and influence on reservoir properties and paleoenvironmental analysis. *Journal of Sedimentary Petrology*, v. 47, p. 3-31.

Wilson, M.J., 1987. *A handbook of determinative methods in clay mineralogy*. Blackie & Son Limited 549 p.

Winsauer, W.O., and McCardell, W.M., 1953. Ionic double-layer conductivity in reservoir rock. *Transactions of AIME*, v. 198, p. 129-134.

Wladerhaug, O., 1990. A fluid inclusion study of quartz-cemented sandstones from offshore mid-norway - possible evidence for continued quartz cementation during oil emplacement. *Journal of Sedimentary Petrology*, v. 60, p. 202-210.

Wopfner, H., 1966. A case history of the Gidgealpa Gas Field, South Australia. *Australian Oil & Gas Journal*, v. 12, p. 29-53.

Worthington, P.F., 1985. The evaluation of shaly-sand concepts in reservoir evaluation. *The Log Analyst*, v. 26, p. 23-39.

Wyllie, M.R.J., Gregory, A.R., and Gardner, L.W., 1956. Elastic wave velocities in heterogeneous and porous media. *Geophysics*, v. 21, p. 41-70.

Yew, C.C., and Mills, A.A., 1989. The occurrence and search for Permian oil in the Cooper Basin, Australia. *Australian Petroleum Exploration Association Journal*, v. 29, p. 339-359.

Young, I.T., Pevrerini, R.L., Verbeek, P.W., and Van Otterloo, P.J., 1981. A new implementation for the binary and Minkowski operators. *Computer Graphics and Image Processing*, v. 31, p. 189-210.

Youngs, B.C., 1975. The hydrology of the Gidgealpa Formation of the western and central Cooper Basin. Geological Survey of South Australia. Report of Investigations 43, 35p.

Zinkernagel, U., 1978. Cathodoluminescence of quartz and its application to sandstone petrology. *Contribution to Sedimentology* 8, Amesterdam, Elsevier, 69 p.

Zuffa, G.G., 1985. Optical analysis of arenites: Influence of methodology on compositional results, In: G.G., Zuffa, (ed.), Provenance of Arenites: Riedel Publishing Co.

ACKNOWLEDGMENTS

I am deeply grateful to the many people and institutions who assisted me to complete this research:

- SANTOS Ltd. is acknowledged for financial support during the study
- R. Seggie, R. Schlichting, L. Sepaeovich and R. McLean, from SANTOS Ltd.,
- Dr. D. Gravestock and E. Alexander from the Mines and Energy Department, South Australia (MESA)
- J. Terlet and H. Rosser from the Centre for Electron Microscopy and Microstructure Analysis
- Dr. K. Turnbull, W. Mussared, J. Stanley from the Geology Department, University of Adelaide
- Dr. P. Boult from the University of South Australia
- Dr. S. E. Phillips from Phillips-Gerrard Petrophysical Services
- B. Logan and his staff from the Core Library
- Wiltshire Geological Services for providing digital electronic log data.

I would like to express gratitude to the staff and students at the National Centre for Petroleum Geology and Geophysics (NCPGG) who helped me during the course of this study. I thank my supervisors, the late Dr. W.J. Stuart, Dr. N.M. Lemon and Prof. C. Griffiths for their invaluable advice and support. I am indebted to Dr. P. Tingate, Dr. J. Schulz-Rojahn and Mr. A. Mitchell for their encouragement and assistance through the duration of this study. M. Sutton, B. Wallis and N. Mann are acknowledged for their support and assistance.

I have also held useful discussions with researchers, who have visited the NCPGG, Dr. W. Galloway, Prof. R. Moussavi Harami, Dr. J. Collen.

The text of the thesis and the accompanying papers in Appendix 1 have benefited greatly from numerous editors and reviewers. They are acknowledged fully in the published papers.

Finally, my greatest acknowledgment goes to my wife and daughter, since without their never-ending support, encouragement and patience, the completion of this study would not have been possible.

Reservoir Characterisation of the Tirrawarra Sandstone in the Moorari and Fly Lake Fields, Southern Cooper Basin, South Australia

M.R. REZAEE

APPENDICES

Appendix 1	Copies of publications
Appendix 2	Point-count data
Appendix 3	XRD results
Appendix 4	Electron microprobe results of siderite
Appendix 5	Electron microprobe results of quartz
Appendix 6	Oxygen and carbon stable isotope results
Appendix 7	Fluid inclusions microthermometry results
Appendix 8	Mercury injection capillary pressures data
Appendix 9	CEC data
Appendix 10	Core analysis data
Appendix 11	Microporosity from BSE image analysis of kaolinite
Appendix 12	Wire-line log data
Appendix 13	Calculated sonic porosity from different equations
Appendix 14	Sonic porosity form the new equations
Appendix 15	Effective porosity from the new equation
Appendix 16	Water saturation from different equations

Rezaee, M.R. and Griffiths, C.M. (1996). Pore geometry controls on porosity and permeability in the Tirrawarra Sandstone Reservoir, Cooper Basin, South Australia. In *San Diego official program: 1996 AAPG Annual Convention*, May 19-22, 1996, San Diego Convention Center, San Diego, California.

Rezaee, M.R. and Griffiths, C.M. (1996). Porosity from sonic log in Kaolin-bearing Sandstones: a case study in the Tirrawarra Sandstone Reservoir, Australia. In *17th European Formation Evaluation Symposium (SPWLA)*, Amsterdam, The Netherlands, 3-7 June, 1996.

Rezaee, M.R. and Griffiths, C.M. (1996). Water saturation of Kaolin-bearing Sandstones: a case study in the Tirrawarra Sandstone Reservoir, Australia. In *17th European Formation Evaluation Symposium (SPWLA)*, Amsterdam, The Netherlands, 3-7 June, 1996.

Rezaee, M.R. and Lemon, N.M. (1996). Petrophysical evaluation of Kaolinite-bearing Sandstones: I: Water saturation (S_w), an example of the Tirrawarra Sandstone Reservoir, Cooper Basin, Australia. In *SPE Asia Pacific Oil and Gas Conference*, 28-31 October, Adelaide, Australia.

Rezaee, M.R. and Lemon, N.M. (1996). Influence of depositional environment on diagenesis and reservoir quality: Tirrawarra Sandstone Reservoir, Southern Cooper Basin, Australia. *Journal of Petroleum Geology*, 19(4), 369-391.

Rezaee, M.R. and Lemon, N.M. (1996). Controls on pore geometry in the Tirrawarra Sandstone Reservoir, Cooper Basin, Australia. In *San Diego official program: 1996 AAPG Annual Convention*, May 19-22, 1996, San Diego Convention Center, San Diego, California.

Rezaee, M.R. and Lemon, N.M. (1997). Estimation of effective porosity, Tirrawarra Sandstone, Cooper Basin, Australia. *Exploration Geophysics*, 28(2), 114 - 118.

Rezaee, M.R. and Schulz-Rojahn, J.P. (1998). Application of quantitative back-scattered electron image analysis in isotope interpretation of Siderite Cement: Tirrawarra Sandstone, Cooper Basin (Australia). In S. Morad (Ed.), *Carbonate Cementation in Sandstones: distribution patterns and geochemical evolution* (pp. 1-26). Oxford, UK: Blackwell Publishing Ltd.

Rezaee, M.R. and Tingate, P.R. (1996). Precipitation temperatures and origin of quartz cement and its influence on the Tirrawarra Sandstone Reservoir quality, Southern Cooper Basin, South Australia. In D. Senior and R. Abell (Leaders), *13th Australian Geological Convention*, Canberra, 19-23 February 1996.

Rezaee, M.R. and Tingate, P.R. (1996). Trace element composition of quartz cement: a key to reveal origin of Silica?. In R.H. Worden, *Quartz cement: origin and effects on hydrocarbon reservoirs: [IAS workshop, 13th-14th May 1996]*, Belfast, Northern Ireland: Geofluids Research Group, Queen's University of Belfast.

Rezaee, M.R. and Tingate, P.R. (1997). Origin of quartz cement in the Tirrawarra Sandstone, southern Cooper Basin, South Australia. *Journal of Sedimentary Research*, 67(1), 168-177.

Rezaee, M.R., Lemon, N.M. and Seggie, R.J. (1997). Tectonic fingerprints in siderite cement, Tirrawarra Sandstone, southern Cooper Basin, Australia. *Geological Magazine*, 134(1), 99-112.